Universität für Bodenkultur Wien
University of Natural Resources
and Life Sciences, Vienna

Doctoral Dissertation

Polymer biointerfaces for plasmonic nanostructures enabling fast, multiplexed, and sensitive detection of biomarkers

submitted by

DI[in] Simone HAGENEDER, BSc

in partial fulfilment of the requirements for the academic degree

Doktorin der Bodenkultur (Dr.nat.techn.)

Vienna, September 2021

Supervisors:
Dr. Jakub Dostalek and Prof. Dr. Wolfgang Knoll
Department of Nanobiotechnology and BioSensor Technologies, Austrian Institute of Technology

Acknowledgements

First of all, my deepest gratitude goes to Jakub Dostalek, who supported me professionally and personally during my journey. He has been a great supervisor, always available for advice and discussion. Thanks to him, I have grown to be a proficient scientist during the past years. The outcome of this research would never be possible without his support.

Furthermore, I want to thank Prof. Wolfgang Knoll for letting me do the PhD in his group and for his guidance.

Many thanks go to all the former and current colleagues at the BST group for the positive and thriving work atmosphere. Because of them, it was a pleasure to go to work every single day. Especially I am indebted to Stefan Fossati, my partner in a long PhD journey, Martin Bauch and Imran Khan, my favorite physicists, who were always available for advice. Special thanks go to my close colleagues and friends Nestor, Anıl, Jakob and Seba for scientific and personal support at all times and for proof-reading this thesis.

An extraordinary appreciation goes to the great women in my life for their support, advice, and love in all façades, especially the brilliant scientists which I am honored to call my friends: Hulan, Priya, Vanessa, Daria, Chiara, and Bernadette, it was a pleasure to share part of my path with you.

Thanks to Alexander for being there and always encouraging me, especially in times of difficulty.

Lastly, I would like to thank my whole family, particularly my parents, who helped cultivate an intellectual culture early on in my life, and always showed me their unconditional support. In addition, special gratefulness goes to my grandfather, who taught me to work hard to reach my goals and always keep an open mind.

To him, I dedicate this work.

Affidavits

I hereby declare that I have authored this dissertation independently, and that I have not used any assistance other than that which is permitted. The work contained herein is my own except where explicitly stated otherwise. All ideas taken in wording or in basic content from unpublished sources or from published literature are duly identified and cited, and the precise references included. Any contribution from colleagues is explicitly stated in the authorship statement of the published papers.
I further declare that this dissertation has not been submitted, in whole or in part, in the same or a similar form, to any other educational institution as part of the requirements for an academic degree.
I hereby confirm that I am familiar with the standards of Scientific Integrity and with the guidelines of Good Scientific Practice, and that this work fully complies with these standards and guidelines.

Vienna, September 2021

Simone Hageneder

Abstract

There is an increasing need in society for rapid, cost effective, and reliable detection of biomolecules for the purpose of diagnosing diseases, including early diagnosis of non-communicable and infectious diseases. Over the last years, these needs have been addressed by research in numerous biosensor technologies, where several key challenges must be addressed in order to enable accurate analysis of the low abundant species present in complex biological fluids. These challenges concern sensitivity and specificity in modalities that allow direct detection of the species without the need for extensive sample preparation steps and time-consuming (mostly enzymatic) amplification strategies.

The thesis combines optical biosensing methods that take advantage of metallic structures with tailored plasmonic characteristics. The work is particularly focused on their utilization for signal amplification, multiplexing with the ability to achieve femtomolar detection limits for proteins and implementation of the biosensor into compact readout devices.

First, plasmonic nanostructured surfaces were specially designed to be manufactured by scaled-up lithography methods and to be employed for weak optical signal amplification in surface plasmon resonance and surface plasmon-enhanced fluorescence spectroscopy readout of affinity binding events. Second, advanced biointerface architectures were developed in order to serve as an affinity binding matrix at the sensor surface. Several interdependent aspects of the sensor surface post-modification, of minimizing non-specific interactions and of additional (non-optical) signal enhancement were investigated. Finally, responsive polyelectrolyte brushes and poly[N-isopropylacrylamide (pNIPAAm)]-based hydrogels were used for sensitive detection of biomarkers in clinical saliva and plasma samples.

Kurzfassung

In der Gesellschaft besteht ein zunehmender Bedarf an einem schnellen, kosteneffizienten und zuverlässigen Nachweis von Biomolekülen, insbesonders in der Frühdiagnose von nicht übertragbaren und infektiösen Krankheiten. In den letzten Jahren wurden dafür zahlreiche Biosensortechnologien entwickelt, bei denen mehrere zentrale Herausforderungen gelöst werden müssen, um eine genaue Analyse der in komplexen biologischen Flüssigkeiten in nur geringer Menge vorkommenden Analyten zu ermöglichen. Diese Herausforderungen betreffen die Empfindlichkeit und Spezifität von Sensormodalitäten, die einen direkten Nachweis der Spezies ermöglichen, ohne dass umfangreiche Probenvorbereitungsschritte und zeitaufwändige (meist enzymatische) Amplifikationsstrategien erforderlich sind.

Diese Dissertation kombiniert optische Biosensormethoden, die sich metallische Strukturen mit maßgeschneiderten plasmonischen Eigenschaften zunutze machen. Die Arbeit konzentriert sich insbesondere auf deren Nutzung zur Signalverstärkung, auf Multiplexing und auf die mögliche Implementierung in kompakte Auslesegeräte, mit der Fähigkeit Proteinmoleküle bis zu femtomolaren Konzentrationen zu detektieren. Zuerst wurden spezielle plasmonische nanostrukturierte Oberflächen entwickelt, die mit skalierbaren Lithographieverfahren hergestellt werden und zur Verstärkung von schwachen optischen Signalen verwendet werden können. Diese werden für die Auslesung von Affinitätsbindungen mittels Oberflächenplasmonenresonanz und oberflächenplasmonenverstärkter Fluoreszenzspektroskopie eingesetzt. Zweitens wurden Biointerface-Architekturen entwickelt, um als Affinitätsbindungsmatrix an der Sensoroberfläche zu dienen. Dabei waren mehrere voneinander abhängige Aspekte der Post-Modifikation der Sensoroberfläche, der Minimierung unspezifischer Wechselwirkungen und der zusätzlichen (nicht-optischen) Signalverstärkung von Interesse. Schließlich wurde die Verwendung von reaktionsfähigen Polyelektrolytbürsten und Hydrogelen auf Poly[N-Isopropylacrylamid (pNIPAAm)]-Basis für den empfindlichen Nachweis von Biomarkern in klinischen Speichel- und Plasmaproben durchgeführt.

Figures

Acronyms

2D two dimensional. 18

3D three dimensional. 18

AI artificial intelligence. 4

ATR attenuated total internal reflection. 5–7

BRE biorecognition element. x, 2, 3, 9, 17–20, 22, 28, 63, 123

Da Dalton. 15

DNA desoxyribonucleic acid. 2, 17

EDC 1-ethyl-3-(3-dimethylaminopropyl)carbodiimide. 18

ELISA enzyme-linked immunosorbent assay. 19

EM electromagnetic. 123

fM femtomolar. 99

FO-SPR fiber-optic SPR. ix, 11

FoM figure of merit. 15

fwhm full width half maximum/minimum. 15

GC-SPR grating-coupled SPR. 10, 85

HOW hydrogel optical waveguide. ix, 12

Ig immunoglobulin. 19, 63

IoT Internet of Things. 4

K_D (equilibrium) dissociation constant. 3, 19

LbL layer by layer. 20

LCST lower critial solution temperature. 123

LOD limit of detection. 3, 15, 99, 123

L_p penetration depth. ix, 5, 6, 14

LSP localized surface plasmon. ix, 5, 12–14, 16

LSPR localized surface plasmon resonance. x, 13, 123

MAbs monoclonal antibodies. 19

MIP molecularly imprinted polymer. 20

MPG multi-period plasmonic grating. 99

MW molecular weight. 15, 21

NHS N-hydroxysuccinimide. 18

nM nanomolar. 3

OWS optical waveguide spectroscopy. ix, 11, 12, 49

PCR polymerase chain reaction. 142

PEF plasmon-enhanced fluorescence. 16, 17, 33, 49, 63, 99, 123

PEG poly(ethylene glycol). 23

pM picomolar. 3, 123

PNA peptide nucleic acid. 2

pNIPAAm poly(N-isopropylacrylamide). 63, 123

POC point of care. 4, 28, 33

PSP propagating surface plasmon. ix, 5, 6, 12–14

RCA rolling circle amplification. 49, 142

RI refractive index. ix, x, 8, 11–15

RIU refractive index units. 14, 15

RNA ribonucleic acid. 2, 17

RU refractive units. 14

SAM self-assembled monolayer. 20, 21, 23

SEIRAS surface-enhanced infrared absorption spectroscopy. 16

SERS surface-enhanced raman spectroscopy. 16

SI-ATRP surface initiated atom transfer radical polymerization. 21

SP surface plasmon. ix, x, 4–12, 15–17

SPFS surface plasmon enhanced spectroscopy. 4, 16, 33

SPP surface plasmon polariton. 4

SPR surface plasmon resonance. ix, 3–5, 7–15, 19, 27, 28

ssDNA single stranded deoxyribonucleic acid. 49

TE transverse electric. 12

TIR total internal reflection. 7

TM transverse magnetic. ix, 6, 12

TNF-α tumor necrosis factor alpha. 85, 141

UV-NIL UV-nanoimprint lithography. 28, 142

Table of Contents

CHAPTER 1

Introduction Into Biosensors

For decades, the demand for quick and easy-to-use yet reliable, sensitive, and specific sensors for detecting molecules or monitoring molecular interactions increased continuously. These tools have been widely researched, leading to a broad range of applications, from diagnosing certain diseases and monitoring therapeutic drugs to environmental observations, food safety and control, and biodefense and security. Since the earliest days of biosensing, advances in the field have been driven by practical considerations, working towards applications for creating a digital signal proportional to the concentration of a specific molecule.[1]

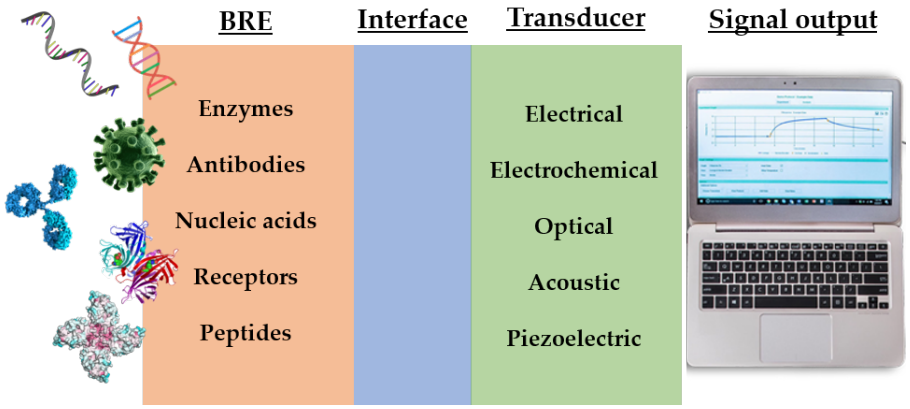

Figure 1.1: Scheme of biosensor components: Specific interaction of target molecules with the biorecognition elements results in a binding event, which is subsequently transformed into a readable signal employing a transducer.

By definition, biosensors are "integrated receptor–transducer devices, which are able to provide selective quantitative or semi-quantitative analytical information using a biological recognition element".[2] This description already states the two most important components a biosensor consists of, a biorecognition element (BRE) and a transducer. Furthermore, in a standard representation, a biosensor is divided into four parts, as depicted in fig. 1.1) Sensing elements or BREs, which should specifically interact with the targeted analyte 2) an interface, which provides an environment where the BRE sit, 3) a transducer, which converts the physical or chemical change associated with the binding event into a readable, electrical signal and 4) a set of electronic signal amplifiers, processors and an interface for data analysis.

Biosensors are often categorized according to their transduction mechanism or their type of biorecognition element. Depending on the physical or chemical property measured (the type of transducer), biosensors are divided into optical, electrochemical, acoustic, calorimetric, or piezoelectric-based devices.[3] Biosensors can be classified according to the BRE, nucleic acid-based (desoxyribonucleic acid (DNA), RNA ribonucleic acid (RNA),peptide nucleic acid (PNA),..),[4] protein-based (antibodies,..), peptide-based[5], or cell-based sensors can be differentiated.[1]

Since the first biosensor was developed in the 1960s for glucose monitoring,[7] the global market has expanded to a value of 25.5 billion USD in 2021. The field is expected to reach 36.7 billion USD by 2026.[8] When compared to other areas like industrial processes and environmental analysis, the healthcare sector has the most significant share by far,

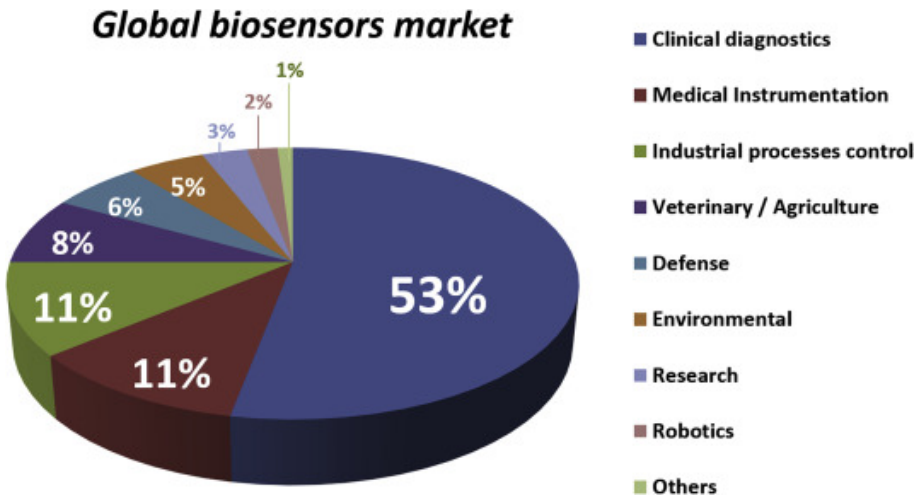

Figure 1.2: Global biosensor market in 2015 (reproduced under CC BY 4.0 © 2019.[6])

as 64% of the market is dedicated to medicine-related activities (see fig.1.2). [6]

In this context, medical diagnostics require biosensors able to detect biomarkers with sufficient sensitivity and thus prevent diseases or enable treatment at the earliest stage possible. In the first stages of cancer[9, 10], bacterial and viral infections[11], neuropsychiatric disorders[12], or cardiovascular diseases[13], only very low concentrations of biomarkers are present in the sample to be analyzed.[14] Therefore, a detection limit far below picomolar (pM) concentration in actual biological samples is crucial for viable commercial applications, which are much needed in the field.[14] Moreover, better sensitivity would enable new insights into disease onset and progression, particularly concerning various cancers.

According to the *IUPAC*, the International Union of Pure and Applied Chemistry, *Sensitivity* is the "slope of the calibration curve," which defines how well the method can discriminate changes in concentration. However, it is worth noting that in the field of biosensing, contrary to the definition, sensitivity is often used synonymously for the lowest detectable target analyte concentration (limit of detection (LOD)).[15] To enhance the sensitivity and improve the LOD of a sensor, finding the optimal combination of BRE and transducer is of utmost importance. On the one hand, catalytic biosensors are commonly utilized in conjunction with electrochemical detection. For example, most commercial glucose biosensors are based on enzymatic detection, where the oxidation of the analyte is catalyzed by an enzyme (most often glucose oxidase). The resulting current is shuttled to the electrode through artificial electron acceptors or mediators. The signal intensity can be directly translated to the concentration of glucose in the blood.[16]

On the other hand, affinity biosensors are preferably used with optical transducers, most prominently SPR, especially for the real-time observation of biomolecular interactions, which will be introduced in the following chapters.[17] The ability to reach an LOD below pM concentration depends on the type of the assay and, in the case of affinity biosensors, especially the affinity of the BRE to the analyte. With high affinity, LODs in the attomolar range can be easily achieved. However, this is most often not the case as most assays have an (equilibrium) dissociation constant (K_D) even above the nanomolar (nM) range.[18]

Furthermore, the transduction system as well as instrumentation set the boundaries for the performance of the sensor. Next to sensitivity, the main performance characteristics for biosensor development are the specificity of the sensor device and the response time.[19] The *specificity* (or selectivity) is the ability to discriminate a specific analyte in a complex

sample containing large amounts of other species. The main challenge causing reduced specificity is the non-specific binding of non-target compounds in the sample matrix. The *sensor response time* is defined by mass transport effects[20] and limited by the diffusion of the analyte to the surface. These can be optimized through the development of better microfluidic systems and lab-on-a-chip applications.[21] Additionally, especially in biomarker detection and research, the detection of a single analyte is often insufficient, as only changes in a panel of biomarkers enable a accurate diagnosis or provide reliable information on progression status.[10] Therefore, multiplexing, the possibility to detect a variety of analytes with one test.[22], is another major challenge in biosensor development. *Multiplexed sensors* can be beneficial as minimally invasive tests for early diagnosis of cancer using nucleic acids[23], proteins[24], or autoantibodies[25]. Additionally, it saves time and money for the patient as well as for the health care system. Furthermore, *point of care (POC)* diagnostics directly at the point-of-care are increasingly popular, requiring sample analysis outside a laboratory environment.[26] In this case, the focus in development lies not only in enhancing sensitivity, but they should also be robust, reliable, specific, fast, and easy to use by untrained persons without additional medical equipment. The readout can be as simple as by naked eye using lateral flow devices, like in pregnancy or COVID-19 rapid antigen tests, but these types of devices usually provide only a qualitative result.[27, 28, 29] However, even devices using more advanced integrated sample treatment and qualitative readout in the sensor can be miniaturized to a wearable size, e.g., as a watch.[30] Moreover, analysis and even the interpretation of the results using smartphones is paving the way for digital or mobile health (mHealth)[31], which can provide means for assisted health monitoring, including personalized interactions with the POC device.[32] Even further, due to advancements in fields like data analytics and the promotion and implementation of concepts like Internet of Things (IoT) and artificial intelligence (AI), monitoring of healthcare using POC devices holds great promise for the near future.[33]

1.1 Surface Plasmons

As this work mainly involves the use of surface plasmon resonance (SPR) sensors in conjunction with surface plasmon field-enhanced fluorescence (surface plasmon enhanced spectroscopy (SPFS)), as well as both surface and localized surface plasmon effects and optical waveguide phenomena to improve assays for the detection of molecules, these will be introduced below. Surface Plasmons (SPs) or surface plasmon polaritons (SPPs) can be described as waves originating from a collective oscillation of electron density at the

interface of a metal (e.g., gold) and a dielectric (e.g., liquid, gas, or solid).[34] SPs traveling along an interface of flat or corrugated continuous metallic films are termed propagating surface plasmons (PSPs). In contrast, SPs resonantly excited at nanostructures with a size much below the wavelength are referred to as localized surface plasmons (LSPs), both possibilities are depicted in fig. 1.3.

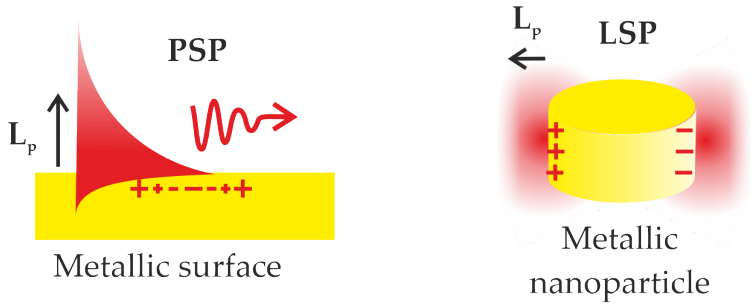

Figure 1.3: Scheme of PSPs and LSPs indicating the charge distributions and penetration depth L_p. (Adapted by permission from Springer Nature © 2016.[35])

1.2 History of SPs

Surface plasmons were first observed and described by Wood by shining polarized light onto a metallic diffraction grating, and a pattern of dark and bright bands appeared in the reflected light spectrum.[36] The phenomenon was only later explained by Fano through theoretical analysis, associating it to the "quasi-stationary waves [..] which can be strongly excited on the surface of metallic gratings".[37] At the end of the 1950s, the SPR theory was developed and scientifically proven, describing the energy loss associated with the SPs occurring when an electron beam passed through metallic thin films in contact with the dielectric.[38, 39, 40] The optical excitation of SPs by attenuated total internal reflection (ATR) was shown in the 1960s by Otto[41] and Kretschmann and Raether.[42, 43] Based on these findings, Nylander and Liedberg developed the first SPR biosensor device, capable of label-free and real-time observation of biomolecular binding studies.[44] In 1990, Pharmacia brought the first commercial instrument to the market, the BIAcore,[45] which was further improved in sensitivity, automation, multiplexing, simplicity, and throughput. Since then, commercial SPR-based biosensors have been used to detect molecules and to study their interactions in academic (i.e., life and material sciences), industry (i.e., pharmaceutical drug discovery, material characterization), and medical research(i.e., clinical studies for identification of targets). However, most commercialized SPR biosensors are not designed for application outside of laboratories and for in-field

measurements. Therefore, research is continuously seeking to improve the applicability on-site and enhance performance parameters like sensitivity and selectivity.

1.3 Propagating Surface Plasmon Resonance

PSPs are 2D electromagnetic waves propagating along a metal-dielectric interface with a TM transverse magnetic polarization. Thereby the propagation constant β can be defined as:

$$\beta = k_0 \sqrt{\frac{n_m^2 n_d^2}{n_m^2 + n_d^2}}, \tag{1.1}$$

where n_m and n_d are the refractive indices of metal and dielectric, respectively. Furthermore, $k_0 = 2\pi/\lambda = \omega/c$, the propagation constant of light in a vacuum with an angular frequency ω, wavelength λ, and velocity of light in a vacuum c.[46, 47]

The SP modes that probe the dielectric medium have an electric field intensity of $|E|^2$, which perpendicularly decays away from the interface with a penetration depth L_p. This electromagnetic field distribution exhibits an evanescent wave profile. The probing depth for an adjacent medium is usually defined as $L_p/2$, which for a gold surface in contact with water and an excitation light with $\lambda = 633nm$, yields about 100 nm. This means that a slice with such thickness can be utilized for selective optical sensing experiments. [35, 48, 49]

When depicted in a $k - \omega$ diagram (fig. 1.4), the SP dispersion curve and the light line of the dielectric ($\omega = ck$) do not intersect at any point. The propagation constant β is always greater than the wave vector k of light. Therefore, SPs cannot be excited by a light beam directly impinging at a flat metal surface. The energy and momentum of the incident light beam must be matched with those of the SPs, which is not possible without employing special couplers.[50] These different matching configurations will be further discussed, namely ATR based on prism coupling in Otto or Kretschmann configuration, diffraction gratings, optical waveguides, or fiber optic systems.[51]

1.3.1 Prism coupling

For the prism coupling, additional momentum is added via a prism providing a higher refractive index n_p, which means a beam which is reflected at the prism-metal interface

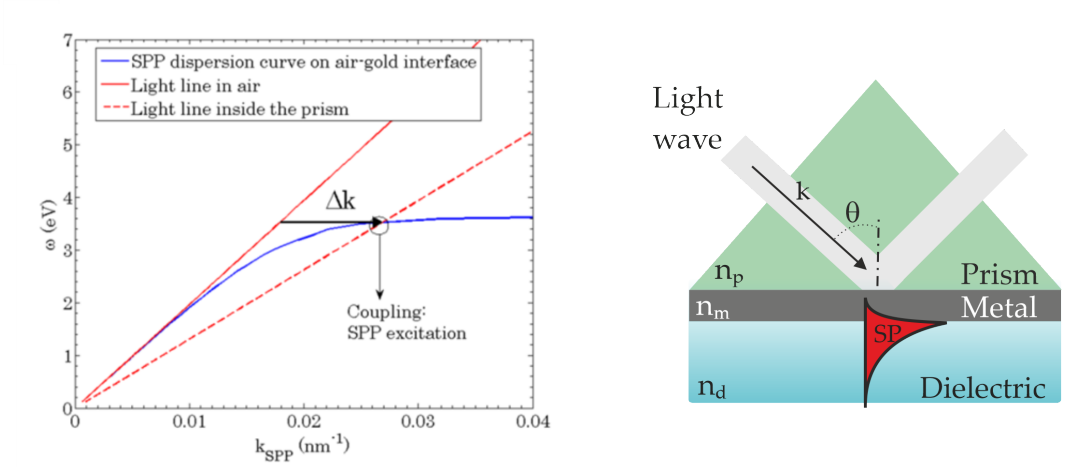

a) b)

Figure 1.4: a) $k - \omega$ graph showing the dispersion relation of SPs and light in air and with a prism (reproduced under CC BY 3.0 © 2012[52]) and b) prism coupling using Kretschmann configuration.

will have an in-plane momentum of [50, 53]

$$k_x = k_0 n_p sin\theta \tag{1.2}$$

This allows excitement of SPs at the outer interface between a metal and a dielectric with lower refractive index $n_d < n_p$. In the diagram in 1.4 (a), this additional momentum leads to an occurrence of an intersection of the dispersion curves of the SPs and the light line inside the prism (see 1.4 (a)). In the most common case of prism coupling of SPs using Kretschmann configuration of attenuated total reflection (ATR), a thin metal film is directly placed on top of a high refractive index prism (1.4 (b)). If the photons from the excitation beam propagate through the prism and are made incident at the thin metal layer, a part of the light energy is reflected into the prism, and a part tunnels through the metal. The metal acts as a mirror at a certain angle of incidence and reflects all the light back into the prism (= total internal reflection (TIR)). If the angle is above the critical angle of TIR, photons can tunnel through the metal film in the form of an evanescent wave and excite SPs at the interface. The back-reflected light intensity decreases until it reaches a minimum, at the SPR angle, where the SPs take up most of the energy.[47, 54]

A practical example for sensing using angular modulation is depicted in fig. 1.5 (a-c). The intensity of the light reflected to the detector is recorded as a function of the incidence

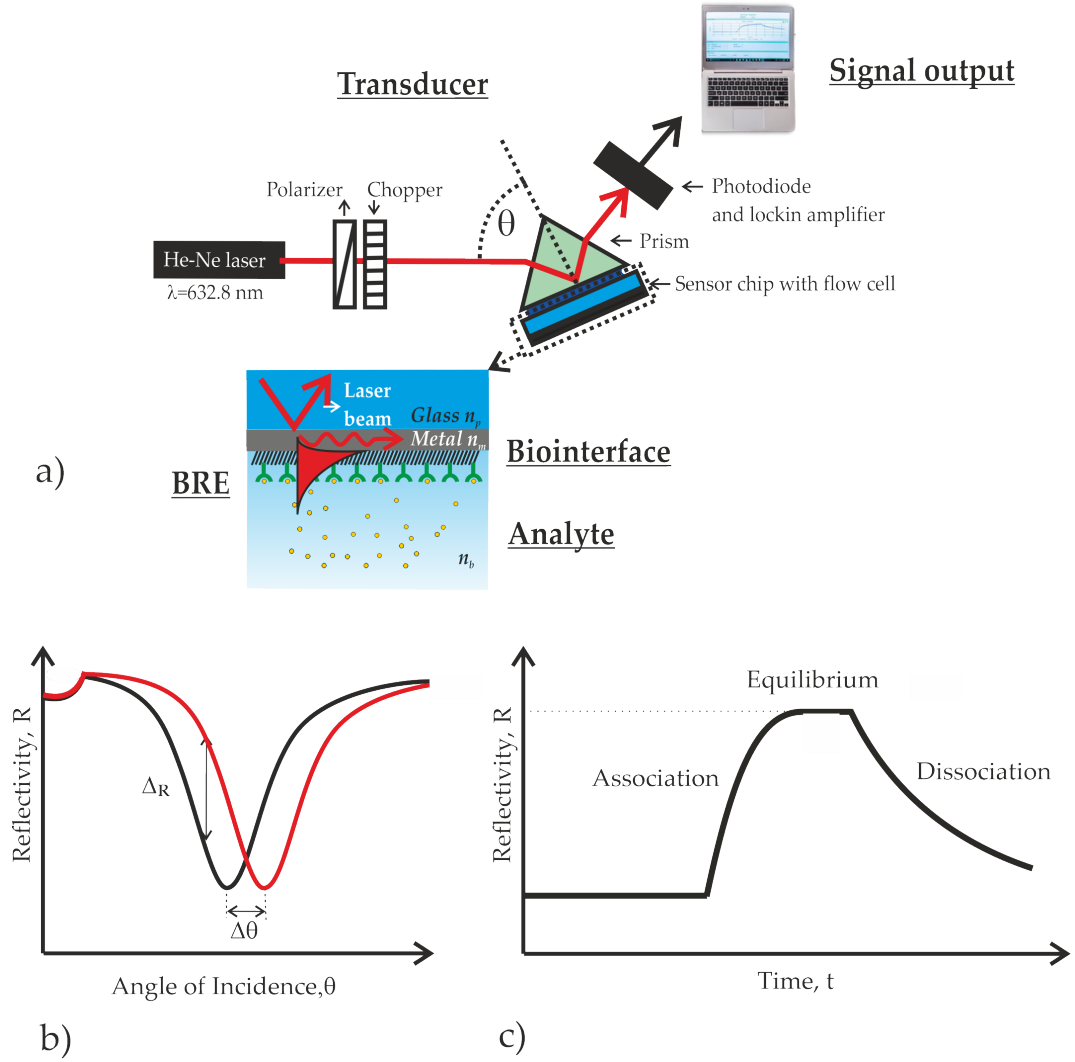

Figure 1.5: a) Example of optical system highlighting the most important components of the biosensor b) Angular reflectivity spectra and shift in the SPR angle due to binding and subsequent RI increase at the sensor chip surface and c) corresponding sensogram.

angle θ. Any refractive index increase in the dielectric layer (n_d) (i.e., through the binding of an analyte leading to mass accumulation on the surface) leads to an increase of the propagation constant β of the SP. Then, the coupling condition will be fulfilled only if the wave vector of the incoming light is greater than before. This is accompanied by a shift in the position of the reflectivity minimum, the resonant angle θ, of the curve, as shown in fig. 1.5 (b). Practically, each binding event on the surface leads to an electrical signal processed via respective instruments and software into readable data

that can be further processed. By setting the incidence angle to a fixed position in the part of the reflectivity curve with the highest derivative (largest changes), variations in reflectivity can be monitored as a function of time (see fig. 1.5 (c), enabling real-time monitoring of binding events and deriving kinetic parameters of affinity interactions in a so-called sensogram.[55] Thereby each step of biomolecular interactions can be followed and analyzed. A typical experiment starts by recording a baseline in buffer, then the analyte is injected into the system and its binding to the BRE on the surface can be tracked as an increase in the response in the sensogram (= association phase). After the reaction reaches an equilibrium where no further change in the SPR signal can be observed, the buffer is again injected into the system, leading to a dissociation phase, seen as a decrease in SPR response.

The described angular modulation (depicted in fig. 1.5 (a) is the most commonly implemented method, which is also used in BIAcore apparats.[44] Nevertheless, the SPR can also be monitored through other characteristics of the light wave coupled to SPs, e.g., intensity, phase, polarization, or wavelength modulation of the light. [56, 57]

1.3.2 Grating coupling

Another way to achieve phase-matching of an incident wave with SPs is the use of diffraction on periodically corrugated metallic surfaces (see fig. 1.6). Thereby, the missing wavevector Δk_x enables the phase-matching of the far-field light beam with the wavevector $k_x = ksin\theta$ to the SP propagation constant β by:

$$\Delta k_x = m\frac{2\pi}{\Lambda} \tag{1.3}$$

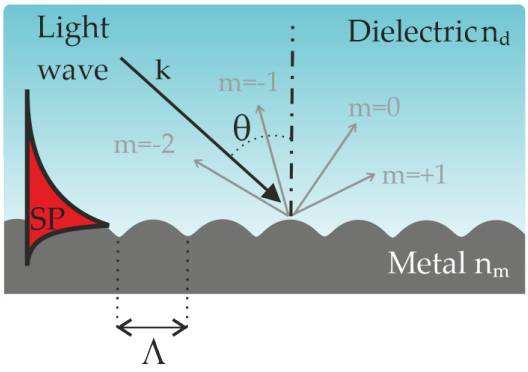

Figure 1.6: Schematics of the excitation of SPs on a diffraction grating.

and

$$\beta = ksin\theta \pm \Delta k_x \tag{1.4}$$

where $m = 0, \pm 1, \pm 2, ..$ are attributed to the diffraction orders generated in the reflected light beam and Λ is the periodicity of the grating.[50, 58] Similar to prism coupling, the wavevector can be tuned.

The resonant wavelength is determined by the period and the amplitude of the grating. Analogously to prism coupling, the SP excitation is manifested as a minimum in the reflected light, as depicted in fig. 1.7.

With typical (grating-coupled SPR (GC-SPR)), the incident and reflected beam have to pass the flow cell harboring the sample solution, requiring it to be optically transparent and making the measurement prone to scattering or absorption of the passing light and fluctuations of the passing liquid.[59] This leads to a decreased stability of the sensor in comparison to the Kretschmann configuration. Additionally, GC-SPR requires more complex mathematical models for prediction of the sensor response and to design the structures.[58] Therefore, although systems based on gratings have been developed alongside the prism coupled systems,[60, 61, 62] they remained the "alternative" approach as prism coupling is predominately used for commercial SPR sensor instruments nowadays due to their simple handling and high sensitivity. Nevertheless, compared to the relatively

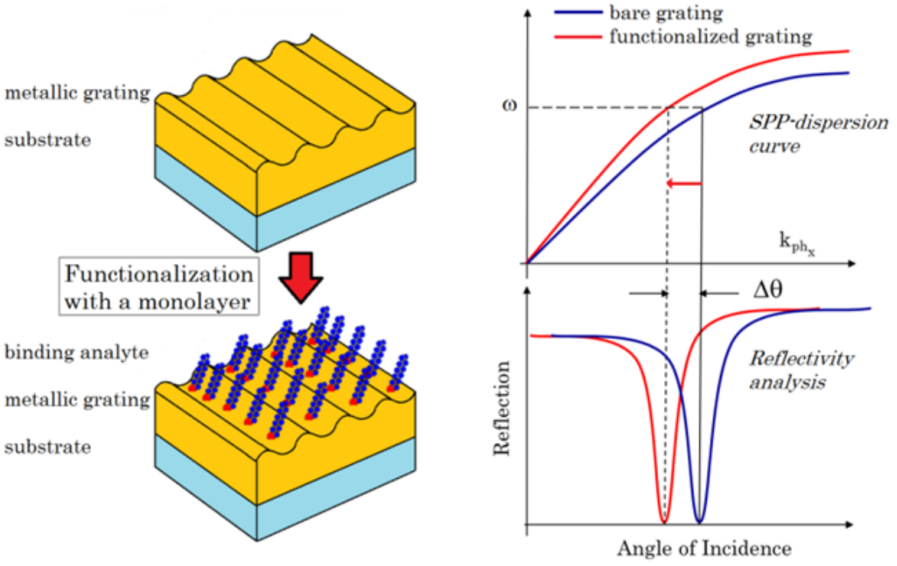

Figure 1.7: GC-SPR (reproduced under CC BY 3.0 © 2012 [52])

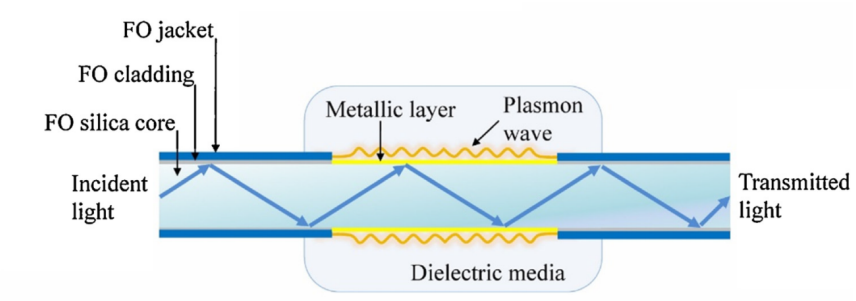

Figure 1.8: Schematic of commonly used FO-SPR (Reprinted with permission from Elsevier from [69])

"bulky" prism coupling systems, there is no need for precise control of the layer thickness of the metal; they can be cheaply made, offering the possibility for scale-up to industrial dimensions.[63]

1.3.3 Waveguide coupling

SPR measurements can also be utilized by resonant interaction between modes of a dielectric waveguide and SPs in various configurations.[56, 64, 65, 66]

Fiber-optic SPR (FO-SPR)

With optical fibers, the cylindrical higher refractive index core of the fiber serves as an optical waveguide. SPR sensing takes place on the outer surface of the fiber, where the cladding is stripped off and a gold layer deposited (see fig. 1.8).[67, 68] Different wavelengths at which the light is coupled are sweeped through, and the intensity of each wavelength coupling with the plasmons varies if mass accumulates (e.g., a binding event takes place).

Optical Waveguide Spectroscopy

The SPR techniques described so far deal with optical fields confined to a region a few hundred nm above the transducing surface. Observation beyond these regions can be made possible by using additional guided waves supported by layers attached on top of the SPR supporting metal film. If there is for example a polymer film attached to the metal surface with a sufficiently large RI and thickness, it is possible to excite dielectric waveguides, a technique called optical waveguide spectroscopy (OWS).[70, 71]

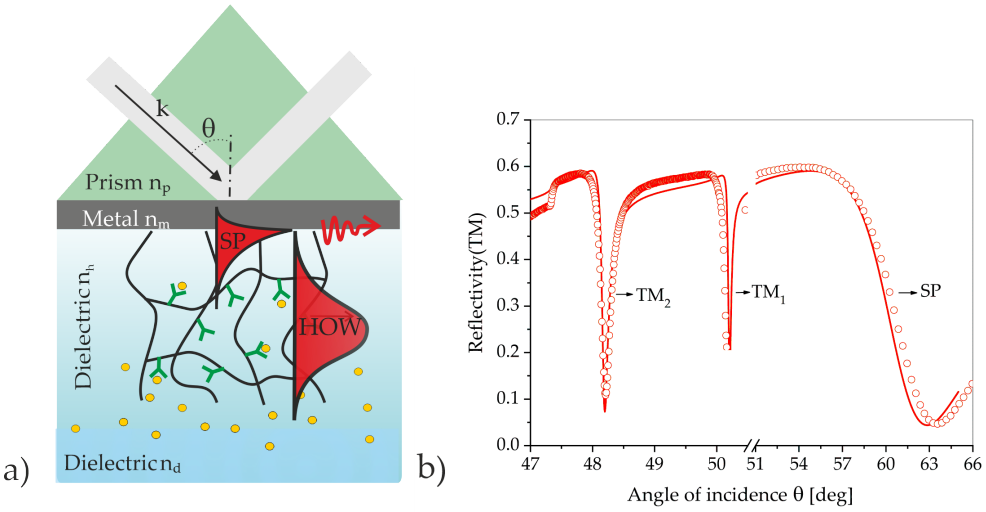

Figure 1.9: OWS using Kretschmann configuration: a) Schematic of the excitation of the polymer [hydrogel optical waveguide (HOW)] as well as SP waves. b) Example of TM reflectivity spectra measured in a µm thick dielectric layer.

In the Kretschmann configuration, it is possible to implement waveguide spectroscopy additionally to the SPR in order to observe characteristic changes in the optical properties of the layers (e.g., through a binding event), like thickness and RI, independently. The changes can be observed in real-time and with higher accuracy than with regular SPR in a range from 100 nm up to several microns away from the surface.[72] In addition to the SPR minimum peak, extra waveguide modes appear as dips in the angular reflectivity spectrum at angles that fulfill the phase-matching condition between the light beam and the guided dielectric wave at the sensor surface.[73]

By analyzing the different waveguide modes measured in reflectivity for transverse magnetically polarized, (TM-) see fig. 9) and transverse electrically polarized, (transverse electric (TE)-) polarization and fitting them with a Fresnel reflectivity-based model, the properties of the biointerface can be assessed.[73]

1.4 Localized Surface Plasmon Resonance

SPs do not only travel along the interface of flat or corrugated continuous metallic surfaces like shown above – propagating surface plasmons (PSPs), they can also be excited at nanostructures smaller than the λ of the incident optical wave and are then termed localized surface plasmons (LSPs).

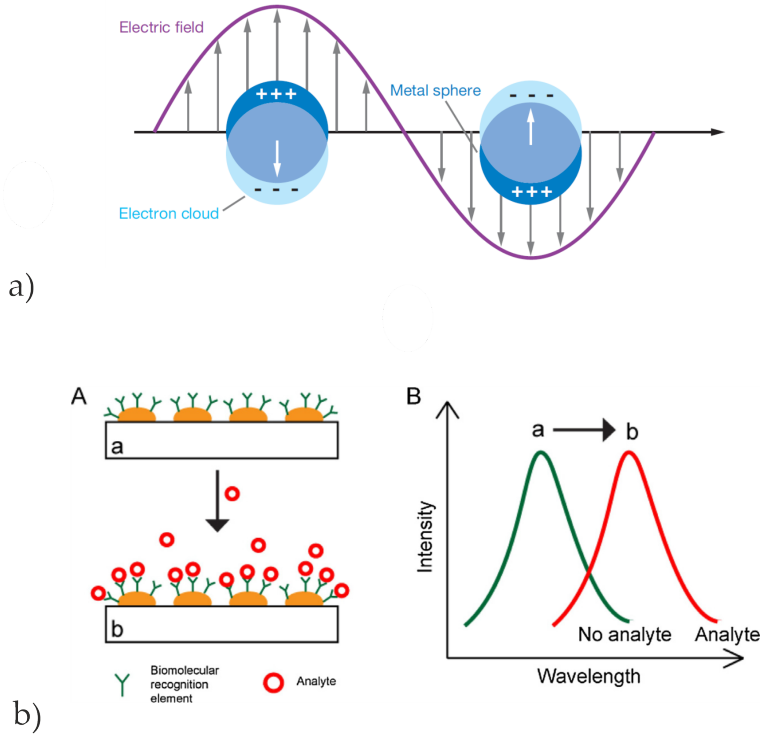

Figure 1.10: : a) Scheme of LSPR on a metal nanoparticle (reproduced with permission from Annual Reviews[74]) b) LSPR sensing on a metal nanostructure. Through the change in RI by binding of an analyte, a peak-wavelength shift is induced. (Reprinted with permission from Elsevier from [75])

Compared to the former, the incident light is much more confined to the surface, and when its energy is coupled into LSPs, a strong electromagnetic field intensity is generated around the nanostructures. Any changes in the vicinity of this field (e.g., a change of RI through a binding event) can be seen as spectral changes (i.e., the plasmon peak position in the absorption wavelength spectrum of transmitted light) (see fig. 1.10 (b)). The spectral position depends on many properties like size, shape, or material of the nanostructures and the interaction with other structures and the surrounding environment.[76, 77, 78] Compared to PSPs, LSPs can only probe several nanometres away from the surface.[79] The biosensors presented until now are also termed refractometric sensors, as refractive index changes upon reactions on the surface are tracked by monitoring variations in the SPR spectral characteristics, e.g., coupling angle θ_{spr} or resonant wavelength λ_{spr}, which are then fitted with respective analytical functions. An approximate surface mass density

Γ of the biolayer is calculated by:

$$\Gamma = d(n_b - n_s)\frac{\delta c}{\delta n}, \tag{1.5}$$

where Γ is given in mass per area, (e.g., pg/mm^2), d is the thickness of the biolayer, n_b and n_b are the refractive indices of the biolayer and the solvent, respectively, and $\frac{\delta c}{\delta n}$ is the incremental change in refractive index with the concentration, which for depending on the biomolecules is around 0.1-0.2 $\frac{mm^3}{mg}$.[80, 81] Often, especially in commercial Biacore™ instruments, the term refractive units (RU) is used as a unit for surface coverage, which is defined as:[54]

$$1RU \rightarrow 1\frac{pg}{mm^2}. \tag{1.6}$$

The changes measured in coupling angle θ_{spr} or wavelength λ_{spr} due to refractive index changes depend on the thickness of the biolayer, as the probing field exponentially decreases with the probing depth $L_p/2$.[82] The refractive index sensitivity of an SPR biosensor is defined as a ratio of SPR coupling angle $\delta\theta_{spr}$ or wavelength shift $\delta\lambda_{spr}$ and the RI change.

$$S_{\theta b} = \frac{\delta\theta spr}{\delta n_b}, \tag{1.7}$$

$$S_{\lambda b} = \frac{\delta\lambda spr}{\delta n_b}. \tag{1.8}$$

The refractive index sensitivity of a prism-based system is around 1000-10000 nm/refractive index units (RIU) or 100-200°/RIU, whereas, in grating-coupler-based SPR sensors, it is around half of these values.[58] Refractive index units (RIU) are the relative change in the refractive index of the medium, a quantity to describe SPR sensitivity based on the bulk fluid, which gives a reasonable estimate for the sensor's performance. Nevertheless, it is not necessarily identical to the sensitivity for detecting biomolecular binding events happening on the surface, which is more accurately expressed by the term of surface coverage introduced before.[83, 84] The longer probing depth $L_p/2$ of PSPs leads to around 20 times higher bulk refractive index sensitivity for PSP biosensors in comparison to LSP sensors, but a very similar sensing performance, especially at thicknesses below 10 nm, due to the stronger localization of the LSP.[74, 85, 86] Performance can also be

characterized by the figure of merit (FoM):[87]

$$FoM = \frac{S_b}{fwhm}, \tag{1.9}$$

where full width half maximum/minimum (fwhm) is the full width at half-maximum (or minimum) of the SPR dip or peak. often dimensioned at RIU^{-1}.[88] The *resolution* is the smallest change in the RI, which produces a change that can be resolved by the device. It is typically expressed as the standard deviation of the baseline noise σ, divided by the sensitivity of the respective detection approach, $S_{b\theta}$ or $S_{b\lambda}$

$$RI - resolution = \frac{\sigma}{S_b}. \tag{1.10}$$

For prism-based systems, the resolution is usually around $10^{-6} - 10^{-7}$ RIU, which is the relative change in the RI of the medium, whereas grating based-systems and optical fiber-based systems are around $10^{-4} - 10^{-6}$ RIU.[58, 89] Another parameter which is also termed analytical sensitivity is the *limit of detection* (LOD). It is the lowest concentration of the analyte that can be reliably detected[90] and both assay and instrument dependent. In this work, it is defined as:

$$LOD = X_b + 3SD, \tag{1.11}$$

where X_b is the mean concentration of the blank and S_b is the standard deviation of the blank. Standard SPR biosensing instruments can detect a monolayer of large analytes with a molecular weight molecular weight (MW) above 1000 Dalton (Da).[55, 54] To detect smaller MW analytes, concepts to improve sensitivity and LOD have been investigated intensively in the field, leading to advances in instrumentation, novel structures, and sensing approaches[51], as well as in the context of surface functionalization and assay design. For instance, in refractometric sensing, the signal can be enhanced simply through competition and inhibition assays [91, 92] or sandwich assays using nanoparticles as labels.[93] Additionally, the change in the conformational structure of molecules or any other effects leading to a redistribution of mass on the surface can utilize the different penetration depths of the SPs and make detecting low MW analytes with SPR possible.[94, 95] Besides that, methods have been established, which are utilizing the enhanced and confined electromagnetic field intensity exhibited by SPs on metal surfaces,

including surface-enhanced raman spectroscopy (SERS)[96], surface-enhanced infrared absorption spectroscopy (SEIRAS)[97], and SPFS[98], the latter will be discussed further below.

1.5 Fluorescence and Plasmon-Enhanced Fluorescence Spectroscopy

Fluorescence is to a process where a photon is absorbed by a molecule, a fluorophore, at a particular wavelength λ_{abs} and re-emitted at a longer wavelength λ_{em}.[99] Absorption and emission transitions upon fluorescence are traditionally depicted by using the Jablonski diagram (see fig. 1.11 (a).[100]

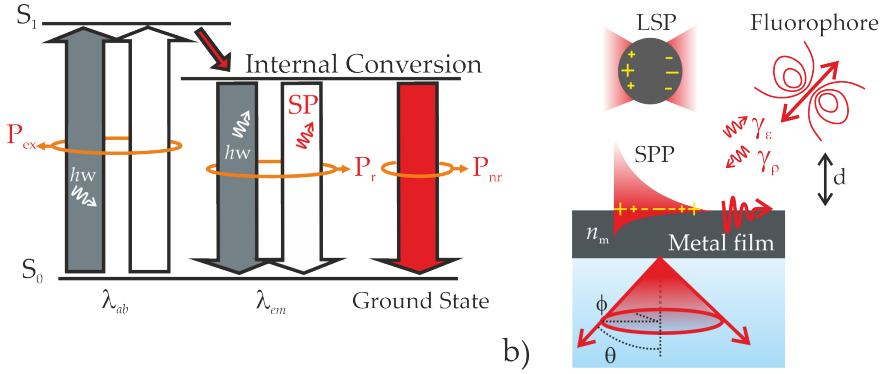

Figure 1.11: a) Jablonski diagram b) Schematic of SP field modes coupled with a fluorophore (reproduced under CC BY 2.0 © 2013 [101])

By absorbing a photon, the orbital electron at the ground state S_0 is shifted into an excited state with higher energy, followed by a rapid relaxation to the lowest vibrational level of the S_1 state corresponding to internal conversion. Then, a photon can be emitted as the electron shifts back to the S_0 ground state. Through this process, λ_{em} is longer than λ_{abs} due to the Stoke's shift. Both SPs and LSPs can be employed for fluorescence signal amplification, a technique termed plasmon-enhanced fluorescence (PEF). The fluorescent molecules are coupled with the strong electromagnetic field of SPs confined at the surface of metallic thin films or nanostructures, as depicted in the scheme in fig. 1.11 (b) [98, 101, 102] For optical waveguide fluorescence spectroscopy, at the resonance angles of the modes, the guided waves can be used to excite fluorophores in the thin film.[103] For fluorescent assays, the emitters are usually organic fluorophores conjugated with biomolecules (proteins, peptides, nucleic acids) serving as labels.[104] The light used for the excitation of SPs is coincident with the λ_{abs} of the used fluorescence dye.

Three main mechanisms contribute to the PEF: 1) The rate of excitation from ground to excited state is enhanced at λ_{abs},[105, 106] 2) the quantum yield is changed by opening additional radiative decay channels by SPs[107] and 3) the emission is altered to allow more directional distribution confined to certain angles for higher collection efficiency at λ_{em}.[108]

1.6 Biointerface architectures

A crucial step in biosensor design is the combination of the usually inorganic materials on the substrate with the organic layers to form a functional biointerface. Especially important is the immobilization strategy to align with the choice of the BRE, which can be proteins, antibodies, peptides, aptamers, DNA, RNA, and many more. The immobilization method depends firstly on the application, the size and the characteristics of the analyte, and the type of BRE to be bound to the surface. Essential considerations are first to preserve the structure of the BRE and its functionalities, secondly to orient the BRE in a favorable direction, and thirdly, to assure a high density of BREs on the surface (sometimes steric hindrance effects have to be taken into account). The fourth important point is to provide an architecture which is allowing the least possible amount of unspecific binding to the surface. Because not only the desired specific interaction contributes to the signal of the sensor, but also non-specific interaction of other species in the matrix may cause a false response or block the surface.

1.6.1 Immobilization strategies

Due to its chemical inertness and stability, gold is the most widely employed metal for the excitation of SPs in biosensing. As a result, various protocols for its modification have been developed and optimized over the years.[109] The most straightforward approach of attaching a BRE to the surface is physical adsorption to a metal surface. Basic forces determine these interactions at the molecular level, mainly ionic, hydrophobic, and polar interactions between the molecules and the surface.[110] The disadvantage of this technique is, on the one hand, the often low surface coverage and random orientation, but also the tendency of the molecules to rearrange in their energetically most favorable state over time, impact reliability and reproducibility of the assay.[111, 112] These limitations have led to the development of more advanced architectures through controlled introduction of specific functional groups on the surface.

Covalent coupling

Functional groups can couple BRE covalently to the surface via an activation step. Carboxylic groups are widely used as they can effortlessly be introduced in two dimensional (2D) or three dimensional (3D) architectures (see sec.1.6.3 and 1.6.4) and can couple reactive nucleophiles to the surface. These can be primary amine groups (e.g., in the amino acid lysine in peptides or proteins) to form amide bonds or hydroxyl groups to form covalent ester bonds. For coupling in aqueous solutions, the carbodiimide reagent 1-ethyl-3-(3-dimethylaminopropyl)carbodiimide (EDC) is utilized to create a reactive O-acylisourea group which can couple with the amine group[110, 112, 113] (see fig. 1.12). N-hydroxysuccinimide (NHS) is often used as an ester-forming compound to stabilize

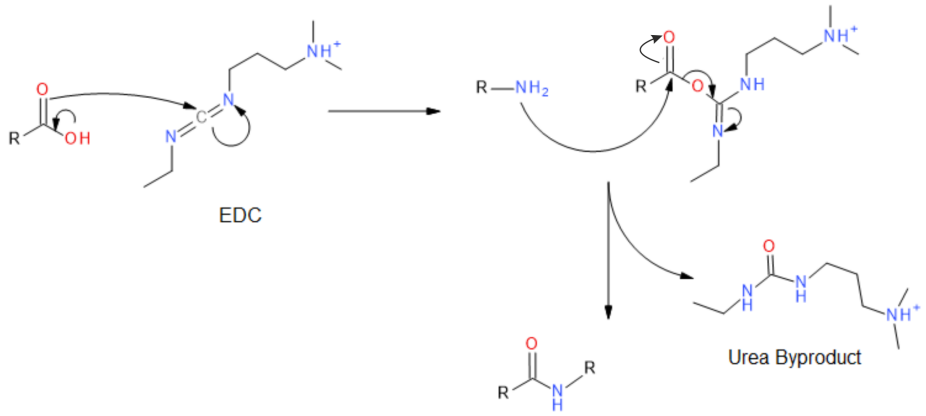

Figure 1.12: Activation of carboxylic acid groups and formation of a covalent amide bond with the BRE (reproduced under CC BY-SA 4.0 © 2019 [114]

the O-acylisourea intermediate group before forming the covalent bond. The addition of ethanolamine in excess blocks any remaining activated groups.[115] The coupling conditions often require optimization depending on the molecules (e.g. pH, ionic strength, time). Usually, a slightly acidic buffer is used, as most proteins are positively charged, and electrostatic attraction to the negatively charged surface allows a higher immobilization yield through the local attraction.[116] Another coupling mechanism is the copper(I)-catalyzed 1,3-dipolar cycloaddition of azide and alkynes to form 1,2,3-triazoles, termed "click chemistry."[111, 117, 118] It is highly selective, fast, irreversible, and provides a high yield. A subclass of click chemistry reactions is termed bioorthogonal reactions, which are highly selective and work completely inert without metal catalysts, which might be interfering with biological systems.[119] Other covalent coupling techniques include the coupling of thiol groups to reactive groups like pyridyl disulfides, maleimide,

and acyl halide derivates; or coupling of aldehyde groups to amines and hydrazines.[120]

Affinity interactions

A commonly used non-covalent interaction for the immobilization of BRE is the specific interaction of immunoglobulin (Ig)G antibodies' F_c region with protein G or A. Thereby, the binding sites of the antibodies, the F_{ab} variable regions, remain accessible for efficient capturing of analytes.[121, 122] Even wider-spread is the coupling via avidin-biotin, exhibiting a non-covalent but high-affinity interaction with a K_D around 10^{-15} M.[123, 124] Similar to protein G and A coupling, it provides an oriented immobilization and shows high stability in harsh conditions. Biotin is a small molecule, which permits multiple labels attached without influencing conformation or functionality. Avidin and its neutravidin and streptavidin derivatives are the most widely used forms, varying in their isoelectric points and carbohydrate moieties attached to them, but all exhibiting four biotin-binding sites for the coupling.[125]

1.6.2 Assays and BRE

This thesis concerns affinity biosensors, which represent a sub-class of sensors relying on ligand-binding interaction between the BRE and the analyte constituting an assay. The oldest type of assays are immunoassays[126] (Nobel prize in 1977), based on the unique properties of antibodies to bind to many natural and synthetic analytes with high specificity and strength.[127] Antibodies can be divided into five main isotypes: IgG, IgA, IgD, IgM, IgE, and they exist as monomers, dimers (IgA), and pentamers (IgM). In addition, B cell-derived polyclonal antibodies are a "mixture" of antibodies with different affinities and epitope binding sites[128], whereas monoclonal antibodies (MAbs)[129] deriving from a single parent cell have identical specificity. In the simplest form of an immunoassay, an antigen and its matching antibody bind for qualitative or quantitative detection of one or the other. In SPR biosensors with a direct assay format, the analyte is detected through a change of mass on the probed surface (see chapter 1.3) without further amplification steps. Thus, the signal generated by the transducer is directly proportional to the amount of analyte in the sample. Nevertheless, in many instances, the signal generated through the mass change is not measurable and the detection of target analyte requires an additional enhancement step. This can be done through competitive, inhibition, or sandwich assay formats,[127] based on the same analytical principles as enzyme-linked immunosorbent assay (ELISA) [130, 131] routinely used in labs. In a sandwich format, the secondary molecule, for example an additional antibody,

is bound to the analyte, which is captured by the BRE with another epitope. This additional mass change can lead to a stronger sensor signal than the analyte on its own. To further enhance the signal, the secondary molecule can be labeled with nanoparticles for even larger mass changes or fluorophores for detection independently of mass changes on the surface. The assay schemes of immunoassays can be readily converted to other types of BREs as well. Not only monoclonal or polyclonal antibodies, but antibody fragments (Fc fragments, nanobodies)[132] can serve as BRE, as well as whole (modified) cells, receptors, proteins, or nucleic acids. Biomolecules can be engineered to perform recognition not present in nature like (oligo-) peptides, oligonucleotides, or aptamers, and synthetic materials can be used to mimic biorecognition, like molecularly imprinted polymers (MIPs).[133]

1.6.3 2D Architectures

Many strategies have been pursued in order to introduce reactive groups onto the surface and minimize non-specific interactions with other species. Three major rganic thin films are most dominantly used to form 2D architectures: self-assembled monolayers (SAMs), Langmuir-Blodgett films, and layer by layers (LbLs) preparations. [134] The most widely used ones are SAMs based on the spontaneous self-formation of ordered structures on gold reacted with thiol molecules.[135, 136] Through strong coordination of the metal with the sulfur ion and van der Waals and hydrophobic forces between the hydrocarbon chains, stable and densely packed monolayers are formed (depicted in fig. 1.13),[137] which have been used for biosensing in various forms.[138]

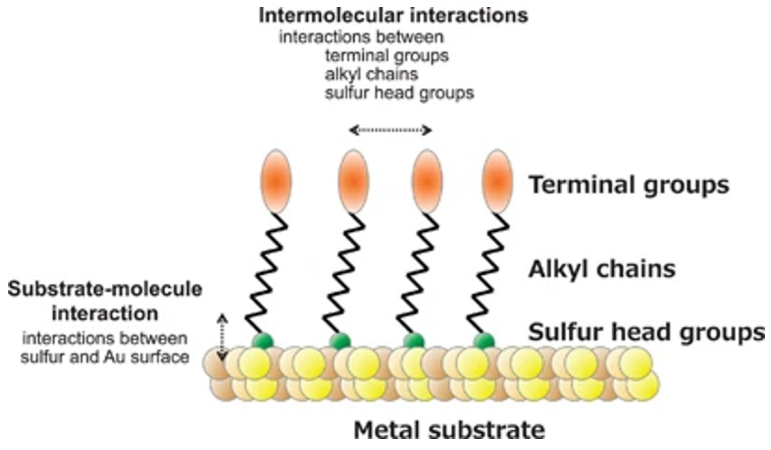

Figure 1.13: SAM formation on a metal surface (reprinted by permission from © 2013[139])

1.6.4 3D Architectures

Polymer Brushes

Polymer brush layers are composed of polymer chains individually attached to the solid surface at one end. Due to their adjustable chain length and various chemical modification, they have been used for versatile applications in and outside the sensing world.[140, 141]

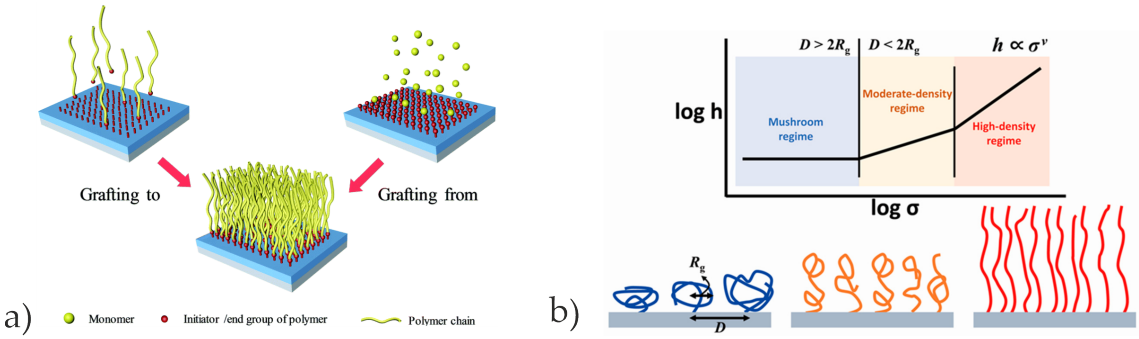

Figure 1.14: a) Formation of polymer brushes using "grafting to" and "grafting from" approaches (Reproduced with permission from the Royal Society of Chemistry [142]) b) Scheme of polymer brush conformation and thickness depending on grafting density on a solid support. (reproduced under CC BY 4.0 © 2015 by the authors[143])

There are two main methods of preparing polymer brush coatings: *"grafting to"* and *"grafting from"* (see fig. 1.14). "Grafting to" approaches, similar to SAM assembly, implies reacting a pre-synthesized polymer from a solution or a melt with the surface under appropriate conditions.[144, 145] The brush structure on the surface is created through a functionalized end group of preformed polymer chains.[146] This method is simple and easily scalable but is limited by the thickness of the formed layers as well as a lower surface coverage and grafting density σ, the space between individual chains.[147] For this reason, and also because heterogeneous chains and brushes with higher MW can be grown, most polymer brushes are *"grafted from"* the surface. *"Grafting from"* processes are bottom-up strategies, which allow growing brushes via initiator molecules anchored to the surface firstly, followed by a subsequent polymerization process. Especially since the development of living radical polymerization techniques[148] like surface initiated atom transfer radical polymerization (SI-ATRP), numerous designs and techniques for their growth have been developed.[149, 150, 151] The radius of gyration (or root-mean-square radius of gyration, R_g) is an often-used measure for the chain configuration.[152] If the distance D between the individual chains is much larger than R_g ($D > 2R_g$), that is, the grafting density is low, the conformation is resembling a more globular mushroom

shape, whereas higher grafting densities provide a more extended structure of tightly packed stretched chains (brushes).[153, 154, 143] Fig. 1.14 (b) shows this correlation of the grafting density σ to the thickness h and the brush conformation. In general, in the brush regime, the thickness h can be described as

$$h \propto N\sigma^{v} \tag{1.12}$$

where N is the degree of polymerization, and v an exponent, which itself is depending on grafting density and solvent quality.[154, 155]

Surface-attached hydrogels

Another possibility is to anchor a polymer network to the surface using multiple attachment points. Thin layers of a polymeric gel, a viscoelastic but deformable material[156] can increase the mechanical stability while still exhibiting the high surface to volume ratio of polymer brushes.[153] These networks are called hydrogels if they are swollen in water, which is made possible by a hydrophilic nature of the repeating units in the polymer chain, which can be introduced by functional moieties with high polarity.[156] The individual polymer chains are interconnected through structural moieties, which are most often introduced into the polymers during synthesis.[157] These crosslinks can either be of chemical or physical nature and prevent the dissolving of the network. An important parameter is the swelling ratio of the hydrogel network, which is defined by the total volume of the swollen system divided by the volume of the polymer. The more crosslinks are introduced into the network, the less swollen and more compact the hydrogel becomes.[158] The hydrophilic polymers that build the network can occur in nature (e.g., sugars [159, 160] or proteins[161]), or can be synthetically prepared (acrylamides[162], sulfobetaines, or carboxybetaines[163]). Following other interface architectures discussed, surface-attached hydrogel layers can be *"grafted to"* using preformed polymers or *"grafted from"* using initiators on the surface.[156] A significant advantage is the environment these materials provide on a sensor surface. They allow integration into sensor devices while preserving the structure of the BRE and its functionalities, as, due to their high water content, they resemble a living biological system and can be considered biocompatible. They further can be microstructured and selectively attached and crosslinked. Through their high surface to volume ratio and consequently rapid diffusion of solutions (even with large molecules) into the network, fast sensor response times can be achieved.[153, 164] Hydrogels, as well as polymer brushes[165] and microgels[166], can

also be responsive, changing their properties by applying an external stimulus. This can be ionic strength[167], temperature[168], pH[169] or illumination[170]. The hydrogel structure changes shape or volume, dissolves or assembles, or may switch between different states of hydrophilicity and hydrophobicity.[171] Thin responsive polymer films as interface architectures are often termed "smart materials" as they can serve as sensors, actuators, and autonomous devices.

Antifouling surfaces

Preventing non-specific adsorption (*fouling*) while sensing in complex media represents an ever-present challenge in biosensing. Biofluids like urine, saliva, and blood (and its constituents serum and plasma) contain a high concentration of complex mixtures of proteins, which deposit on the sensor surface and change the surface properties of the sensor. These effects can lead to an unspecific signal even orders of magnitudes higher than the specific one, which is particularly prohibitive for the direct detection formats of biomolecules.[149, 172] Thiol SAMs with multiple poly(ethylene glycol) (PEG) groups have been used for decades for biocompatibility and minimizing unspecific binding[173, 174], as it contains basic ether bonds and a low polymer-water interfacial energy[175], creating a hydration layer close to the surface, which is improving with increasing thickness.[176, 177] These mixed SAMs in varying ratios can simultaneously suppress non-specific interactions and provide functional head groups for post modifications,[110, 178] exhibiting, e.g., carboxylic or biotin moieties. As they present a simple method to connect different materials in a *"bottom-up"* approach and provide reasonably good protection against fouling, they have become the most used kind of organic monolayer.[137] However, for sensing in undiluted and more complex biological matrices, the properties of PEG surface hydration layers are not sufficiently resistant against non-specific binding as even a tiny amount limits the performance in an application for smaller molecules or less concentrated samples. Therefore, methods were investigated to reduce the non-specific interactions including using zwitterionic materials with positively and negatively charged moieties, e.g., phosphocholine, sulfobetaine, and carboxybetaine.[179, 180] These can be attached to the surface via SAMs[181], by *"grafted-from"* polymers[150, 182] or even introduced onto the surface using thicker polymer networks like hydrogels. Compared to more simple approaches, they provide a dense surface hydration layer that derives not only from hydrogen bonding but from stronger ionic solvation by the zwitterionic materials.[179, 183] An overview of the development in antifouling polymers is shown in fig. 1.15. These materials also provide proven biocompatibility features, as they are now

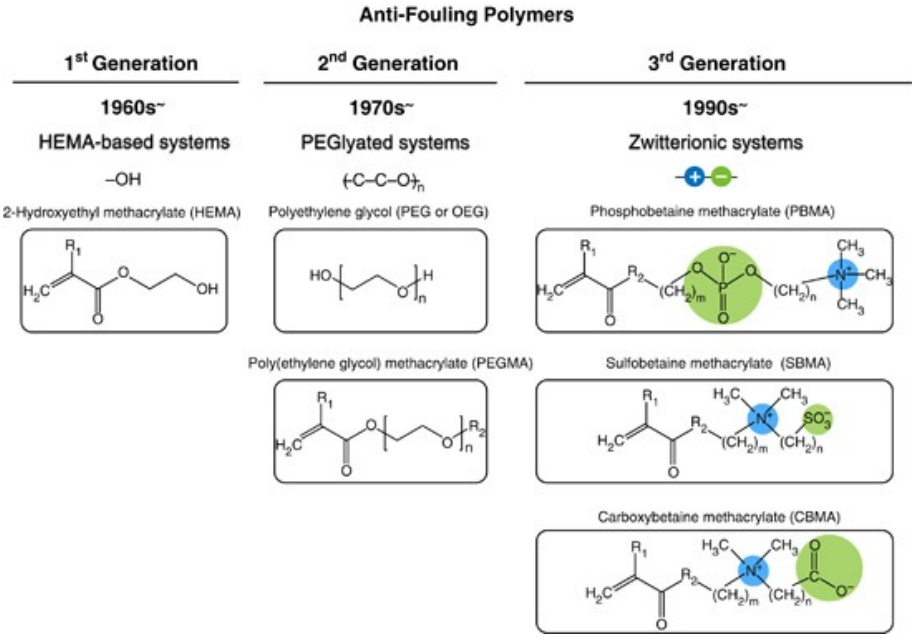

Figure 1.15: Structure of different motives developed over the years to show resistance to non-specific adsorption. (reprinted with permission from Nature, Copyright © 2014, The Society of Polymer Science, Japan[185])

widely employed not only for sensors but also in contact lenses, carriers for drugs, and implants.[172, 184]

CHAPTER 2

Research Aims

The current progress in the development of bioanalytical methods has significantly impacted diverse fields of medical diagnostics, food control, and environmental analysis. Through the last years, we have witnessed how numerous biosensor technologies have been gradually introduced into daily lives as simple, fast, and reliable analysis of chemical and biological species is gaining importance. Most prominently, this field concerns detecting harmful compounds and biomolecules that serve as biomarkers present at trace amounts in complex biological fluids. Detection of such analytes is typically employed in central laboratories using methods relying on enzymatic amplification and extensive sample pre-treatment. Rapid detection using assays with direct detection format holds the potential to overcome these limitations and therefore is of utmost importance for biosensing technologies. In order to address this challenge, research has focused on enhancing accuracy and improving sensitivity of biosensors at the level of assay development, biointerface design, and transducing mechanism. Until now, this research was typically focused only on the improvement of individual biosensor subparts. However, specific applications in the biomedical field can be addressed only when all these aspects are delicately orchestrated.

This thesis presents several strategies for enhancing the analytical performance of optical biosensors for sensitive readout of heterogeneous assays on the sensor surface by combining surface plasmon resonance (SPR) and fluorescence, tailoring of polymer biointerface architectures resistant to fouling, and implementation of optical and non-optical amplification of the output optical signal. This work contributes to both developments of

methods as well as applications, especially in the context of medically relevant analytes and point-of-care (POC) diagnostics.

A considerable part of this work deals with the design of specific types of biointerfaces suitable for evanescent wave optical biosensors. For this, it is crucial that one can control the specific interaction of the analyte present in the analyzed liquid sample and the biorecognition elements (BREs) attached to the solid sensor surface. In order to selectively capture target analytes from complex bodily fluids or food samples at the surface where it is optically probed, precise chemical modifications are necessary. In this work, the specificity is improved by polymer architectures minimizing non-specific interactions on the sensor surface that otherwise interfere with the specific signal (chapter 3.1). Responsive hydrogels are utilized for their ability to respond to external stimuli, and moreover, this work includes a study of how these features are integrated with plasmonic nanostructures with dual output optical signal enhancement (chapter 3.3 and 3.6).

Often the transduction system itself is a limiting component for the performance of the overall sensor, e.g., SPR changes induced by the capture of target analyte may not be associated with sufficiently strong surface mass density increase, particularly for low concentrations or small-sized analytes. To address this challenge and reach high sensitivity, the combination of SPR with fluorescence (chapter 3.1 - 3.3) and optical waveguide spectroscopy (chapter 3.2) was pursued, nanostructured surfaces for optical enhancement of signals were designed (chapter 3.4 - 3.6), and BREs were selectively attached in certain spots of highest optical signal enhancement. Additionally, the analytes were preconcentrated through the means of a hydrogel binding matrix (chapter 3.3 and 3.6).

Developing devices to be used for POC is another direction that is gaining importance. Thereby, the sensor's sensitivity and analytical performance still play a crucial role, but the emphasis is also put on simplicity and ease of use, robustness, and the possibility of scaling-up the amplifying nanostructures for their potential mass production. In the optical sensors based on grating-structured surfaces developed within the thesis, the structures are prepared by UV-nanoimprint lithography (UV-NIL) and provide means to implement simple and compact sensor devices (chapter 3.4 and 3.5).

Overall, this work presents several routes of combined efforts towards the development of facile strategies for sensitivity improvement of plasmonic biosensors, which is not at the expense of other important performance characteristics, including the range of detection, reproducibility, stability and the ability of assay multiplexing. Finally, this thesis takes

into account the interplay of key biosensor elements, which, when acting together, can make the overall device a viable tool for the rapid analysis of complex biological samples.

CHAPTER 3

Individual Studies

The central part of this thesis is formed by six papers published in peer-reviewed journals. These individual studies are presented here in consecutive chapters. The first three studies (chapters 3.1-3.3) deal with biointerface design and detection of nucleic acids and proteins in a real-world setting, whereas the second part (chapter 3.4-3.6) emphasizes the optical aspects of plasmonic biosensors and the implementation of new optical readers with (nano-) plasmonic surfaces for sensing.

3.1 Plasmonic Hepatitis B biosensor for the analysis of clinical saliva

Riedel, T., **Hageneder, S.,** Surman, F., Pop-Georgievski, O., Noehammer, C., Hofner, M., Brynda, E., Rodriguez-Emmenegger, C. and Dostalek, J. Plasmonic hepatitis B biosensor for the analysis of clinical saliva. Analytical chemistry, 2017, 89(5), 2972-2977. https://doi.org/10.1021/acs.analchem.6b04432

Co-authorship paper: I conducted experiments for SPFS measurements, did data analysis, and was involved in the discussion, manuscript preparation, and graphs design. TR was responsible for concept and manuscript preparation and was involved in experiments. FS, OP-G, and EB were responsible for anti-fouling surface synthesis and characterization. CN and MH were involved in the discussion and provided saliva samples. JD was responsible for project design, discussion, and manuscript preparation.

The utilization of an antifouling biointerface architecture based on *"grafted-from"* poly(HPMA-co-CBMAA) brushes in combination with PEF readout allowed the detection of disease biomarkers in clinical saliva samples, a complex matrix. The enhanced specificity and sensitivity of this approach hold potential for utilization in POC sensing.

analytical chemistry

Article

pubs.acs.org/ac

Plasmonic Hepatitis B Biosensor for the Analysis of Clinical Saliva

Tomáš Riedel,*[,†] Simone Hageneder,[‡] František Surman,[†] Ognen Pop-Georgievski,[†] Christa Noehammer,[§] Manuela Hofner,[§] Eduard Brynda,[†] Cesar Rodriguez-Emmenegger,*[,†,∥] and Jakub Dostálek*[,‡]

[†]Institute of Macromolecular Chemistry AS CR v.v.i., Heyrovsky Sq. 2, 162 06 Prague 6, Czech Republic

[‡]Biosensor Technologies, AIT-Austrian Institute of Technology GmbH, Muthgasse 11, 1190 Vienna, Austria

[§]Molecular Diagnostics, Health and Environment Department, AIT-Austrian Institute of Technology GmbH, Muthgasse 11, 1190 Vienna, Austria

[∥]DWI – Leibniz Institute for Interactive Materials and Institute of Technical and Macromolecular Chemistry, RWTH Aachen University, Forckenbeckstraße 50, 52074 Aachen, Germany

Supporting Information

ABSTRACT: A biosensor for the detection of hepatitis B antibodies in clinical saliva was developed. Compared to conventional analysis of blood serum, it offers the advantage of noninvasive collection of samples. Detection of biomarkers in saliva imposes two major challenges associated with the low analyte concentration and increased surface fouling. The detection of minute amounts of hepatitis B antibodies was performed by plasmonically amplified fluorescence sandwich immunoassay. To have access to specific detection, we prevented the nonspecific adsorption of biomolecules present in saliva by brushes of poly[(*N*-(2-hydroxypropyl) methacrylamide)-*co*-(carboxybetaine methacrylamide)] grafted from the gold sensor surface and post modified with hepatitis B surface antigen. Obtained results were validated against the response measured with ELISA at a certified laboratory using serum from the same patients.

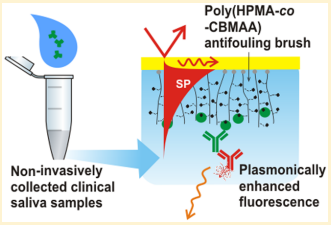

Analytical tests that become available for detection of a broad spectrum of molecular biomarkers in blood plasma or serum provide a powerful tool for diagnosis of diseases. However, the invasive nature of blood collection complicates the analysis for special populations (e.g., elderly people, small children) and in situations when blood sampling is not possible or patients impose high risk of infection. Noninvasive sample collection holds potential to solve this problem, bring the analysis closer to the patient, and set the basis for point-of-care analysis with increased frequency of individual tests, thus enhancing the chances for early diagnosis.

The use of easily accessible bodily fluids, in particular the use of saliva, is an attractive alternative to blood as a large number of disease biomarkers are also present in this fluid and its collection is inexpensive, completely noninvasive, and minimally disturbing for the patient.[1] Saliva is a complex fluid containing a variety of glycoproteins, antibodies, growth factors, carbohydrates, salts, hormones, mucus, and bacteria that leach from blood by passive, as well as active transport.[2] In the past, saliva had already been used to monitor oral health and periodontal diseases.[3] With the advance of modern biochemical techniques more biomarkers for systemic diseases were identified in saliva.[4]

Specific antibodies against epitopes displayed on the capside of the hepatitis B virus (hepatitis B surface antigen-HBsAg) are secreted to blood upon infection or vaccination. The evaluation of the presence of antibodies against HBsAg (anti-HBs) in serum allows confirming the recovery and immunity in patients, as well as checking for the efficiency of vaccination.[5] Hepatitis B virus (HBV) can cause potentially life-threatening diseases, such as chronic hepatitis, cirrhosis, or even liver cancer, and therefore, it represents one of the major global health threats. Especially in African countries, HBV is highly prevalent and causes rising infections[6] that are associated with about 0.8 million deaths every year related to hepatitis B.[7] HBV can be easily transmitted by the contact with infected blood or body fluids.[8]

The use of saliva as a diagnostic tool for the analysis of biomarkers actively or passively transferred from blood (such as anti-HBs) is challenging as they are typically present at concentrations several orders of magnitude lower than in plasma, and thus it requires platforms with substantially enhanced sensitivity.[9−11] Plasmonics has recently emerged as new nanophotonics research field that provides sensitive means for direct label-free detection of biomarkers.[12] In addition, plasmonics increasingly finds its application for the amplification of weak optical signals in optical spectroscopy-based analytical techniques.[13] Among these, plasmonic amplification of fluorescence paved new ways for advancing single molecule studies.[14] In addition, it has been increasingly applied in optical systems that employ fluorescence readout of assays relying on ensembles

Received: November 10, 2016
Accepted: February 7, 2017
Published: February 7, 2017

DOI: 10.1021/acs.analchem.6b04432
Anal. Chem. 2017, 89, 2972−2977

of fluorophores coupled with biomolecules.[15,16] The plasmon-enhanced fluorescence (PEF) that is also referred to as metal-enhanced fluorescence (MEF) exploits the extremely strong electromagnetic field intensity that occurs upon the resonant excitation of surface plasmons (SPs) at metallic nanostructures and on thin metal films. This phenomenon originates from collective oscillations of electron density at these structures and they enable increasing the intensity of emitted fluorescence light from emitters in their close proximity. When fluorophores are used as labels in immunoassays, their coupling with SPs enhances the fluorescence light intensity extracted from the surface where the assay takes place. This type of amplification thus allows resolving lower amount of captured target molecules and concomitantly improving the limit of detection of an assay.

In spite of high sensitivity of plasmonic biosensors that enable reaching limit of detection < fM concentrations,[12] we witnessed limited success in translation of these systems to clinical praxis. For example, several hepatitis plasmonic biosensor system utilizing label-free surface plasmon resonance (SPR) detection of binding induced refractive index changes were developed.[17,18] However, these biosensors were typically applied only for the analysis of model samples such as spiked buffer or pooled diluted serum. Arguably, the key problem in the analysis of clinically relevant samples by plasmonic biosensors is the fouling of their metallic surface with tethered ligands for specific capture of target analyte.[19,20] To solve this problem, research in surface chemistries and architectures was pursued to decrease or completely eliminate the adverse effect of fouling and thereby maximize the efficiency. The most widely used surface modifications are based on poly(ethylene glycol) (PEG), for example, self-assembled monolayers (SAM) terminated with short oligoethylene glycol (OEG). While this approach is able to completely eliminate the nonspecific adsorption of albumin, it fails when complex samples (such as blood plasma/serum and saliva) are analyzed.[21,22]

In this work, a biosensor for the noninvasive analysis of anti-HBs antibodies in clinical saliva samples is presented. It takes advantage of highly sensitive plasmon-enhanced fluorescence readout and novel antifouling poly[(*N*-(2-hydroxypropyl) methacrylamide)-*co*-(carboxybetaine methacrylamide)] (poly-[HPMA-*co*-CBMAA]) polymer brush. This recently developed brush retains its properties even after the immobilization of large surface mass density of ligands.[23] This combination addresses the two key challenges in the biomarker analysis in saliva that are associated with extremely low analyte concentration and severe unspecific interactions with the biosensor surface.

EXPERIMENTAL SECTION

Materials. 1-Ethyl-3-(3-(dimethylamino)propyl) carbodiimide hydrochloride (EDC) and *N*-hydroxysuccinimide (NHS) were purchased from GE Healthcare Life Sciences. 1,4,8,11-Tetramethyl-1,4,8,11-tetraazacyclotetradecane (Me4Cyclam, 98%), CuCl (≥99.995%), and $CuCl_2$ (99.999%) were purchased from Sigma-Aldrich and used as received. HBsAg antigen (recombinant, adw subtype) and monoclonal mouse antihepatitis B virus surface antigen antibodies (anti-HBs) were purchased from Hytest (Turku, Finland). Secondary antibodies against mouse antibody (Alexa Fluor 647 Goat Anti-Mouse IgG (H+L)), and against the human antibodies (Alexa Fluor 647 Goat Anti-Human IgG (H+L)) were purchased from Molecular Probes (Eugene, OR, US). Initiator *ω*-mercaptoundecyl bromoisobutyrate was synthesized according to the literature procedure.[24] The monomers (3-acryloylaminopropyl)-(2-carboxyethyl) dimethylammonium (carboxybetaine methacrylamide, CBMAA) and *N*-(2-hydroxypropyl)methacrylamide (HPMA) were synthesized according to the literature.[25−27] The buffers used were phosphate buffered saline (PBS, 10 mM disodium hydrogen phosphate, 2 mM potassium phosphate, 137 mM sodium chloride, 2.7 mM potassium chloride, pH 7.4), HEPES buffer (10 mM, pH 7.5), and sodium acetate buffer (SA, 10 mM, pH 5).

Biological Samples. Saliva samples were collected from eight healthy donors who were either vaccinated or not-vaccinated against Hepatitis B. The samples were centrifuged for 5 min at 16000*g* and the supernatant was aliquoted. Saliva aliquots were stored at −80 °C before analysis. The donors did not consume food nor liquids for 30 min prior to collecting of samples. The titer of anti-HBs antibodies in serum was tested using enzyme-linked immunoassays (ELISA) done in CE certified laboratory Labors, in Vienna (Austria). The serum was collected from the same donors and at the same time as saliva.

Preparation of Sensor Chips. BK7 glass slides with 2 nm chromium and 50 nm gold films were prepared by high vacuum evaporation. The surface of gold was subsequently rinsed with ethanol and deionized water, dried and cleaned with ozone for 20 min (UVO cleaner, Jelight). Afterward, the gold surface was overnight incubated in a 1 mM solution of *ω*-mercaptoundecyl bromoisobutyrate in ethanol. This compound served as an initiator in the synthesis of poly(HPMA-*co*-CBMAA) brushes as described in more detail in our previous work.[23] Briefly, for the catalyst solution, 7 mL degassed methanol were transferred (under argon atmosphere) into a Schlenk tube with 354 *μ*mol (35 mg) of CuCl, 78 *μ*mol (10.5 mg) of $CuCl_2$, and 472 *μ*mol (121 mg) of Me_4Cyclam and stirred until complete dissolution. A second Schlenk tube, at 0 °C, contained 16.6 mg (2.4 g) of HPMA and 2.9 mmol (0.7 g) of CBMAA dissolved in 12 mL of degassed water and 5 mL of deoxygenated methanol. The catalyst solution was added using a gastight syringe. Polymerization on the substrates with the initiator SAM was done at 30 °C for 2 h. Samples were washed thoroughly and stored in water until usage.

Immobilization of HBsAg. The antigen HBsAg was immobilized to the brushes via the carboxylate groups carried by CBMAA that were previously activated using the EDC/NHS. First, the brush surface was contacted with SA buffer pH 5. Subsequently, the surface was reacted with a freshly prepared solution 1:1 v/v of EDC (0.4 M) and NHS (0.1 M) for 10 min. Then the surface was rinsed with SA and HEPES buffers for 1 min each and the antigen, HBsAg (25 $\mu g \cdot mL^{-1}$ in HEPES buffer), was flowed over the surface for up to 10 min. Any unreacted active ester groups were let to hydrolyze by flowing PBS for 90 min.

Optical Setup. The time-resolved readout of sandwich assay on the sensor chip was performed by using a setup depicted in Figure 1. It combines angular interrogation of SPR with plasmonically amplified fluorescence detection.

Monochromatic beam with transverse magnetic polarization and a wavelength of λ_{ex} = 633 nm was used to excite SPs on the sensor surface. Intensity of the excitation beam was attenuated to 1.5 *μ*W and it was coupled to a 90° prism made of LASFN9 glass. To the prism base, a sensor chip with gold layer modified by poly(HPMA-*co*-CBMAA) brushes was optically matched by using an immersion oil (from Cargille Inc., USA). A transparent flow-cell (volume 10 *μ*L) was clamped to flow analyzed samples over the surface of the sensor chip at flow rate of 15 $\mu L \cdot min^{-1}$ by

DOI: 10.1021/acs.analchem.6b04432
Anal. Chem. 2017, 89, 2972−2977

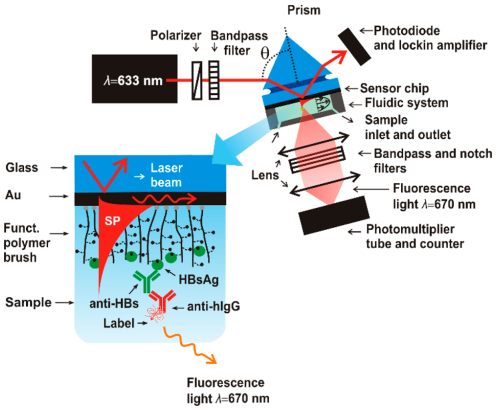

Figure 1. Schematics of plasmon-enhanced fluorescence spectroscopy biosensor with a detail of sensor chip with poly(HPMA-*co*-CBMAA) brush functioning as a binding matrix.

using a peristaltic pump. The angle of incidence of the excitation beam was adjusted to around $\theta \approx 60°$ at which the resonant coupling to SPs at the interface between gold and polymer brushes occurs. The enhanced field intensity of SPs at λ_{ex} excited fluorophore labels on the sensor surface and the fluorescence light emitted at longer wavelength of λ_{em} through the flow cell was collected by a lens with numerical aperture 0.2. The fluorescence beam was focused at the input of a photomultiplier that was connected to a counter. The output fluorescence intensity was recorded in time by using software Wasplas developed at Max Planck Institute for Polymer Research in Mainz (Germany). The fluorophore Alexa Fluor 647 and respective filters were used for the excitation wavelength of λ_{ex} = 633 nm and emission wavelength of λ_{em} = 670 nm. Band pass filter FL632.8−10 from Thorlabs (UK) was employed to select the excitation wavelength λ_{ex} and band-pass filter 670FS10−25 from L.O.T.-Oriel (Germany) and notch filter XNF-632.8−25.0 M from CVI Melles Griot (Germany) were installed for collecting light at emission wavelength λ_{em}. All measurements were carried out at room temperature $T \approx 25$ °C.

RESULTS AND DISCUSSION

Preparation and Characterization of Brushes Architecture. Polymer brushes of poly(HPMA-*co*-CBMAA) were successfully grown from a densely packed SAM of *ω*-mercaptoundecyl bromoisobutyrate on Au via surface initiated atom transfer radical polymerization (SI-ATRP) as described and characterized in detail before.[23] The thickness of the brushes was determined by ellispometry in dry state h_{dry} = 29.2 ± 2.3 nm and when hydrated in water h_{sw} = 81.5 ± 1.7 nm. X-ray photoelectron spectroscopy and Fourier transform infrared grazing angle specular reflectance spectroscopy were utilized to prove the chemical structure of the brushes. The core level C 1s spectrum (Figure 2 a) of the brushes is characterized by C−C, C−H (285.0 eV), C*−C(=O)− from the secondary chemical shifts induced to the carbon atoms in the vicinity to amide and charged carboxylic groups (285.5 eV), C−N (286.1 eV), C−OH (286.9 eV), C(=O)−NH (288.0 eV), and C(=O)−O$^-$ carboxylate (288.7 eV). The high resolution N 1s spectrum of the brushes (Figure 2 b) is characterized by a prevailing amide

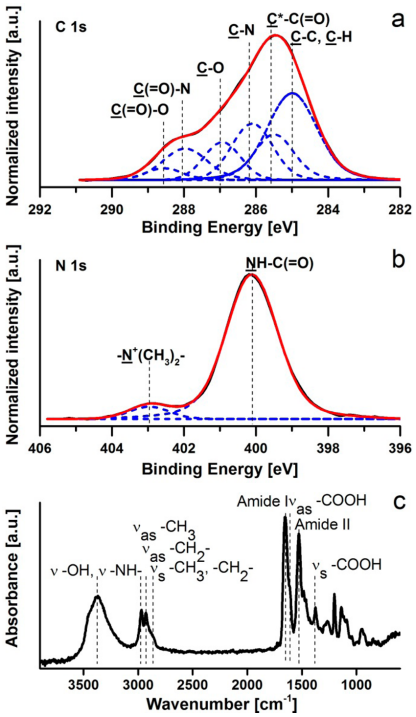

Figure 2. Characterization of the poly(HPMA-*co*-CBMAA) copolymer brush. (a) High resolution of C 1s and (b) N 1s XPS spectra and (c) FTIR GASR spectrum.

contribution (400.1 eV) and a contribution characteristic for the charged quaternary ammonium of the CBMAA comonomer (403.0 eV). The O 1s spectrum is presented in the SI. Further evidence of the chemical composition of the brushes was obtained by FTIR GASR. Figure 2 c depicts the spectrum of poly(HPMA-*co*-CBMAA) brushes which exhibits both a band at 1376 cm^{-1} and a shoulder band at 1610 cm^{-1} corresponding to the symmetric and asymmetric stretching modes of COO$^-$ stemming from CBMAA as well as it shows the amide I and amide II bands at 1527 and 1653 cm^{-1} originating from the HPMA. The morphology of the surface of the brushes was observed using an AFM microscope which can be found in the SI. The functionalization of the gold-coated sensors rendered the surface more hydrophilic as evidenced by the dynamic contact angles of θ_{adv} = 34 ± 0.5°; θ_{rec} = 15.3 ± 3.3.

Selection of an adequate biofunctionalization procedure is of great importance to achieve high loading of immobilized ligands. In particular, the pH of buffer plays a key role as discussed detail in SI. First, carboxylate groups are converted to succinimidyl ester in water and rinsed with SA. The pH of SA buffer (pH 5) is preferred due to the lower rate of hydrolysis of succinimidyl ester compared to alkaline solutions.[28] After the activation of carboxylate groups (negatively charged) of CBMAA to form succinimidyl ester (neutral), using EDC/NHS, the surface becomes positively charged (stemming from quaternary ammonium groups). Therefore, by using a buffer with a pH

DOI: 10.1021/acs.analchem.6b04432
Anal. Chem. 2017, 89, 2972−2977

above the isoelelectric point of the chosen ligand (HBsAg with pI ~4.5)[29] this protein exhibits negative charge and is attracted to the surface by Coulombic force which leads to a higher yield in the immobilization on the brush. After the subsequent rinsing with buffer, the unreacted active esters hydrolyze back to carboxylate groups and the (close to) neutral net charge of the polymer brush is restored. The loading of HBsAg on the brushes was controlled by the reaction time and the herein used chips carried the surface mass density of HBsAg of $\Delta\Gamma = 0.52 \pm 0.03$ $\mu g \cdot cm^{-2}$ as determined by SPR measurements. This value corresponds to about a monolayer as was reported for proteins exhibiting similar molecular weight.[30] Comparable surface mass density has been shown previously for SAM-based architectures, however, the resistance to fouling was largely impaired.[31]

The resistance of the poly(HPMA-*co*-CBMAA) brush to the fouling was evaluated for saliva samples collected from healthy individuals. Since the immobilization of bioreceptors may change the antifouling properties, the fouling of brushes functionalized with HBsAg was evaluated for samples from individuals that showed negative response in the ELISA serum test. As illustrated by SPR sensorgrams in Figure 3, the surface mass density change upon 10 min flow of saliva samples over the sensor surface with and without HBsAg was measured. The protein deposition from undiluted 100% saliva and samples with 10% saliva diluted by PBS was not measurable on pristine poly(HPMA-*co*-CBMAA) brushes, see Figure 3a and Figure 3b.

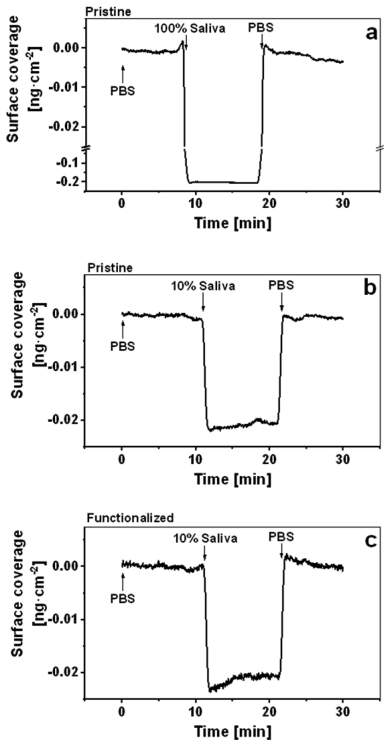

Figure 3. SPR characterization of the fouling on pristine and functionalized poly(HPMA-*co*-CBMAA) brush: (a) Pristine surface in contact with 100% saliva, (b) pristine surface in contact with 10% saliva, and (c) surface modified with HBsAg in contact with 10% saliva.

Importantly, the resistance to the fouling of poly(HPMA-CBMAA) brush is retained even after the HBsAg is immobilized with surface mass density as large as 0.5 $\mu g \cdot cm^{-2}$, see Figure 3c. This is a key observation as the functionalization of brushes composed from individual homopolymers (HPMA and CBMAA) is known to severely deteriorate their antifouling properties.[31] This effect can be ascribed to the reaction of too many functional groups (e.g., carboxyl of CBMAA) leading to a net positive charge or cross-linking of the chains. The herein reported approach enables efficient biofunctionalization of the polymer brush because of the presence of carboxyl groups in CBMAA while preserving antifouling properties of the polymer brush owing to the HPMA units.

Analysis of Clinical Saliva Samples. Clinical saliva samples collected from 8 healthy human donors were used and prepared as described in the methods section. The total amount of sample needed for one analysis was only 15 μL. The response of developed plasmonic biosensor for each saliva sample was compared with the results obtained by ELISA for serum samples from the same donor. The ELISA analysis was carried out by an independent certified laboratory (Labors.at, Vienna, Austria). According to ELISA, the tested saliva samples were obtained from donors that showed negative response in serum (samples D, F, H, antibody titer below the detection limit of ELISA 0.002 $IU \cdot mL^{-1}$), positive response in serum (B, E, G, 0.068–0.645 $IU \cdot mL^{-1}$) and highly positive response (A, C, > 1 $IU \cdot mL^{-1}$).

The SPR detection principle was tested for the analysis of saliva samples collected from donors which were known to exhibit highly positive response in serum. These serum samples were analyzed by using an identical instrument with the same brush surface architecture.[23] While the direct binding of anti-HBs human IgG could be easily observed from serum samples, no measurable positive response was obtained from saliva samples, even after binding of secondary antibody against human IgG (hIgG). Therefore, the PEF biosensor was used in order to increase the sensitivity as described further.

The developed PEF assay is illustrated in Figure 4. First, a stable baseline in fluorescence signal acquired in time was established upon a flow of PBS over the surface of HBsAg-functionalized brushes. Then a calibration step was performed in which PBS spiked with mouse anti-HBs was flowed at 10 pM concentration through the sensor for 10 min. This antibody was labeled with Alexa Fluor 647 dye and therefore the injection is

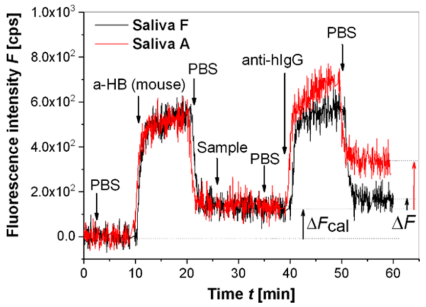

Figure 4. Example of kinetics of fluorescence signal for negative and highly positive saliva samples.

DOI: 10.1021/acs.analchem.6b04432
Anal. Chem. 2017, 89, 2972−2977

accompanied by increased fluorescence signal F. The sensorgram in Figure 4 shows that an abrupt change occurs at time t = 10 min due to the excitation of fluorophores present in the bulk. Between the time t = 10 and 20 min, a gradual increase in the signal occurs because of the affinity binding to the immobilized antigen HBsAg. At time t = 20 min the sensor surface is rinsed with buffer and the fluorescence signal drops to an increased level ΔF_{cal} which is proportional to the amount of affinity bound anti-HBs molecules.

After 5 min rinsing, an analyzed 10% saliva sample was flowed over the sensor surface for 10 min. At this time no fluorescence change is observed as the human hIgG specific to HBsAg are not labeled. To detect the presence of these antibodies on the surface, the sensor was rinsed for 5 min with PBS and the antihuman IgG labeled with Alexa Fluor 647 dye (anti-hIgG, 4 μg·mL^{-1} in PBS) was injected. This compound was flowed for 10 min between t = 40 and 50 min. Similarly as in the calibration step, the fluorescence signal rapidly increased upon the injection and then gradually rose due to the affinity binding to captured hIgG. An additional rinsing with PBS for 5 min was applied and the difference in the fluorescence intensity ΔF before and after the flow of detection anti-hIgG was determined. In order to compensate for small changes in the alignment, the sensor response was defined as a ratio $\Delta F/\Delta F_{cal}$.

Figure 5a compares the obtained normalized fluorescence response $\Delta F/F_{cal}$ for saliva samples with values determined by ELISA for serum. The PEF saliva analysis was performed in triplicate for each sample and showed error bars represent the standard deviation (SD) of measured values. The average SD

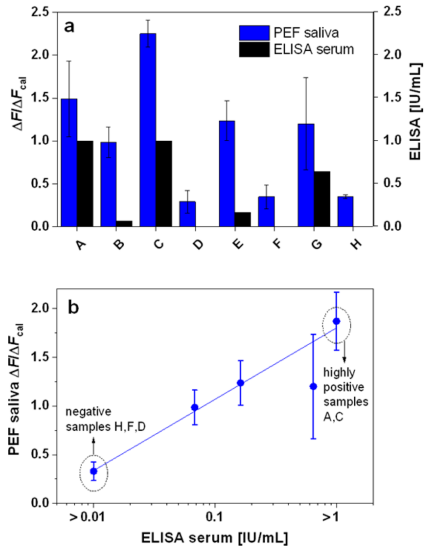

Figure 5. (a) Comparison of the response of PEF biosensor to saliva samples collected from donors A-H compared to ELISA-based characterization of respective serum samples. (b) Overview of PEF sensor response as a function of concentration in serum as determined by ELISA. Indicated errors represent standard deviation for samples measured in triplicate, the response and error to negative and highly positive samples is averaged, line shows a linear fit with r-square (COD) value of 0.89.

associated with chip-to-chip variations of the PEF assay output is 26% of the mean value of fluorescence response $\Delta F/F_{cal}$. This relatively high error can be partially ascribed to the noise in the detected fluorescence signal (as observed in Figure 4) which can be improved by using plasmon-enhanced fluorescence schemes with higher enhancement factor and thus improved signal-to-noise ratio.[32,33] In addition, the reproducibility of the assay that involves multiple manually performed steps including saliva centrifugation, dilution of supernatant with buffer, sensor calibration with labeled mouse IgG, and sequential flow of saliva sample and labeled antihuman IgG may be improved by using automatized flow injection system. The plotted dependence of PEF saliva response on respective ELISA serum response in Figure 5b shows that it can be fitted with a linear function (r-square value of 0.89, the ELISA response is presented in log scale on the horizontal axis). In this graph, the response for samples collected from negative donors (H, F, D) and highly positive donors (A, C) was averaged. The results of PEF analysis of saliva samples indicate that highly positive saliva samples (average fluorescence response of 1.87, SD = 0.3) can be reliably discriminated from negative samples (average fluorescence response of 0.33, SD = 0.1). Interestingly, the PEF response to saliva samples is not proportional to that acquired by ELISA for serum samples as the slope of the respective dependence in a log−log representation substantially differs from 1 (is of about 0.3). Therefore, such dependence in conjunction with relatively high error bars does not allow for accurate quantitative measurements in the range between 0.01 and 1 IU·mL^{-1}. The reason for such deviations may be attributed to different composition of saliva compared to serum which may affect the assay. In addition, we assume that the hIgG antibodies present in saliva and serum can bind to HBsAg with a range of affinity constants. As in ELISA the immobilized antigen is typically incubated for much longer time (hours) compared to the presented PEF sensor (10 min), the lower affinity fraction of hIgG against HBsAg may not be detected by the PEF biosensor while in ELISA it can contribute to the sensor signal.

CONCLUSIONS

We report for the first time the successful implementation of a plasmonic biosensor for the analysis of human IgG against hepatitis B surface antigen in clinical saliva samples. The work pursued enhanced specificity and sensitivity to analyze minute amounts of biomarkers in the complex saliva matrix. This was achieved by the design of a novel antifouling biointerface architecture based on poly(HPMA-*co*-CBMAA) brushes in combination with surface plasmon-enhanced fluorescence detection principle. It is worth of noting that regular SPR biosensor with identical surface architecture and assay did not show measurable signal for analyzed clinical saliva samples and made the use of plasmonically enhanced fluorescence detection principle necessary. The biosensor showed excellent resistance to fouling from saliva samples and allowed distinguishing of highly positive clinical saliva samples (respective serum ELISA response >1 IU/mL) and negative clinical saliva samples (respective serum ELISA response <0.01 IU/mL). It is envisioned that the achieved results will pave the way to new class of biosensor technologies that can be deployed outside centralized laboratories and which take advantage of the analysis of bodily fluids that are collected completely noninvasively. In conjunction with miniaturized PEF readers[34] and more sensitive plasmonic architectures[32,33] the presented approach is among others

DOI: 10.1021/acs.analchem.6b04432
Anal. Chem. 2017, 89, 2972−2977

expected to find its applications in clinical practices for diagnosis and measuring of the antibody titers.

■ ASSOCIATED CONTENT

Supporting Information

The Supporting Information is available free of charge on the ACS Publications website at DOI: 10.1021/acs.analchem.6b04432.

Characterization of poly(HPMA-*co*-CBMAA) brushes by using X-ray photoelectron spectroscopy (XPS), Fourier transform infrared grazing angle specular reflectance spectroscopy (FTIR-GASR), and atomic force microscopy (AFM) (PDF)

■ AUTHOR INFORMATION

Corresponding Authors

*E-mail: riedel@imc.cas.cz. Phone: +420 296 809 333. Fax: +420 296 809 410.

*E-mail: rodriguez@dwi.rwth-aachen.de. Phone: +49 241 8023362. Fax: +49 241 80 23301.

*E-mail: jakub.dostalek@ait.ac.at. Phone: +43 (0) 50550 4470. Fax: +43 (0) 50550 4450.

ORCID

Cesar Rodriguez-Emmenegger: 0000-0003-0745-0840

Jakub Dostálek: 0000-0002-0431-2170

Author Contributions

The manuscript was written through contributions of all authors. All authors have given approval to the final version of the manuscript.

Funding

T.R., E.B., F.S., and O.P.-G. are grateful for the support from the Grant Agency of the Czech Republic (GACR) under Contract No. 15-09368Y and P205-12-G118, the Ministry of Education, Youth and Sports of CR within the National Sustainability Program II (Project BIOCEV-FAR LQ1604), by the project "'BIOCEV'" (CZ.1.05/1.1.00/02.0109) and by OPPK (CZ.2.16/3.1.00/21545), from the European Regional Development Fund. SH and JD were supported by Austrian Science Fund (FWF) through the project ACTIPLAS (P 244920-N20), and FEMTECH Frauen in Forschung and Technologie Initiative of the Austrian Ministry for Transportation, Innovation and Technology No. 840988. C.R.-E. acknowledges support of the Center for Chemical Polymer Technology (CPT) under the support of the EU and the federal state of North Rhine-Westphalia (Grant EFRE 30 00 883 02).

Notes

The authors declare no competing financial interest.

■ REFERENCES

(1) Lee, Y.-H.; Wong, D. T. *Am. J. Dent.* **2009**, *22*, 241−248.

(2) Rehak, N. N.; Cecco, S. A.; Csako, G. *Clin. Chem. Lab. Med.* **2000**, *38*, 335−343.

(3) Patil, P. B.; Patil, B. R. *J. Indian Soc. Periodontol.* **2011**, *15*, 310−317.

(4) Rathnayake, N.; Åkerman, S.; Klinge, B.; Lundegren, N.; Jansson, H.; Tryselius, Y.; Sorsa, T.; Gustafsson, A. *PLoS One* **2013**, *8*, e61356.

(5) Gitlin, N. *Clinical Chemistry* **1997**, *43*, 1500−1506.

(6) Schweitzer, A.; Horn, J.; Mikolajczyk, R. T.; Krause, G.; Ott, J. J. *Lancet* **2015**, *386*, 1546−1555.

(7) Lozano, R.; Naghavi, M.; Foreman, K.; Lim, S.; Shibuya, K.; Aboyans, V.; Abraham, J.; Adair, T.; Aggarwal, R.; Ahn, S. Y.; et al. *Lancet* **2012**, *380*, 2095−2128.

(8) Noppornpanth, S.; Sathirapongsasuti, N.; Chongsrisawat, V.; Poovorawan, Y. *Southeast Asian J. Trop. Med. Public Health* **2000**, *31*, 419−421.

(9) Brandtzaeg, P. *Ann. N. Y. Acad. Sci.* **2007**, *1098*, 288−311.

(10) Patidar, K. A.; Parwani, R. N.; Wanjari, S. P. *J. Oral Sci.* **2011**, *53*, 97−102.

(11) Chiappin, S.; Antonelli, G.; Gatti, R.; De Palo, E. F. *Clin. Chim. Acta* **2007**, *383*, 30−40.

(12) Homola, J. *Chem. Rev.* **2008**, *108*, 462−493.

(13) Stewart, M. E.; Anderton, C. R.; Thompson, L. B.; Maria, J.; Gray, S. K.; Rogers, J. A.; Nuzzo, R. G. *Chem. Rev.* **2008**, *108*, 494−521.

(14) Khatua, S.; Paulo, P. M.; Yuan, H.; Gupta, A.; Zijlstra, P.; Orrit, M. *ACS Nano* **2014**, *8*, 4440−4449.

(15) Liebermann, T.; Knoll, W. *Colloids Surf., A* **2000**, *171*, 115−130.

(16) Lakowicz, J. R.; Ray, K.; Chowdhury, M.; Szmacinski, H.; Fu, Y.; Zhang, J.; Nowaczyk, K. *Analyst* **2008**, *133*, 1308−1346.

(17) Choi, Y.-H.; Lee, G.-Y.; Ko, H.; Chang, Y. W.; Kang, M.-J.; Pyun, J.-C. *Biosens. Bioelectron.* **2014**, *56*, 286−294.

(18) Zheng, S.; Kim, D.-K.; Park, T. J.; Lee, S. J.; Lee, S. Y. *Talanta* **2010**, *82*, 803−809.

(19) Helton, K. L.; Nelson, K. E.; Fu, E.; Yager, P. *Lab Chip* **2008**, *8*, 1847.

(20) Blaszykowski, C.; Sheikh, S.; Thompson, M. *Biomater. Sci.* **2015**, *3*, 1335−1370.

(21) Chung, J. W.; Kim, S. D.; Bernhardt, R.; Pyun, J. C. *Sens. Actuators, B* **2005**, *111*−*112*, 416−422.

(22) Rodriguez-Emmenegger, C.; Hasan, E.; Pop-Georgievski, O.; Houska, M.; Brynda, E.; Alles, A. B. *Macromol. Biosci.* **2012**, *12*, 525−532.

(23) Riedel, T.; Surman, F.; Hageneder, S.; Pop-Georgievski, O.; Noehammer, C.; Hofner, M.; Brynda, E.; Rodriguez-Emmenegger, C.; Dostálek, J. *Biosens. Bioelectron.* **2016**, *85*, 272−279.

(24) Jones, D. M.; Brown, A. A.; Huck, W. T. S. *Langmuir* **2002**, *18*, 1265−1269.

(25) Rodriguez-Emmenegger, C.; Schmidt, B. V.; Sedlakova, Z.; Subr, V.; Alles, A. B.; Brynda, E.; Barner-Kowollik, C. *Macromol. Rapid Commun.* **2011**, *32*, 958−965.

(26) Rodriguez-Emmenegger, C.; Houska, M.; Alles, A. B.; Brynda, E. *Macromol. Biosci.* **2012**, *12*, 1413−1422.

(27) Ulbrich, K.; Šubr, V.; Strohalm, J.; Plocová, D.; Jelínková, M.; Říhová, B. *J. Controlled Release* **2000**, *64*, 63−79.

(28) Hermanson, G. T. In *Bioconjugate Techniques*, 3rd ed.; Academic Press: Boston, 2013; pp 229−258.

(29) Lee, Y. S.; Kim, B. K.; Choi, E. C. *Arch. Pharmacal Res.* **1998**, *21*, 521−526.

(30) Vaisocherová-Lísalová, H.; Surman, F.; Víšová, I.; Vala, M.; Špringer, T.; Ermini, M. L.; Šípová, H.; Šedivák, P.; Houska, M.; Riedel, T. s.; et al. *Anal. Chem.* **2016**, *88*, 10533−10539.

(31) Vaisocherová, H.; Ševců, V.; Adam, P.; Špačková, B.; Hegnerová, K.; de los Santos Pereira, A.; Rodriguez-Emmenegger, C.; Riedel, T.; Houska, M.; Brynda, E.; Homola, J. *Biosens. Bioelectron.* **2014**, *51*, 150−157.

(32) Bauch, M.; Dostalek, J. *Opt. Express* **2013**, *21*, 20470−20483.

(33) Wang, Y.; Brunsen, A.; Jonas, U.; Dostálek, J.; Knoll, W. *Anal. Chem.* **2009**, *81*, 9625−9632.

(34) Toma, K.; Adam, P.; Vala, M.; Homola, J.; Knoll, W.; Dostalek, J. *Opt. Express* **2013**, *21*, 10121−10132.

DOI: 10.1021/acs.analchem.6b04432
Anal. Chem. 2017, 89, 2972−2977

Supporting Information: Plasmonic hepatitis B biosensor for the analysis of clinical saliva

Tomáš Riedel, [*,†] Simone Hageneder, [‡] František Surman, [†] Ognen Pop-Georgievski, [†] Christa Noehammer, [§] Manuela Hofner, [§] Eduard Brynda, [†] Cesar Rodriguez-Emmenegger, [*,†,||] Jakub Dostálek[*,‡]

[†] Institute of Macromolecular Chemistry AS CR v.v.i., Heyrovsky Sq. 2, 162 06 Prague 6, Czech Republic

[‡] Biosensor Technologies, AIT-Austrian Institute of Technology GmbH, Muthgasse 11, 1190 Vienna, Austria

[§] Molecular Diagnostics, Health and Environment Dpt., AIT-Austrian Institute of Technology GmbH, Muthgasse 11, 1190 Vienna, Austria

[||] DWI – Leibniz Institute for Interactive Materials and Institute of Technical and Macromolecular Chemistry, RWTH Aachen University, Forckenbeckstraße 50, 52074 Aachen, Germany

Corresponding Author

* Tomáš Riedel, E-mail: riedel@imc.cas.cz, Phone: +420 296 809 333, Fax: +420 296 809 410
Cesar Rodriguez-Emmenegger, E-mail: rodriguez@dwi.rwth-aachen.de, Phone: +49 241 8023362, Fax: +49 241 80 23301.
Jakub Dostálek, E-mail: jakub.dostalek@ait.ac.at, Phone: +43 (0) 50550 4470, Fax: +43 (0) 50550 4450.

Characterization of the brush architecture

X-ray photoelectron spectroscopy (XPS)

XPS measurements were carried out with a K-Alpha$^+$ spectrometer (ThermoFisher Scientific, East Grinstead, UK). The samples were analyzed using a micro-focused, monochromated Al Kα X-ray source (400 μm spot size) at an angle of incidence of 30° (measured from the surface) and an emission angle normal to the surface. The kinetic energy of the electrons was measured using a 180° hemispherical energy analyzer operated in the constant analyzer energy mode (CAE) at 200 eV and 50 eV pass energy for the survey and high resolution spectra respectively. Data acquisition and processing were performed using Thermo Advantage software. The XPS spectra were fitted with Voigt profiles obtained by convolving Lorentzian and Gaussian functions. The analyzer transmission function, Scofield sensitivity factors, and effective attenuation lengths (EALs) for photoelectrons were applied for quantification. EALs were calculated using the standard TPP-2M formalism. All spectra were referenced to the C1s peak of hydrocarbons at 285.0 eV. The BE scale was controlled by the well-known position of the photoelectron C-C and C-H, C-O and C(=O)-O peaks of

polyethylene terephthalate and Cu 2p, Ag 3d, and Au 4f peaks of metallic Cu, Ag and Au, respectively. The BE uncertainty of the reported measurements and analysis is in the range of ±0.1 eV.

The XPS analysis verified the covalent structure of the poly(HPMA-*co*-CBMAA) brushes grown from the initiator SAM on Au via SI-ATRP. The core level C 1s spectrum (Figure 2 a) of the brushes is characterized by C-C, C-H (285.0 eV), C*-C(=O)- from the secondary chemical shifts induced to the carbon atoms in the vicinity to amide and charged carboxylic groups (285.5 eV), C-N (286.1 eV), C- OH (286.9 eV), C(=O)-NH (288.0 eV) and C(=O)-O- carboxylate (288.7 eV). The high resolution N 1s spectrum of the brushes is characterized by a prevailing amide contribution (400.1 eV) and a contribution characteristic for the quaternary ammonium cation of the CBMAA comonomer (403.0 eV). The corresponding O 1s spectrum was fitted with two contributions arising from the C=O (531.4 eV) and C-O (532.6 eV) moieties of HPMA and CBMAA. Table S1 reports the surface atomic concentration of the identified moieties. Based on the obtained XPS results, the composition of the poly(HPMA-*co*-CBMAA) brushes was estimated to be 87% HPMA and 13% CBMAA.

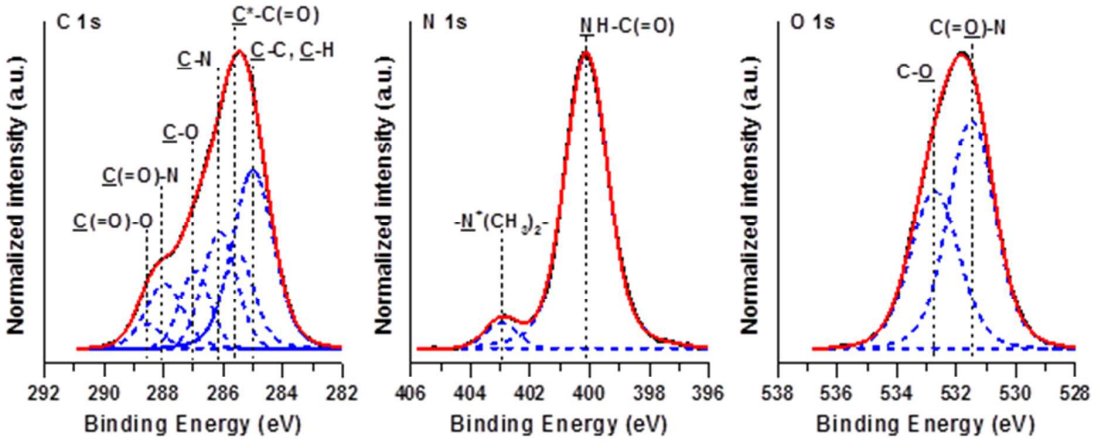

Figure S1. High resolution C 1s, O 1s and N 1s XPS spectra of poly(HPMA-*co*-CBMAA) brushes grown from the sensor surface by SI-ATRP. Measured spectra are presented with black lines, while their corresponding fitted envelopes are presented in red. The individual contributions of different functional groups are represented with dotted blue lines.

Table S1. Surface concentration of chemical moieties present on the surfaces of poly(HPMA-*co*-CBMAA) brushes as determined by XPS.

	Moiety	Binding energy [eV]	Surface concentration [atomic %]
C1s	C-C, C-H	285.0	27.1 ± 0.7
	C*-C=O	285.5	10.7 ± 0.6
	C-N	286.1	13.5 ± 0.2
	C-O	286.9	9.6 ± 1.2
	C(=O)-NH	288.0	8.1 ± 0.4
	C(=O)-O	288.7	1.8 ± 0.8
N1s	NH-C(=O)	400.1	10.5 ± 0.1
	$N^{+}(CH_3)_2$	403.0	0.6 ± 0.1
O1s	O=C	531.4	7.5 ± 0.4
	O-C	532.6	10.6 ± 0.6

Fourier transform infrared grazing angle specular reflectance spectroscopy (FTIR-GASR)

FTIR-GASR was carried out using a Nicolet Nexus 870 with a SAGA attachment. In total 256 scans at a resolution of 2 cm^{-1} were recorded for each sample and processed with OMNIC software. The spectrometer was purged continuously with dry air.

The FTIR GASR spectrum of poly(HPMA-*co*-CBMAA) brushes (Fig. S2) exhibits both a band at 1376 cm^{-1} and a shoulder band at 1610 cm^{-1} corresponding to the symmetric and asymmetric stretching modes of COO^- stemming from CBMAA as well as it shows the amide I and amide II bands at 1527 and 1653 cm^{-1} originating from the HPMA.

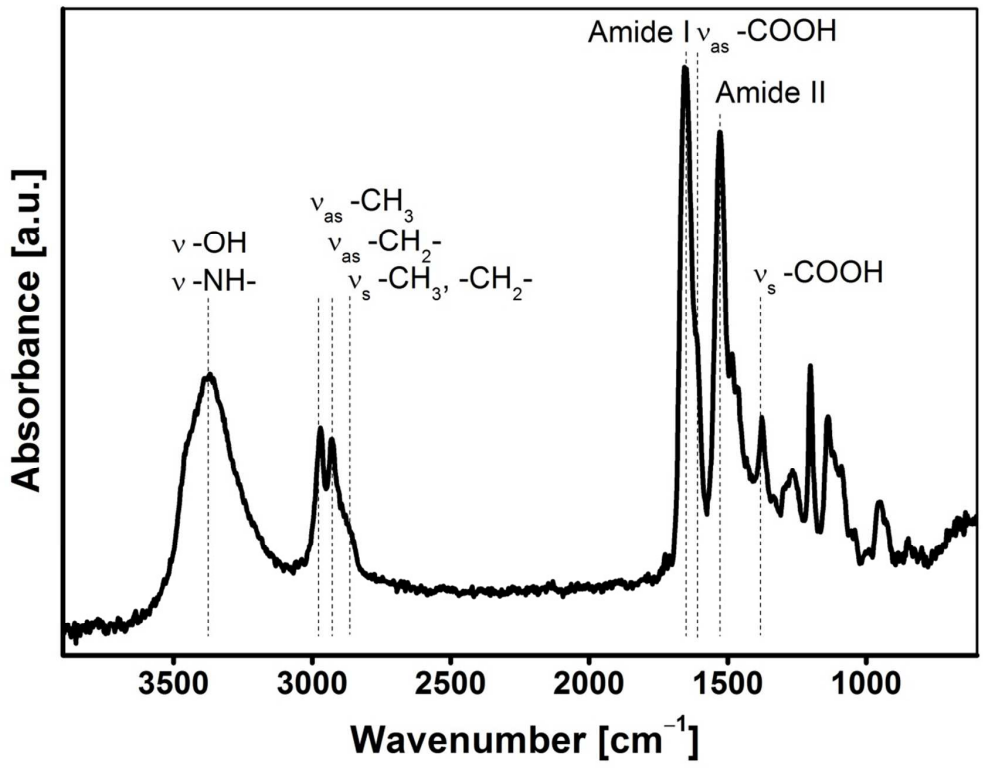

Figure S2. FTIR GASR spectrum of the poly(HPMA-co-CBMAA) brush.

Atomic force microscopy (AFM)

Multimode AFM Nanoscope IIIa (Digital Instruments) was used to investigate the topography of the polymer brushes. The scans were performed in tapping mode in water. Area of 5x5 µm2 was scanned at a rate 0.5 Hz and analyzed using Gwyddion software.

The AFM images showed smooth and homogenous coverage with the polymer brush without any uncovered areas (Fig. S3). The roughness (root mean square) of the surface was Rq = 1.4±0.1 nm.

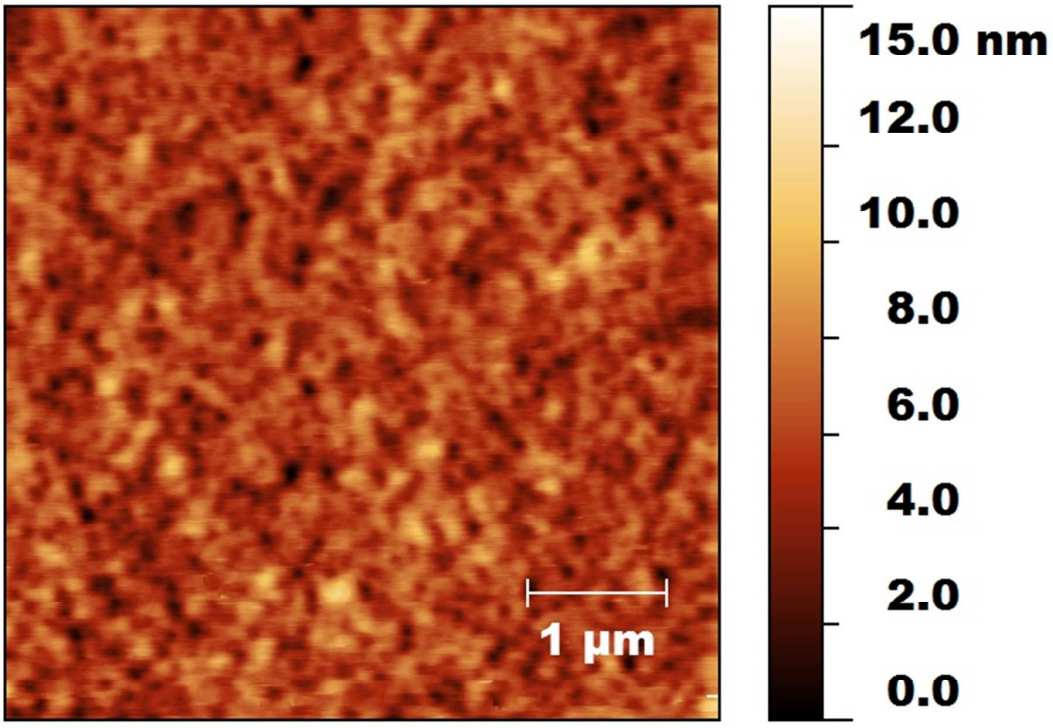

Figure S3. A topographical image of the poly(HPMA-*co*-CBMAA) brush. Scale bar is 1 µm.

Post-modification of brushes with protein ligand

The selection of the buffer was optimized based on the following premises: (1) Favor activation of carboxylic groups (formation of N-hydrosuccynimide active ester) over the hydrolysis of the active ester, and (2) the amidation of proteins to the carboxylic groups of the brushes over the hydrolysis of the N-hydrosuccynimide. The active ester is more prone to

hydrolysis at basic pH compared to slightly acidic conditions, that is why we performed the activation in SA buffer and water. Moreover, the SA buffer better solubilizes any residual EDC or NHS which could remain on the surface. The immobilization of the antigen (pI 4.6) [Lee, Y. S.; Kim, B. K.; Choi, E. C., Physicochemical properties of recombinant hepatitis B surface antigen expressed in mammalian cell (C127). Archives of Pharmacal Research 1998, 21 (5), 521-526] is conducted at 7.4 in HEPES buffer. The copolymer brushes are composed of HPMA (neutral) a betaine (quaternary ammonium always positively charge and carboxylate: negatively charged above pH 4) and some betaines activated (only the quaternary ammonium). Thus the surface in the immobilization procedure can only be positively charged. At pH 7.4 (HEPES) the antigen is slightly negatively charged (pI 4.6). Therefore the antigen will be attracted to the surface increasing the efficiency of the covalently coupling. The sample is then incubated in PBS so that any unreacted succinimide group is hydrolyzed.

3.2 In situ monitoring of rolling-circle amplification on a solid support by surface plasmon resonance and optical waveguide spectroscopy

The following chapter is reprinted with permission from:

Lechner, B.*, **Hageneder, S.*,** Schmidt, K., Kreuzer, M. P., Conzemius, R., Reimhult, E., Ivan Barišić, I. & Dostalek, J., 2021. In Situ Monitoring of Rolling Circle Amplification on a Solid Support by Surface Plasmon Resonance and Optical Waveguide Spectroscopy. ACS Applied Materials & Interfaces. https://doi.org/10.1021/acsami.1c03715

(*contributed equally)

First author paper: BL and I were working jointly on the experiment design, conduction and analysis, results discussion, writing the initial manuscript and figure preparation, reviewing and editing the final paper. JD was the supervising author and was involved with concept formation, results discussion, and manuscript composition. KS and MPK supported the experiments. RC and IB were responsible for padlock design and involved in experiment design and discussion. ER was involved in discussion and manuscript review.

The following chapter deals with the real-time observation of the growth and (ion-) responsiveness of polyelectrolyte single stranded deoxyribonucleic acid (ssDNA) brushes tethered to a surface. PEF combined with OWS allows the *in-situ* and real-time observation of rolling circle amplification (RCA) prolongation of ssDNA chains in the form of an electrolyte brush, as well as conformation changes in the bioarchitecture through changes in the ionic environment and intra- and interchain crosslinking by oligonucleotide staples. Furthermore, this observed compaction of the brushes was more than ten times, providing a valuable feature for signal enhancement in an analytical application.

ACS APPLIED MATERIALS & INTERFACES

www.acsami.org Research Article

In Situ Monitoring of Rolling Circle Amplification on a Solid Support by Surface Plasmon Resonance and Optical Waveguide Spectroscopy

Bernadette Lechner, Simone Hageneder, Katharina Schmidt, Mark P. Kreuzer, Rick Conzemius, Erik Reimhult, Ivan Barišić, and Jakub Dostalek*

Cite This: https://doi.org/10.1021/acsami.1c03715 Read Online

ACCESS | Metrics & More | Article Recommendations | Supporting Information

ABSTRACT: The growth of surface-attached single-stranded deoxyribonucleic acid (ssDNA) chains is monitored *in situ* using an evanescent wave optical biosensor that combines surface plasmon resonance (SPR) and optical waveguide spectroscopy (OWS). The "grafting-from" growth of ssDNA chains is facilitated by rolling circle amplification (RCA), and the gradual prolongation of ssDNA chains anchored to a gold sensor surface is optically tracked in time. At a sufficient density of the polymer chains, the ssDNA takes on a brush architecture with a thickness exceeding 10 μm, supporting a spectrum of guided optical waves traveling along the metallic sensor surface. The simultaneous probing of this interface with the confined optical field of surface plasmons and additional more delocalized dielectric optical waveguide modes enables accurate *in situ* measurement of the ssDNA brush thickness, polymer volume content, and density gradients. We report for the first time on the utilization of the SPR/OWS technique for the measurement of the RCA speed on a solid surface that can be compared to that in bulk solutions. In addition, the control of ssDNA brush properties by changing the grafting density and ionic strength and post-modification via affinity reaction with complementary short ssDNA staples is discussed. These observations may provide important leads for tailoring RCA toward sensitive and rapid assays in affinity-based biosensors.

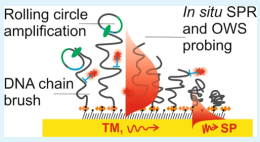

KEYWORDS: *rolling circle amplification, DNA, polyelectrolyte brushes, surface plasmon resonance, optical waveguide spectroscopy, surface plasmon-enhanced fluorescence, biointerfaces*

INTRODUCTION

The analysis of nucleic acids using polymerase chain reaction (PCR) has become a central method in numerous important fields ranging from screening hereditary diseases, detecting infectious pathogens, and cancer diagnosis to forensics and food quality control.[1−5] In the past decades, PCR-based methods have been gradually advancing, and we witnessed their implementation in a broad spectrum of analytical tools, including real-time PCR, digital PCR, and DNA sequencing.[6−8] In addition, there are pursued alternative approaches to PCR that allow a faster and simpler analysis of nucleic acid-based analytes without the need of thermocycling, such as isothermal rolling circle amplification (RCA)[9−11] and loop-mediated isothermal amplification (LAMP).[12,13] All these methods rely on enzymatic reactions with nucleic acids and are predominantly used in bulk solutions. However, the deployment of DNA amplification reactions at solid surfaces holds the potential to expand the performance of DNA analytical technologies through, for example, efficient multiplexing.[14,15] In addition, surface DNA amplification reactions may open doors to other types of sensor modalities and assay amplification strategies suitable for the detection of different analytes, including proteins that cannot be directly amplified and are typically detected by immunoassays.[16−18]

RCA enables generating densely packed single-stranded deoxyribonucleic acid (ssDNA) chains that form polyelectrolyte brush layers. Common techniques to observe such surface-attached polymer chains are ellipsometry,[19,20] fluorescence imaging,[21,22] X-ray photoelectron spectroscopy,[23] and angle-resolved near-edge X-ray absorption fine structure spectroscopy (NEXAFS).[24] However, these techniques typically provide information on the final structure and cannot be used to monitor the RCA growth process. The observation of soft ssDNA brushes in contact with a solvent was performed by atomic force spectroscopy, and the obtained thickness was substantially lower compared to the length of the ssDNA chains.[25] A chain length of up to several kilobases was determined for RCA-grown ssDNA brushes using enzymatic cleavage from the surface and subsequent gel electrophoresis, yielding a prolongation rate in the order of magnitude of several tens of bases/sec at the surface.[25] It should be noted

Received: March 3, 2021
Accepted: June 16, 2021

ACS Applied Materials & Interfaces www.acsami.org Research Article

Table 1. Overview of the Used Oligonucleotides and Their Respective Molecular Weight (M_w)[a]

Oligonucleotide	Sequence (5'→ 3')	M_w (kDa)
Linear padlock probe (LP) (TS+/.../C2CA+/.../TS+)	TGTGATACAGCTTTCTTGCGCGTGTATGCAGCTCCTCGAGTAGCCGC AGTTCGCGCCGCAGGGCCGATACGTGTAACTTAT	25
Target (biotin/TS-)	biotin/TTTTTTTTTTTTTTTTTTTTAAGAAAGCTGTATCACAATAAGTT ACACGTATCGG	17.3
Labeling sequence (C2CA+/Cy5)	Cy5/GTGTATGCAGCTCCTCGAGTA	7
Randomized labeling sequence (random/Cy5)	Cy5/CAGCATCAGCTACGACTACGACTG	7.8
Stapling sequence (BA+/Cy5)	Cy5/TTATTGTGATACAGCTGGCCGATACGTGTAAC	10.4

[a]The (+) sequences are complementary to their corresponding (−) sequences, and colors indicate the parts that affinity hybridize.

that the growth of ssDNA using RCA on solid surfaces differs from that in bulk due to steric hindrance and slowed down diffusion of molecules associated with the interface carrying densely packed neighboring chains.[26]

Surface plasmon resonance (SPR) represents an established method for the observation of polymer thin films and molecular interaction analysis at solid surfaces.[27] It relies on the probing of (typically) a gold sensor surface using a tightly confined field of surface plasmons (SPs)—optical waves originating from the coupled collective oscillations of charge density and the respective electromagnetic field. SPR biosensors allow tracking molecular binding events accompanied by an increase or a re-distribution of the refractive index occurring in close proximity to the metallic sensor surface in real time.[28] To observe thicker polymer architectures such as crosslinked networks forming hydrogels, the SPR technique was combined with optical waveguide spectroscopy (OWS).[29,30] The analysis of detuning the resonant optical coupling to multiple dielectric waveguide modes (traveling along the surface with a more delocalized field profile than SPs) enables obtaining a more detailed picture of the interface. It allows for encoding multiple resonances to the measured optical spectra and, for example, accessing the information on the swelling and collapsing of polymer brushes in simpler means than with probing only by SPR.[31] Among others, OWS was utilized for the observation of hydrogel thin-film density gradients and for determining the responsive characteristics of polymers to external stimuli.[32,33] Moreover, the enhanced field intensity occurring upon the resonant excitation of SPs and optical waveguide (OW) modes has also been exploited for the optical amplification of weak fluorescence signals in a technique referred to as SP-enhanced fluorescence spectroscopy (SPFS).[34,35] The combined SPR and SPFS measurement allows distinguishing binding events of different molecular species and determining, for example, the incorporation of nucleotides to ssDNA strands attached to a gold surface using the Klenow fragment of a polymerase enzyme.[36]

We report on the combination of SPR, OWS, and SPFS for the *in situ* observation of RCA on a solid metal surface. This approach provided means for real-time monitoring of the growth of ssDNA chains that form a polyelectrolyte brush architecture with a thickness of above 10 μm. Furthermore, it was utilized to determine its important characteristics such as the grafting density of oligonucleotide chains, polymer volume content, time-dependent average chain length, reaction speed in terms of the number of nucleotides incorporated per minute, and the impact of the ionic strength on the thickness of the polyelectrolyte brush. Moreover, this technique was utilized for kinetic measurements of affinity binding of biomolecules occurring inside these brushes by labeling the chains and investigating the effect of intra- and inter-chain crosslinking with short ssDNA staples.

EXPERIMENTAL SECTION

Materials. The hydroxyl-(HS-$[CH_2]_{11}$-EG_6-OH)- and biotin-(HS-$[CH_2]_{11}$-EG_6-biotin)-terminated alkane oligo(ethylene glycol) (OEG)-thiols were purchased from ProChimia Surfaces (Poland). Phosphate-buffered saline (PBS, 137 mM NaCl, 2.7 mM KCl, 12 mM phosphate, pH = 7.4), nuclease-free water (NFW), Tween 20, and ethanol (EtOH) were obtained from VWR Chemicals (Germany). PBS Tween (PBST) was prepared by adding Tween 20 [0.05% (v/v)] to PBS. Hellmanex III, sodium chloride (NaCl), calcium chloride ($CaCl_2$), potassium chloride (KCl), magnesium chloride ($MgCl_2$), and sucrose were ordered from Sigma-Aldrich (Germany). Bovine serum albumin (BSA) was purchased from New England Biolabs (United Kingdom) and was diluted with NFW to a final concentration of 0.2 mg/mL (NFW-BSA). Neutravidin (NA, M_w = 67 kDa), phi29 DNA polymerase (φ-29 Pol), and deoxynucleotide triphosphates (dNTPs) were obtained from Thermo Scientific (Germany) and Ampligase DNA ligase from Biozym (Germany). The DNA oligonucleotides, summarized in Table 1, were acquired from Integrated DNA Technologies (Belgium).

Sensor Chip Preparation. Substrates made from BK7 (Assistant, Germany) or N-LASF9 (Hellma GmbH, Germany) glass were subsequently sonicated in 1% (v/v) Hellmanex III, ultrapure water ($R \geq 18.2$ MΩ/cm^2), and ethanol, followed by thorough rinsing with pure ethanol and drying in a stream of pressured air. Afterward, they were loaded into a vacuum thermal evaporator (HHV Ltd, Auto306 Lab Coater, UK) to deposit 2 nm-thick chromium and 50 nm-thick gold (MaTeck, Germany) layers in a vacuum better than 10^{-6} mbar. The freshly prepared gold layers were modified using a mixed-thiol self-assembled monolayer (SAM) by immersion in 1 mM ethanolic solution containing a mixture of thiols with biotin and hydroxyl headgroups dissolved at a molar ratio of 1:4. After overnight incubation, the glass substrates with a SAM-modified gold surface were rinsed with pure EtOH, dried under a nitrogen stream, and stored in the dark under an argon atmosphere until further use.

Growth of the ssDNA Brushes. NA (125 μg/mL in PBST) was flowed over the sensor surface for 90 min and allowed to bind to the biotin-functionalized SPR sensor chip, which was modified with a mixed-thiol SAM. The surface was rinsed with PBST, and the biotinylated target sequence (biotin/TS) hybridized with the circular padlock (CP) probe was reacted with the sensor surface for 30 min. Then, RCA was conducted for 1−4 h under a continuous flow of a solution with phi29-DNA polymerase (φ29-Pol) and the respective reagents. A detailed description of the preparation of the CP and the RCA reaction on the surface can be found below.

Ligation. The padlock probe sequence (LP, 90 nM) was ligated in the presence of the biotinylated target sequence (biotin/TS-, 40 nM) and 75 units of DNA ligase in NFW-BSA with the respective ligation

https://doi.org/10.1021/acsami.1c03715
ACS Appl. Mater. Interfaces XXXX, XXX, XXX−XXX

buffer (20 mM Tris-HCl, 25 mM KCl, 10 mM $MgCl_2$, 0.5 mM NAD, and 0.01% Triton X-100) in a total volume of 500 μL. Ligation was conducted for 2 h at 50 °C at 700 rpm on a shaker, and it was terminated by heating the solution to 85 °C for 5 min.

Rolling Circle Amplification. RCA was conducted with 100 units of φ29-Pol and 100 μM of each dNTP in NFW-BSA with the respective buffer constituents (33 mM Tris-acetate, 10 mM Mg-acetate, 66 mM K-acetate, 0.1% Tween 20, and 1 mM DTT) in a total volume of 500 μL. Prior to the RCA, the sensor chip was rinsed with φ29-Pol buffer without the dNTPs to establish a baseline in the sensor response. The RCA product was hybridized with Cy5 fluorophore-labeled C2CA+ oligonucleotide (C2CA+/Cy5) at a concentration of 10 nM in PBST for 15 min, which was followed by a buffer-rinsing step for 5 min.

Optical Instrument. A home-built SPR/OWS optical system based on the Kretschmann configuration (see Figure 1) was used for

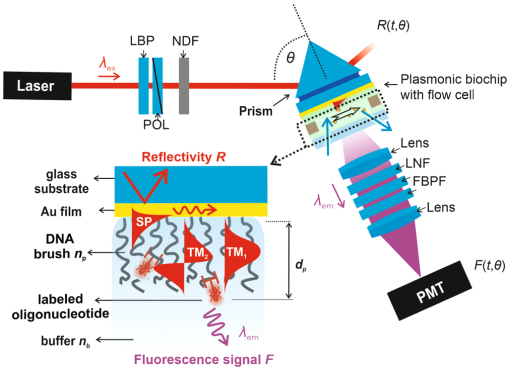

Figure 1. Optical configuration used for the combined SPR, OWS, and SPFS measurements.

the resonant excitation of SP and dielectric OW modes at the sensor chip carrying a gold layer with the mixed-thiol-OEG-OH/biotin SAM and in the course of the experiment generated ssDNA brushes. This sensor chip was optically matched to a 90° LASF9 glass prism base using refractive index immersion oil (Cargille Laboratories, USA) and was mounted on a rotation stage. A HeNe laser beam at a wavelength of λ_{ex} = 632.8 nm passed through a laser band-pass filter (LBF) and neutral density filter (NDF) and was coupled to the prism impinging at the sensor chip surface at a controlled angle of incidence θ. The intensity of the reflected beam R was measured with a photodiode connected to a lock-in amplifier. A transparent flow cell was clamped against the sensor chip to transport liquid samples along the sensor surface. The flow cell was composed of a glass substrate with drilled inlet and outlet ports and a thin PDMS gasket that defined a reaction chamber volume of 10 μL. The flow cell was connected with Tygon tubing (inner diameter = 0.25 mm) to a peristaltic pump to flow liquid samples kept at room temperature with a flow rate set to 50 μL/min. All reaction mixtures containing proteins and enzymes were continuously re-introduced by closing the tubing loop. The reflected beam intensity R was monitored as a function of the angle of incidence θ or time t to resolve changes in resonant excitation of SP and OW modes that manifest themselves as a series of dips in $R(\theta)$. The polarization of the excitation beam was set to transverse magnetic (TM) or transverse electric (TE) using a polarizer (POL). In addition, the resonantly coupled SPs and OWs were utilized for the excitation of Cy5 fluorophore labels conjugated with ssDNA that binds to the RCA-synthesized ssDNA chains at the sensor surface. These fluorophores emitted fluorescence light at a shifted wavelength of λ_{em} = 670 nm, which was collected through the transparent flow cell using a lens and made to pass through a fluorescence band-pass filter (FBPF, 670FS10-25 from Andover Corporation Optical Filter, USA) and a laser notch (LNF, XNF-632.8-25.0M, CVI Melles Griot, USA) filter. The spectrally clean fluorescence beam was focused using an additional lens at the input of a photomultiplier tube (PMT, H6240-01 from Hamamatsu Photonics, Japan). The intensity of the fluorescence signal F was measured with a photon counter (53131A from Agilent, USA) in counts per second (cps). The optical instrument was operated with dedicated software (Wasplas, developed at Max Planck Institute for Polymer Research, Mainz, Germany; see more details in the Supporting Information).

Sensor Readout and Data Analysis. The SPR measurement started with recording the angular reflectivity spectrum $R(\theta)$ for a gold sensor surface that carried a mixed-thiol SAM in contact with PBST. Time-dependent measurements $R(t)$ were performed at an angle of incidence θ set in the vicinity to the SPR dip within the range, where the reflectivity linearly decreases with the angle of incidence θ. The recorded variations in reflectivity $R(t)$ were converted to refractive index unit (RIU) changes using a calibration. This calibration was performed by measuring $R(t)$ upon the flow of aqueous solutions containing 1, 2, and 4% (w/w) of sucrose, which increases the bulk refractive index by $\Delta n_b = 1.4 \times 10^{-3}$, 2.9×10^{-3}, and 5.8×10^{-3} RIU, respectively. After each immobilization or reaction step (NA, target sequencelcircular padlock, RCA), the sensor surface was rinsed with PBST, and an angular reflectivity spectrum $R(\theta)$ was recorded. These curves were fitted with a Fresnel reflectivity-based model using dedicated software (Winspall, developed at Max Planck Institute for Polymer Research, Mainz, Germany). The polymer brushes were approximated as a dielectric layer with a thickness d_p and refractive index n_p, which were determined by fitting the resonant angles of a series of dips in the measured reflectivity curves $R(\theta)$ that are associated with the resonant excitation of SP and OW modes. The modes measured in TE and TM polarization were fitted in parallel, and the birefringence was omitted.

The surface mass density of the polymer layer was calculated as $\Gamma = d_p(n_p - n_b)/(dn/dc)$, where n_p and n_b are the refractive indices of the attached layer and of the buffer, respectively, and d_p is the thickness of the protein/ssDNA layer. The incremental change in the refractive index with the concentration (dn/dc) for DNA and protein was set to 0.17 and 0.2 mm^3/mg, respectively.[37,38] Surface mass density Γ was obtained in ng/mm^2, and it was converted into a grafting density σ of attached molecules per area (in $nmol/mm^2$) using their respective molecular weights (M_w). A summary of the used mathematical models can be found in the Supporting Information.

RESULTS AND DISCUSSION

As illustrated in Figure 2, the "grafting-from" growth of ssDNA polymer chains was initiated by capturing a circular padlock (CP) probe that was hybridized with the target sequence (TS) to facilitate solid-phase RCA at the sensor surface.[39] The padlock probe sequence was designed to hybridize with the specific TS that is present in the clinically highly important antibiotic resistance gene bla_{OXA-48}.[40] For the proof of concept, the linear padlock probe (LP) was hybridized with the synthetic TS that was conjugated with biotin (biotin/TS-). The subsequent ligation reaction enzymatically sealed the gap between the 5′ and 3′ ends of the target recognition arms of the LP when hybridized with the TS. This step is highly specific and led to the circularization of the padlock probe—CP. Afterward, the created target sequencelcircular padlock duplex (biotin/TS-lCP) was anchored to the sensor chip gold surface in an oriented manner.[41] This was done through biotin moieties incorporated to the mixed-thiol SAM, which allowed the binding of NA, serving as a linker for the immobilization of the biotin/TS-lCP construct.

Isothermal RCA was initiated by the addition of φ29-polymerase, which sequentially incorporates nucleotides (dNTPs) on the TS- free 3′ end to form long ssDNA chains composed of multiple reverse-complementary repeats of the

https://doi.org/10.1021/acsami.1c03715
ACS Appl. Mater. Interfaces XXXX, XXX, XXX−XXX

ACS Applied Materials & Interfaces www.acsami.org Research Article

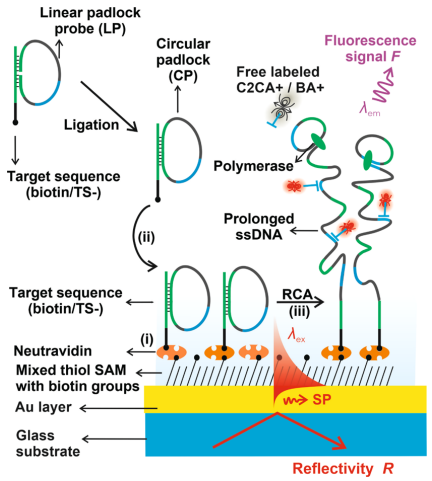

Figure 2. Schematics of the biointerface architecture and the growth of the ssDNA brush.

CP sequence. Then, the RCA product was reacted with C2CA + or BA+ oligonucleotides conjugated with Cy5 fluorophores (C2CA+/Cy5 and BA+/Cy5, respectively). All immobilization procedures were monitored using an optical setup, which combined surface plasmon resoance (SPR) and surface plasmon-enhanced fluorescence spectroscopy (SPFS) (see Figure 1). The SPR detection principle allowed us to acquire time-dependent kinetics of the sensor response $R(t)$, while the recorded angular reflectivity curves $R(\theta)$ were used for probing the biointerface with multiple SP and OW modes in order to determine changes in the ssDNA polymer architecture thickness d_p and refractive index n_p, reflecting increasing surface mass density Γ. Furthermore, the fluorescence intensity, originating from fluorophore-labeled biomolecules that were affinity-bound to the ssDNA chains and excited via the resonantly coupled SP and OW modes, was recorded in time $F(t)$ and as a function of the angle of incidence $F(\theta)$. These SPFS recordings enabled monitoring events that yield only subtle changes in the refractive index and hence cannot be measured with SPR.

Implementation of the Assay on a Plasmonic Sensor.

Figure 3a shows a typical SPR sensorgram $R(t)$ upon the subsequent binding of (i) NA, (ii) the biotin/TS oligonucleotide hybridized to the circular padlock probe—CP, and (iii) RCA followed by the binding of C2CA+/Cy5. The affinity binding of the tetravalent NA to the biotin headgroups on the thiol-SAM led to an increase in the SPR response to ΔR_{NA} = 3.8 mRIU. The free biotin-binding pockets allowed us to anchor the oligonucleotide biotin/TS|CP duplex in a following step, which changed the SPR response of $\Delta R_{biotin/TS|CP}$ = 1.2 mRIU. After the contacting of φ29-Pol and dNTPs with the sensor surface, a gradual increase in the sensor signal $R(t)$ was observed, which corresponds to the binding of the polymerase and the subsequent prolongation of ssDNA chains tethered to the sensor surface via the biotin tag. In this experiment, the RCA reaction was terminated after 1 h by removing nucleotides from the flow cell (through rinsing with a buffer), and an increase in the SPR signal ΔR_{RCA} = 2.3 mRIU was measured with respect to the baseline after the oligonucleotide immobilization. The abrupt jumps in the SPR response occurring upon rinsing the sensor surface with ligation and RCA buffers are ascribed to variations in the bulk refractive index n_b due to different buffer compositions. The generated ssDNA chains are composed of repeating C2CA—sequences and TS—sequences complementary to the CP. In order to confirm their presence, complementary C2CA+/Cy5 and control non-complementary (random/Cy5) Cy5-labeled oligonucleotides were reacted with the sensor surface after each reaction step. As seen in the recorded fluorescence signal $F(t)$ before conducting RCA, the signal increased abruptly after the injection of fluorophores conjugated to short oligonucleotides but dropped back to its baseline level after the rinsing with buffer. This rapid increase in the fluorescence signal is explained by the excitation of the Cy5 fluorophores in the bulk solution. After running the RCA, the introduction of the control non-complementary oligonucleotides conjugated with Cy5 showed a small change in the fluorescence intensity of $\Delta F_{random/Cy5}$ = 600 cps. However, the reaction with a specific oligonucleotide was accompanied by a 130-fold stronger increase in the fluorescence intensity of $\Delta F_{C2CA+/Cy5}$ = 80,000 cps, proving the successful synthesis of ssDNA chains by RCA.

To determine the surface mass density Γ of the incorporated molecules on the surface, the reflectivity curves $R(\theta)$ were measured in between each reaction step, as shown in Figure

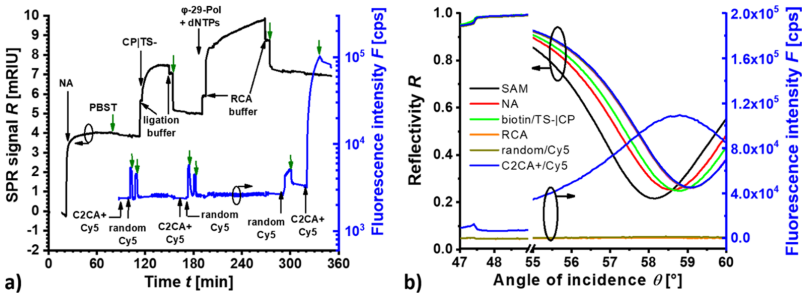

Figure 3. (a) Example of the kinetic SPR signal $R(t)$ and fluorescence signal $F(t)$ upon capture of neutravidin, the CP and the generation of the ssDNA polymer brush through RCA on the sensor surface. (b) Respective angular reflectivity $R(\theta)$ and fluorescence $F(\theta)$ scans measured between the reaction steps.

D
https://doi.org/10.1021/acsami.1c03715
ACS Appl. Mater. Interfaces XXXX, XXX, XXX−XXX

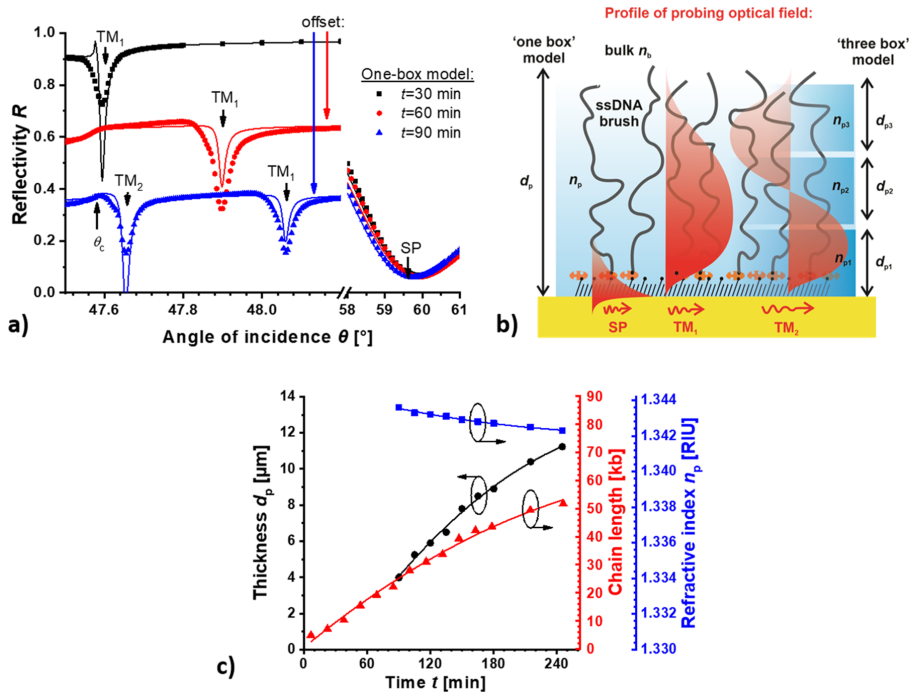

Figure 4. (a) Angular reflectivity curves $R(\theta)$ (measured data are shown as symbols, and fitted curves using the "one-box model" are showed as lines). For better data visualization, the reflectivity curves $R(\theta)$ measured at 60 and 90 min for $\theta < 50°$ are offset by a factor of 0.3 and 0.6, respectively (offset indicated with red and blue arrows). (b) Schematics of probing the ssDNA brushes with distinct distribution of electromagnetic field amplitude of SP and OW modes and used models approximating the optical properties of the brush. (c) Determined time-dependent thickness d_p and refractive index n_p together with estimated polymer chain length. Determined values are shown as symbols and fitted with a polynomial function (lines).

3b, and fitted with a Fresnel reflectivity-based model. The black curve in Figure 3b shows the resonant excitation of SPs on the gold surface carrying a mixed thiol SAM, which manifests itself as a dip in the angular reflectivity $R(\theta)$. This dip is centered at the resonance angle $\theta = 58.15°$, and it shifted to a higher angle ($\theta = 58.6°$) upon the conjugation of NA to the biotin headgroups and after immobilization of the biotin/TSlCP duplex ($\theta = 58.75°$). These shifts translate to a grafting density σ of 3.1×10^{-5} and 1.8×10^{-5} nmol/mm^2 for the immobilized NA and targetlpadlock duplex, respectively. A closer look at this number revealed that only ~59% of the immobilized NA molecules reacted with a biotin-tagged oligonucleotide strand. This can be ascribed to the fact that NA shows ~7 nm center-to-center distance at full surface coverage,[42] and thus, the subsequent reaction with the 81 nt circularized padlock probe exhibiting a diameter of ~9 nm was likely to be sterically hindered.[43]

The shift in the SPR angle after the RCA to $\theta = 59°$ cannot be independently attributed to the bound polymerase and the generated RCA product. However, the excitation of Cy5 fluorophores in $F(\theta)$ was only observed after hybridizing the RCA product with its specific C2CA+/Cy5 oligonucleotide. This proves the presence of the ssDNA chains within the evanescent field of SPs, as their excitation enhanced the emitted fluorescence intensity. Thus, it can be observed as a peak in the spectrum $F(\theta)$ at the angle where a dip occurs in the SPR reflectivity curve $R(\theta)$. It is worth noting that only the fluorescence-based measurement provides this confirmation, as the change in the SPR detection channel gave a negligible shift in $R(\theta)$ after the specific binding of C2CA+/Cy5 that exhibits too low molecular weight M_w.

***In Situ* Monitoring of Chain Growth.** Several research groups investigated RCA on the solid surface using SPR and reported that the measured output signal saturated, and increasing the reaction time was assumed to not change the properties of the generated ssDNA chains for reaction times, t, above 1 h.[44−48] In general, this optical measurement allows us to monitor changes occurring only within the evanescent field of SPs that probe a distance of up to about 100 nm from the gold surface. In the following study, we attempted to optically probe farther from the surface and investigate ssDNA chains generated by the RCA for several hours on the gold surface with a grafting density of CP probes $\sigma_{\text{biotin/TSlCP}} = 2.6 \times 10^{-5}$ nmol/mm^2 (detailed calculations can be found in the Supporting Information). In these measurements, we continuously recorded reflectivity curves $R(\theta)$ in order to *in situ* optically track the prolongation of ssDNA brushes every 15 min. Interestingly, after 30 min of reaction, we observed an additional resonant dip in $R(\theta)$ close to the critical angle $\theta_c = 47.5°$ (besides the SPR dip at $\theta \sim 59°$); see Figure 4a. This resonant dip in the reflectivity spectrum can be attributed to the resonant excitation of dielectric OW modes traveling along

https://doi.org/10.1021/acsami.1c03715
ACS Appl. Mater. Interfaces XXXX, XXX, XXX−XXX

the surface. The excitation of such waves (for transverse polarized light marked as $TM_{1,2,3...}$) is a signature of the presence of a ssDNA polymer layer with a refractive index n_p higher than that of the bulk solution n_b and a thickness d_p exceeding 100 nm. Furthermore, we took advantage of the interrogation of the resonant excitation of OW modes to optically probe DNA polymer strands stretching beyond the regular probing depth of SPR upon their prolongation by the RCA reaction (see Figure 4b). At thicknesses d_p > 100 nm, the growth of ssDNA chains occurs outside the evanescent field of SPs, and thus, only OWS enables their monitoring from the independent measurements of the thickness d_p and the refractive index n_p of the respective polymer layer. This was possible by fitting the measured angular reflectivity curves $R(\theta)$ exhibiting a series of resonant dips (Figure 4b) with a Fresnel reflectivity-based model. For the analysis of the obtained data, the surface-attached ssDNA brush was first represented by a homogeneous dielectric layer with a uniform refractive index n_p in contact with a semi-infinite medium exhibiting a bulk refractive index of the buffer (n_b = 1.336). This approach is referred to as the "one-box model," and Figure 4c shows the obtained time dependence of these two parameters, which reveals gradual incorporation of nucleotides by RCA that leads to the generation of d_p = 11.2 μm-thick brush after 4 h of reaction. In general, at least two resonant features need to be fitted to determine both the refractive index n_p and thickness d_p independently, and thus, this was possible only for times t > 90 min. Interestingly, the (average) refractive index n_p of the ssDNA brush determined from OWS was gradually decreasing upon the RCA reaction, reaching a value of n_p = 1.3423 after t = 240 min. This can indicate that the prolongation stops on some strands and the brush gets diluted as it grows away from the surface analogously to chain termination in a polymerization reaction (which is often observed for surface-initiated polymerization of thick polymer brushes). In the presented study, it would be the result of the loss of steric access to strands buried in the thick brush. Additionally, it can be seen that the SPR coupling angle gradually decreases in time after the initial phase of RCA. This occurs even at times t when the ssDNA chains grow far away from the SP evanescent field, and therefore, it can be explained by rearrangement of this part of the brush at close vicinity to the gold surface that is associated with possible chain stretching.

The respective gradually increasing thickness d_p and slowly decreasing refractive index n_p were used to calculate the accumulated surface mass density Γ_{RCA} at each given time point (see the Supporting Information for details). At the end of the reaction at time t = 4 h, a massive increase in the surface mass density of Γ_{RCA} = 415 ng/mm^2 was determined. This corresponds to ~16 MDa ($\Gamma_{RCA}/\sigma_{biotin/TS|CP}$) or ~52 kb per oligonucleotide strand and indicates that the padlock probe (81 nt) was in average amplified ~640 times on each chain. Interestingly, the average (contour) length of the ssDNA chains obtained from the number of repeats of 48.6 nm-long LP yields about 31.2 μm. This value corresponds to the configuration, where the effective thickness of the brush d_p is almost a third of the contour length of the grafted ssDNA chains.

From the dependence of the number of nucleotides incorporated to the ssDNA polymer chains (shown as the red curve in Figure 4c), an average extension rate of ~215 nt/min can be deduced. This value is substantially slower than the one obtained at 30 °C by Soengas et al. in bulk solutions yielding >10^3 nt/min.[49] At this point, it should be noted that the determined amplification rate should be seen as the minimum speed of nucleotide incorporation by φ 29-Pol on a solid support-based platform that is affected by the chain folding, gradual dilution when moving away from the surface, and diffusion of nucleotides to the surface.

As mentioned above, the chain prolongation does not proceed identically for all the chains, and a certain distribution of their length can be expected. In addition, the stretching of the chains can differ at the inner and outer sides of the brush. The impact of these phenomena can be assessed by determining the gradient of the ssDNA brush layer density in the direction perpendicular to the surface. As seen in Figure 5a, three or more OW modes ($TM_{1,2,3}$) became apparent in the measured reflectivity spectra $R(\theta)$ after 2 h of reaction, and then, a clear deviation between the measured and fitted curves occurs (we fitted the number of OW modes and the angular position of the first and last one). Therefore, the "one-box model" was extended by splitting the layer into three segments and fitting the refractive index independently for each of them. As schematically shown in Figure 4b, this refined model allows us to take into account a gradient in the brush density with a lower refractive index n_b of the layer on its outer interface (in contact with buffer) and a higher refractive index n_b at its inner surface (where it is attached to the gold surface). The fitting with such a "three-box model" is presented in Figure 5b for t =

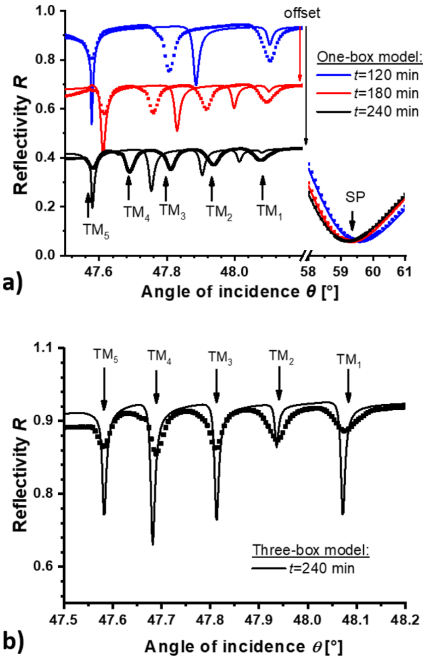

Figure 5. (a) Measured $R(\theta)$ at the growth time of t = 120, 180, and 245 min that is fitted with the Fresnel reflectivity model using the "one-box" approximation. The reflectivity curves $R(\theta)$ measured at 180 and 240 min are shifted, respectively, by a factor of 0.3 and 0.6 in respect to the one measured at 120 min. (b) Comparison of the fitting with "three-box" approximation for data acquired at t = 240 min.

https://doi.org/10.1021/acsami.1c03715
ACS Appl. Mater. Interfaces XXXX, XXX, XXX−XXX

240 min. It shows that the angular positions of all five supported OW modes can be fitted, and the first compartment exhibited a thickness of d_{p1} = 3.8 μm followed by the second one with d_{p2} = 6.0 and third with d_{p3} = 2.9 μm. The fitted refractive index decreased from n_{p1} = 1.3434 at the gold surface to n_{p2} = 1.3410 in the middle part and n_{p3} = 1.3384 for the outer segment of the polymer brush. This analysis suggests that the polymer volume content (proportional to the layer refractive index n_p) is decreasing with distance from the gold surface, and it can be ascribed to a length distribution of the RCA-generated ssDNA polymer chains or possibly more stretched conformation of polymer chains at the outer than the inner interface. The total thickness ($d_{p1} + d_{p2} + d_{p3}$ = 12.7 μm) is slightly higher than the one obtained in the "one-box model", and the weighted refractive index of the attached layer of $(n_{p1}\cdot d_{p1} + n_{p2}\cdot d_{p2} + n_{p3}\cdot d_{p3})/(d_{p1} + d_{p2} + d_{p3})$ = 1.3411 is slightly decreased. However, the corresponding overall surface mass density and respective average polymer chain length of 48 kb per immobilized padlock probe at a reaction duration of 240 min are comparable for both models.

Response of the ssDNA Brush to Ion Environments. Recent studies have shown that the DNA structure is highly dependent on its surrounding aqueous environment,[50] which is of high importance in sensor applications of surface-attached ssDNA brushes.[51] Especially, the presence of specific cation species causes changes in inter-nucleotide distances[52] and can strongly affect the grafting density[53,54] and hybridization regimes of DNA on solid supports.[55,56] Figure 6a shows a schematic of the effect of increasing ionic strength on the DNA brush, which leads to its compression or expansion. Furthermore, we exposed the ssDNA brush to electrolytes containing monovalent (NaCl and KCl) and divalent ($MgCl_2$ and $CaCl_2$) cations to study their impact on the ssDNA brush. The influence on DNA brush thickness d_p and its corresponding refractive index n_p was determined by fitting the reflectivity spectrum $R(\theta)$ and exhibiting SP and OW resonances with the "one-box model" approximation in different ionic solutions (we used ssDNA brushes prepared by RCA with a reaction time that did not allow for the probing with multiple OW modes, and thus, the more accurate "three-box model" was not possible to use). The refractive index of the bulk aqueous solution n_b was determined from SPR on a bare gold surface or from the position of the critical angle θ_c. An additional option for the observation of the swelling and collapsing of the ssDNA brushes offers the SP- and OW-enhanced fluorescence spectroscopy. After the affinity binding of Cy5-conjugated DNA strands (C2CA+/Cy5 or BA+/Cy5), such changes lead to variations in the fluorescence signal originating from the respective part of the architecture selectively probed with the SP or OW field. The evanescent field of resonantly excited SPs excites the fluorophores in a thin (~100 nm) slice at the inner side of the brush, whereas the OWs are more delocalized and can probe the whole brush volume (see Figure 4b). Therefore, compacting the ssDNA brush carrying affinity-bound molecules conjugated with fluorophores is associated with an increase in the SP-enhanced fluorescence signal, whereas the expansion of the structure has the opposite effect.

As the example in Figure 6b illustrates for the brush structures with C2CA+/Cy5, the exposure of the brush to an ionic solution can lead to the compression and expansion of the structure. The compression is manifested as a shift of the SPR to higher angles and the respective increase in the SP-

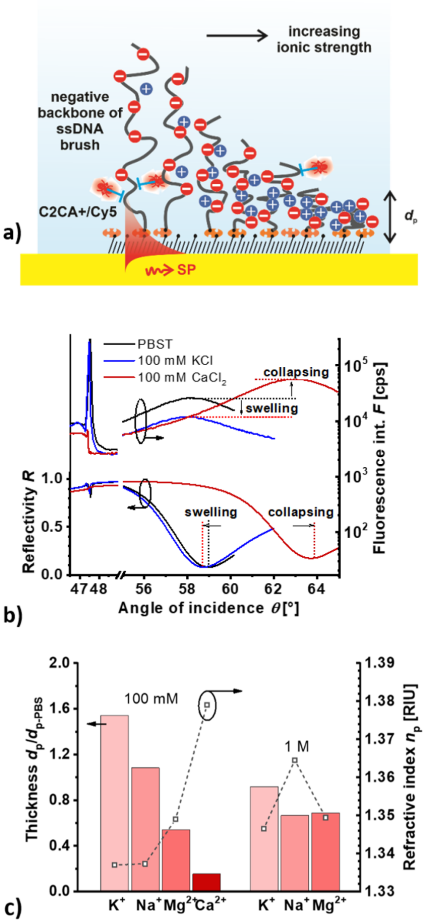

Figure 6. (a) Schematics of the response of the ssDNA brush to different ionic environments. (b) Measured angular reflectivity scans $R(\theta)$ and angular fluorescence intensity scans $F(\theta)$ in 150 mM PBST buffer and in 100 mM KCl and $CaCl_2$ solutions. (c) Evaluated thickness and refractive index changes in respect to the 2.2 μm-thick brush in PBST buffer in electrolytes containing monovalent and divalent cations at different concentrations.

enhanced fluorescence intensity. The expansion is seen as a shift of the SPR angle to lower values and a drop in the SP-enhanced fluorescence intensity. The analysis of the reflectivity curves $R(\theta)$ revealed that the ssDNA brush expanded, and its thickness d_p increased by a factor of 2.2 and 1.1 (compared to that measured in PBST $d_{p\text{-PBST}}$) when the surface-bound ssDNA strands were exposed to a solution with K^+ and Na^+ ions, respectively, at a molar concentration of 100 mM. Interestingly, the divalent Mg^{2+} and Ca^{2+} ions impose an opposite effect, and a decrease in the thickness d_p by a factor of 1.6 and 6.6 is observed, respectively, at the same 100 mM concentration. The particularly strong collapse of the brush in the presence of Ca^{2+} suggests a specific effect of this ion as all other compounds, K^+, Na^+, and Mg^{2+}, did not produce a

https://doi.org/10.1021/acsami.1c03715
ACS Appl. Mater. Interfaces XXXX, XXX, XXX−XXX

ACS Applied Materials & Interfaces www.acsami.org Research Article

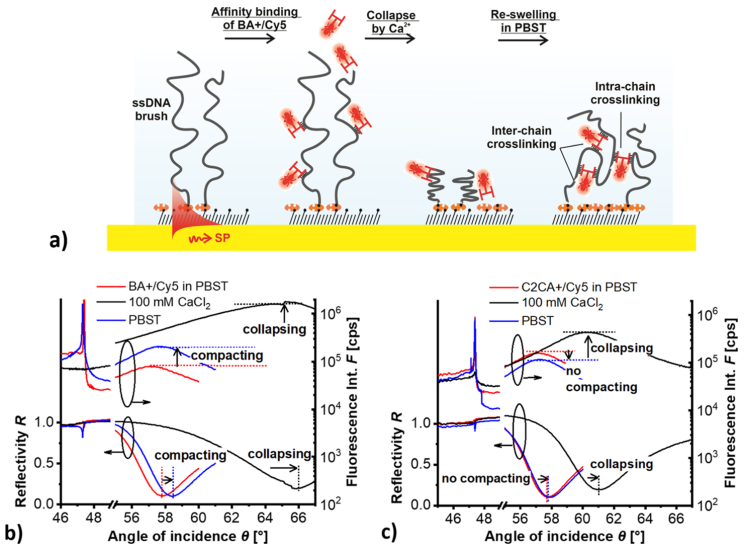

Figure 7. (a) Schematics of the affinity binding of BA staples to the ssDNA brush and its compression by incubation with $CaCl_2$ and re-swelling. Measured angular reflectivity scans $R(\theta)$ and angular fluorescence intensity scans $F(\theta)$ for (b) for the incubation in 100 mM $CaCl_2$ followed by rinsing with PBST and (c) for control experiment with the RCA brush that was affinity reacted with C2CA+/Cy5.

similarly strong change even at 1 M concentration; see Figure 6c. In PBST, the peak fluorescence intensity upon the probing by SPs was $F_{SP(PBST)} = 2.6 \times 10^4$ cps, whereas for the excitation via the OW mode, it was 1 order of magnitude stronger, $F_{TM1(PBST)} = 3.9 \times 10^5$ cps. This difference can be attributed to the fact that the volume probed by the OW mode is larger and thus enables excitation of all Cy5 fluorophores inside the brush. In the presence of monovalent K^+ ions at a concentration of 100 mM, the fluorescence intensity of the fluorescence peak accompanied with the SP mode excitation decreased by a factor of 2.1, which indicates that the ssDNA strands stretched away from the sensor surface, and therefore, fewer fluorophores could be excited by its confined field. In the presence of Ca^{2+} ions at a concentration of 100 mM, the fluorescence intensity excited via SPs in close vicinity of the metal surface increased by a factor of 2.2. These changes confirm the observations obtained from the fitting of reflectivity curves, and the difference in the magnitude of the decrease and increase factors can be attributed to the additional effect of bleaching.

Let us note that similar observations have been attributed to the negatively charged ssDNA backbone that changes its molecular conformation and gets compacted through electrostatic crosslinking in buffers containing Ca^{2+} and Mg^{2+}.[23,57] Our results revealed a much stronger impact of Ca^{2+} ions that can be ascribed to this effect, while Mg^{2+} ions mainly seem to contribute to the Debye screening of the charge interactions, probably due to the higher affinity of Ca^{2+} ions to the DNA bases.[58] Importantly, the changes generated by the exposure of the ssDNA brush to Ca^{2+}, Mg^{2+}, K^+, and Na^+ are reversible, and the ssDNA brush re-arranged its structure back to the original state after rinsing with PBST.

An additional route to manipulate the long ssDNA chains is explored based on short oligonucleotides that carry two sequences complementary to spatially separated parts of ssDNA repeating motifs generated by RCA. Such oligonucleotides can serve as staples that crosslink the neighboring polymer chains or force the individual chains to fold and take on a more compact conformation. As seen in Figure 7a, this approach was investigated using a nucleotide, BA+/Cy5, which has two binding parts with complementary sequences to the RCA-generated ssDNA chains (marked in the sequences presented in Table 1). After flowing the 10 nM solution with BA+/Cy5 over the surface with the ssDNA brush for 15 min, the molecules diffuse inside the polymer architecture and bind (as seen from the comparison of the angular fluorescence scans $F(\theta)$ in Figure S1). The binding occurs in the whole volume of the brush architecture as the fluorescence signal increased in both SP-enhanced fluorescence (peak at $\theta = 58.5°$, probing the volume close to the chip surface) and OW-enhanced fluorescence (peak close to the critical angle exciting the fluorescence throughout the brush).

Interestingly, the binding of BA+/Cy5 did not significantly change the conformation of the ssDNA chains, as the angular positions of SP and OW modes were not altered. This indicates that the BA+ sequences were predominantly able to bind with one of its parts and did not act as crosslinks. Therefore, the ssDNA chains hybridized with BA+/Cy5 staples were exposed to 100 mM Ca^{2+}, which was shown to compact the ssDNA chains and enable bringing their spatially distinct segments closer to each other. As can be seen in Figure 7b, the Ca^{2+} ions induced a strong shift of the SP resonant angle to about $\theta = 66°$ on the brush reacted with BA+/Cy5, which corresponds to a collapse by a factor of 65, as obtained from fitting the reflectivity curves $R(\theta)$. This value is stronger than the factor of 26 observed for the same brush hybridized with C2CA+/Cy5 (Figure 7c), and it can be ascribed to the additional effect of BA+/5 crosslinking of ssDNA chains. In addition, the collapse leads to a more pronounced change than that observed in Figure 6b,c (which is assumed to be caused by

https://doi.org/10.1021/acsami.1c03715
ACS Appl. Mater. Interfaces XXXX, XXX, XXX−XXX

diluting the surface density of ssDNA chains tethered on the surface with $\sigma = 3.2 \times 10^{-6}$ nmol/mm^2). Moreover, when switching back to PBST, the ssDNA brush hybridized with the C2CA+ sequence returned to its original state, but the one modified with BA+/Cy5 partially retained the collapsed nature, as documented by the shifted SPR angle and increased SP-enhanced fluorescence peak. The intensity of the SP-enhanced fluorescence signal increased in PBST by a factor of 2.7 after the collapse of the BA+/Cy5 structure, while that of C2CA5+/Cy5 decreased by a factor of 1.33. These changes are in agreement with those obtained from fitting $R(\theta)$ and confirm that the stronger compression of the ssDNA brush architecture can be obtained by a combination of crosslinking with specific DNA staples and ionic environment change.

CONCLUSIONS

For the first time, we report on the *in situ* and real-time observation of RCA prolongation of ssDNA chains above 10 μm when attached to a solid surface. The grown ssDNA chains take the form of a brush, and they are probed by a combination of SPR and OWS methods, enabled by the fact that a sufficiently thick polymer layer can serve as an optical dielectric waveguide. The analysis of the spectrum of guided waves traveling along this interface with "grafted-from" densely packed ssDNA chains provides an efficient means to monitor their elongation and determine key characteristics of the RCA reaction on a solid surface. Such observations are difficult to achieve with other techniques that are typically only able to characterize the DNA brush after its synthesis is finished, and their use is complicated by the soft and fragile nature of the ssDNA brush. On the other hand, it is worth noting that the presented approach provides detailed information only when the thickness of the brush layer is sufficiently high (several micrometers) and the probing of the interface over an area of about one mm^2 is needed in order to record sharp dielectric OW resonances. Due to this fact, it is not feasible to investigate the behavior of sparsely immobilized DNA chains that do not form the thick brush layers when small amounts of padlock probes are immobilized on the solid surface. We demonstrate how this platform can be used to monitor conformation changes of ssDNA in response to an ionic strength-triggered collapse of the ssDNA brush and its intra- and inter-chain crosslinking via specifically designed oligonucleotide staples. A combination of DNA staples and ionic change allowed compacting the RCA-generated brush by a factor of >10, which can be useful in analytical application with plasmonic biosensor readout for enhancing the sensitivity by dragging the molecules to the plasmonic hotspot on the surface.

ASSOCIATED CONTENT

Supporting Information

The Supporting Information is available free of charge at https://pubs.acs.org/doi/10.1021/acsami.1c03715.

Details on the operation of the used optical configuration, used mathematical model for the analysis of the thin ssDNA brush layer, and example optical spectra for the probing of the thin ssDNA brush layer by combined SPR, OWS, and SPFS (PDF)

AUTHOR INFORMATION

Corresponding Author

Jakub Dostalek − *Biosensor Technologies, AIT-Austrian Institute of Technology GmbH, 3430 Tulln an der Donau, Austria; FZU-Institute of Physics, Czech Academy of Sciences, Prague 182 21, Czech Republic;* orcid.org/0000-0002-0431-2170; Phone: +43 (0) 6642351773; Email: jakub.dostalek@ait.ac.at; Fax: +43 (0) 505504450

Authors

Bernadette Lechner − *Biosensor Technologies, AIT-Austrian Institute of Technology GmbH, 3430 Tulln an der Donau, Austria; CEST Competence Center for Electrochemical Surface Technologies, 3430 Tulln an der Donau, Austria;* orcid.org/0000-0002-4949-5118

Simone Hageneder − *Biosensor Technologies, AIT-Austrian Institute of Technology GmbH, 3430 Tulln an der Donau, Austria;* orcid.org/0000-0002-7200-3257

Katharina Schmidt − *Biosensor Technologies, AIT-Austrian Institute of Technology GmbH, 3430 Tulln an der Donau, Austria*

Mark P. Kreuzer − *Biosensor Technologies, AIT-Austrian Institute of Technology GmbH, 3430 Tulln an der Donau, Austria; Instituto de Nanosistemas, Universidad Nacional de San Martín, San Martín CP 1650 Provincia de Buenos Aires, Argentina*

Rick Conzemius − *Molecular Diagnostics, Health & Environment, AIT Austrian Institute of Technology GmbH, 1210 Vienna, Austria*

Erik Reimhult − *Institute for Biologically Inspired Materials, Department of Nanobiotechnology, University of Natural Resources and Life Sciences Vienna (BOKU), Vienna 1190, Austria;* orcid.org/0000-0003-1417-5576

Ivan Barišić − *Molecular Diagnostics, Health & Environment, AIT Austrian Institute of Technology GmbH, 1210 Vienna, Austria;* orcid.org/0000-0002-1301-6197

Complete contact information is available at: https://pubs.acs.org/10.1021/acsami.1c03715

Author Contributions

S.H. and B.L. contributed equally. All authors have given approval to the final version of the manuscript.

Notes

The authors declare no competing financial interest.

ACKNOWLEDGMENTS

This work was supported by the Austrian Research Promotion Agency (FFG) with ERANET project PLABAN, grant agreement no. 861578, and by the program FemTech. In addition, J.D. acknowledges support from the ESIF and MEYS (FZU researchers, technical and administrative staff mobility—CZ.02.2.69/0.0/0.0/18_053/0016627). M.P.K acknowledges the funding from European Commission via H2020 Marie Skłodowska-Curie Actions project HYMADE with grant agreement no. 645686.

REFERENCES

(1) Boehm, C. D. Use of Polymerase Chain Reaction for Diagnosis of Inherited Disorders. *Clin. Chem.* **1989**, *35*, 1843−1848.

(2) Lynch, C.; Fleming, R. A Review of Direct Polymerase Chain Reaction of DNA and RNA for Forensic Purposes. *Wiley Interdiscip. Rev.: Comput. Mol. Sci.* **2019**, *1*, No. e1335.

(3) Cree, I. A. Diagnostic RAS Mutation Analysis by Polymerase Chain Reaction (PCR). *Biomol. Detect. Quantif.* **2016**, *8*, 29−32.
(4) Yang, S.; Rothman, R. E. PCR-Based Diagnostics for Infectious Diseases: Uses, Limitations, and Future Applications in Acute-Care Settings. *Lancet Infect. Dis.* **2004**, *4*, 337−348.
(5) De Medici, D.; Kuchta, T.; Knutsson, R.; Angelov, A.; Auricchio, B.; Barbanera, M.; Diaz-Amigo, C.; Fiore, A.; Kudirkiene, E.; Hohl, A.; Horvatek Tomic, D.; Gotcheva, V.; Popping, B.; Prukner-Radovcic, E.; Scaramaglia, S.; Siekel, P.; To, K. A.; Wagner, M. Rapid Methods for Quality Assurance of Foods: The Next Decade with Polymerase Chain Reaction (PCR)-Based Food Monitoring. *Food Anal. Methods* **2015**, *8*, 255−271.
(6) Dewey, F. E.; Pan, S.; Wheeler, M. T.; Quake, S. R.; Ashley, E. A. DNA Sequencing Clinical Applications of New DNA Sequencing Technologies. *Circulation* **2012**, *125*, 931−944.
(7) Wood, S. A.; Pochon, X.; Laroche, O.; Ammon, U.; Adamson, J.; Zaiko, A. A Comparison of Droplet Digital Polymerase Chain Reaction (PCR), Quantitative PCR and Metabarcoding for Species-Specific Detection in Environmental DNA. *Mol. Ecol. Resour.* **2019**, *19*, 1407−1419.
(8) Wittwer, C. T.; Herrmann, M. G.; Gundry, C. N.; Elenitoba-Johnson, K. S. J. Real-Time Multiplex PCR Assays. *Methods* **2001**, *25*, 430−442.
(9) Liu, D.; Daubendiek, S. L.; Zillman, M. A.; Ryan, K.; Kool, E. T. Rolling Circle DNA Synthesis: Small Circular Oligonucleotides as Efficient Templates for DNA Polymerases. *J. Am. Chem. Soc.* **1996**, *118*, 1587−1594.
(10) Fire, A.; Xu, S. Q. Rolling Replication of Short DNA Circles. *Proc. Natl. Acad. Sci. U.S.A.* **1995**, *92*, 4641−4645.
(11) Zanoli, L.; Spoto, G. Isothermal Amplification Methods for the Detection of Nucleic Acids in Microfluidic Devices. *Biosensors* **2013**, *3*, 18−43.
(12) Lau, H. Y.; Botella, J. R. Advanced DNA-Based Point-of-Care Diagnostic Methods for Plant Diseases Detection. *Front. Plant Sci.* **2017**, *8*, 1−14.
(13) Notomi, T.; Okayama, H.; Masubuchi, H.; Yonekawa, T.; Watanabe, K.; Amino, N.; Hase, T. Loop-Mediated Isothermal Amplification of DNA. *Nucleic Acids Res.* **2000**, *28*, No. e63.
(14) Lizardi, P. M.; Huang, X.; Zhu, Z.; Bray-Ward, P.; Thomas, D. C.; Ward, D. C. Mutation Detection and Single-Molecule Counting Using Isothermal Rolling-Circle Amplification. *Nat. Genet.* **1998**, *19*, 225−232.
(15) Barišić, I.; Petzka, J.; Schoenthaler, S.; Vierlinger, K.; Noehammer, C.; Wiesinger-Mayr, H. Multiplex Characterization of Human Pathogens Including Species and Antibiotic-Resistance Gene Identification. *J. Med. Microbiol.* **2016**, *65*, 48−55.
(16) Adessi, C. Solid Phase DNA Amplification: Characterisation of Primer Attachment and Amplification Mechanisms. *Nucleic Acids Res.* **2000**, *28*, No. e87.
(17) Tjong, V.; Yu, H.; Hucknall, A.; Rangarajan, S.; Chilkoti, A. Amplified On-Chip Fluorescence Detection of DNA Hybridization by Surface-Initiated Enzymatic Polymerization. *Anal. Chem.* **2011**, *83*, 5153−5159.
(18) Ericsson, O.; Jarvius, J.; Schallmeiner, E.; Howell, M.; Nong, R. Y.; Reuter, H.; Hahn, M.; Stenberg, J.; Nilsson, M.; Landegren, U. A Dual-Tag Microarray Platform for High-Performance Nucleic Acid and Protein Analyses. *Nucleic Acids Res.* **2008**, *36*, No. e45.
(19) Chi, Y. S.; Jung, Y. H.; Choi, I. S.; Kim, Y.-G. Surface-Initiated Growth of Poly d(A-T) by Tag DNA Polymerase. *Langmuir* **2005**, *21*, 4669−4673.
(20) Chow, D. C.; Chilkoti, A. Surface-Initiated Enzymatic Polymerization of DNA. *Langmuir* **2007**, *23*, 11712−11717.
(21) Bracha, D.; Karzbrun, E.; Daube, S. S.; Bar-Ziv, R. H. Emergent Properties of Dense DNA Phases toward Artificial Biosystems on a Surface. *Acc. Chem. Res.* **2014**, *47*, 1912−1921.
(22) Huang, F.; Zhou, X.; Yao, D.; Xiao, S.; Liang, H. DNA Polymer Brush Patterning through Photocontrollable Surface-Initiated DNA Hybridization Chain Reaction. *Small* **2015**, *11*, 5800−5806.
(23) Petrovykh, D. Y.; Kimura-Suda, H.; Whitman, L. J.; Tarlov, M. J. Quantitative Analysis and Characterization of DNA Immobilized on Gold. *J. Am. Chem. Soc.* **2003**, *125*, 5219−5226.
(24) Khan, M. N.; Tjong, V.; Chilkoti, A.; Zharnikov, M. Spectroscopic Study of a DNA Brush Synthesized in Situ by Surface Initiated Enzymatic Polymerization. *J. Phys. Chem. B* **2013**, *117*, 9929−9938.
(25) Barbee, K. D.; Chandrangsu, M.; Huang, X. Fabrication of DNA Polymer Brush Arrays by Destructive Micropatterning and Rolling-Circle Amplification. *Macromol. Biosci.* **2011**, *11*, 607−617.
(26) Palanisamy, R.; Connolly, A. R.; Trau, M. Considerations of Solid-Phase DNA Amplification. *Bioconjugate Chem.* **2010**, *21*, 690−695.
(27) Dostálek, J.; Knoll, W. Plasmonics. In *Polymer Science: A Comprehensive Reference*; Matyjaszewski, K., Möller, M., Eds.; Elsevier B.V.: Amsterdam, 2012; Vol. 2, pp 647−659.
(28) Homola, J. Surface Plasmon Resonance Sensors for Detection of Chemical and Biological Species. *Chem. Rev.* **2008**, *108*, 462−493.
(29) Beines, P. W.; Klosterkamp, I.; Menges, B.; Jonas, U.; Knoll, W. Responsive Thin Hydrogel Layers from Photo-Cross-Linkable Poly(N-Isopropylacrylamide) Terpolymers. *Langmuir* **2007**, *23*, 2231−2238.
(30) Toomey, R.; Freidank, D.; Rühe, J. Swelling Behavior of Thin, Surface-Attached Polymer Networks. *Macromolecules* **2004**, *37*, 882−887.
(31) Ferrand-Drake Del Castillo, G.; Emilsson, G.; Dahlin, A. Quantitative Analysis of Thickness and PH Actuation of Weak Polyelectrolyte Brushes. *J. Phys. Chem. C* **2018**, *122*, 27516−27527.
(32) Zhang, Q.; Wang, Y.; Mateescu, A.; Sergelen, K.; Kibrom, A.; Jonas, U.; Wei, T.; Dostalek, J. Biosensor Based on Hydrogel Optical Waveguide Spectroscopy for the Detection of 17β-Estradiol. *Talanta* **2013**, *104*, 149−154.
(33) Junk, M. J. N.; Anac, I.; Menges, B.; Jonas, U. Analysis of Optical Gradient Profiles during Temperature- and Salt-Dependent Swelling of Thin Responsive Hydrogel Films. *Langmuir* **2010**, *26*, 12253−12259.
(34) Toma, M.; Jonas, U.; Mateescu, A.; Knoll, W.; Dostalek, J. Active Control of SPR by Thermoresponsive Hydrogels for Biosensor Applications. *J. Phys. Chem. C* **2013**, *117*, 11705−11712.
(35) Wang, Y.; Brunsen, A.; Jonas, U.; Dostálek, J.; Knoll, W. Prostate Specific Antigen Biosensor Based on Long Range Surface Plasmon-Enhanced Fluorescence Spectroscopy and Dextran Hydrogel Binding Matrix. *Anal. Chem.* **2009**, *81*, 9625−9632.
(36) Stengel, G.; Knoll, W. Surface Plasmon Field-Enhanced Fluorescence Spectroscopy Studies of Primer Extension Reactions. *Nucleic Acids Res.* **2005**, *33*, No. e69.
(37) Tumolo, T.; Angnes, L.; Baptista, M. S. Determination of the Refractive Index Increment (Dn/Dc) of Molecule and Macromolecule Solutions by Surface Plasmon Resonance. *Anal. Biochem.* **2004**, *333*, 273−279.
(38) Theisen, A.; Johann, C.; Deacon, M. P.; Harding, S. *Refractive Increment Data-Book for Polymer and Biomolecular Scientists*; Nottingham University Press: Nottingham, 2000.
(39) Nilsson, M.; Malmgren, H.; Samiotaki, M.; Kwiatkowski, M.; Chowdhary, B.; Landegren, U. Padlock Probes: Circularizing Oligonucleotides for Localized DNA Detection. *Science* **1994**, *265*, 2085−2088.
(40) Barišić, I.; Schoenthaler, S.; Ke, R.; Nilsson, M.; Noehammer, C.; Wiesinger-Mayr, H. Multiplex Detection of Antibiotic Resistance Genes Using Padlock Probes. *Diagn. Microbiol. Infect. Dis.* **2013**, *77*, 118−125.
(41) Su, X.; Wu, Y.-J.; Robelek, R.; Knoll, W. Surface Plasmon Resonance Spectroscopy and Quartz Crystal Microbalance Study of Streptavidin Film Structure Effects on Biotinylated DNA Assembly and Target DNA Hybridization. *Langmuir* **2005**, *21*, 348−353.
(42) Tsortos, A.; Papadakis, G.; Mitsakakis, K.; Melzak, K. A.; Gizeli, E. Quantitative Determination of Size and Shape of Surface-Bound DNA Using an Acoustic Wave Sensor. *Biophys. J.* **2008**, *94*, 2706−2715.

J
https://doi.org/10.1021/acsami.1c03715
ACS Appl. Mater. Interfaces XXXX, XXX, XXX−XXX

(43) Thibault, T.; Degrouard, J.; Baril, P.; Pichon, C.; Midoux, P.; Malinge, J.-M. Production of DNA Minicircles Less than 250 Base Pairs through a Novel Concentrated DNA Circularization Assay Enabling Minicircle Design with NF-KB Inhibition Activity. *Nucleic Acids Res.* **2017**, *45*, No. e26.
(44) He, P.; Liu, L.; Qiao, W.; Zhang, S. Ultrasensitive Detection of Thrombin Using Surface Plasmon Resonance and Quartz Crystal Microbalance Sensors by Aptamer-Based Rolling Circle Amplification and Nanoparticle Signal Enhancement. *Chem. Commun.* **2014**, *50*, 1481−1484.
(45) Huang, Y.-Y.; Hsu, H.-Y.; Huang, C.-J. C. A Protein Detection Technique by Using Surface Plasmon Resonance (SPR) with Rolling Circle Amplification (RCA) and Nanogold-Modified Tags. *Biosens. Bioelectron.* **2007**, *22*, 980−985.
(46) Shi, D.; Huang, J.; Chuai, Z.; Chen, D.; Zhu, X.; Wang, H.; Peng, J.; Wu, H.; Huang, Q.; Fu, W. Isothermal and Rapid Detection of Pathogenic Microorganisms Using a Nano-Rolling Circle Amplification-Surface Plasmon Resonance Biosensor. *Biosens. Bioelectron.* **2014**, *62*, 280−287.
(47) Xiang, Y.; Deng, K.; Xia, H.; Yao, C.; Chen, Q.; Zhang, L.; Liu, Z.; Fu, W. Isothermal Detection of Multiple Point Mutations by a Surface Plasmon Resonance Biosensor with Au Nanoparticles Enhanced Surface-Anchored Rolling Circle Amplification. *Biosens. Bioelectron.* **2013**, *49*, 442−449.
(48) Xiang, Y.; Zhu, X.; Huang, Q.; Zheng, J.; Fu, W. Real-Time Monitoring of Mycobacterium Genomic DNA with Target-Primed Rolling Circle Amplification by a Au Nanoparticle-Embedded SPR Biosensor. *Biosens. Bioelectron.* **2015**, *66*, 512−519.
(49) Soengas, M. S.; Gutiérrez, C.; Salas, M. Helix-Destabilizing Activity of Φ29 Single-Stranded DNA Binding Protein: Effect on the Elongation Rate during Strand Displacement DNA Replication. *J. Mol. Biol.* **1995**, *253*, 517−529.
(50) Gil, P. S.; Lacks, D. J.; Parisse, P.; Casalis, L.; Nkoua Ngavouka, M. D. Single-Stranded DNA Oligomer Brush Structure Is Dominated by Intramolecular Interactions Mediated by the Ion Environment. *Soft Matter* **2018**, *14*, 9675−9680.
(51) Rao, A. N.; Grainger, D. W. Biophysical Properties of Nucleic Acids at Surfaces Relevant to Microarray Performance. *Biomater. Sci.* **2014**, *2*, 436−471.
(52) Nkoua Ngavouka, M. D.; Bosco, A.; Casalis, L.; Parisse, P. Determination of Average Internucleotide Distance in Variable Density SsDNA Nanobrushes in the Presence of Different Cations Species. *Macromolecules* **2014**, *47*, 8748−8753.
(53) Castelino, K.; Kannan, B.; Majumdar, A. Characterization of Grafting Density and Binding Efficiency of DNA and Proteins on Gold Surfaces. *Langmuir* **2005**, *21*, 1956−1961.
(54) Herne, T. M.; Tarlov, M. J. Characterization of DNA Probes Immobilized on Gold Surfaces. *J. Am. Chem. Soc.* **1997**, *119*, 8916−8920.
(55) Gong, P.; Levicky, R. DNA Surface Hybridization Regimes. *Proc. Natl. Acad. Sci. U.S.A.* **2008**, *105*, 5301−5306.
(56) Peterson, A. W. The Effect of Surface Probe Density on DNA Hybridization. *Nucleic Acids Res.* **2001**, *29*, 5163−5168.
(57) Bosco, A.; Camunas-Soler, J.; Ritort, F. Elastic Properties and Secondary Structure Formation of Single-Stranded DNA at Monovalent and Divalent Salt Conditions. *Nucleic Acids Res.* **2014**, *42*, 2064−2074.
(58) Hackl, E. V.; Kornilova, S. V.; Blagoi, Y. P. DNA Structural Transitions Induced by Divalent Metal Ions in Aqueous Solutions. *Int. J. Biol. Macromol.* **2005**, *35*, 175−191.

https://doi.org/10.1021/acsami.1c03715
ACS Appl. Mater. Interfaces XXXX, XXX, XXX−XXX

3.3 Responsive hydrogel binding matrix for dual signal amplification in fluorescence affinity biosensors and peptide microarrays

Hageneder, S., Jungbluth, V., Soldo, R., Petri, C., Pertiller, M., Kreivi, M., Weinhaeusel, A., Jonas, U. and Dostalek, J., Responsive hydrogel binding matrix for dual signal amplification in fluorescence affinity biosensors and peptide microarrays, 2021, ACS Applied Materials & Interfaces, 13(23), 27645-27655 https://doi.org/10.1021/acsami.1c05950

First author paper: I was responsible for the concept, experiment design, chip fabrication, data processing and interpretation, graphs, and manuscript writing and revision. VJ and MP were supporting some experiments. RS was conducting microarray spotting, readout, and partial data processing; CP synthesized polymers, MK was involved in assay optimization. AW and UJ were involved in the discussion and manuscript preparation. JD was supervising the project, responsible for overall direction and planning, and involved in manuscript preparation.

In this chapter, a thermoresponsive poly(N-isopropylacrylamide) (pNIPAAm) based polymer was used in the biointerface architecture. It was shown that even after post-functionalization of the polymer with peptide BREs, the responsive properties of the matrix remained. The analysis of human IgG in diluted plasma was possible due to the low fouling polymer structure and the sensitive readout with PEF. Through the thermally induced collapse of the responsive interface, an increase in the fluorescence intensity by a factor of 5 was observed. Both optical- and interface-based amplification make it possible to measure real-time fluorescence with a combined enhancement factor of more than 100 times.

ACS APPLIED MATERIALS & INTERFACES

www.acsami.org Research Article

Responsive Hydrogel Binding Matrix for Dual Signal Amplification in Fluorescence Affinity Biosensors and Peptide Microarrays

Simone Hageneder, Vanessa Jungbluth, Regina Soldo, Christian Petri, Matthias Pertiller, Marjut Kreivi, Andreas Weinhäusel, Ulrich Jonas, and Jakub Dostalek*

Cite This: ACS Appl. Mater. Interfaces 2021, 13, 27645−27655 Read Online

ACCESS | Metrics & More | Article Recommendations | Supporting Information

ABSTRACT: A combined approach to signal enhancement in fluorescence affinity biosensors and assays is reported. It is based on the compaction of specifically captured target molecules at the sensor surface followed by optical probing with a tightly confined surface plasmon (SP) field. This concept is utilized by using a thermoresponsive hydrogel (HG) binding matrix that is prepared from a terpolymer derived from poly(*N*-isopropylacrylamide) (pNIPAAm) and attached to a metallic sensor surface. Epi-illumination fluorescence and SP-enhanced total internal reflection fluorescence readouts of affinity binding events are performed to spatially interrogate the fluorescent signal in the direction parallel and perpendicular to the sensor surface. The pNIPAAm-based HG binding matrix is arranged in arrays of sensing spots and employed for the specific detection of human IgG antibodies against the Epstein−Barr virus (EBV). The detection is performed in diluted human plasma or with isolated human IgG by using a set of peptide ligands mapping the epitope of the EBV nuclear antigen. Alkyne-terminated peptides were covalently coupled to the pNIPAAm-based HG carrying azide moieties. Importantly, using such low-molecular-weight ligands allowed preserving the thermoresponsive properties of the pNIPAAm-based architecture, which was not possible for amine coupling of regular antibodies that have a higher molecular weight.

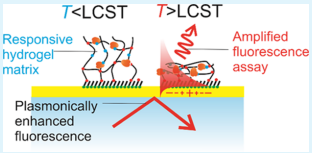

KEYWORDS: *thermoresponsive hydrogel, pNIPAAm, plasmon-enhanced fluorescence, microarrays, click chemistry, peptide, serotesting, biomarkers*

INTRODUCTION

Responsive hydrogel (HG) materials are increasingly employed in optical analytical technologies, where they are employed to serve in three-dimensional binding matrices for the specific capture of the target analyte and to suppress unspecific interactions of abundant molecules present in the analyzed liquid samples,[1,2] facilitate readout and amplify the sensor response to specific binding events,[3] and allow for manipulating small volumes of analyzed aqueous samples on miniature sensor chips.[4]

Responsive HGs are often combined with metallic nanostructures, and among others, their on-demand swelling and collapse were utilized in colorimetric[5] and surface-enhanced Raman spectroscopy (SERS)-based sensors.[6−8] These sensor modalities take advantage of the resonant excitation of surface plasmons (SPs) that exhibit a tightly confined profile of the electromagnetic field associated with collective oscillations of the charge density at the metal surface. The implementation of responsive HGs allows for the active control of near-field coupling between localized SPs at metallic nanoparticles,[9] and they can be tailored to trap target molecules and deliver them to the zones referred to as plasmonic hotspots. The plasmonic confinement of electromagnetic field intensity at such hotspots was further enhanced by approaching metallic nanostructures through the collapse of a responsive HG that serves as a host material or a thin spacer.[6,10]

The majority of thermoresponsive HGs used in the analytical technologies are derived from poly(*N*-isopropylacrylamide) (pNIPAAm), a polymer exhibiting a lower critical solution temperature (LCST) of 32 °C,[11] at which it switches between a hydrophilic expanded state (T < LCST) and a hydrophobic collapsed state (T > LCST). In order to allow for post-modification of the pNIPAAm network with functional biomolecules, mostly copolymers have been used for the incorporation of moieties enabling the controlled coupling of protein molecules.[12,13] The large surface area of HG films renders them the ability to host high amounts of biomolecules that can function as ligands in affinity biosensors. Such an extended three-dimensional biointerface can affinity-bind target molecules from the analyzed samples with an efficiency that outperforms that of traditionally used two-dimensional surface architectures in surface plasmon resonance (SPR) and

Received: March 31, 2021
Accepted: April 28, 2021
Published: June 3, 2021

ACS Applied Materials & Interfaces www.acsami.org Research Article

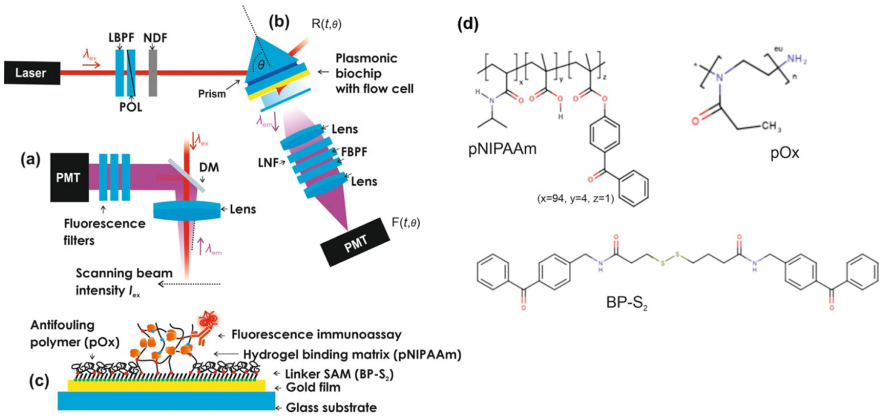

Figure 1. Optical configuration used for the readout of affinity binding on the biochip with arrays of HG sensing spots based on (a) epi-illumination fluorescence configuration (EPF) and (b) total interal reflection fluorescence (TIRF) readout combined with SPR that utilizes a laser band pass filter (LBPF), polarizer (POL), neutral density filter, laser notch filter (LNF), fluorescence bandpass filter (FBPF), and photomultiplier (PMT). (c) Schematics of the biochip with arrays of HG sensing spots and (d) chemical structure of the used photocross-linkable pNIPAAm-based polymer, passivating polyoxazoline (pOx), and the benzophenone-disulfide (BP-S_2) linker forming a SAM on the gold surface of the biochip.

surface plasmon-enhanced fluorescence (PEF) biosensors.[12,14,15]

Similar to SERS, an improved readout accuracy can also be achieved for other types of plasmon sensors with the HG binding matrix. Then, its switching to the collapsed state can cause compaction of the specifically bound analyte to a smaller volume. This approach can be particularly beneficial for the PEF readout, as the plasmonic amplification of fluorescence emission is strongly dependent on the distance from the metal surface and requires delicate control of the biointerface architecture. However, we witnessed that only a few works have explored this concept until now. It was reported that responsive HG binding matrix-enhanced fluorescent signal amplification was carried out for PEF immunoassays with the collapse of the system triggered by ionic strength[16] and temperature[10,17] stimulus. However, these works demonstrated possible detection only in model samples, under conditions that are not suitable for practical applications, and reveal that the responsive characteristics of the used pNIPAAm-based HG matrix substantially deteriorate after conjugation with high-molecular-weight ligands such as antibodies.[10,17]

More recently, peptides have been frequently explored as ligands, offering the advantage of cost-efficient and reproducible synthesis, increased long-term stability, and more controlled ways for their immobilization.[18,19] In this work, we explore several routes to utilize a spatially resolved fluorescence readout of assays that takes advantage of arrays of antibody and peptide ligands incorporated in the pNIPAAm-based HG matrix. The possibility of using the temperature-induced collapse of the HG for compacting the captured analytes is demonstrated for the PEF readout, yielding a dual amplification functionality. This study reveals the importance of the choice of the ligand used for the post-modification of the HG matrix as only the use of low-molecular-weight components such as peptides allowed preserving the responsive properties and implementing the dual amplification concept.

EXPERIMENTAL SECTION

Materials. All reagents were used as received. 1-Ethyl-3-(3-dimethylaminopropyl)carbodiimide (EDC) was obtained from Sigma-Aldrich (Germany). Alkyne-modified peptides were custom-made by JPT (Berlin, Germany) mapping epitopes of Epstein−Barr virus (EBV) nuclear antigen or of the enzyme carbonic anhydrase XII (CA12), which can be found in literature.[20] The recognition sequences of these peptides were CA12: HLQHVKYKGQEAFVP; EBV1: PGRRPFFHPVGEADY; EBV2: AQPAPQAPYQGYQEP; EBV3: YQEPPPPQAPYQGYQ; and EBV4: FHPVGEADYFEYHQE.

The monoclonal antibody against human CA12 peptide (AMAb90639) was purchased from Atlas Antibodies, Bromma, Sweden. Goat detection antibodies anti-mouse and anti-human IgG (H + L) conjugated with Alexa Fluor 647 (anti-mIgG-AF647 and anti-hIgG-AF647) were purchased from Thermo Fisher. IgG from the mouse serum (mIgG) and human serum (hIgG), phosphate-buffered saline (PBS), Tween 20, Hellmanex III, and bovine serum albumin (BSA) were purchased from Merck-Sigma-Aldrich (Austria). Pooled human plasma samples were obtained from Innovative Research (USA). Sodium acetate buffer (ACT) was made using sodium acetate and acetic acid; both obtained from VWR Chemicals (Austria). All buffers were prepared with deionized water (Arium Pro, Sartorius Stedim). 2D-Azide Glass slides (#10400621) were purchased from PolyAn, Berlin, Germany.

Synthesis of the Polymer and Linker. 2-Azidoethan-1-aminium chloride was synthesized as follows based on the procedure in the literature:[21] 9.83 g of 2-bromoethylamine hydrobromide (48 mmol) was dissolved in 25 mL of water, to which a solution of 9.75 g of sodium azide (150 mmol) in 25 mL of water was added at room temperature. The mixture was heated at 80 °C overnight until the completion of the reaction, then the volume was concentrated to around 10 mL, and the mixture was cooled in an ice bath. The reaction conversion was followed by silica gel thin-layer chromatography (eluent: chloroform/methanol/conc. aqueous ammonia—13/5/1; staining: ninhydrine). 150 mL of diethylether was added to the flask, followed by 8 g of KOH powder under vigorous stirring and keeping the temperature below 10 °C. The organic phase was separated, and the aqueous phase was further extracted two times, with 50 mL of diethyl ether. The combined organic phases were dried over anhydrous K_2CO_3, the solvent removed, resulting in yellowish oil. Afterward, 50 mL of 4 M HCl was added. The solvent was

https://doi.org/10.1021/acsami.1c05950
ACS Appl. Mater. Interfaces 2021, 13, 27645−27655

removed and dried in a vacuum at 50 °C overnight. Yield: 4.80 g (39.2 mmol, 82%).

4-Sulfotetrafluorophenol (TFPS) and the benzophenone-disulfide BP-S2 (see Figure 1) were synthesized as described in the literature (see ref[22,23]). The pNIPAAm-based terpolymer was synthesized using *N*-isopropylacrylamide, methacrylic acid, and *N*-(4-benzoylphenyl)-acrylamide (94:5:1 ratio).[24] Shortly, 4-aminobenzophenone (20.3 mmol, 4.00 g) was dissolved in dichloromethane (DCM) (50 mL), and the solution cooled with an ice-water bath to 0 °C. Na_2CO_3 (20.3 mmol, 2.15 g) was added, and the resulting dispersion stirred for 20 min at 0 °C. Acryloyl chloride (26.4 mmol, 2.39 g, 2.12 mL) was diluted with DCM (50 mL) and added dropwise to the dispersion at 0 °C. After complete addition, the reaction mixture was allowed to warm to room temperature and stirred for 16 h. The formed solid was filtered off, and the reaction mixture extracted with aq. $NaHCO_3$ solution (5 wt %, 3 × 100 mL) and water (3 × 100 mL). The organic layer was separated and dried over $MgSO_4$, filtered, and the solvent evaporated, giving the title compound as a brownish solid. Yield: 33% (6.73 mmol, 1.69 g). ^{1}H NMR (400 MHz, chloroform-*d*): δ [ppm] = 7.85−7.46 (m, 9H); 6.51−6.47 (dd, 1H); 6.31−6.24 (dd, 1H); 5.85−5.83 (dd, 1H). Anti-fouling polymer poly(2-ethyl-2-oxazoline) (pOx) was synthesized as reported.[25]

Preparation and Structuring of HG Layers. The HG structures were prepared on BK7 or LASFN9 glass substrates, cleaned for 15 min by consecutive sonicating in 1% (v/v) Hellmanex III aqueous solution and deionized water, and a final sonication in ethanol puriss. After drying the substrates under a stream of compressed air, they were coated with 2 nm chromium and 50 nm gold by a vacuum thermal evaporation instrument AUTO 306 (from HHV Ltd., UK) at a pressure below 10^{-6} mbar. Immediately after the evaporation of metal layers, the slides were immersed overnight in a 1 mM solution of BP-S_2 in dimethyl sulfoxide (DMSO) to form a self-assembled monolayer (SAM). After rinsing with ethanol, 100 μL of a pNIPAAm terpolymer solution with concentrations from 0.5−2.5% (w/w) in pure ethanol was spun on top, at 2000 rpm for 120 s, using SpinCoatG3-P8, (from SCS, IN, USA). The polymer layer was subsequently dried at 50 °C in a vacuum oven for a minimum of 4 h and then irradiated with UV-light at 365 nm (UV lamp Bio-Link 365, Vilber Lourmat) with 2 J/cm^2 dose to cross-link and simultaneously attach the polymer to the surface. The layer thickness depends linearly on the concentration of the polymer solution spun on the surface.

Post-modification of HG Layers with Peptides. For the click coupling of alkyne-modified peptides to azide groups introduced to the HG network, copper-mediated cyclization[26] was used. First, the carboxyl groups in the pNIPAAm-based network were activated with EDC and TFPS for 15 min, washed with ACT buffer pH 5, and then exposed to 2.6 μM 2-azidoethan-1-aminium chloride in ACT pH 5 for 1 h. After washing, passivation was done with ethanolamine, continued by either drying and storage or using in experiments immediately after. For the attachment of peptides to the azide groups, a solution of 0.05 M $CuSO_4{\cdot}5H_2O$ in 3:1 DMSO/*t*-butanol and a solution of 0.05 M tris((1-benzyl-4-triazolyl)methyl)amine (TBTA) in 3:1 DMSO/*t*-butanol was mixed 1:2. To 1.5 μL of this solution, 0.75 μL of 0.1 M Na-ascorbate in water was added, as well as 2 μL of the peptide solution, which was dissolved in PBS at a stock concentration of 500 μM. 4.38 μL of DMSO and 1.37 μL of H_2O was added to a final volume of 10 μL. All reagents were freshly prepared. A volume of 7.5 μL was put onto the chip and allowed to react in the dark for 2 h, covered with a coverslip (20 × 20 mm). The chip was rinsed with water and PBS with 1 mg/mL BSA and 0.05% Tween (PBST).

For the spotting of peptides on microarrays, peptides dissolved to a concentration of 80 μM (from 500 μM stock in DMSO) in an aqueous buffer containing 10% DMSO, 1.25 mM Na-ascorbate, 1 mM hydroquinone, and 0.95 mM $CuSO_4$ (which equals to around 16 fmol of the peptide on each spot on which a volume of 0.2 nL was delivered) were degassed and microspotted by using the contactless spotter Marathon Argus (from Arrayjet, UK). The sensor chips were either directly used for further immunoassay experiments or stored in an argon atmosphere and preventing light exposure for up to several months without affecting its performance.

Post-modification of HG Layers with Antibodies. Carboxyl groups present in the pNIPAAm-based HG were activated using EDC and TFPS (21 and 75 mg, respectively) in 1 mL of water for 15 min. Immediately after washing with ACT buffer pH 4, IgG in ACT pH 4 was spotted using printer Omnigrid arrayer (from GeneMachines, San Carlos, CA, USA) with SMP 3 pins (from TeleChem International Inc., Sunnyvale, CA, USA) under adjusted air humidity (55−60%). Alternatively, the whole surface was brought in contact with the IgG solution and allowed to react for 1 h. After rinsing, the possible unreacted groups were passivated with 1 M ethanolamine pH 8.5 in water for 15 min and used for further assay experiments or stored at 4 °C in the dark in an argon atmosphere for several weeks without deterioration in the performance.

Optical Instruments. Two different readout methods were used in the course of the experiments (Figure 1). A PowerScanner (from Tecan, Switzerland) that utilizes the epi-illumination fluorescence (EPF) geometry was used for the scanning of arrays spots (endpoint measurements) (λ_{ex} = 635 nm, λ_{em} = 676 nm). *In situ* observation of the assay steps and layer modifications was done by an instrument built in-house. It relies on the Kretschmann configuration of attenuated total reflection and allows for combined readout based on SPR and PEF. Shortly, a He−Ne laser (2 mW) emitting at λ_{ex} = 632.8 nm was made passing through a laser bandpass filter (LBPF, Thorlabs, FL632.8-10), a chopper model 197 (from Signal Recovery, USA) set to frequency f = 933 Hz, and a polarizer (POL) and was coupled to a 90° prism made of high refractive index glass LASFN9 with an optically matched glass substrate (using immersion oil) carrying a thin gold layer. A flow cell made of a transparent glass substrate with drilled inlet and outlet ports was clamped on top of the substrates, which, for temperature-control, had a Peltier element as described previously.[12] A polydimethylsiloxane gasket (thickness: 100 μm; volume: 5 μL) and tubing Tygon LMT-55 (from Ismatec, Germany) with an inner diameter of 0.25 mm was used for the transportation of the liquids using a peristaltic pump (from Ismatec, Germany) at a flow rate of 15 μL/min. The intensity of the laser beam reflected at the sensor surface R was measured as a function of the angle of incidence θ or time t by a photodetector connected to a lock-in amplifier (from EG&G, USA). The enhanced field intensity associated with the resonant excitation of SPs was used for the excitation of Alexa Fluor 647 fluorophores. The emitted fluorescence light intensity F at the emission wavelength λ_{em} = 670 nm was detected by a photomultiplier tube (PMT, H6240-01, Hamamatsu, Japan) after a set of filters [laser notch filter (LNF) XNF-632.8-25.0M (from Melles Griot, CVI, USA) and 2 bandpass filter FBPF FB670-10 (from Thorlabs, USA) and 670FS10-25 (from Andover Corporation Optical Filter, USA)]. Both readout signals (reflectivity and fluorescence intensity changes) were recorded using Wasplas software developed at the Max Planck Institute for Polymer Research, Mainz, Germany.

Human IgG Detection by Peptide Ligands. Chips with a pNIPAAm-based HG layer were spotted with a pattern of alternating CA12 and EBV1-4 peptides (see above) and processed by blocking the surface with DIG easyHyb (Roche), washed two times for 15 min with a working PBS buffer with dissolved 0.05% Tween and 1 mg/mL BSA. Then, the surface was reacted with pooled hIgG at a concentration of 0.3 mg/mL (corresponding to 2 μM) for 1 h, followed by incubation with 2 μg/mL AF647 anti-hIgG (corresponding to 13 nM) for 45 min. After the rinsing and drying steps, the readout was done using the microarray scanner.

Observation of Thin HG Layer Swelling. Thin pNIPAAm-based HG layers were characterized by SPR to determine the dependence of the thickness d_h and the swelling ratio SR on temperature T in the range between 20 and 40 °C. The measured reflectivity spectra $R(\theta)$ were analyzed by fitting with a Fresnel reflectivity model implemented in software Winspall, developed at the Max Planck Institute for Polymer Research, Mainz, Germany. The method of matching the surface mass density measured in dry and

https://doi.org/10.1021/acsami.1c05950
ACS Appl. Mater. Interfaces 2021, 13, 27645−27655

ACS Applied Materials & Interfaces www.acsami.org Research Article

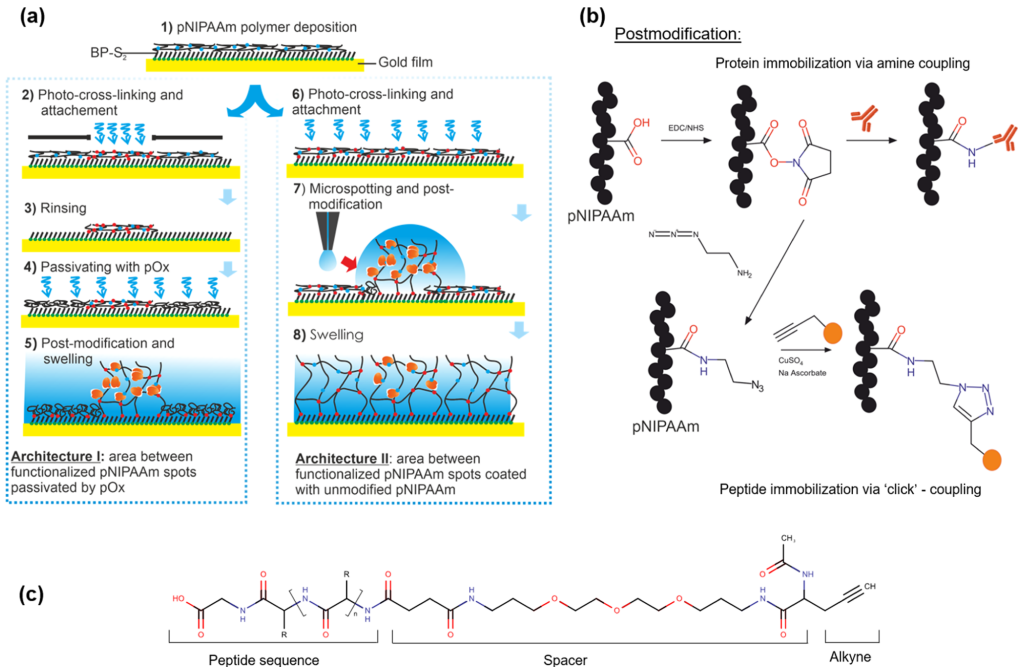

Figure 2. (a) Preparation routes for the microarrays with a pNIPAAm-based HG binding matrix. (b) Post-modification of pNIPAAm-based HG with protein and peptide molecules. (c) Structure of the used peptide ligands.

swollen states was used, and the SR was calculated as the ratio of the swollen film thickness to the dry film thickness (SR = $d_h/d_{h\text{-}dry}$).

Observation of the Assay in Biological Fluids by PEF. Thin HG layers bearing either no ligand or EBV4 peptide immobilized *via* click coupling (see above) were used for PEF detection. First, unspecific binding was tested with 2 μg/mL AF647 anti-hIgG, then human plasma diluted 1:10 in PBST was flowed over the surface for 30 min. After rinsing with PBST for 5 min, detection was performed for 15 min with 2 μg/mL AF647 anti-hIgG. Each step was observed and analyzed as described before.

RESULTS AND DISCUSSION

A tailored pNIPAAm-based HG was utilized in the form of a thin layer that was attached to a metallic sensor surface and post-modified with the antibody and peptide ligands for the affinity capture of target species. The analyte molecules captured from the analyzed aqueous sample at the sensor surface were then reacted with fluorophore-labeled detection antibody (dAb) in order to establish a sandwich assay format. The focused optical beam at the excitation wavelength of the fluorophore (λ_{ex}) was laterally scanned over the surface carrying arrays of sensing spots reacted with dAb, and the output fluorescent signal was collected at the fluorophore emission wavelength (λ_{em}) by an instrument relying on an epi-illumination configuration—EPF (Figure 1a). In order to observe the swelling of the HG layer in the direction perpendicular to the surface, the biochip surface was probed with the evanescent optical field at the fluorophore excitation wavelength λ_{ex}. Then, an optical setup that combines SPR and PEF was employed with an optical configuration resembling the TIRF (Figure 1b).

Preparation of Array HG Sensing Spots. The arrays of sensing spots were prepared using a polymer network formed by photocross-linking of a pNIPAAm-based terpolymer layer attached to a solid substrate (Figure 1c,d). The pNIPAAm-based layer exhibited a thickness of $d_{h\text{-}dry}$ = 120 nm in the dry state, and it was anchored atop of a glass substrate with a 50 nm thick gold film and BP-S_2 SAM (Figure 1d). As illustrated in Figure 2, BP-S_2 serves as a linker and two routes for the preparation of arrays of sensing spots were pursued, yielding either a laterally structured pNIPAAm-based HG layer conjugated with ligands (surface architecture I) or a continuous pNIPAAm-based HG layer that was locally post-modified with ligands by using microspotting (surface architecture II). The used pNIPAAm-based HG was allowed to swell in water after its preparation, yielding a thickness of d_h = 700 nm (as demonstrated by the following SPR study) corresponding to a swelling ratio SR = $d_h/d_{h\text{-}dry}$ of 5.8.

In the first route toward surface architecture I, the deposited pNIPAAm-based polymer was cross-linked by UV light through a stencil mask with square arrays of circular apertures exhibiting a diameter of 500 μm and a period of 800 μm. An irradiation dose of 2 J/cm^2 was used to simultaneously cross-link and attach the polymer chains to the gold surface by the photoactivated benzophenone groups carried by their backbone and by the BP-S2 linker on the gold surface (Figure 2a, step 2). After rinsing with ethanol (Figure 2a, step 3), the pNIPAAm polymer chains outside the irradiated zones were washed away, leaving the surface with unreacted BP-S_2. To

https://doi.org/10.1021/acsami.1c05950
ACS Appl. Mater. Interfaces 2021, 13, 27645−27655

ACS Applied Materials & Interfaces www.acsami.org Research Article

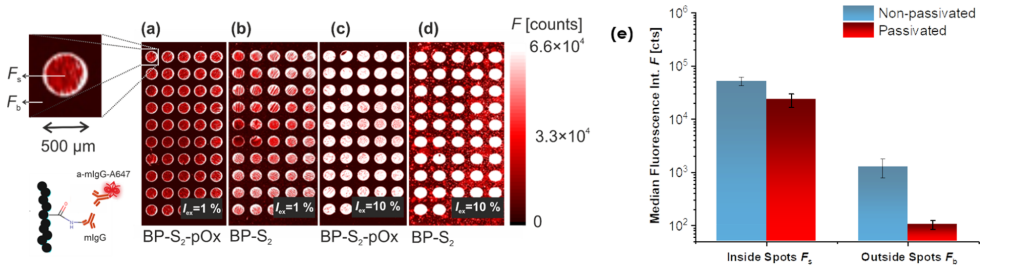

Figure 3. Fluorescence images of biochip architecture I acquired by EPF: (a,c) arrays with a pOx-passivated area between the sensing spots and (b,d) arrays without the pOx passivation. The images were measured (a,b) with the excitation power I_{ex} = 1% and (c,d) with the excitation power I_{ex} = 10%. (e) Comparison of the average fluorescence intensities F_s and F_b for excitation power I_{ex} = 1%.

protect this hydrophobic area and thus prevent the unspecific adsorption of biomolecules from the analyzed samples, a thin layer of noncross-linkable pOx was coupled on these zones. This polymer was deposited over the whole biochip surface area, followed by the irradiation with UV light (Figure 2a, step 4) upon which the pOx polymer chains in contact with BP-S_2 attached to the gold surface. After additional rinsing of the surface, the pOx on the already coated sensing spots and further away from the gold surface was washed away. Therefore, pOx forms a thin monolayer only outside the circular sensing spots where its chains are in direct contact with the BP-S_2. Also, it is worth noting that the thin pOx "grafted to" polymer brush layer does not form a network as its polymer backbone does not carry benzophenone groups. Such an architecture was then used for the post-modification with functional biomolecules serving as ligands (Figure 2a, step 5). It is utilized for protein ligands by using amine-coupling through reacting carboxyl groups with EDC and TFPS. In addition, the coupling of peptide ligands carrying alkyne tags was performed by converting the carboxyl groups on the pNIPAAm-based polymer chains to azide moieties with amine−azide (Figure 2b). As only the pNIPAAm-based polymer carrying carboxylic groups is employed for the post-modification, the anchoring of the antibody or peptide ligands does not occur on the zones outside the sensing spots with pOx moieties.

In the second route toward architecture II, the whole pNIPAAm-based polymer layer was uniformly cross-linked with UV light using the same dose of 2 J/cm^2, followed by rinsing of loosely bound polymer chains (Figure 2a, step 6). Then, the carboxylic groups present in the photocross-linked pNIPAAm-based polymer networks were activated by EDC and TFPS, and the functional biomolecules were immobilized inside the polymer networks in defined, spatially controlled areas by microspotting (Figure 2a, step 7). After the subsequent rinsing and passivating the remaining activated carboxyl groups with ethanolamine, the HG film was swollen, yielding arrays of functional molecules attached to flexible polymer chains inside the pNIPAAm-based networks (Figure 2a, step 8).

Observation of Affinity Binding with Architecture I. The arrays of sensing spots were *in situ* post-modified with an antibody ligand (mouse immunoglobulin G—mIgG) and were allowed to bind its affinity partner that was labeled with a fluorophore (anti-mIgG-AF647). For the used concentration of 12 nM and a time of 45 min, the affinity reaction reached saturation, and the majority of accessible mIgG binding sites inside the HG was assumed to bind with anti-mIgG-AF647. After the washing and drying steps, the fluorescence images were acquired with the EPF geometry by scanning the excitation beam at λ_{ex} = 635 nm over the arrays and recording the fluorescent signal F emitted at λ_{em} = 670 nm.

The acquired fluorescence images are presented in Figure 3, and they show a series of bright spots with a size of 500 μm that correspond to the HG-coated zones where the a-mIgG-AF647 biomolecules were affinity captured to covalently coupled mIgG. As shown in the inset of Figure 3a, fluorescence intensity inside the spots is homogeneously distributed, and one can observe a brighter rim at their circumference. This can be attributed to the possible lateral swelling of the cylindrically shaped HG coating at the sensing spots occurring at its vertically oriented walls (besides the swelling in the perpendicular direction at the horizontally oriented interfaces, which is investigated by SPR further). This effect may enhance the accessibility of the binding sites and locally increase the amount of captured biomolecules. The averaged fluorescent signal from inside the spots F_s and outside the spots F_b was compared for biochip architecture I with the pOx passivation (a,c) and without the passivation (b,d). The excitation beam power was set to either 1% (a,b) or 10% (c,d) to distinguish the weaker background fluorescence intensity originating from outside the spots F_b. For a lower excitation power of 1%, the fluorescence intensity collected from inside the spots F_s was about 50% lower on the chip with the pOx passivation than that without (F_s = 23,000 *vs* 50,000 counts). This can be attributed to the hindered diffusion of biomolecules through the HG due to the higher cross-linking density associated with the double exposure to UV light. For the stronger excitation power I_{ex} = 10%, the fluorescent signal F_s was above the saturation level (Figure 3c,d).

The fluorescent signal in the area between the sensing spots F_b originates from the unspecific physisorption of the ligands upon the post-modification step and the subsequent affinity binding and/or physisorption of anti-mIgG-AF647. These effects are particularly pronounced for the hydrophobic surface of the BP-S2 SAM and are substantially suppressed by the pOx passivation. The obtained data confirmed that the background signal F_b outside the spots decreased by more than 1 order of magnitude when the pOx passivation was used (F_b = 100 *vs* 1200 counts for the excitation power I_{ex} = 1%). This difference is clearly visually observed from the images acquired for the increased excitation power of 10%.

In order to quantify the quality of the biointerface in fluorescent microarrays, the signal-to-noise ratio (SNR) is

https://doi.org/10.1021/acsami.1c05950
ACS Appl. Mater. Interfaces 2021, 13, 27645−27655

often used. It is defined as SNR = $F_s - F_b/\sigma(F_b)$, where $\sigma(F_b)$ states for the standard deviation of the background signal.[27] The SNR in the field of microarrays is affected by the surface chemistry utilized for the spotting (e.g., epoxy, nitrocellulose, and HG) as well as the deviations occurring during all preparation, hybridization, and scanning steps. Usually, an SNR above 3 is considered as a useable threshold[28] and, here, the values of 1160 and 104 are obtained for the pOx-passivated and nonpassivated surfaces, respectively, when the excitation power was set to I_{ex} = 1%.

Observation of Affinity Binding with Architecture II. The EPF readout was also employed to characterize spatially controlled affinity binding on biochip architecture II by using the same immunoassay. Here, the mIgG serving as the ligand was delivered onto a series of sensing spots by using microspotting with a tip that dispenses a 0.7 nL liquid volume over the pNIPAAm-based photocross-linked layer with the carboxylic groups pre-activated by EDC and TFPS. The concentration of the mIgG serving as the ligand in the spotted droplets was set in the range from 0 to 3 μM, and the microspotted arrays were arranged in a lattice with a period of 300 μm.

After the affinity binding of anti-mIgG-AF647 to the covalently immobilized mIgG (following the same protocol as for architecture I), the biochip was rinsed, dried, and the fluorescence intensity images were acquired. As Figure 4a shows a series of bright fluorescence spots are observed due to the affinity binding in the spotted areas, and the diameter of each spot was about 100 μm. The acquired intensity exhibits maximum in the middle of the spot, and it decreases when moving away from its center (which gives the impression of decreasing spot area with decreasing mean intensity F_s). It also illustrates the dependence of the mean intensity F_s and F_b on the microarray scanner settings, either in a high dynamic range (left) or with a high gain (right). Figure 4b shows the fluorescence signal intensity F_s from the affinity-bound a-mIgG-A647 depending on the concentration of the mIgG ligand used for the microspotting and covalent coupling to pNIPAAm-based polymer chains. It reveals that above mIgG concentration of 1 μM, the response F_s flattens as all available activated carboxyl groups in the pNIPAAm-based HG layer were used for the amine coupling of the ligand. However, the fluorescence intensity F_s reaches the reader saturation values for a more than one order of magnitude higher excitation power of I_{ex} = 50% compared to the architecture II (when the scanner is set for high gain). This observation indicates that the microspotting protocol used in the architecture II provides lower immobilization yield than the *in situ* incubation in architecture I and thus, deteriorated SNR varying between 20 and 250 was achieved.

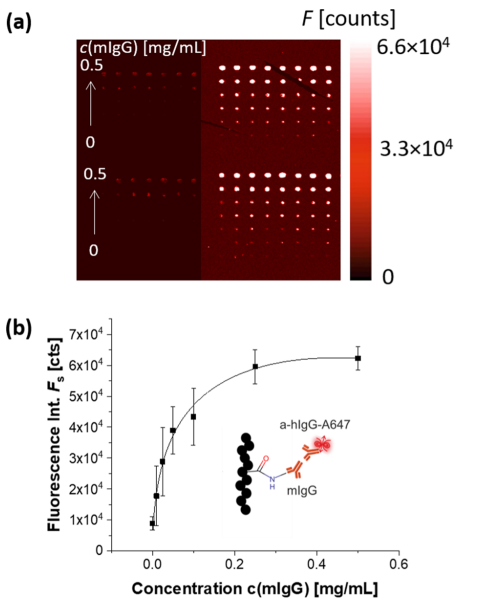

Figure 4. (a) Fluorescence observation of architecture II acquired by EPF with varying concentrations of spotted mIgG after incubation with fluorescently labeled anti-mIgG-AF647 dissolved at 12 nM concentration. 50% laser intensity and scanner configured for high (left) and low (right) dynamic ranges. (b) Comparison of the fluorescence intensity emitted from the sensing spots F_s after the assay with the scanner set to the high dynamic range. The error bars represent the standard deviation of the eight spots for each concentration.

Nevertheless, architecture II allows a straightforward immobilization of different ligands in the array format and thus, it is further exploited for the spotting of four peptides with sequences derived from the EBV antigen (EBV1-4)[29] together with the control CA12 peptide derived from the enzyme carbonic anhydrase XII. These peptides were spotted by dispensing 0.2 nL of a solution spiked with each peptide ligand at a concentration of 80 μM on the pNIPAAm-based polymer layer. Before the microspotting, the carboxylic groups carried by the pNIPAAm-based polymer chains were converted to azide groups (Figure 2b), so the peptides bearing a propargylglycine (alkyne) side group can covalently couple by a copper-mediated click reaction. The prepared peptide microarrays were employed to detect human IgG (hIgG) collected from blood donors' plasma, reactive against the EBV. In this experiment, the sensor chip was sequentially exposed to isolated hIgG dissolved at a concentration of 0.3 mg/mL (2 μM) followed by the binding of captured hIgG with anti-hIgG conjugated with AF647 (13 nM). Figure 5 summarizes the

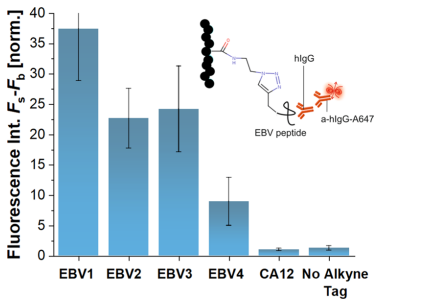

Figure 5. Fluorescence intensities for architecture II after the affinity capture of hIgG pooled with known reactivity against EBV followed by tagging with the fluorescently labeled secondary antibody in comparison with the control CA12. All values are relative to an untagged peptide.

https://doi.org/10.1021/acsami.1c05950
ACS Appl. Mater. Interfaces 2021, 13, 27645−27655

results and reveals that the spots with the specific peptides EBV1-4 show a 9 to 30-fold stronger fluorescent signal F_s in comparison to the control spots with the CA12 peptide and bare pNIPAAm-based polymer network (where peptides without the alkyne tag were spotted).

Furthermore, the performance of the peptide arrays prepared on the 3D pNIPAAm-based HG film was compared to that on the commercial substrate carrying the 2D monolayer interface with azide groups (2D-Azide from PolyAn, Germany). Under identical conditions as in the previous experiments presented in Figure 5, antigenic peptide EBV4 with an alkyne group on either the C or N terminus was spotted onto both interfaces of commercial 2D-Azide and of 3D pNIPAAm-based HG that was post-modified with an 2-azidoethan-1-aminium chloride. As a mock control, there was also spotted EBV4 peptide with a biotin end group. Figure 6

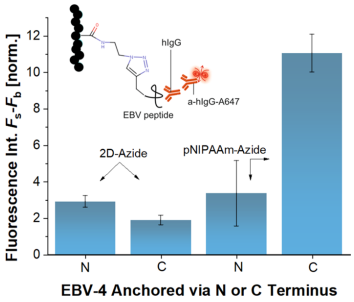

Figure 6. Fluorescence intensities relative to biotin control for architecture II after the affinity capture of hIgG pooled with known reactivity against EBV4 followed by tagging with a fluorescently labeled secondary antibody for commercial 2D-Azide slides (PolyAn) and 3D HG slides, with the alkyne tag bound to either N or C terminus of the peptide.

shows that specific fluorescent signal F_s−F_b acquired on the 2D-Azide slides carrying the EBV4 peptide immobilized *via* the N and C terminus was higher by a factor of 1.8 and 2.7, respectively, with respect to that for the mock control. Such moderate signal strength suggests that the peptide with the biotin tag was probably also partially immobilized onto the control spots carried by the 2D-Azide surface. Importantly, a stronger signal increase of 6 and 10-fold was measured for the EBV4 peptide immobilized *via* the N and C terminus, respectively, on the 3D pNIPAAm-based HG when compared to the mock control.

Interestingly, the peptide orientation clearly affected the fluorescence response on a HG matrix as a 3-fold higher signal was measured for the C-terminal bound peptide compared to the N-terminal one. This is different for the 2D-Azide surface, and it can be ascribed to the effect of steric hindrance that is partially elevated when ligands are conjugated to flexible polymer chains forming the HG interface. When comparing the SNR, a value of 67 was obtained for the 2D-Azide slides, and a slightly better SNR of 88 was determined for the 3D pNIPAAm-based HG matrix. In a nutshell, these experiments confirm an enhanced signal and a possible implementation of assays utilizing both amine coupling and click chemistry for the conjugation of protein as well as peptide ligands, respectively, to the pNIPAAm-based polymer network that can then serve as a binding matrix.

Dual Amplification of the Fluorescent Signal—Plasmonic Excitation and Temperature-Induced Collapse. The responsive properties of the pNIPAAm-based HG matrix offer additional means to manipulate the captured target molecules by exploiting its temperature-induced collapse. Upon pNIPAAm-based HG compaction occurring above its LCST, the affinity-captured biomolecules inside the polymer network structure are dragged toward the gold surface, as shown in Figure 7a. Then, the fluorophore labels bound in the

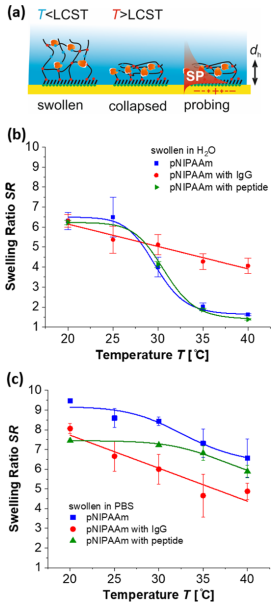

Figure 7. (a) Schematic of the SPR probing of swelling changes and responsive properties of the pNIPAAm-based HG in contact with (b) H_2O and (c) PBS that is affected by the post-modification with high (mIgG)- and low (peptide)-molecular-weight ligands. Swelling ratios are derived from the SPR signal and are fitted with the sigmoidal function (lines) (obtained error bars are derived from standard deviation of the SR).

HG matrix after the specific capture of the target analyte can be placed at the optimum distance from the metal surface in order to benefit from the optical amplification based on PEF.[30] This amplification originates from the probing by the confined field of increased intensity of SPs, which translates to the enhanced fluorescence emission rate without changing the background signal.

To utilize this concept, we first characterized changes in the responsive properties of the pNIPAAm-based HG layer after its post-modification with the high-molecular-weight IgG ligand (MW = 160 kDa) and smaller peptide ligand (MW = 2.3 kDa). The thickness of the HG layer d_h was measured as a function of temperature T by using SPR.[12] As shown in Figure 7b, the measured changes in the HG layer thickness d_h were normalized with that obtained for a dry polymer film $d_{h\text{-}dry}$ to yield to swelling ratio SR = $d_h/d_{h\text{-}dry}$. For the pristine

https://doi.org/10.1021/acsami.1c05950
ACS Appl. Mater. Interfaces 2021, 13, 27645−27655

pNIPAAm-based HG in contact with water, the HG layer collapses at a temperature between T = 30 and 35 °C, which is in agreement with the pNIPAAm LCST of 32 °C. The swelling ratio SR correspondingly drops by a factor of 4.7 when increasing the temperature from T = 20 to 40 °C. The response of the pNIPAAm-based HG to temperature changes is strongly suppressed after its post-modification with IgG molecules as the SR changed only by a factor of 1.6 when increasing the temperature from T = 20 to 40 °C. This observation agrees with our previous study, and it can be ascribed to the hydrophilic nature of IgG that dominates over the properties of pNIPAAm polymer networks when switched to a hydrophobic state above the LCST.[17] Importantly, the response of the same HG layer that was post-modified with a lower molecular weight peptide EBV4 (MW = 2.3 kDa) is preserved as the swelling ratio SR changes by a factor of 4.3 when increasing temperature T from 20 to 40 °C. This change is similar to that observed for the pristine pNIPAAm HG layer in contact with water. However, the thermoresponsive characteristics are strongly suppressed when it is swollen in PBS. Like in our previous studies, the swelling ratio SR gradually decreases with the increase of temperature T from 20 to 40 °C by only a small factor of about 1.5, which can be ascribed to the presence of ions in the solution.[31]

Finally, the peptide-functionalized pNIPAAm-based binding matrix was explored for the affinity capture of the target analyte from the pooled human plasma and for its detection by using a dual amplification strategy. The affinity captured hIgG against EBV was compacted at the sensor surface using a temperature stimulus, and the surface plasmon-enhanced fluorescence was used for its detection. In this experiment, the sensor chip with the pNIPAAm-based HG was attached atop of a glass substrate with a 50 nm thick gold layer, and it was post-modified with the EBV4 peptide. The thickness of the HG was set to $d_{h\text{-}dry}$ = 40 nm in order to match with the penetration depth of the probing field of resonantly excited SPs (about 100 nm). The sensor chip was then loaded to an optical system for the combined SPR and PEF measurements. In the PEF modality, the excitation of the fluorescent signal was utilized *via* the enhanced field intensity of the SPs at the fluorophore excitation wavelength λ_{ex}. In the used system, the resonant coupling to SPs was tuned by varying the angle of incidence θ and it is manifested as a dip in the reflectivity spectrum $R(\theta)$ and respective peak in the fluorescence intensity spectrum $F(\theta)$, as shown in Figure 8.

The swollen HG film carrying immobilized EBV4 peptides was reacted with a pooled human plasma, diluted 1:10 in PBST buffer. The whole concentration of hIgG in the plasma is around 8.5 mg/mL,[32] and a small fraction is specific to EBV. First, the surface of pristine (unmodified) pNIPAAm-based HG with no peptide ligand immobilized was exposed to the pooled human plasma (diluted with PBS 1:10) followed by the reaction with the detection antibody a-hIgG-A647 for 15 min at a concentration of 13 nM. Afterward, the same experiment was performed for the pNIPAAm-based HG that was post-modified with the EBV4 peptide. After each step, the reflectivity scan $R(\theta)$ was measured together with the fluorescence intensity spectrum $F(\theta)$. As shown in Figure 8b, the affinity binding of hIgG against EBV is manifested as a peak in the fluorescence angular spectrum $F(\theta)$ located close to the angle θ where the resonance excitation of SPs occurs [manifested as a dip in the respective $R(\theta)$]. These graphs reveal that increasing the temperature from T = 25 to 40 °C

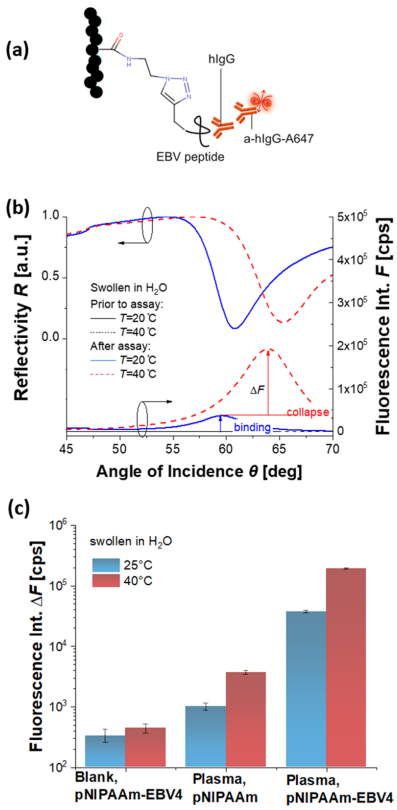

Figure 8. (a) Schematics of the sandwich assay with the peptide ligand in the thermoresponsive pNIPAAm-based binding matrix. (b) Angular reflectivity and fluorescence intensity scans at temperatures of T = 25 and 40 °C before and after the assay, a-EBV antibodies from the diluted human plasma, followed by anti-hIgG-AF647. (c) Comparison of the peak fluorescence intensities of only anti-hIgG-AF647, unspecific binding of plasma to the HG without a ligand, and specific detection of a-EBV antibodies in the plasma through the peptide assay, both for swollen and collapsed states of the HG binding matrix. Error bars were determined as 3× the standard deviation of the fluorescent signal.

leads to a shift in the SPR reflectivity dip by about 5° due to the increase of the refractive index on the gold surface associated with the collapse of the polymer network. Notably, the fluorescence peak also shifts by the same angle, and its peak intensity increases by a factor of 5 for the affinity capture of hIgG against EBV in water. This additional enhancement can be attributed to the dragging of target molecules closer to the gold surface, where the maximum plasmonic enhancement occurs. The summary of the peak fluorescence intensities ΔF presented in Figure 8c compares the signal acquired for control experiments and the specific detection of a-EBV antibody. In the first control, a nonmodified HG was directly reacted with detection antibody a-hIgG-A647 and its unspecific sorption leads to an increase of the fluorescent signal of about ΔF = 600 cps. The same was done for the EBV4 peptide-modified HG

https://doi.org/10.1021/acsami.1c05950
ACS Appl. Mater. Interfaces 2021, 13, 27645−27655

layer as a second control, which showed an even lower increase of ΔF = 300 cps. The third control was performed in the nonmodified HG layer exposed to 10% pooled human plasma followed by reacting with detection antibody a-hIgG-A647, which showed a higher response of $\Delta F = 10^3$ cps. Finally, the specific detection of a-EBV antibodies in 10% pooled plasma was tested and revealed a strong signal of $\Delta F = 3 \times 10^4$ cps at room temperature T = 25 °C. From the angular scans, $F(\theta)$ follows that the peak fluorescent signal further increases by a factor of 5 to $\Delta F = 1.5 \times 10^5$ cps, when the temperature is changed from T = 25 °C to 40 °C and the pNIPAAm-based HG collapses at the metallic surface. From these data, no apparent fluorescent background signal due to the autofluorescence of the pNIPAAm network itself was observed and when calculating the SNR ratio (analogously as on the microarray experiments above), a value of 1550 and 8000 was determined for 25 and 40 °C, respectively, highlighting the advantage of a dual amplification approach.

CONCLUSIONS

A thin responsive HG layer was tailored to serve as an affinity binding matrix in assays with a fluorescence readout, and its utilization to dual amplification strategy was explored. It is based on the combination of optical enhancement and efficient pre-concentration of captured analytes by the HG compaction triggered by an external stimulus. This concept was carried out using a pNIPAAm-based terpolymer with functional and photoreactive groups, allowing the facile post-modification by ligand molecules and photocross-linking and patterning arrays of sensing spots. Antibody and peptide ligands were conjugated with the pNIPAAm-based three-dimensional polymer network through amine and click coupling, respectively, for the specific capture of target biomolecules. The ability to perform analysis in complex samples is demonstrated by the detection of human IgG against EBV in the human plasma with a set of peptide ligands. The developed responsive biointerface is documented to provide improved performance characteristics with respect to commercial sensor chips with azide groups arranged in a regular two-dimensional architecture.

The pNIPAAm-based thermoresponsive biointerface platform was employed on a sensor chip for surface plasmon-enhanced fluorescence measurements, which in conjunction with specific metallic nanostructures can provide optical enhancement in the acquired fluorescent signal by a factor of 300.[30,33] Compared to our previous studies with large-molecular-weight antibody ligands,[17] post-modification with low-molecular-weight peptides offers the advantage of preserving the thermoresponsive properties of pNIPAAm-based polymer networks, and it translates into a pronounced increase in the fluorescence intensity by a large factor of 5. The combination of optical- and analyte-compaction-based amplification holds the potential to benefit from both the high binding capacity of the swollen HG binding matrix and probing with the tightly confined electromagnetic field associated with the excitation of SPs on metallic thin films and nanostructures. It can provide a route for efficient *in situ* fluorescence measurements with the combined enhancement factor $>10^3$ under realistic conditions and complex samples. Moreover, new sensor modalities can be developed for rapid and sensitive fluorescence monitoring of biomolecular binding events and affinity interactions in conjunction with fast temperature actuation, which for instance, is possible by plasmonic heating.[34]

ASSOCIATED CONTENT

Supporting Information

The Supporting Information is available free of charge at https://pubs.acs.org/doi/10.1021/acsami.1c05950.

IR spectrum and ^{1}H and ^{13}C NMR spectra of 2-azidoethylamine, ^{1}H and ^{13}C NMR spectra of benzophenone disulfide, ^{1}H NMR spectra of 4-benzophenylacrylamide and the pNIPAAm-based terpolymer, and comparison of ^{1}H NMR spectra of the terpolymer and pOx (PDF)

AUTHOR INFORMATION

Corresponding Author

Jakub Dostalek − *Biosensor Technologies, AIT-Austrian Institute of Technology GmbH, Tulln an der Donau 3430, Austria; FZU-Institute of Physics, Czech Academy of Sciences, Prague 182 21, Czech Republic;* orcid.org/0000-0002-0431-2170; Phone: +43 (0) 50550 4470; Email: jakub.dostalek@ait.ac.at; Fax: +43 (0) 50550 4450

Authors

Simone Hageneder − *Biosensor Technologies, AIT-Austrian Institute of Technology GmbH, Tulln an der Donau 3430, Austria;* orcid.org/0000-0002-7200-3257

Vanessa Jungbluth − *Biosensor Technologies, AIT-Austrian Institute of Technology GmbH, Tulln an der Donau 3430, Austria;* Present Address: Dipartimento di Scienze Chimiche, Università degli Studi di Catania, Catania, Italy.; orcid.org/0000-0002-3176-2839

Regina Soldo − *Molecular Diagnostics, Health & Environment, AIT Austrian Institute of Technology GmbH, Vienna 1210, Austria;* Present Address: Greiner Bio-One, Greinerstraße 70, Kremsmünster, Austria.

Christian Petri − *Macromolecular Chemistry, Department Chemistry—Biology, University of Siegen, Siegen 57076, Germany*

Matthias Pertiller − *Biosensor Technologies, AIT-Austrian Institute of Technology GmbH, Tulln an der Donau 3430, Austria;* orcid.org/0000-0002-6315-2306

Marjut Kreivi − *Ginolis Ltd, Oulunsalo 90460, Finland;* Present Address: VTT-Technical Research Centre of Finland, Kaitoväylä 1, Oulu FIN-90590, Finland.; orcid.org/0000-0002-6288-2155

Andreas Weinhäusel − *Molecular Diagnostics, Health & Environment, AIT Austrian Institute of Technology GmbH, Vienna 1210, Austria*

Ulrich Jonas − *Macromolecular Chemistry, Department Chemistry—Biology, University of Siegen, Siegen 57076, Germany;* orcid.org/0000-0002-2161-4541

Complete contact information is available at: https://pubs.acs.org/10.1021/acsami.1c05950

Notes

The authors declare no competing financial interest.

ACKNOWLEDGMENTS

All the authors received support from the European Union's Horizon 2020 research and innovation program under grant agreement no. 633937, project ULTRAPLACAD. Additionally,

S.H. and J.D. were partially supported by the Austrian Research Promotion Agency (FFG) with grant agreement no. 861578 (ERANET project PLABAN) and by the Lower Austria project IKTHEUAP number WST3-F-5030820/010-2019. J.D. acknowledges support from the ESIF and MEYS (Project "FZU researchers, technical and administrative staff mobility"—CZ.02.2.69/0.0/0.0/18_053/0016627).

■ ABBREVIATIONS

EDC, 1-ethyl-3-(3-dimethylaminopropyl)carbodiimide
TFPS, 4-sulfotetrafluorophenol
ACT, acetate buffer
DCM, dichloromethane
DMSO, dimethyl sulfoxide
EBV, Epstein−Barr virus
FBPF, fluorescence bandpass filter
HG, hydrogel
IgG, immunoglobulin G
LNF, laser notch filter
LCST, lower critical solution temperature
MW, molecular weight
PEF, plasmon-enhanced fluorescence
pNIPAAm, poly(*N*-isopropylacrylamide)
PBS, phosphate-buffered saline
SAM, self-assembled monolayer
SNR, signal-to-noise ratio
SPR, surface plasmon resonance
TM, transverse magnetic
TBTA, tris((1-benzyl-4-triazolyl)methyl)amine

■ REFERENCES

(1) Mesch, M.; Zhang, C.; Braun, P. V.; Giessen, H. Functionalized Hydrogel on Plasmonic Nanoantennas for Noninvasive Glucose Sensing. *ACS Photonics* **2015**, *2*, 475−480.
(2) Jiang, Y.; Colazo, M. G.; Serpe, M. J. Poly(N-isopropylacrylamide) microgel-based etalons for the label-free quantitation of estradiol-17β in aqueous solutions and milk samples. *Anal. Bioanal. Chem.* **2018**, *410*, 4397−4407.
(3) Manikas, A. C.; Aliberti, A.; Causa, F.; Battista, E.; Netti, P. A. Thermoresponsive PNIPAAm Hydrogel Scaffolds with Encapsulated AuNPs Show High Analyte-Trapping Ability and Tailored Plasmonic Properties for High Sensing Efficiency. *J. Mater. Chem. B* **2015**, *3*, 53−58.
(4) Hilber, W. Stimulus-Active Polymer Actuators for next-Generation Microfluidic Devices. *Appl. Phys. A: Mater. Sci. Process.* **2016**, *122*, 751.
(5) Choe, A.; Yeom, J.; Shanker, R.; Kim, M. P.; Kang, S.; Ko, H. Stretchable and Wearable Colorimetric Patches Based on Thermoresponsive Plasmonic Microgels Embedded in a Hydrogel Film. *NPG Asia Mater.* **2018**, *10*, 912−922.
(6) Elashnikov, R.; Mares, D.; Podzimek, T.; Švorčík, V.; Lyutakov, O. Sandwiched Gold/PNIPAm/Gold Microstructures for Smart Plasmonics Application: Towards the High Detection Limit and Raman Quantitative Measurements. *Analyst* **2017**, *142*, 2974−2981.
(7) Álvarez-Puebla, R. A.; Contreras-Cáceres, R.; Pastoriza-Santos, I.; Pérez-Juste, J.; Liz-Marzán, L. M. Au@pNIPAM Colloids as Molecular Traps for Surface-Enhanced, Spectroscopic, Ultra-Sensitive Analysis. *Angew. Chem., Int. Ed.* **2009**, *48*, 138−143.
(8) Mueller, M.; Tebbe, M.; Andreeva, D. V.; Karg, M.; Alvarez Puebla, R. A.; Pazos Perez, N.; Fery, A. Large-Area Organization of PNIPAM-Coated Nanostars as SERS Platforms for Polycyclic Aromatic Hydrocarbons Sensing in Gas Phase. *Langmuir* **2012**, *28*, 9168−9173.
(9) Tokarev, I.; Tokareva, I.; Minko, S. Optical Nanosensor Platform Operating in Near-Physiological Ph Range via Polymer-Brush-Mediated Plasmon Coupling. *ACS Appl. Mater. Interfaces* **2011**, *3*, 143−146.
(10) Quilis, N. G.; Hageneder, S.; Fossati, S.; Auer, S. K.; Venugopalan, P.; Bozdogan, A.; Petri, C.; Moreno-Cencerrado, A.; Toca-Herrera, J. L.; Jonas, U.; Dostalek, J. UV-Laser Interference Lithography for Local Functionalization of Plasmonic Nanostructures with Responsive Hydrogel. *J. Phys. Chem. C* **2020**, *124*, 3297−3305.
(11) Heskins, M.; Guillet, J. E. Solution Properties of Poly(N-Isopropylacrylamide). *J. Macromol. Sci., Part A: Pure Appl.Chem.* **1968**, *2*, 1441.
(12) Aulasevich, A.; Roskamp, R. F.; Jonas, U.; Menges, B.; Dostálek, J.; Knoll, W. Optical Waveguide Spectroscopy for the Investigation of Protein-Functionalized Hydrogel Films. *Macromol. Rapid Commun.* **2009**, *30*, 872−877.
(13) Zhang, Q.; Wang, Y.; Mateescu, A.; Sergelen, K.; Kibrom, A.; Jonas, U.; Wei, T.; Dostalek, J. Biosensor based on hydrogel optical waveguide spectroscopy for the detection of 17β-estradiol. *Talanta* **2013**, *104*, 149−154.
(14) Andersson, O.; Larsson, A.; Ekblad, T.; Liedberg, B. Gradient Hydrogel Matrix for Microarray and Biosensor Applications: An Imaging SPR Study. *Biomacromolecules* **2009**, *10*, 142−148.
(15) Wang, Y.; Brunsen, A.; Jonas, U.; Dostálek, J.; Knoll, W. Prostate Specific Antigen Biosensor Based on Long Range Surface Plasmon-Enhanced Fluorescence Spectroscopy and Dextran Hydrogel Binding Matrix. *Anal. Chem.* **2009**, *81*, 9625−9632.
(16) Huang, C.-J.; Jonas, U.; Dostálek, J.; Knoll, W. Biosensor Platform Based on Surface Plasmon-Enhanced Fluorescence Spectroscopy and Responsive Hydrogel Binding Matrix. *Optical Sensors*; International Society for Optics and Photonics, 2009; Vol. *7356*; p 735625.
(17) Toma, M.; Jonas, U.; Mateescu, A.; Knoll, W.; Dostalek, J. Active Control of SPR by Thermoresponsive Hydrogels for Biosensor Applications. *J. Phys. Chem. C* **2013**, *117*, 11705−11712.
(18) King, P. J. S.; Saiani, A.; Bichenkova, E. V.; Miller, A. F. A de novo self-assembling peptide hydrogel biosensor with covalently immobilised DNA-recognising motifs. *Chem. Commun.* **2016**, *52*, 6697−6700.
(19) Liu, Q.; Wang, J.; Boyd, B. J. Peptide-Based Biosensors. *Talanta*. Elsevier B.V. May 1, 2015, *136*; pp 114−127. DOI: DOI: 10.1016/j.talanta.2014.12.020.
(20) Waheed, A.; Sly, W. S. Carbonic Anhydrase XII Functions in Health and Disease. *Gene*. Elsevier B.V. August 5, 2017, *623*, pp 33−40. DOI: DOI: 10.1016/j.gene.2017.04.027.
(21) Blake, S.; Capone, R.; Mayer, M.; Yang, J. Chemically Reactive Derivatives of Gramicidin A for Developing Ion Channel-Based Nanoprobes. *Bioconjugate Chem.* **2008**, *19*, 1614−1624.
(22) Gee, K. R.; Archer, E. A.; Kang, H. C. 4-Sulfotetrafluorophenyl (STP) Esters: New Water-Soluble Amine-Reactive Reagents for Labeling Biomolecules. *Tetrahedron Lett.* **1999**, *40*, 1471−1474.
(23) Sergelen, K.; Petri, C.; Jonas, U.; Dostalek, J. Free-Standing Hydrogel-Particle Composite Membrane with Dynamically Controlled Permeability. *Biointerphases* **2017**, *12*, 051002.
(24) Petri, C. *Synthesis and Characterization of Novel Photo-crosslinkable Poly (2-Oxazoline)-Based Hydrogel Systems for the Application as Biosensor Matrix*; Universität Siegen, 2018.
(25) Tauhardt, L.; Frant, M.; Pretzel, D.; Hartlieb, M.; Bücher, C.; Hildebrand, G.; Schröter, B.; Weber, C.; Kempe, K.; Gottschaldt, M.; Liefeith, K.; Schubert, U. S. Amine End-Functionalized Poly(2-Ethyl-2-Oxazoline) as Promising Coating Material for Antifouling Applications. *J. Mater. Chem. B* **2014**, *2*, 4883−4893.
(26) Meldal, M.; Tornøe, C. W. Cu-Catalyzed Azide−Alkyne Cycloaddition. *Chem. Rev.* **2008**, *108*, 2952−3015.
(27) Rampal, J. B. *Microarrays*; Springer, 2007; Vol. *1*.
(28) Tu, Y.; Stolovitzky, G.; Klein, U. Quantitative Noise Analysis for Gene Expression Microarray Experiments. *Proc. Natl. Acad. Sci. U.S.A.* **2002**, *99*, 14031−14036.
(29) Hettegger, P.; Huber, J.; Paßecker, K.; Soldo, R.; Kegler, U.; Nöhammer, C.; Weinhäusel, A. High Similarity of IgG Antibody

https://doi.org/10.1021/acsami.1c05950
ACS Appl. Mater. Interfaces 2021, 13, 27645−27655

Profiles in Blood and Saliva Opens Opportunities for Saliva Based Serology. *PLoS One* **2019**, *14*, No. e0218456.
(30) Bauch, M.; Toma, K.; Toma, M.; Zhang, Q.; Dostalek, J. Plasmon-Enhanced Fluorescence Biosensors: A Review. *Plasmonics* **2014**, *9*, 781−799.
(31) Vagias, A.; Sergelen, K.; Koynov, K.; Košovan, P.; Dostalek, J.; Jonas, U.; Knoll, W.; Fytas, G. Diffusion and Permeation of Labeled IgG in Grafted Hydrogels. *Macromolecules* **2017**, *50*, 4770.
(32) Laub, R.; Baurin, S.; Timmerman, D.; Branckaert, T.; Strengers, P. Specific Protein Content of Pools of Plasma for Fractionation from Different Sources: Impact of Frequency of Donations. *Vox Sang.* **2010**, *99*, 220−231.
(33) Fossati, S.; Hageneder, S.; Menad, S.; Maillart, E.; Dostalek, J. Multiresonant Plasmonic Nanostructure for Ultrasensitive Fluorescence Biosensing. *Nanophotonics* **2020**, *9*, 3673−3685.
(34) Baffou, G.; Quidant, R. Thermo-Plasmonics: Using Metallic Nanostructures as Nano-Sources of Heat. *Laser Photonics Rev.* **2013**, *7*, 171−187.

https://doi.org/10.1021/acsami.1c05950
ACS Appl. Mater. Interfaces 2021, 13, 27645−27655

Supporting Information

Responsive hydrogel binding matrix for dual signal amplification in fluorescence affinity biosensors and peptide microarrays

Simone Hageneder[†], Vanessa Jungbluth[†#], Regina Soldo[‡^], Christian Petri[§], Matthias Pertiller[†], Marjut Kreivi[‖], Andreas Weinhäusel[‡], Ulrich Jonas[§], Jakub Dostalek[†⊥*]

[†] Biosensor Technologies, AIT-Austrian Institute of Technology GmbH, Konrad-Lorenz-Straße 24, 3430 Tulln an der Donau, Austria

[‡] Molecular Diagnostics, Health & Environment, AIT Austrian Institute of Technology GmbH, Giefinggasse 4, 1210 Vienna, Austria

[§] Macromolecular Chemistry, University of Siegen, Department Chemistry – Biology, Adolf-Reichwein-Strasse 2, 57076 Siegen, Germany

[‖] Ginolis Ltd, Automaatiotie 1, 90460 Oulunsalo, Finland

[⊥] FZU-Institute of Physics, Czech Academy of Sciences, Na Slovance 2, Prague 182 21, Czech Republic

* Corresponding Author E-mail: jakub.dostalek@ait.ac.at

Polymer synthesis:
- 2-Azidoethylamine:

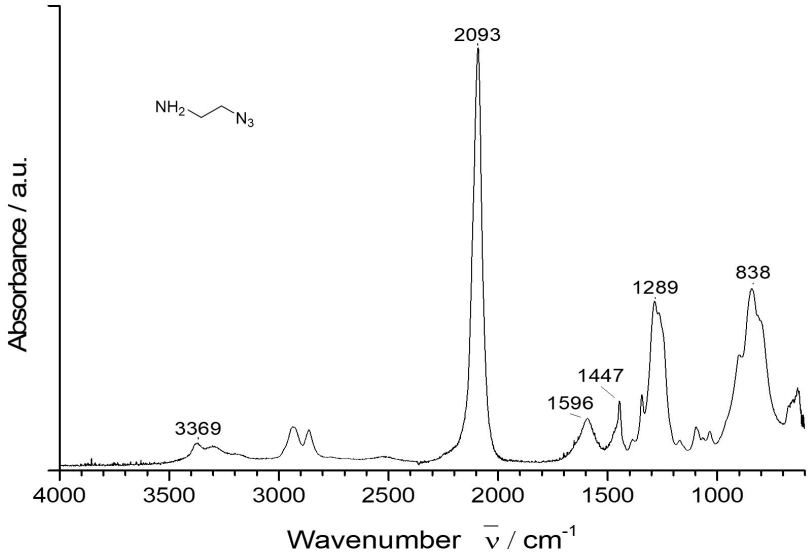

Figure S1: IR spectrum of 2-azidoethylamine

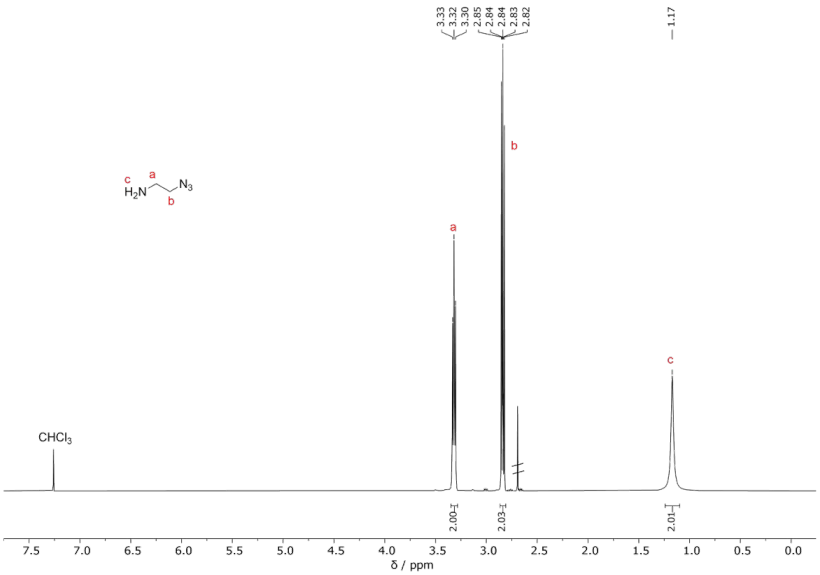

Figure S2: ^{1}H NMR spectrum (400 MHz) of 2-azidoethylamine recorded in $CDCl_3$.

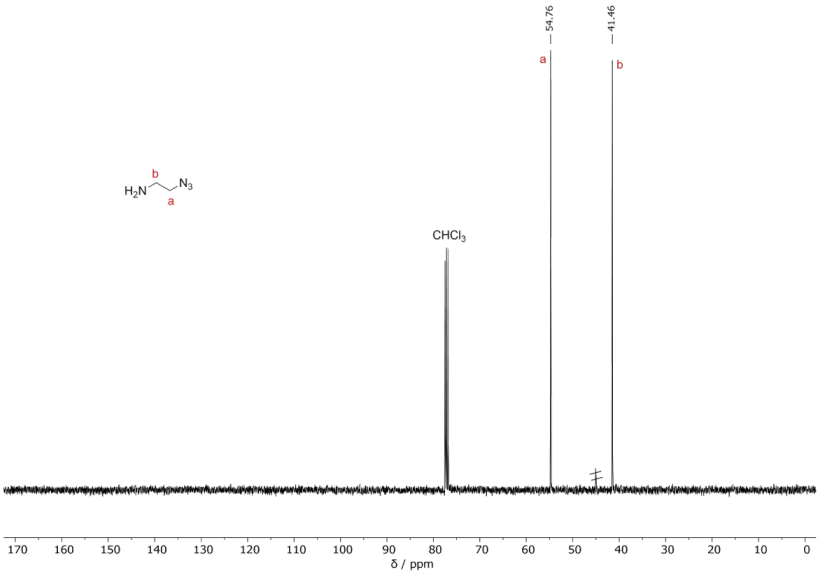

Figure S3: ^{13}C NMR spectrum (101 MHz) of 2-azidoethylamine recorded in $CDCl_3$.

- Benzophenone-disulfide BP-S_2:

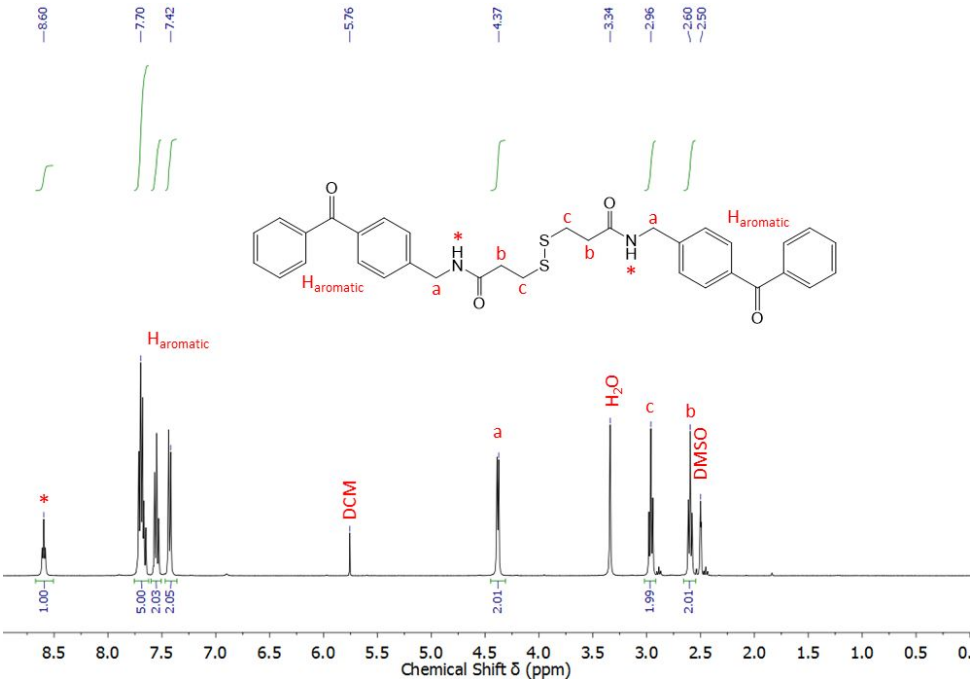

Figure S4: ^{1}H NMR spectrum of 3,3'-disulfanediylbis[N-(4-benzoylbenzyl)propanamide] recorded in DMSO-d_6.

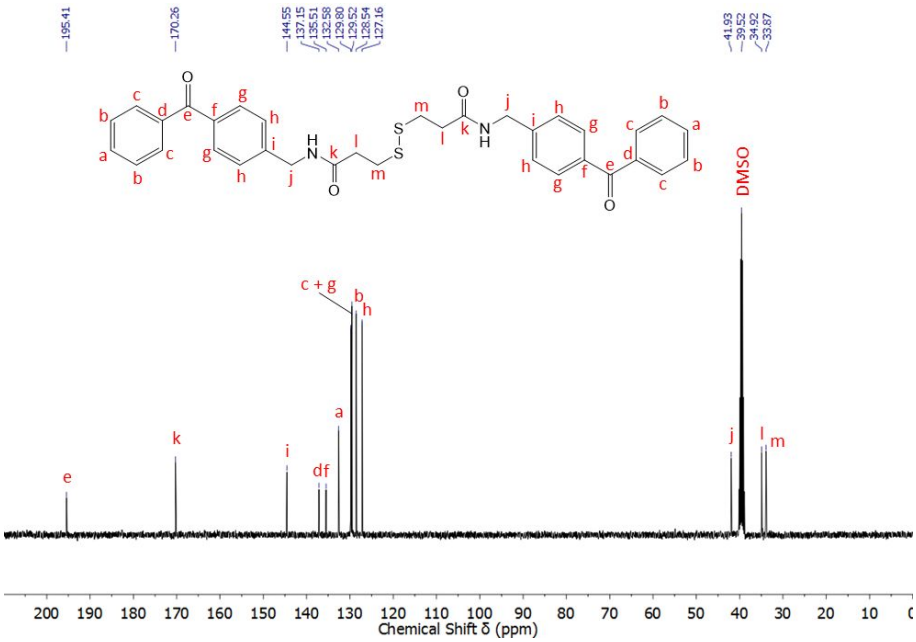

Figure S5: ^{13}C-NMR spectrum of 3,3'-disulfanediylbis(N-(4-benzoylbenzyl)propanamide) (DMSO).

- pNIPAAm-based terpolymer:

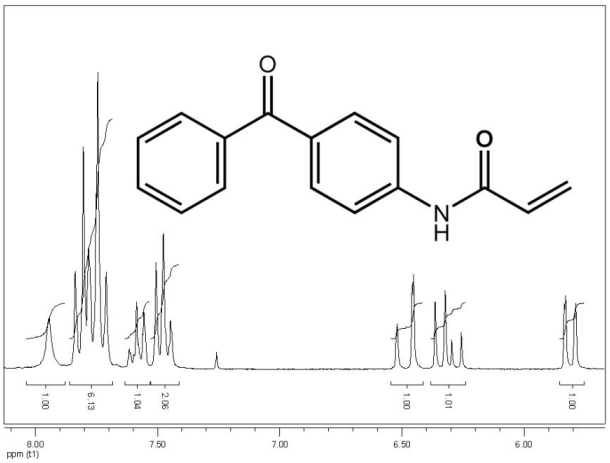

Figure S6: ^{1}H-NMR of 4-benzophenylacrylamide.

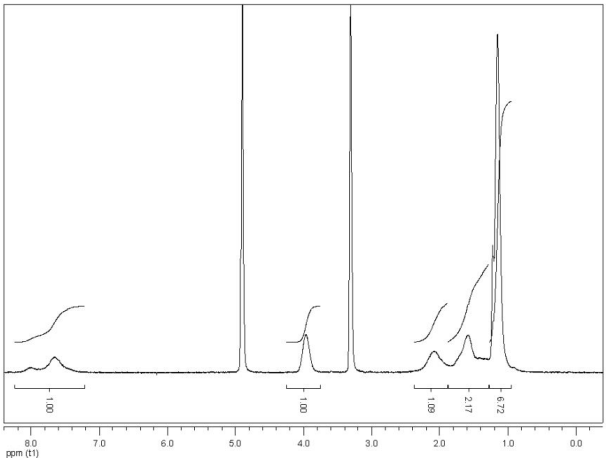

Figure S7: ^{1}H-NMR of pNIPAAm-based terpolymer *N*-isopropylacrylamide, methacrylic acid, and *N*-(4-benzoylphenyl)acrylamide (94:5:1 ratio) in *d*-methanol.

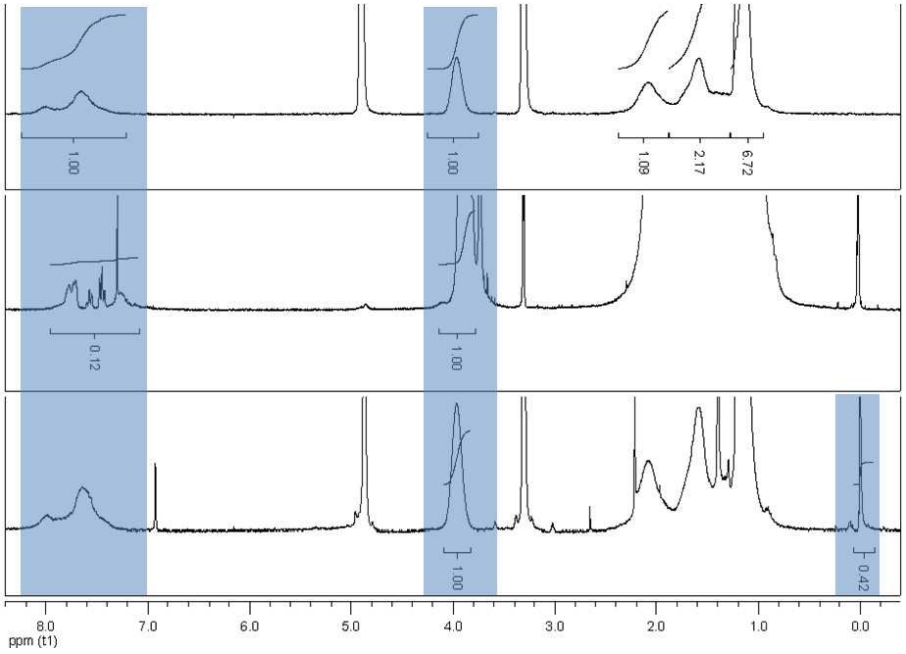

Figure S8: Comparison of ^{1}H-NMR spectra of the terpolymer measured in *d*-methanol (top), after addition of D_2O and *d*-chloroform (middle), and after preparation of the TMS-ester (bottom, measured in *d*-methanol).

- poly(2-ethyl-2-oxazoline) (pOx):

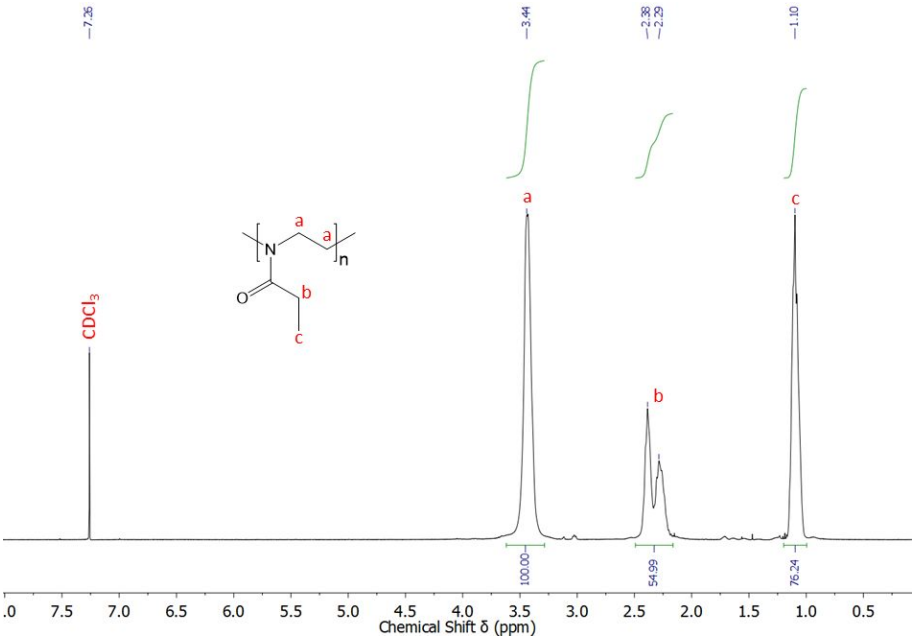

Figure S9: ^{1}H-NMR spectrum of poly(2-ethyl-2-oxazoline) ($CDCl_3$).

3.4 Multi-diffractive grating for surface plasmon biosensors with direct back-side excitation

The following publication is reprinted under the terms of the OSA Open Access Publishing Agreement.

Hageneder, S., Fossati, S., Ferrer, N. G., Güngörmez, B., Auer, S. K., and Dostalek, J. Multi-diffractive grating for surface plasmon biosensors with direct back-side excitation, 2020, Optics Express, 28(26) 39770-39780 https://doi.org/10.1364/OE.410416

First author paper: I designed and conducted experiments, prepared chips, did data evaluation, graphs, and was involved in writing the manuscript. SF provided computational simulations and supervised chip production, and N-GF and BG were involved in the preparation and optimization of chips. SKA was recoding and evaluating surface topography, and JD was responsible for the concept, reader design, manuscript preparation, graphs, and result interpretation.

In this chapter, optical amplification was exploited through a new design of structures for GC-SPR readout. Refractometric sensing by probing from the back-side of the grating sensor chip allowed the observation of the affinity binding of tumor necrosis factor alpha (TNF-α), an important inflammation biomarker. This configuration enables avoiding the light beam passing through the flow cell with the sample, minimizing perturbations from flow or scattering effects which could influence the sensor's accuracy.

Research Article | Vol. 28, No. 26 / 21 December 2020 / Optics Express 39770
Optics EXPRESS

Multi-diffractive grating for surface plasmon biosensors with direct back-side excitation

SIMONE HAGENEDER,[1] STEFAN FOSSATI,[1] NICOLAS-GUILLERMO FERRER,[1,2] BATUHAN GÜNGÖRMEZ,[1,3] SIMONE K. AUER,[1,4] AND JAKUB DOSTALEK[1,5,*]

[1]AIT-Austrian Institute of Technology GmbH, Konrad-Lorenz-Strasse 24, Tulln 3430, Austria
[2]University of Tokyo, Department of Advanced Materials Science, Kashiwanoha 5-1-5, Kashiwa, Chiba 277-8561, Japan
[3]Department of Materials Science and Engineering, Gebze Technical University, Gebze, Kocaeli, Turkey
[4]CEST Kompetenzzentrum für elektrochemische Oberflachentechnologie GmbH, TFZ, Wiener Neustadt 2700, Austria
[5]FZU-Institute of Physics, Czech Academy of Sciences, Na Slovance 2, Prague 182 21, Czech Republic
*jakub.dostalek@ait.ac.at

Abstract: A multi-diffractive nanostructure is reported for the resonant excitation of surface plasmons that are cross-coupled through a thin metallic film. It consists of two superimposed periodic corrugations that allow diffraction excitation of surface plasmons on the inner side of a thin metal film and their subsequent phase matching with counterpropagating surface plasmons travelling to the opposite direction on its other side. This interaction leads to establishing of a set of cross-coupled Bragg-scattered surface plasmon modes that exhibit an electromagnetic field localized on both metal film interfaces. The reported structure is attractive for surface plasmon resonance biosensor applications, where direct optical probing can be done through the substrate without the need of optical matching to a high refractive index prism. In addition, it can be prepared by mass production – compatible means with UV-nanoimprint lithography and its biosensing performance characteristics are demonstrated by refractometric and biomolecular affinity binding studies.

1. Introduction

Metallic nanostructures increasingly serve for optical probing of biomolecules and their interactions in important fields of analytical technologies and life science research. They allow for the resonant coupling of light to surface plasmon modes originating from collective oscillations of electron density and associated electromagnetic field that is tightly confined on the metallic surface. Such confinement of electromagnetic field leads to the enhancement of its intensity and local density of optical states, and it has been exploited in surface plasmon resonance (SPR) biosensors [1] as well as for the amplification of weak optical spectroscopy signal including Raman scattering [2], fluorescence [3] and near-infrared absorption [4].

The majority of SPR biosensors utilize sensor chips with a thin metallic film supporting propagating surface plasmons (PSPs). In Kretschmann configuration of attenuated total internal reflection (ATR) method, these sensor chips are optically matched to an optical prism for the coupling of PSPs at the outer side of the metallic film with an optical beam travelling through the sensor chip substrate [5]. The outer sensor surface is brought in contact with an analyzed liquid sample, and the molecular binding events are observed by interrogating resonant excitation of PSPs in the wavelength [6] or angular [5] reflectivity spectrum. Alternative approaches based on diffraction grating-based excitation of PSPs [7] were pursued, and also metallic nanostructures supporting localized surface plasmons (LSPs) [8] were used to avoid the optical matching of sensor chips to bulky ATR prism. The wavelength interrogation of LSPs can be utilized from both

#410416 https://doi.org/10.1364/OE.410416
Journal © 2020 Received 23 Sep 2020; revised 12 Nov 2020; accepted 16 Nov 2020; published 16 Dec 2020

Research Article | Vol. 28, No. 26 / 21 December 2020 / Optics Express 39771
Optics EXPRESS

sample and sensor chip sides in transmission [9] or reflection mode [10]. This measurement can be performed by dedicated instruments [11] and also by using already established optical readers deployed in standard molecular biology laboratories. These particularly include microtiter plates where the bottom wells carry adsorbed gold nanoparticles prepared by chemical synthesis [12] and thin metallic films perforated with arrays of nanoholes by lithography [13,14].

In general, the measurement in reflection mode from the substrate side of a sensor chip carrying plasmonic nanostructures offers the advantage of avoiding passing the probing optical beam through the analyzed liquid sample. This back-side coupling allows for rapid direct analysis of complex matrices (such as minimally processed blood) that absorb or scatter light. Also, it offers improved stability for the *in situ* SPR measurements, which otherwise require using of transparent flow-cells and make the measurements prone to respond to the sample flow fluctuations. The separation of the fluidic and the optical parts of the plasmonic sensor chip was reported by cross-coupled PSP modes on thin gold films that are perforated with arrays of nanoholes and attached to a low refractive index dielectric film [15]. This configuration takes advantage of refractive index symmetrical geometry that enables cross-coupling of PSP at opposite interfaces leading to the establishment of long-range surface plasmon modes [16]. Another possible approach to diffraction-based excitation of PSPs on non-conformal diffraction gratings was demonstrated on metallic films that were corrugated only on inner side [17]. However, the preparation of such nanostructures for back-side excitation of coupled PSPs or LSPs can be only prepared by using methods involving multiple lithography steps. Typically, periodic arrays of plasmonic nanoholes and discs are prepared by electron beam lithography, which offers precise control of the nanostructure geometry. However, it represents an approach relying on complex infrastructure that is suitable only for research as the fabrication over larger areas > 100 μm is slow. Among others, UV-laser interference lithography [18] and UV-nanoimprint lithography combined with lift-off [19], dry etching steps [20], or template stripping [21,22] have been proposed, but they elevate this limitation only partially.

In this paper, we report on a new approach for back-side excitation of PSPs based on multi-periodic gratings (MPG) coated with a thin metallic film. The structure is based on a corrugation profile with multiple superimposed relief periodic modulations that have been explored before for the broadband plasmonic absorbers [23], multi-resonant plasmonic nanostructures for the amplification of weak fluorescence signal [24], and SPR biosensors with Bragg-scattered surface plasmons [25]. We report for the first time on tailoring this geometry for the cross-coupling of PSPs across a thin metallic film and implement it for real-time *in situ* observation of molecular binding-induced refractive index changes based on detuning of the tailored plasmonic resonance that is measured with the back-side excitation geometry.

2. Materials and methods

2.1. Preparation of multi-diffractive grating structures

The MPG structure was recorded by UV laser interference lithography (UV-LIL) with Lloyd's mirror configuration. Positive photoresist Microposit S1805 from Microchem (USA) was spun on a BK7 glass substrate at 4500 rpm for 45 seconds (yielding a thickness of 500 nm) and dried on a hot plate at 98 °C for 120 sec. Afterwards, the substrate was mounted to the UV-LIL setup and exposed to the field of two interfering collimated beams (with an intensity of 32 μW cm^{-2}) emitted from a HeCd laser IK 3031 R-C from Kimmon (Japan) at wavelength λ=325 nm. The angle of the interfering beams was set to 69°05' and 47°10' deg, which corresponds to periods of Λ_1=455 and Λ_2=239 nm, respectively. To record the MPG structure, the photoresist layer was sequentially exposed to the interference field at each respective angle. For the preparation of crossed gratings, the sequential exposure to interference field was carried out twice for two orientations of the sample rotated by 90 degrees. The relief corrugation was etched into the photoresist by a developer AZ 303 from MicroChemicals (Germany) diluted by distilled water at

Research Article | Vol. 28, No. 26 / 21 December 2020 / Optics Express 39772
Optics EXPRESS

a ratio of 1:15. For the measurements discussed below, we used a grating C2.2.ABPO with a recording time of the period Λ_1 of 10 min, recording time of the period Λ_2 of 25 min, and the development time 90 s.

Prepared photoresist grating was cast to polydimethylsiloxane (PDMS) Sylgard 184 from Dow Corning (USA). Multiple generation copies were prepared, and PDMS was cured at elevated temperature to fine-tune the periods and the modulation depth of the recorded structure and to serve as a working stamp after the detachment of the cured polymer. Cleaned BK7 glass substrates were coated with the UV-curable polymer Amonil MMS 10 from AMO GmbH (Germany) by spin-coating at 3000 rpm for 120 s. Then, the PDMS working stamp was placed on the top of the fluid Amonil layer and, after 5 min rest time, irradiated by UV light with a dose of 2 J cm^{-2} (UV lamp Bio-Link 365, Vilber Lourmat). Finally, the PDMS working stamp was detached from the UV-cured Amonil MMS 10, leaving a copy of the master structure on the glass substrate. The copied MPG structure was placed on a hot plate at 120 °C for 4 min, then coated with 50 nm of gold by vacuum thermal evaporation by using an instrument HHV AUTO 306 from HHV Ltd (UK) in vacuum better than 10^{-6} mBar.

2.2. Optical setup

A polychromatic light beam emitted from a halogen light source LSH102 from LOT-Oriel (Germany) was coupled to a multimode optical fiber M25L02 from Thorlabs (UK). The beam emitted from the optical fiber end was collimated by using a lens with f=30 mm and made normally incident at the gold MPG surface through the glass substrate. The reflected beam was collected from a multimode optical fiber M26L02 from Thorlabs (UK) by using a collimator F810SMA-635 from Thorlabs (UK) and delivered to a spectrometer HR4000 from Ocean Optics (USA) or Shamrock 303i from Andor (USA). Raw wavelength spectra of the light beam reflected from the MPG surface were normalized with a spectrum acquired for a reference flat gold surface. A flow-cell was clamped against the grating sensor chip, and it consisted of a polished plastic substrate with drilled input and output ports and a thin PDMS gasket. The volume of the flow-cell was 10 µL, and analyzed liquid samples were flowed through by using the peristaltic pump REGLO Digital MS-4/8 from Ismatec (Switzerland) and tubing with a 0.64 mm inner diameter from Ismatec Wertheim (Germany) at a flow rate of 80 µL/min. The sensing spot in the flow-cell was illuminated by a polychromatic beam with a diameter of about 5 mm. The normalized reflectivity spectra were evaluated by a dedicated software developed in-house by using LabView from National Instruments (USA). The sequentially acquired specular reflectivity spectra $R_0(\lambda)$ were processed by a routine centroid [26] in the selected wavelength range λ_{n1} - λ_{n2} in order to track the refractive index changes in realtime. The reflectivity spectra $R_0(\lambda)$ were acquired with an integration time of 5 ms and the accumulation of 300 was used to reduce noice. The centroid wavelength was determined from discrete reflectivity values $R_0(\lambda_i)$ as:

$$\lambda_{cen} = \sum_{i=N_1}^{N_2} \lambda_i [R_t - R_0(\lambda_i)] / \sum_{i=N_1}^{N_2} [R_t - R_0(\lambda_i)], \quad (1)$$

where N_1 and N_2 are indexes that define pixels over which the centroid routine was applied, λ_i is the wavelength corresponding to the i^{th} detector pixel, and R_t is a threshold.

2.3. Optical simulations

Finite element method was employed as implemented in a diffraction grating solver DiPoG (Weierstrass Institute, Germany). A grating in a computation cell with a length of up to Λ=4.6 µm and height 1 µm was approximated by a mesh of triangles (convergence check was performed by increasing the number of triangles). Cartesian coordinates with the x and z axes in the plane of the MPG structure and y-axis perpendicular to the MPG structure were used as seen in Fig. 1(a).

Research Article | Vol. 28, No. 26 / 21 December 2020 / Optics Express 39773
Optics EXPRESS

The corrugation profile with two superimposed relief gratings (period Λ_1=0.46 μm and Λ_2=0.242 μm) and were defined as higher harmonics: $y = a_1 \sin(2\pi/\Lambda \cdot n_1 \cdot x) + a_2 \sin(2\pi/\Lambda \cdot n_2 \cdot x)$, where a_1 and a_2 states for amplitudes and n_1=10 and n_2=19. In the used numerical model, the set of Maxwell equations was solved by using the PARDISO solver of sparse linear systems developed at University of Basel (Switzerland).

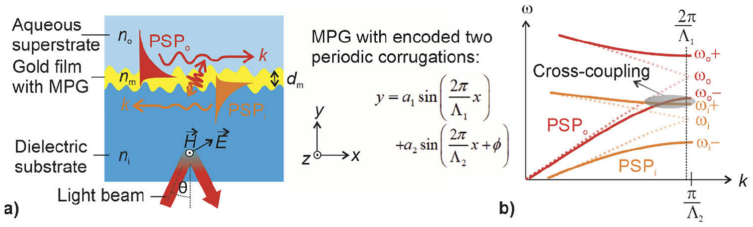

Fig. 1. Schematics of a) the cross-coupling of PSPs across a thin metallic film on an MPG with encoded longer period Λ_1 and shorter period Λ_2. b) Schematics of the dispersion relation of PSPs at the outer and inner interfaces that is folded into first Brillouin zone.

2.4. Biomolecular binding study

After the deposition of 50 nm thick gold layer to the MPG surface, its surface was modified with a self-assembled thiol monolayer (SAM) by immersion in ethanolic solution with dissolved thiols carrying functional biotin (0.2 mM HS-C11-EG6-Biotin) and passivating oligoethylene glycol groups (0.8 mM HS-C11-EG6-OH) from Prochimia Surfaces in Gdynia (Poland). After overnight incubation, the substrates with MPG were rinsed with ethanol, dried in a stream of nitrogen and stored in argon atmosphere until further use. For the affinity binding measurements, a flow cell was clamped onto the surface of the MPG, and phosphate-buffered saline (137 mM NaCl, 2.7 mM KCl, 12 mM phosphate buffer, pH 7.4, no. E504) from VWR (USA) spiked with 0.05% Tween 20 BioXtra, from SigmaAldrich, (USA) (PBST) was flowed until a stable baseline of the sensor response λ_{cen} is reached. Then, the calibration was done using PBST spiked with sucrose at concentrations of 1, 2 and 4%. Afterwards, the surface was reacted with neutravidin (NA) from Thermo Scientific (Austria) and biotinylated monoclonal capture antibody cAB #13-7349-81 from eBioscience (Austria). This antibody is specific to human tumor necrosis alpha (TNF-α) BMS301 from eBioscience (Austria), and a sandwich immunoassay format was implemented by using a secondary monoclonal antibody sAB against another part of TNF-α #14-7348-81 from eBioscience (Austria).

3. Results and discussion

In order to resonantly excite PSP modes that are cross-coupled through a thin gold film, a relief profile of MPG with two superimposed periodic corrugations is investigated. As illustrated in Fig. 1(a), there is assumed the geometry where a collimated optical beam is travelling through a dielectric substrate (refractive index of glass n_i) and impinges on a corrugated thin gold film (refractive index n_m, thickness of d_m). A normally incident beam (θ=0) is coupled to the PSPs at the inner interface between the substrate n_i and gold n_m by the first-order diffraction on grating corrugation component with a period Λ_1. In general, this corrugation component also allows to couple the incident beam to PSP modes travelling along the outer interface between the gold film n_m and a lower refractive index dielectric (water with refractive index n_o). However, the coupling efficiency is negligible as the majority of the incident beam intensity is reflected at an

Research Article | Vol. 28, No. 26 / 21 December 2020 / Optics Express 39774
Optics EXPRESS

inner interface with the substrate n_i and does not reach the opposite interface in contact with the superstrate n_o.

To solve this problem, additional corrugation component with a shorter period Λ_2 was superimposed over the corrugation with the period Λ_1. As schematically indicated in the PSP dispersion relation folded to the first Brillouin zone in Fig. 1(b), the introduction of shorter Λ_2 can be utilized for its splitting at the outer and inner interfaces so new Bragg-scattered PSPs occur at distinct wavelengths (represented by frequencies ω_i and ω_o) with an optical bandgap in between. These Bragg-scattered modes are further noted as ω+ and ω- and they are associated with diffraction coupling of counter-propagating PSP modes on the corrugation component Λ_2 at individual interfaces generating standing wave-like modes [27]. In general, the spectral width of the optical bandgap in the dispersion relation of PSP modes at ω_i and ω_o can be tuned, so the short-wavelength Bragg-scattered PSP on the inner interface ω_i^+ overlaps with the long-wavelength Bragg-scattered PSP on the outer interface ω_o^-. Then, these modes become phase-matched along the surface and allow to transfer the electromagnetic field intensity through the metallic film via their penetrating evanescent field tails.

This concept was firstly analyzed by using numerical simulations. In this study, a thickness of the gold film of d_m=50 nm was assumed with conformally corrugated interfaces between the substrate with refractive index n_i=1.5 (BK7 glass) and superstrate with lower refractive index n_o=1 (air) and n_o~1.33 (water). There was used relief profile composed of sinusoidal corrugation with a longer period Λ_1=460 nm superimposed over additional sinusoidal corrugation exhibiting a shorter period Λ_2=242 nm. Firstly, we simulated zero-order reflectivity spectrum R_0 for the corrugation profile, in which the amplitude for the long period Λ_1 component was set to a_1=10 nm and the shorter period component Λ_2 was not present by assuming a_2=0 nm. Then, the first order excitation of the PSP mode at the inner interface occurs and manifests itself as a dip in the wavelength spectrum of R_0 centered at a wavelength λ_i=745 nm, Fig. 2(a). When increasing the refractive index of the dielectric at the outer interface from n_o=1.33 to 1.35, a negligible shift in the resonance wavelength $\delta\lambda_i$=0.7 nm occurs as the majority of the field intensity associated with this resonance is confined at the opposite inner interface with the glass substrate [see the profile of magnetic field amplitude in Fig. 2(c)].

When introducing the shorter period component Λ_2 forming the complete MPG structure with the amplitudes a_1=10 and a_2=10 nm, the resonance at λ_i splits and two overlapping dips occur at wavelengths of λ_{i1}=724 and λ_{i2}=744 nm. Interestingly, when increasing the refractive index at the outer interface from n_0=1.33 to 1.35, both resonances shift by about 6.5 nm and the coupling strength to shorter wavelength resonance λ_{i1} increases while that to λ_{i2} decreases, Fig. 2(b). The reason that the split resonance can be efficiently detuned by the refractive index change at the outer interface n_o is due to the fact that the associated field profile is confined at both interfaces as cross-coupling of PSPs through the metallic film occurs, Fig. 2(c). Notably, the coupling strength to the cross-coupled PSPs is decreased compared to the geometry when PSPs travelling on the individual interface are excited with the selected corrugation amplitude a_1. The coupling strength can be optimized by tuning this parameter as indicated by the following experimental study.

Experimentally, the MPG structure was prepared by sequential recording of the periodic interference field with periods Λ_1 and Λ_2 into a photoresist layer by using UV-LIL. The corrugation profile was then etched to the layer by a developer, and the tuning of modulation depths a_1 and a_2 was facilitated by controlling the irradiation time of each step and by the adjusting development time. Afterwards, the structure was cast to PDMS in order to serve as a working stamp, and multiple copies were prepared by transferring the corrugation to a UV-curable polymer Amonil followed by the coating with a gold film with a thickness of d_m=50 nm. The corrugation profile was observed by atomic force microscopy (AFM), as presented in Fig. 3(a). It shows a crossed structure where the MPG corrugation profile was recorded in both x and z directions and the fast Fourier transform analysis presented in Fig. 3(b) revealed the parameters of Λ_1=462.0 nm,

Research Article | Vol. 28, No. 26 / 21 December 2020 / Optics Express 39775
Optics EXPRESS

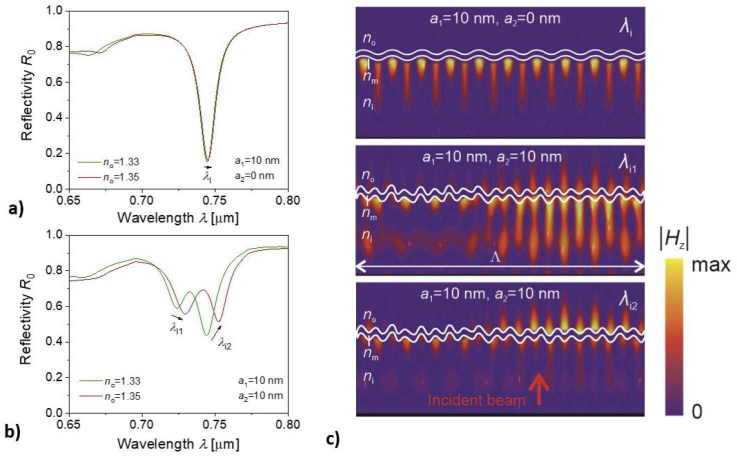

Fig. 2. Simulated reflectivity R_0 for transverse magnetically polarized normally impinging beam from a substrate at the structure with a) encoded single period (a_1=10 nm, a_1=0) and b) two periods (a_1=10 nm, a_1=10 nm). c) Near field distribution of magnetic field intensity $|H_z|$ in the xy plane at wavelength λ_i, λ_{i1} and λ_{i2}. The simulations were carried out for a super-period Λ=4.6 μm, longer period Λ_1=460 nm, shorter period Λ_2=242 nm, and n_o=1.33.

Λ_2=236.4 nm, a_1=13 nm and a_2=4 nm. It is worth of noting that the period Λ_1 was selected to slightly deviate from the $2\Lambda_2$ (as was originally studied on gratings with photonic bandgap [28]) in order to lift out the sensitivity on the mutual phase between these corrugations ϕ. The reason is that the used UV-LIL recording of the MPG structure does not allow for controlling this parameter and by introducing a small offset the phase dependence is averaged when irradiating surface with area at mm^2 scale.

The MPG structure on a glass substrate was used as a sensor chip, and its top outer surface was clamped against a flow-cell, see Fig. 3(c). Then, a polychromatic light beam was made reflected from the inner surface of the gold film on the sensor chip and its spectrum was analyzed by a spectrometer. As described further, there were observed changes in the specular reflectivity spectrum $R_0(\lambda)$ due to the variations of the refractive index of a liquid n_o flowed through the flow-cell as well as upon refractive index changes induced by molecular binding events. Reflectivity spectra $R_0(\lambda)$ were firstly measured for refractive index n_o=1 (air was present in the flow-cell) and n_o=1.33 (water was flowed through the flow-cell), Fig. 4(a). In contact with air, reflectivity spectra measured from the inner substrate side (BK7 glass) and the outer superstrate side (flow-cell) show resonances manifested as a dip in $R_0(\lambda)$. For the inner substrate side, the dip is centered at a wavelength close to 720 nm (red curve, ω_{i+}) which is spectrally separated from that observed from the superstrate outer side at 575 nm (blue curve, ω_{o-}). When increasing the outer refractive index to n_o=1.33, the reflectivity spectrum $R_0(\lambda)$ measured from the inner superstrate side (green curve) changes and exhibits two spectrally separated dips. These two dips are located at wavelengths of 650 nm (ω_{o+}) and 720 nm (ω_{o-}), and they can be interpreted as first-order diffraction coupling by the corrugation component Λ_1 to PSP modes that are Bragg-scattered on the outer interface by the corrugation component Λ_2. Importantly, the spectral position of the resonance ω_{o-} is coincident with ω_{o+} that is observed when probing from the inner substrate

Research Article | Vol. 28, No. 26 / 21 December 2020 / Optics Express 39776
Optics EXPRESS

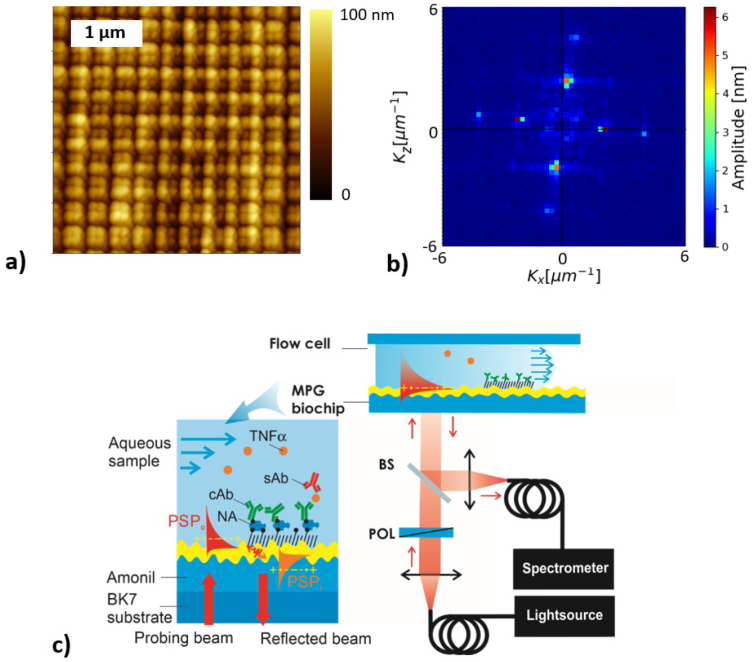

Fig. 3. a) AFM observation of the topography of the prepared MPG corrugation carrying the recorded corrugation with longer period Λ_1=462 nm, a_1=13 nm and shorter period Λ_2=236.4 nm, a_2=10.5 nm as determined by b) Fourier transform analysis. c) Schematics of the sensor chip with the MPG corrugation and the optical setup for the measurement of spectral reflectivity R_0 with beam splitter (BS) and polarizer (POL).

side. Therefore, the overlaid resonance shows a character of two superimposed Lorentzian dips. A similar profile is observed when the reflectivity $R_0(\lambda)$ is measured from the inner substrate side (black curve), which further confirms that a cross-coupling of PSP modes through the metallic film occurs as predicted by the simulations in Fig. 2(b). The small deviations in the measured resonance spectral position and the stronger coupling can be attributed to the effect of roughness of the gold film that was not taken into account in the mode, increased modulation amplitude a_1, and possible differences in the optical constants of used thin films.

In order to investigate this phenomenon in more detail, the bulk refractive index of the aqueous solution on the outer surface of the sensor chip was changed from n_o=1.33 to 1.38, and the reflectivity $R_0(\lambda)$ was measured from the inner substrate side. As Fig. 4(b) shows, the spectral shape of the resonance dip changes and the lower wavelength component (centered at λ_{i1}) red shifts and become more pronounced. The longer wavelength part (centered at λ_{i2}) also red shifts, but its coupling strength decreases when increasing n_o. This observation is in qualitative agreement with the simulations presented in Fig. 2(b) and confirms that the proposed concept allows for the cross-coupling of PSP modes through the metallic film and to optically monitor changes in the refractive index from the opposite side.

Research Article | Vol. 28, No. 26 / 21 December 2020 / Optics Express 39777
Optics EXPRESS

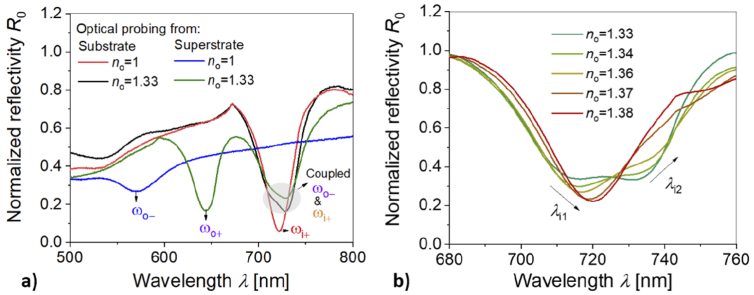

Fig. 4. a) Measured reflectivity R_0 with a beam normally incident at the sensor chip carrying MPG from its substrate (n_i) and superstrate (n_o) sides and air (n_o=1) and water (n_o=1) on the top. b) A detail of the reflectivity spectrum in the spectral region with cross-coupled surface plasmon resonance and refractive index on the top of the structure varied between n_o=1.33 and 1.38.

To implement the developed MPG structure for *in situ* realtime SPR measurements, the reflectivity spectra R_0 were acquired in time, and a centroid method was applied in the spectral region where the cross-coupled SPR dip occurs. This approach was chosen as the variation in the coupling strength to the two overlapped resonances λ_{i1} and λ_{i2} appears to be more pronounced than the spectral shifts $\delta\lambda_{i1}$ and $\delta\lambda_{i2}$. In general, the centroid wavelength λ_{cen} is blue-shifted when increasing the refractive index of the outer dielectric medium n_o, as illustrated in Fig. 5(a). This trend is opposite to classical SPR (where a red shift occurs) due to the observed coupling strength changes of respective dips at λ_{i1} and λ_{i2}. To test the performance of the approach, we tracked the centroid wavelength λ_{cen} in real-time upon changing the bulk refractive index n_o and upon the affinity binding of biomolecules on the gold MPG surface. Before this experiment, the MPG sensor chip was modified by a mixed thiol SAM with biotin head groups. Then the chip was loaded to the optical reader, and a baseline in the sensor signal λ_{cen} was established upon a flow of working buffer PBST, see Fig. 5(b). The centroid threshold parameter was optimized and the best signal-to-noise-ratio was obtained close to R_t=0.5, similar to the previous works where a shift in the SPR resonance dip was measured in reflectivity spectra [26]. Afterwards, the PBST solution was spiked with sucrose (1%, 2%, and 4%) and sequentially flowed over the surface to increase the bulk refractive index (δn_o=1.4 × 10^{-3}, 2.8 × 10^{-3}, 5.6 × 10^{-3} RIU, respectively). As can be seen in Fig. 5(b), the increase in refractive index n_o is accompanied by a stepwise decrease in the sensor signal $\lambda_{cen,}$ from which a sensitivity of S_b=$\delta\lambda_{cen}/\delta n_o$=−252 nm/RIU was determined. For the baseline noise quantified with a standard deviation of $\sigma(\lambda_{cen})$ = 3.75×10^{-3} nm, this sensitivity corresponds to the refractive index resolution of 1.5×10^{-5}. It is worthy of noting that such resolution is comparable to similar sensors with regular grating-coupled SPR (resolution of 6×10^{-6} RIU was reported [29]). The accuracy of the proposed approach is apparently hampered by the fact that the cross-coupled PSP modes travel on both interfaces, while the regular grating-coupled SPR allows for better field confinement by the excitation of PSPs only at individual (active) surface. This can be estimated to reduce the sensitivity (and respectively the refractive index resolution) by a factor of two. Additional parameter that can be used to further optimize the performance of the proposed concept is the thickness of the metal film d_m. In general, decreasing this parameter leads to increasing the coupling strength between the surface plasmon modes travelling along the outer (PSP_o) and inner (PSP_i) by stronger overlapping their field profiles. However, there will also occur an increase in radiative damping of PSP_o that is in general leaky mode into the substrate with higher index of refraction n_i. We assume that then the

Research Article | Vol. 28, No. 26 / 21 December 2020 / Optics Express 39778
Optics EXPRESS

spectral width of the coupled resonance will be broadened and the performance characteristics impeded. The chosen thickness of d_m=50 nm was selected as the radiative damping is still weak and it already allows to achieve the cross-coupling with the prepared MPG topography.

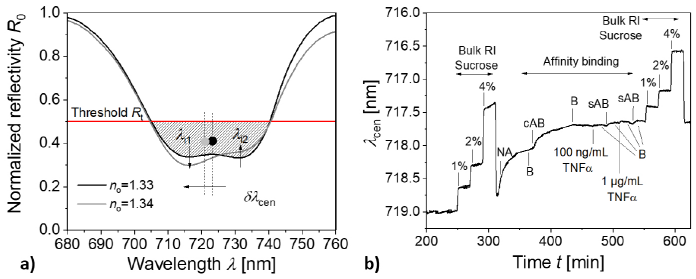

Fig. 5. a) Evaluation of the resonance variations due to refractive index changes by using the centroid method and b) example of the measured kinetics data for bulk refractive index changes δn_0 induced by a flow of buffer solution spiked with sucrose at 1%, 2% and 4% and for the affinity binding on the sensor surface. B indicates the rinsing with PBST.

Finally, the MPG sensor chip was used for the probing of affinity binding of biomolecules that constitute an assay for the detection of a protein biomarker TNF-α – human tumor necrosis factor alpha. Firstly, a solution with neutravidin – NA – dissolved in PBST at a concentration of 125 µg/mL was flowed through the sensor for 45 min. The respective SPR sensor signal presented in Fig. 5(b) shows a gradual decrease of λ_{cen} by 0.75 nm due to the affinity binding of NA to biotin groups carried by the thiol SAM on the gold MPG surface. Then, biotinylated capture antibody – cAB – that is specific to TNF-α was immobilized from PBST solution spiked at a concentration of 2 µg/mL that was flowed over the sensor surface for 45 min. Similar to the previous step, the affinity binding of cAB is manifested as a gradual decrease in λ_{cen}, which levels as a change of 0.30 nm. Afterwards, the sensor surface is used for the detection of TNF-α that was amplified by using a secondary antibody cAB that is also specific to TNF-α. The detection consisted of 15 min flow of TNF-α, 5 min rinsing with PBST, and additional 15 min binding of the sAB dissolved at 500 ng/mL in PBST. As seen in Fig. 5(b), a shift in λ_{cen} (0.028 nm) was measured for direct binding of the TNF-α at a concentration of 100 ng/mL, and an additional drop (0.04 nm) was observed after the sAB amplification. In the second step, the same assay was repeated for the TNF-α concentration increased to 1 µg/mL and the affinity binding resulted in a stronger response (0.036 nm and 0.059 nm, respectively). Let us note that these values are not directly proportional to the TNF-α concentration in a liquid sample as the sensor surface binding capacity probably reached its saturation. At the end of the experiment, the calibration was repeated by changing the bulk refractive index n_o with sucrose spiking of PBST, leading to similar shifts as at the start of the experiment.

4. Conclusions

The proposed concept of multi-period grating – MPG – was theoretically investigated and experimentally demonstrated to provide efficient means for the direct back-side excitation of propagating surface plasmons. Compared to alternative approaches based on long-range surface plasmons relying on low refractive index polymers and localized surface plasmons supported by arrays of metallic nanoparticles, the developed structures can be prepared without complex lithography steps and do not rely on expensive polymer materials. In conjunction with

Research Article | Vol. 28, No. 26 / 21 December 2020 / Optics Express 39779
Optics EXPRESS

advancements in the nanoimprint lithography that can be scaled up using roll-to-roll configuration, large areas carrying MPG structure can be prepared and exploited in various sensor modalities. The refractometric experiment and a model assay experiment confirm that the accuracy of the sensor configuration probed from the back-side sensor chip is similar to that measured for regular grating coupled SPR when the probing is performed through the analyzed liquid sample.

Funding

ESIF and MEYS (CZ.02.2.69/0.0/0.0/18_053/0016627); Lower Austria (WST3-F-5030820/010-2019); Österreichische Forschungsförderungsgesellschaft (861578).

Disclosures

The authors declare no conflicts of interest to this article.

References

1. J. Homola, "Surface plasmon resonance sensors for detection of chemical and biological species," Chem. Rev. **108**(2), 462–493 (2008).
2. M. F. Cardinal, E. V. Ende, R. A. Hackler, M. O. McAnally, P. C. Stair, G. C. Schatz, and R. P. Van Duyne, "Expanding applications of SERS through versatile nanomaterials engineering," Chem. Soc. Rev. **46**(13), 3886–3903 (2017).
3. M. Bauch, K. Toma, M. Toma, Q. Zhang, and J. Dostalek, "Plasmon-enhanced fluorescence biosensors: a review," Plasmonics **9**(4), 781–799 (2014).
4. D. Rodrigo, A. Tittl, N. Ait-Bouziad, A. John-Herpin, O. Limaj, C. Kelly, D. Yoo, N. J. Wittenberg, S. H. Oh, H. A. Lashuel, and H. Altug, "Resolving molecule-specific information in dynamic lipid membrane processes with multi-resonant infrared metasurfaces," Nat. Commun. **9**(1), 2160 (2018).
5. B. Liedberg, C. Nylander, and I. Lunström, "Surface plasmon resonance for gas detection and biosensing," Sens. Actuators **4**, 299–304 (1983).
6. J. Homola, J. Dostalek, S. F. Chen, A. Rasooly, S. Y. Jiang, and S. S. Yee, "Spectral surface plasmon resonance biosensor for detection of staphylococcal enterotoxin B in milk," Int. J. Food Microbiol. **75**(1-2), 61–69 (2002).
7. J. Dostalek, J. Homola, and M. Miler, "Rich information format surface plasmon resonance biosensor based on array of diffraction gratings," Sens. Actuators, B **107**(1), 154–161 (2005).
8. B. Spackova, P. Wrobel, M. Bockova, and J. Homola, "Optical Biosensors Based on Plasmonic Nanostructures: A Review," Proc. IEEE **104**(12), 2380–2408 (2016).
9. A. J. Haes and R. P. Van Duyne, "A nanoscale optical blosensor: Sensitivity and selectivity of an approach based on the localized surface plasmon resonance spectroscopy of triangular silver nanoparticles," J. Am. Chem. Soc. **124**(35), 10596–10604 (2002).
10. O. Kedem, A. Vaskevich, and I. Rubinstein, "Improved Sensitivity of Localized Surface Plasmon Resonance Transducers Using Reflection Measurements," J. Phys. Chem. Lett. **2**(10), 1223–1226 (2011).
11. J. A. Jackman, V. P. Zhdanov, and N. J. Cho, "Nanoplasmonic Biosensing for Soft Matter Adsorption: Kinetics of Lipid Vesicle Attachment and Shape Deformation," Langmuir **30**(31), 9494–9503 (2014).
12. J. Yamamichi, T. Ojima, M. Iida, K. Yurugi, T. Imamura, E. Ashihara, S. Kimura, and T. Maekawa, "Surface chemical approach to single-step measurement of antibody in human serum using localized surface plasmon resonance biosensor on microtiter plate system," Anal. Bioanal. Chem. **406**(18), 4527–4533 (2014).
13. M. Couture, K. K. Ray, H. P. Poirier-Richard, A. Crofton, and J. F. Masson, "96-Well Plasmonic Sensing with Nanohole Arrays," ACS Sens. **1**(3), 287–294 (2016).
14. D. M. Zhang, Y. L. Lu, Q. Zhang, Y. Yao, S. Li, H. L. Li, S. L. Zhuang, J. Jiang, G. L. Liu, and Q. J. Liu, "Nanoplasmonic monitoring of odorants binding to olfactory proteins from honeybee as biosensor for chemical detection," Sens. Actuators, B **221**, 341–349 (2015).
15. M. Vala, C. T. Ertsgaard, N. J. Wittenberg, and S. H. Oh, "Plasmonic Sensing on Symmetric Nanohole Arrays Supporting High-Q Hybrid Modes and Reflection Geometry," ACS Sens. **4**(12), 3265–3274 (2019).
16. D. Sarid, "Long range surface plasma waves on very thin metal films," Phys. Rev. Lett. **47**(26), 1927–1930 (1981).
17. N. C. Lindquist, T. W. Johnson, J. Jose, L. M. Otto, and S. H. Oh, "Ultrasmooth metallic films with buried nanostructures for backside reflection-mode plasmonic biosensing," Ann. Phys. **524**(11), 687–696 (2012).
18. M. Vala and J. Homola, "Multiple beam interference lithography: A tool for rapid fabrication of plasmonic arrays of arbitrary shaped nanomotifs," Opt. Express **24**(14), 15656–15665 (2016).
19. G. Barbillon, "Plasmonic Nanostructures Prepared by Soft UV Nanoimprint Lithography and Their Application in Biological Sensing," Micromachines **3**(1), 21–27 (2012).
20. N. G. Quilis, M. Leveque, I. Khan, W. Knoll, S. Boujday, M. Lamy de la Chapelle, and J. Dostalek, "Tunable laser interference lithography preparation of plasmonic nanoparticle arrays tailored for SERS," Nanscale **10**(21), 10268–10276 (2018).

Research Article | Vol. 28, No. 26 / 21 December 2020 / Optics Express 39780
Optics EXPRESS

21. H. Im, S. H. Lee, N. J. Wittenberg, T. W. Johnson, N. C. Lindquist, P. Nagpal, D. J. Norris, and S. H. Oh, "Template-Stripped Smooth Ag Nanohole Arrays with Silica Shells for Surface Plasmon Resonance Biosensing," ACS Nano **5**(8), 6244–6253 (2011).
22. N. Q. Quilis, M. van Dongen, P. Venugopalan, D. Kotlarek, C. Petri, A. M. Cencerrado, S. Stanescu, J. L. Toca Herrera, U. Jonas, M. Möller, A. Mourran, and J. Dostalek, "Actively tunable collective localized surface plasmons by responsive hydrogel membrane," Adv. Opt. Mater. **7**(15), 1900342 (2019).
23. I. Khan, H. Keshmiri, F. Kolb, T. Dimopoulos, and E. List-Kratochvil, "Plasmonic absorber based on multi-diffractive grating," Adv. Opt. Mater. **4**(3), 435–443 (2016).
24. S. Fossati, S. Hageneder, S. Menad, E. Mailart, and J. Dostalek, "Multiresonant plasmonic nanostructures for ultrasensitive fluorescence biosensing," Nanophotonics **9**(11), 3673–3685 (2020).
25. P. Adam, J. Dostalek, and J. Homola, "Multiple surface plasmon spectroscopy for study of biomolecular systems," Sens. Actuators, B **113**(2), 774–781 (2006).
26. G. G. Nenninger, M. Piliarik, and J. Homola, "Data analysis for optical sensors based on spectroscopy of surface plasmons," Meas. Sci. Technol. **13**(12), 2038–2046 (2002).
27. W. L. Barnes, T. W. Preist, S. C. Kitson, J. R. Sambles, N. K. Cotter, and D. J. Nash, "Photonic gaps in the dispersion of surface plasmons on gratings," Phys. Rev. B **51**(16), 11164–11167 (1995).
28. W. L. Barnes, T. W. Preist, S. C. Kitson, and J. R. Sambles, "Physical origin of photonic energy gaps in the propagation of surface plasmons on gratings," Phys. Rev. B **54**(9), 6227–6244 (1996).
29. D. Kotlarek, M. Vorobii, W. Ogieglo, W. Knoll, C. Rodriguez-Emmenegger, and J. Dostalek, "Compact Grating-Coupled Biosensor for the Analysis of Thrombin," ACS Sens. **4**(8), 2109–2116 (2019).

3.5 Multi-resonant plasmonic nanostructure for ultrasensitive fluorescence biosensing

Fossati, S., **Hageneder, S.,** Menad, S., Maillart, E., & Dostalek, J. Multiresonant plasmonic nanostructure for ultrasensitive fluorescence biosensing, 2020, Nanophotonics, 9(11), 3673-3685. https://doi.org/10.1515/nanoph-2020-0270

Co-authorship paper: I was responsible for the surface architecture, bioassay design and titration experiments, sensor chip fabrication and optimization, data analysis, discussion, and interpretation of the results, and was involved in manuscript writing. SF was responsible for the reader and chip concept, fabrication, and design, performed numerical simulations, and he wrote the manuscript. JD was supervising the project and responsible for the concept design, results discussion, and manuscript writing. SM and EM provided expertise in software development and were involved in discussion.

In the following chapter, multi-period plasmonic grating (MPG) structures were developed for PEF. The fluorescence enhancement factor achieved was of 300× compared to a flat dielectric surface, and ultrasensitive detection of an immunoassay with a LOD of six femtomolar (fM) was demonstrated. In addition, a new PEF reader modality was developed, which allows observation of real-time affinity binding as well as multiplexing through spatially resolved readout of multiple spots.

DE GRUYTER Nanophotonics 2020; ■■■(■■■): 20200270

Research article

Stefan Fossati, Simone Hageneder, Samia Menad, Emmanuel Maillart and Jakub Dostalek*

Multiresonant plasmonic nanostructure for ultrasensitive fluorescence biosensing

https://doi.org/10.1515/nanoph-2020-0270
Received May 6, 2020; accepted July 11, 2020

Abstract: A novel metallic nanostructure for efficient plasmon-enhanced fluorescence readout of biomolecular binding events on the surface of a solid sensor chip is reported. It is based on gold multiperiod plasmonic grating (MPG) that supports spectrally narrow plasmonic resonances centered at multiple distinct wavelengths. They originate from diffraction coupling to propagating surface plasmons (SPs) forming a delocalized plasmonic hotspot associated with enhanced electromagnetic field intensity and local density of optical states at its surface. The supported SP resonances are tailored to couple with the excitation and emission transitions of fluorophores that are conjugated with the biomolecules and serve as labels. By the simultaneous coupling at both excitation and emission wavelengths, detected fluorescence intensity is enhanced by the factor of 300 at the MPG surface, which when applied for the readout of fluorescence immunoassays translates to a limit of detection of 6 fM within detection time of 20 min. The proposed approach is attractive for parallel monitoring of kinetics of surface reactions in microarray format arranged on a macroscopic footprint. The readout by epi-fluorescence geometry (that inherently relies on low numerical aperture optics for the imaging of the arrays) can particularly take advantage of the reported MPG. In addition, the proposed MPG nanostructure can be prepared in scaled up means by UV-nanoimprint lithography for future practical applications.

Keywords: fluorescence; multidiffractive gratings; optical biosensor; plasmonics; ultrasensitive assays.

***Corresponding author: Jakub Dostalek**, Biosensor Technologies, Austrian Institute of Technology GmbH, Konrad-Lorenz-Straße 24, Tulln 3430, Austria; and FZU-Institute of Physics, Czech Academy of Sciences, Na Slovance 2, Prague 182 21, Czech Republic. E-mail: Jakub.Dostalek@ait.ac.at. https://orcid.org/0000-0002-0431-2170
Stefan Fossati and Simone Hageneder: Biosensor Technologies, Austrian Institute of Technology GmbH, Konrad-Lorenz-Straße 24, Tulln 3430, Austria, E-mail: Stefan.Fossati@ait.ac (S. Fossati), Simone.Hageneder@ait.ac.at (S. Hageneder). https://orcid.org/0000-0002-1109-0035 (S. Fossati)
Samia Menad and Emmanuel Maillart: Horiba France SAS, 14, Boulevard Thomas Gobert - Passage Jobin Yvon CS 45002, Palaiseau 91120, France, E-mail: samia.menad@gmail.com (S. Menad), emmanuel.maillart@horiba.com (E. Maillart)

1 Introduction

In a variety of optical biosensors, plasmonic nanomaterials become routinely employed for direct label-free analysis of biomolecules based on the measurement of specific binding-induced refractive index changes [1, 2]. In addition, we witness rapid progress in the implementation of plasmonic nanomaterials for the amplification of weak optical spectroscopy signal in other biosensor modalities relying on fluorescence, Raman scattering, and infrared absorption spectroscopy [3–5].

Plasmon-enhanced fluorescence (PEF) spectroscopy takes advantage of the increased intensity and local density of optical states accompanied with the resonant excitation of surface plasmons (SPs). These resonances originate from collective oscillations of electron density and associated electromagnetic field at the surface of metallic nanostructures. The coupling of SPs with fluorophores allows their lifetime, quantum yield, excitation rate, and far-field angular distribution of the emitted light to be effeciently manipulated [6–8]. These phenomena can be tailored to enhance the sensitivity of fluorescence-based assays where fluorophores are used as labels. Then, plasmonic nanostructures are deployed at the sensor surface to increase the signal-to-noise ratio of detected fluorescence signal that is attributed to the capture of the target analyte from the analyzed liquid sample. In general, detected fluorescence intensity can be enhanced by the combined coupling of SPs with fluorophores at their absorption λ_{ab} and emission λ_{em} wavelengths [9, 10]. This interaction can (i) increase the excitation rate at λ_{ab}, (ii) improve extraction yield of fluorescence light from the sensor surface by narrowing the angular emission range at λ_{em} towards the detector, and (iii) enhance quantum yield. The fact that the coupling with SPs occurs locally within their confined near-field allows only

the fluorescence signal emitted in the close proximity to the sensor surface without increasing the background signal originating from the bulk to be selectively amplified.

The coupling of SPs with fluorophores scales with their near-field intensity strength, which is limited by Ohmic losses causing damping. Metallic nanostructures supporting SPs with decreased damping can provide stronger near-field intensity enhancement, which manifests itself as a spectrally narrower surface plasmon resonance (SPR) [11–13]. However, if the spectral window where SPs are resonantly excited becomes narrower than the Stokes shift of the used fluorophores, the combined coupling at absorption λ_{ab} and emission λ_{em} bands is not possible, potentially leading to a decrease of fluorescence enhancement.

Metallic nanoparticles supporting localized surface plasmons (LSPs) typically exhibit spectrally broad resonances that can be tuned to spectrally overlap with both λ_{ab} and λ_{em} of commonly used organic fluorophores [14]. This, however, holds true only for isolated or randomly arranged metallic nanoparticles, where the excitation of LSPs with an optical wave traveling from the far-field is weakly angular dependent. Periodic arrangement of nanoparticles allows narrowing SPR spectral bands by diffraction coupling of LSPs on individual nanoparticles giving rise to delocalized lattice modes that exhibit sharp dispersive spectral features [11, 12, 15–17]. A wide range of such nanoparticle architectures has been developed to control fluorescence [18–21], allowing the detection of even single molecules [22]. These systems nevertheless are typically suitable for research, and their utilization to practical applications is hampered by the requirement of nanoscale control of emitter placement at the metallic nanoparticle and complex techniques needed for their manufacturing. Besides LSPs, propagating surface plasmon (PSP) modes can be excited on continuous metal films. They exhibit less confined near-field profile compared to LSPs and are dispersive over a broad spectral range. When interacting with fluorophores, the dispersive nature of PSPs can be even exploited to angularly separate emission from fluorophores exhibiting different λ_{em} to distinct angles in the far-field by using the SP-coupled emission [23]. On continuous metal films, periodic corrugation can provide additional momentum in order to diffraction phase-match optical waves propagating in the far field with PSPs. These Bloch-like modes are delocalized along the surface with angular dispersive and narrow spectral characteristics, allowing the excitation of fluorophores at a certain angle, facilitating emission via PSPs, and outcoupling to propagating modes at different angles [24–26]. In order to overlap narrow plasmon resonances with multiple spectral windows, metallic nanoparticle assemblies supporting hybrid SP modes can be used [27, 28]. They are formed by the coupling of multiple metallic nanostructures, and architectures supporting both LSP and PSP modes have been studied [29, 30]. These systems support multiple hybrid SP modes at distinct wavelengths; however, they typically confine electromagnetic near-field intensity at different locations on the structure and thus do not allow for the simultaneous probing of species placed in their proximity at respective spectral windows.

Plasmonic nanostructures can be prepared by a range of lithography techniques providing different level of control over their properties. While large areas of homogeneous flat metallic films are easily prepared by vapor deposition techniques [31], their optical properties are mostly determined by the choice of material. Metal island films, often created by vapor deposition [32], can support LSP modes with local hotspots exhibiting broad size distribution and lack of order. Colloidal lithography techniques allow the preparation of domains with ordered patterns of metallic nanostructures [33]. Electron beam lithography is often employed to create almost arbitrary morphology of metallic nanostructures with high precision [34]. However, it is still considered as complex and not well suited for cost-efficient large-scale production. Laser interference lithography (LIL), a method where interference pattern formed by overlapping coherent light beams is transferred to a photosensitive material, allows us to quickly and relatively inexpensively structure large areas with periodic corrugation such as holographic gratings, nanohole, or nanoparticle arrays [35, 36].

Nanoimprint lithography (NIL) represents another promising approach to address scalability in nanofabrication. Molds carrying a structure that can be prepared by more complex methods are then employed to repeated transfer of the target motives into an imprint resist [37]. The precise replication of patterns with feature size below 20 nm [38] paved the way towards the application in modern semiconductor manufacturing. In parallel, high-throughput NIL methods are developed to produce nanostructured surfaces, even on flexible substrates [39].

Herein, we report a new approach to plasmonic nanostructures supporting multiple tunable resonances with delocalized plasmonic hotspot along the surface and we tailor them for the simultaneous coupling with fluorophores at both their absorption and emission bands. It is based on multiperiod plasmonic gratings (MPGs) that are engineered to diffractively couple near-field SP field to far-field optical waves traveling at desired wavelengths and directions. The optical surfaces are prepared by UV-LIL that is combined with UV-NIL in order to open the door for potential scaled up preparation. The developed type of

MPGs is particularly beneficial for fluorescence biosensors with array detection format and *in situ* readout of reaction kinetics that relies on inherently low numerical aperture optics for the excitation and collecting of fluorescence light. We show that the developed structure offers strong enhancement of fluorescence signal by a factor of 300, enables the monitoring of affinity binding that is not masked by the bulk signal, and, when applied to an immunoassay, allows rapid detection of the target analyte at concentrations as low as 6 fM on multiple spots in microarray format.

2 Materials and methods

2.1 Materials

Microscope slides made of BK7 glass were purchased from Carl Roth (Germany) and used as substrates. The positive photoresist MICROPOSIT S1805 G2 and its developer AZ303 were bought from Microresist (Karlsruhe, Germany), and the nanoimprint resist Amonil MMS10 was acquired from Amo GmbH (Berlin, Germany). The silicone kit DOWSIL Sylgard 184 was purchased from Conrad GmbH (Wels, Austria). Dithiols with carboxylic head group (SPT-0014A6, COOH-OEG6-dithiol) and oligoethylene glycol head group (SPT-0013, OH-OEG3-dithiol) were from SensoPath Technologies (Bozeman, MT, USA). Antimouse IgG conjugated with Alexa Fluor 790 (AF790) came from Thermo Fisher Scientific-Life Technologies (Eugene, OR, USA). Phosphate buffered saline (PBS), 1-ethyl-3-(3-dimethylaminopropyl) carbodiimide (EDC), N-hydroxysuccinimide (NHS), ethanolamine, Tween 20, bovine serum albumin (BSA) and purified mouse IgG were acquired from Sigma–Aldrich Handels-GmbH (Vienna, Austria).

2.2 Preparation of MPG nanostructures

UV-LIL [40] was employed for the preparation of MPG nanostructures. Briefly, a laser beam with λ = 325 nm was collimated and expanded in order to perform the recording over an area of 1 cm^2 with homogenous intensity of about 15 $\mu W/cm^2$. A glass or Si wafer substrate coated with a 500-nm thick film of positive photoresist S1805 was mounted into a Lloyd's mirror configuration to record sinusoidally modulated field intensity formed by the interference of two parts of the beam – one directly impinging at the resist layer and that other reflected by a UV mirror (Figure S1A). The period of the modulation Λ was controlled by changing the angle of the interfering beams θ. Multiple subsequent exposures of different periods Λ were performed in order to yield the target structure. In this work, the exposure of the period of Λ_1 = 564 nm was followed by two additional orthogonal exposures carried out with an interference field period set to $\Lambda_2 = \Lambda_2$ = 583 nm. Between each recording step, the substrate with resist layer was rotated by an azimuthal angle φ along the axis perpendicular to its surface. Next, the structure was etched into the photoresist by a developer and its topography was cast to polydimethylsiloxane (PDMS), which was used as a working stamp for the preparation of multiple copies by UV-NIL (Figure S1B). The PDMS was cured at room temperature for 48 h. For a small reduction of the pattern period, it is possible to cure the stamp at an elevated temperature of 60 °C. The thermal shrinking of the cured working stamp after the cooling to room temperature reduces the pattern period Λ by about 1%. To prepare the plasmonic sensor chips by UV-NIL, glass slides were coated with a 130-nm layer of the nanoimprint resist Amonil MMS10, contacted with the working stamp, allowed to rest for 5 min, and were cured by UV cross-linker Bio-Link (Vilber Lourmat, Collégien, France) with 2 J cm^{-2} irradiation dose at 365 nm (Figure S1C). The PDMS stamp was finally demolded, and the corrugated glass substrates with casted MPG topography on their top were subsequently coated with 4-nm-thick Cr and 100-nm-thick Au layers by vacuum thermal evaporation instrument Auto306 from HHV Ltd (Crawley, UK).

2.3 Characterization of MPG nanostructures

The topography of MPG nanostructures was studied with atomic force microscope PicoPlus from Molecular Imaging (Arizona, USA). The spectrum of PSP modes that are optically excited on the gold-coated MPG structures was observed from reflectivity measurements with the structure clamped against a transparent flow cell that was flooded with water. The polychromatic light beam of a halogen lamp was collimated, polarized with a Glan polarizer, and made impinging at the MPG structure. For a beam incident normal to the surface, a beam splitter cube (CCM1-BS013 from Thorlabs, New Jersey, USA) was used to separate the incident and reflected beams. The reflected light beam was collected by an optical fiber and brought at the input of a spectrograph (Shamrock 303i from, Andor, New York, USA). As a reference, a flat gold-coated glass substrate was used.

2.4 Sensor chip and surface modification

Immediately after the deposition of thin metallic layers, the substrates were incubated in an ethanolic thiol solution of 0.1 mM COOH-OEG6-dithiol and 0.9 mM OEG3-dithiol overnight in order to form a self-assembled monolayer (SAM). After rinsing with ethanol and drying with a stream of compressed air, the prepared samples were stored in argon atmosphere at room temperature until further use to ensure their stability over weeks [41].

2.5 Optical reader

Readout of the binding of biomolecules labeled by a fluorophore on the sensor chip with MPG nanostructure and the investigation of the enhancement strength provided by this nanostructure were carried out using a setup with epi-illumination fluorescence geometry. It was designed to image an area of 4 × 4 mm on the sensor chip with MPG at a scientific EM-CCD camera (iXon 885K from Andor, Belfast, UK) by the optical system with a numerical aperture of NA = 0.2. A monochromatic beam emitted from diode laser iBeam Smart 785S with λ_{ex} = 785 nm from TOptica, Photonics AG (Gräfelfing, Germany) passed through a laser cleanup filter (BP λ_{ex}, LL01-785 from Semrock, Rochester, NY, USA) and a spatial filter consisting of a 60× microscope objective, a 40 µm pinhole, and recollimation lens (lens 1, AC-254-40-B from Thorlabs, Newton, NJ, USA). The central part of the expanded and collimated beam was polarized (POL,

LPVIS100 from Thorlabs, Newton, NJ, USA) and directed towards the sample by a dichroic mirror (DM) module. It comprised a DM (Di02-R785 from Semrock, Rotchester, NY, USA) oriented by 45° with respect to the axis of the module, and its central area with 2-mm projected diameter was coated with 100-nm-thick gold serving as a central mirror (CM). The excitation beam at the wavelength of λ_{ex} = 785 nm was focused at the CM by a lens (lens 2, AC-254-35-B from Thorlabs, Newton, NY, USA), and the reflected beam was recollimated with another lens (lens 3, AC-254-40-B from Thorlabs, Newton, NJ, USA). The collimated excitation beam was made normally incident at the sensor chip surface that carried MPG nanostructure. The distance between the DM module and the sensor chip was set to the focal distance of lens 3. In this configuration, the reflected excitation beam λ_{ex} was focused again at the CM and reflected away from the detector arm. Contrary to the excitation beam λ_{ex}, the fluorescence light emitted from the sensor chip surface at longer wavelength λ_{em} propagated at deviated angles and thus the majority of its intensity passed through the DM module towards the detector. The surface of the sensor chip was imaged at the detector plane by an imaging lens (lens 4, AC-254-80-B from Thorlabs, Newton, NJ, USA). In the detector arm, a notch filter (NF03-785E-25 from Semrock, Rotchester, NY, USA) and a fluorescence bandpass filter (FF01-810/10-25 from Semrock, Rotchester, NY, USA) were used to suppress the intensity of the excitation beam that leaked through the dichroic filter with the CM. Fluorescence images were acquired with a scientific EM-CCD camera operated at −70 °C and with EM gain set to 100. In-house-developed LabView software (LabView 2015, NI, Austin, TX, USA) was used to acquire image series and it comprised the data processing for determining the average signals on arrays of preselected spots and their progression over time.

2.6 Bioassay

For testing the analytical performance that is advanced by using sensor chips with the MPG nanostructure, a transparent flow cell was clamped on their top and the assembly was loaded to an optical fluorescence reader system. The flow cell consisted of a fused silica glass substrate with drilled input and output ports and a thin gasket cut from a 100-µm-thick PDMS sheet. The volume of the used flow chamber defined by the PDMS gasket was of several microliters, and aqueous samples were transported through the flow cell by using a peristaltic pump (from Isamtec, Switzerland).

The sensor chip carried a gold layer modified by a thiol SAM with carboxyl (COOH) and oligoethylene glycol (OEG) groups. In order to covalently couple protein ligands carrying amine groups, the COOH moieties on the thiol SAM were activated by a flow of an aqueous solution with 75 mg mL^{-1} EDC and 21 mg mL^{-1} NHS for 15 min. After rapid rinsing with acetate buffer of pH 4, mouse IgG dissolved (protein ligand) at a concentration of 50 µg mL^{-1} in acetate buffer was flowed through the sensor and allowed to react with the gold sensor chip surface for around 90 min. The unreacted COOH groups were passivated by a 1 M ethanolamine solution in H_2O, adjusted to pH 8.5. Immediately after the functionalization step, the sensor chip was used for the readout of model bioassay and liquid samples with increasing concentration of antimouse IgG conjugated with AF790 were sequentially flowed through the sensor (incubation time of 15 min for each concentration, followed by a rinsing step with buffer). All assay components were dissolved in PBS containing 0.05% Tween 20 and 1 mg mL^{-1} BSA.

2.7 Numerical simulations

The finite-difference time-domain method implemented in commercial software was employed from Lumerical Inc. (Canada). Optical near-field calculation of the electric field intensity distribution was performed at a wavelength that is coincident with the absorption band of the chosen emitter (λ = 785 nm). Fluorophore emission was studied by representing a fluorophore as an oscillating electric dipole. Both absorption $\vec{\mu}_{ab}$ and emission $\vec{\mu}_{em}$ dipoles were assumed randomly oriented, and the respective optical response was averaged over all their possible orientation and locations on the surface. A computation cell was defined with lateral dimensions of 20 × 20 µm along the structure surface and height of 8 µm was used. Perfectly matched layer boundary conditions were applied to all boundaries. Cartesian coordinates were used and the axes in the plane of the structure are noted perpendicular ($\perp$) and parallel ($\parallel$) and the axis perpendicular to the structure as z. The emitter was placed 15 nm above the gold corrugated surface in the z direction. The wavelength-dependent refractive index of gold n_m was modeled by fitting a Drude-Lorentz model to data from the CRC Handbook on Chemistry and Physics while the refractive index of water as bulk medium was assumed nondispersive with n_s = 1.332. To study the spectrum of supported plasmonic modes, the MPG structure was illuminated with a plane wave source from above the bulk dielectric with refractive index n_s. Monitor planes were used 300 nm below and 700 nm above the surface to record the electrical field and calculate transmission and reflectivity. Furthermore, far-field distribution of the fluorescence emission in epi-fluorescence configuration was calculated by applying a far-field transformation to the reflectivity monitor.

3 Theory and experiment

The concept of MPG was pursued for the enhancement of fluorescence signal by using corrugation of a thin metal film with several encoded superimposed periodic modulations. These modulation components enable the precise design of the spectrum of excited plasmonic modes with

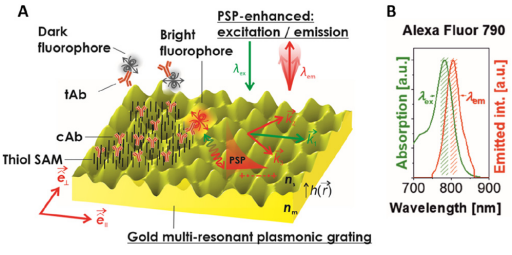

Figure 1: Concept of the MPG-based sensor readout.
(A) Schematics of the surface of multiresonant MPG structure that carries a biointerface on its top to affinity capture fluorophore-labeled biomolecules that are probed by surface plasmon modes at its excitation and emission wavelengths. (B) Example of the absorption and emission spectra for selected fluorophore Alexa Fluor 790.

respect to the characteristics of the used fluorophores. Further, the structure was tailored for the amplification of fluorescence assays that utilize a near-infrared (NIR) fluorophore Alexa Fluor 790 (AF790) as a label. The MPG, schematically shown in Figure 1A, was implemented with grating periods suitable to resonantly excite PSPs on its surface at wavelengths that coincide with the excitation wavelength λ_{ex} = 785 nm and emission wavelength λ_{em} = 810 nm of A790 (see respective absorption and emission peaks in Figure 1B). In the NIR wavelength range, the resonant excitation of PSPs at regular gold grating surfaces is manifested as a spectral dip in the reflectivity spectrum with a width of about $\Delta\lambda_{FWHM}$ = 15 nm, which is substantially narrower than the Stokes shift of available fluorophore labels (including that for the chosen AF790 with $\lambda_{em}-\lambda_{ab}$ = 23 nm). Therefore, the MPG was developed in order to support two distinct plasmonic resonances that provide enhanced intensity of PSP field at both excitation and emission wavelengths of AF790 in order to locally increase the excitation rate (at λ_{ex}) and take advantage of SP-mediated emission with diffractive outcoupling of fluorescence light trapped by PSPs (at λ_{em}) towards the detector. The importance of these contributions to amplify the measured fluorescence intensity is experimentally and theoretically demonstrated, and it is utilized for ultrasensitive fluorescence-based detection of biomolecules.

3.1 Topography of MPG structure

The MPG structure with three superimposed periodic corrugations was investigated and prepared by UV-LIL. A thin photoresist layer was sequentially exposed to series of sinusoidal patterns formed by two coherent interfering plane waves, and the final corrugation structure was yielded by its etching. The first recording of a shorter period Λ_1 = 563 nm was followed by two additional longer periods $\Lambda_2 = \Lambda_3$ = 586 nm that were rotated around the axis perpendicular to the surface by an azimuthal angle of φ = 45° and −45° (see Figure S1A). The superimposed interference field pattern is simulated in Figure 2A, and the respective etched corrugation profile can be described as the following height dependence:

$$h\left(\vec{r}\right) = \sum_{i=1}^{3} a_i \sin\left(\frac{2\pi}{\Lambda_i}\vec{k}_i \cdot \vec{r}\right), \tag{1}$$

where a_i is the amplitude, Λ_i is the period of corrugation components, $\vec{k}_i$ is the unit vector defining its orientation in the MPG plane (i = 1, 2, 3), and $\vec{r}$ is the distance in the plane of the structure. Multiple substrates with identical corrugation profile were prepared by UV-NIL and coated with a 100-nm-thick Au film by vacuum thermal evaporation (Figure S1C). Atomic force microscopy was used to determine the topography of the prepared MPG, and the maximum

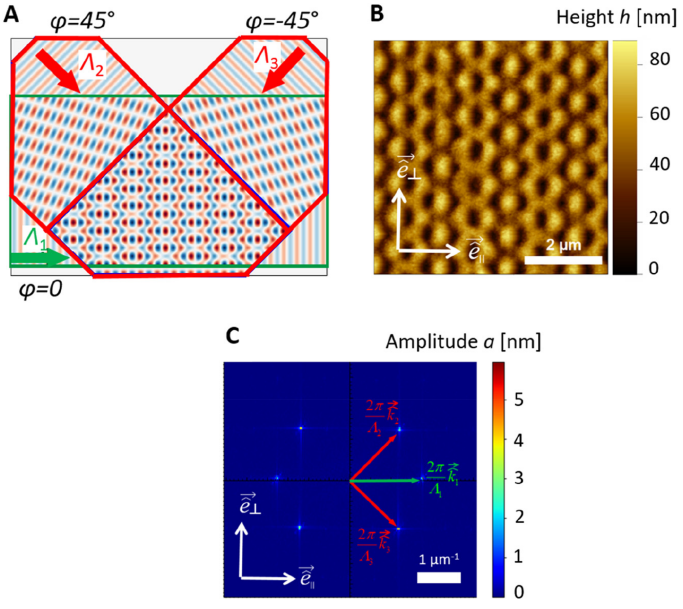

Figure 2: Designed MPG structure. (A) Orientation and periods of sequentially recorded overlaid sinusoidal corrugations by using UV-LIL method. (B) Measured topography of prepared MPG surface by AFM. (C) 2D FFT of the corrugation profile of the MPG structure. UV-LIL, UV-laser interference lithography; FFT, fast Fourier transform; AFM, atomic force microscopy.

corrugation depth of about 70 nm (difference in height of the topography) was observed, Figure 2B. The structure topography was further analyzed in more detail by 2D fast Fourier transform in order to reveal its periodic components. The obtained results are presented in Figure 2C, and they show clear peaks corresponding to recorded superimposed sinusoidal corrugations with periods Λ_1, Λ_2, and Λ_3. The dependence of the respective orientation of $\vec{\hat{k}}_i$ vectors agrees with the azimuthal angles φ used in the recording process. The modulation amplitude for each corrugation was determined to be around $a_1 = a_2 = a_3 = 8$ nm. This value is close to that used for the first order diffraction coupling to PSPs on the gold surface in the NIR part of the spectrum as shown before in literature [42].

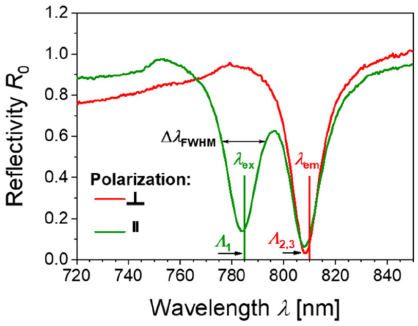

Figure 3: Plasmonic modes. Zero-order reflectivity spectrum measured for the normally incident beam at the MPG surface brought in contact with water (n_s = 1.332).

3.2 Diffraction coupling to SPs by MPG

Periodically corrugated metallic surfaces allow for the phase matching of optical waves propagating in the far field with the near-field PSPs traveling along these surfaces. In general, the investigated geometry of MPG with multiple harmonic components allows fulfilling the phase-matching condition via its individual spectral components or their combination. For shallow corrugations, the wavelength-dependent propagation constant of PSPs in transverse magnetic polarization can be approximated by that for plane metal surface:

$$\vec{k}_{SP} = \frac{2\pi}{\lambda} Re\left\{\sqrt{\frac{n_m^2 \cdot n_s^2}{n_m^2 + n_s^2}}\right\}\left[\vec{e}_{\perp}\sin(\varphi) + \vec{e}_{||}\cos(\varphi)\right], \quad (2)$$

where n_m and n_s are the refractive indices of the metal and the adjacent (water) dielectric, respectively, φ is azimuthal angle, and $e \rightarrow \perp$ and $e \rightarrow ||$ are the unit orthogonal vectors in the plane of the MPG. The momentum of the incident beam becomes phase matched with that of PSPs when the following condition holds:

$$\pm\vec{k}_{SP} = \frac{2\pi}{\lambda} n_s \cos(\theta)\left[\vec{e}_{\perp}\sin(\varphi) + \vec{e}_{||}\cos(\varphi)\right] + \sum_{i=1}^{3} m_i \frac{2\pi}{\Lambda_i}\vec{\hat{k}}_i, \quad (3)$$

where θ and φ are the polar and azimuthal angles, respectively, of a plane wave traveling in the dielectric with a refractive index n_s, Λ_i is the period of corrugation components, $\vec{\hat{k}}_i$ is unit vectors defining its orientation in the MPG plane (i = 1, 2, 3), and integers (m_1, m_2, m_3) refer to a diffraction order.

The prepared gold-coated MPG structure was brought in contact with water exhibiting n_s = 1.332, and the specular reflectivity spectrum R_0 was measured for the normally incident optical beam (θ = 0, φ is arbitrary). As seen in Figure 3, it exhibits two narrow dips centered at wavelengths of 784 and 817 nm and the coupling strength to shorter wavelength resonance can be controlled by the polarization of the incident optical beam. For the parallel polarization, the SPR at shorter wavelength is strongly pronounced, while when rotating the polarization to the perpendicular direction, it diminishes. The longer wavelength SPR dip is not sensitive to polarization changes. This behavior clearly relates to the fact that the short wavelength SPR originates from the diffraction on the corrugation component Λ_1 (which is recorded with only one azimuthal orientation) while the longer wavelength resonance is associated to the corrugation components Λ_2 and Λ_3 (forming a crossed grating with two identical orthogonal corrugations). The spectral position of shorter and longer wavelength resonances observed in the specular zero-order reflectivity spectrum (R_0) can be ascribed by using equation (3) to first-order diffraction coupling. The resonance at 785 nm is associated with the excitation of PSPs via the order (1,0,0) and the one at 810 nm to (0,1,0) and (0,0,1). Interestingly, the higher order coupling is not apparent in the visible-NIR spectral window of measured specular reflectivity R_0. It is worth of noting that the spectral position of short and long wavelength SPRs can be tuned by changing the respective periods Λ_1 and Λ_2/Λ_3 (see Figure S2A) and thus the reported MPG concept can be implemented for other emitters absorbing and emitting at different wavelengths λ_{ab} and λ_{em}, respectively. Moreover, the coupling strength of PSPs with optical wave that impinges from the far field depends on the modulation depth a_i and on the polarization of the incident field with respect to the grating vector as illustrated in Figure S2B.

3.3 Simulations of PEF on MPG

The MPG structure exhibits two distinct resonances that coincide with the absorption and emission wavelengths of the AF790 fluorophore λ_{ab} and λ_{em}, respectively. The coupling of this fluorophore with the enhanced intensity of electric field $|\vec{E}|^2$ of resonantly excited PSPs at these wavelengths was studied using numerical simulations. The fluorophore was represented as an infinitesimally small electric dipole placed at a distance of 15 nm from the gold surface, which was chosen with respect to a typical immunoassay experiment considering the size of immunoglobulin G antibodies (13.7 × 8 × 4 nm [43]) and the fact that it is above the distance where strong quenching occurs [44]. The fluorescence emission has dipole characteristics [45, 46], and it cannot be excited when the orientation of the electric field $\vec{E}$ is perpendicular to the emitter absorption dipole $\vec{\mu}_{ab}$. In the reported experiments, fluorophores were conjugated to proteins by flexible molecular linkers with high degree of rotational freedom, which leads to randomizing its orientation in the fluorescence lifetime and consequently to an isotropic emission profile. Therefore, all possible orientations of the fluorophore absorption $\vec{\mu}_{ab}$ and emission $\vec{\mu}_{em}$ dipole were accounted for and averaged with respect to PSP electric field $\vec{E}$.

The excitation rate of a fluorophore is a function of the scalar product of the local electric field $\vec{E}$ at λ_{ex} and absorption moment of the fluorophore $\vec{\mu}_{ab}$. Assuming the excitation rate is far below saturation, it can be expressed as $\propto|\vec{\mu}_{ab} \cdot \vec{E}|^2$ and thus being proportional to the electric field intensity enhancement $|\vec{E}/\vec{E}_0|^2$ accompanied with the resonant excitation of PSPs, which is strongest for the $\vec{E}$ component perpendicular to the surface. It reaches value $|\vec{E}|^2/|\vec{E}_0|^2 = 160$ (normalized with the intensity of the incident field intensity $|\vec{E}_0|^2$) for the resonant coupling of light to PSPs at λ_{ex} = 785 nm and the distance of 15 nm from the surface after the averaging along the structure corrugation (see Figure S3). This electric field intensity enhancement yields the mean amplification of the excitation rate of the emitter with randomly oriented absorption moment $\vec{\mu}_{ab}$ of 53, compared to an emitter in a homogeneous medium, which is similar to the excitation rate enhancement reported for excitation in attenuated total reflection (ATR) configuration with Kretschmann geometry [47].

After the PSP-enhanced excitation of the fluorophore at λ_{ex}, its emission can also be mediated by these modes at λ_{em} as is analyzed further. These modes are generated upon the emission process by the near-field coupling and travel along the MPG surface. They become subsequently diffraction outcoupled to far-field waves that propagate away from its surface in the perpendicular direction. The emission characteristics mediated by the coupling to PSPs were averaged over all lateral positions and orientations of emission moment $\vec{\mu}_{em}$ (assuming rapid rotation of fluorophore on the surface within the lifetime of its excited state). As shown in the simulated angular distribution of fluorescence intensity emitted to the far field above the MPG in Figure 4A, it exhibits a pattern with multiple narrow dispersive bands that are attributed to first-order diffraction on the corrugation components Λ_1, Λ_2, and Λ_3, with corresponding diffraction order of (±1,0,0), (0,±1,0), and (0,0,±1), respectively. Clearly, these bands converge at the center, which consequently increases the probability of fluorescence emission to waves traveling at small polar angle θ. Assuming a fluorescence collecting cone corresponding to a numerical aperture of 0.2, the MPG structure redirects the fluorescence light, so the detected intensity is enhanced by a factor of 8.2 with respect to a dipole in a homogeneous medium, where the emission is omnidirectional, and a factor of 6.2 compared to a dipole on a flat gold surface. MPG shows an additional 30% improvement compared to previous work utilizing a crossed grating

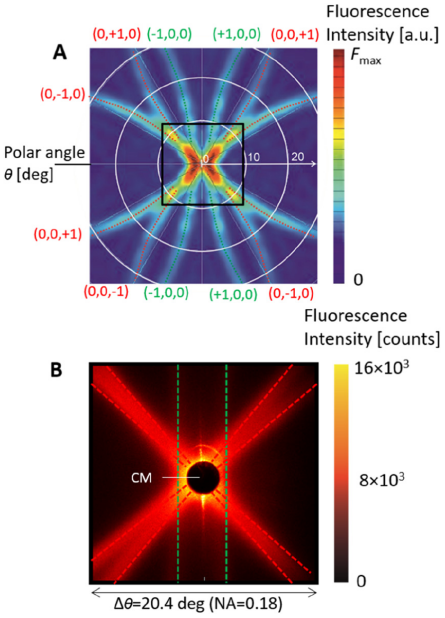

Figure 4: Surface plasmon-coupled emission at λ_{em}.
(A) Simulated and (B) measured angular distribution of fluorescence light emitted from MPG surface with indicated diffraction orders.

that was tuned to couple to plasmons at the excitation wavelength only [48].

3.4 Experimental observation of PEF on MPG

In order to measure the fluorescence signal amplified by the developed MPG nanostructure, its gold surface was modified with a mixed thiol SAM carrying OEG and COOH groups. The OEG thiol in the mixed thiol SAM was used to provide protection against unspecific binding of proteins present in analyzed liquid sample, and the smaller fraction of thiols carrying the COOH end group was employed for the post-modification of the sensor surface with functional groups.

Firstly, mouse IgG conjugated with AF790 was covalently bound to the COOH moieties on the surface by using the amine coupling, and the angular distribution of fluorescence light emitted from MPG was measured. This experiment was performed using an in-house-developed fluorescence reader configured to image the back focal plane of the objective lens placed before the sensor chip with MPG (lens 3 in Figure S4, back focal plane cuts the CM as indicated). The imaged angular distribution of emitted fluorescence light was measured by an EM-CCD detector in the range from $\theta = -10.2$ to 10.2°, Figure 4B. This image shows six dispersive bands originating from first-order outcoupling of PSP-mediated fluorescence emission at λ_{em} at angles that agree with the simulations presented in Figure 4A.

Then, the configuration of the optical system of the reader was changed to image the surface of MPG to the EM-CCD detector to allow fluorescence readout of bioassays on the sensor chip. These measurements were carried out to evaluate the impact of individual components of the investigated MPG nanostructure to the fluorescence enhancement. The imaged area on the sensor chip was prepared so six different zones were coated with the same gold film and carrying the same surface density of IgG conjugated with AF790, see Figure 5A and D. The first reference zone was flat, the second and third zones were corrugated with only one component Λ_2 and Λ_3, the fourth and fifth zones carried two superimposed components Λ_1, Λ_2 and Λ_1, Λ_3, and the sixth zone comprised all components Λ_1, Λ_2, Λ_3 forming the full MPG structure. The sensor chip with all six zones carrying IgG-AF790 conjugates on their top was illuminated with a collimated and linearly polarized beam at λ_{ex}, and the intensity of emitted fluorescence light at λ_{em} was collected and imaged to the EM-CCD detector. In order to distinguish between the impact of plasmonically enhanced excitation at λ_{ex} and plasmon-coupled emission at λ_{em}, the polarization of the excitation beam was rotated so the SPR at the excitation wavelength λ_{ex} was switched on and off (see Figure 3). The obtained fluorescence images are presented in Figure 5A–C. They show increased fluorescence signal in a circular illuminated area that is sliced to sections representing the six zones carrying different combinations of spatial components Λ_1, Λ_2, and Λ_3. The fluorescence intensity was averaged over the surface of each zone, and the value measured outside the illuminated area was subtracted in order to compensate for stray light and a dark signal of the EM-CCD detector. Then, the intensity from structured zones was normalized with that measured on a reference flat surface, and the obtained enhancement factors are summarized in the table included in Figure 5E.

For the perpendicular polarization of the excitation beam $\perp$ (which does not couple to surface PSPs at λ_{ex} via corrugation component Λ_1), the impact of MPG to the SP-coupled emission at λ_{em} was investigated. As Figure 5A shows, the presence of individual corrugations Λ_2 and Λ_3 provided the enhancement factor of collected fluorescence light intensity F of 3.7. On the zones when these components are overlaid with Λ_1, this factor increases to 17, and when all the components $\Lambda_{1,2,3}$ are present, it raises to about 25. Let us note that the latter two enhancement values are substantially higher than the value predicted by simulations for the outcoupling of the emission occurring via PSPs at λ_{em} (factor of 6.2). This observation can be attributed to partial miss alignment of the excitation beam polarization which leads to weak coupling to PSPs at the excitation wavelength λ_{ex}, which amends the excitation rate of the attached fluorophores. For the parallel polarization of the excitation beam ||, the enhancement by individual corrugations Λ_2 and Λ_3 provided the same enhancement factor of 3.7. On the zones where these components are superimposed with Λ_1, the enhancement factor of 248 was measured, which is about 67 times higher than on the surface without this component and which agrees well with the predicted contribution of the enhanced excitation rate at λ_{ex} of 53. On the zone where all components were present, additionally higher enhancement factor of 300 was determined with respect to the flat surface where both the excitation rate enhancement at λ_{ex} by Λ_1 and the improving of collection yield at λ_{em} by Λ_2 and Λ_3 are combined.

3.5 Readout of fluorescence immunoassay kinetics

The ability of the MPG nanostructure to enhance the performance characteristics of a fluorescence assay was

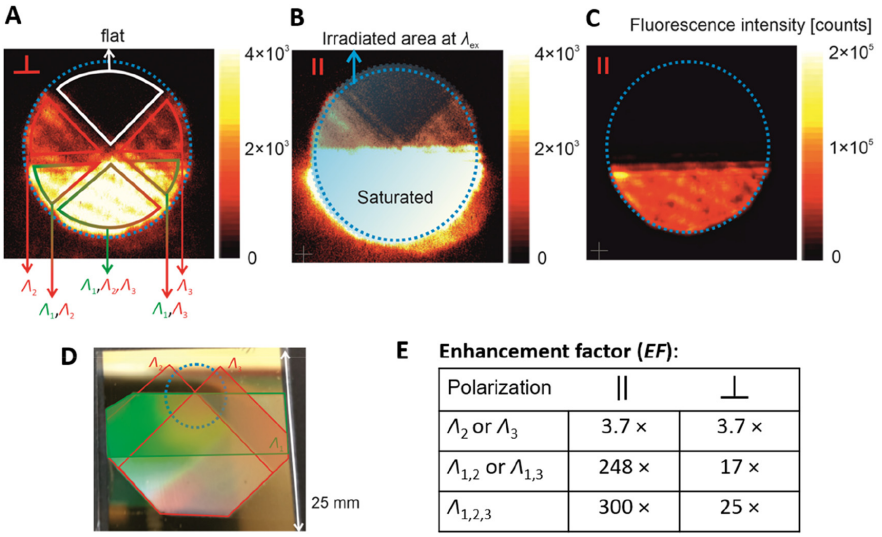

Polarization	∥	⊥
Λ_2 or Λ_3	3.7 ×	3.7 ×
$\Lambda_{1,2}$ or $\Lambda_{1,3}$	248 ×	17 ×
$\Lambda_{1,2,3}$	300 ×	25 ×

Figure 5: Experimentally determined fluorescence enhancement factors. Fluorescence images taken from an area, where different combinations of spatial MPG components are present. Polarization of the excitation beam was (A) orthogonal and (B,C) parallel to the grating Λ_1. (D) Photograph of the prepared MPG with highlighted areas carrying different spectral components of MPG and (E) comparison of the respective enhancement factors with respect to that measured for the flat surface.

demonstrated for a microarray detection format. In this experiment, there was used the optical reader schematically shown in Figure 6A and a sensor chip with MPG nanostructure was interfaced with a flow-cell as indicated in Figure 6B. In this sensor configuration, the fluorescence signal F was measured as a function of time t from 21 circular spots defined on the sensor chip surface (see Figure S5). Each spot exhibited 220-µm diameter, and spot numbers 5, 8, 6, 9, 12, 10, 13, and 16 were defined on the sensor chip area in the flow cell chamber with the full MPG nanostructure coated with gold film. In addition, reference spots 1, 2, 3, 4, 7, 13, and 21 were placed outside the flow cell chamber, and reference spots 11, 15, 20, 14, 17, and 18 were defined inside the flow cell on the area with a flat gold film not carrying the MPG. The gold surface on the MPG inside the flow cell was functionalized by using the same mixed thiol SAM and amine-coupling strategy by mouse IgG molecules that were not labeled by a fluorophore. These biomolecules served as a ligand and allowed for affinity capture of target analyte (antimouse IgG conjugated with AF790) from the aqueous sample transported along the sensor surface through the flow cell chamber.

Initially, buffer was flowed through the sensor for at least 10 min until a stable baseline in the sensor response F_b was established for all sensing spots 1–21. Afterward, a series of samples spiked with a target analyte (antimouse IgG conjugated with AF790) at concentrations between 10 fM and 10 nM was flowed over the sensor surface and its affinity binding at the array sensing spots was monitored through changes in the fluorescence signal F. The fluorescence signal deriving from each spot was averaged from the acquired images over its area and plotted by using in-house-developed LabView-based software. Variations in light source intensity were corrected by subtracting the signal of an illuminated reference spot outside the microfluidic channel from all other curves (spots 1, 2, 3, 4, 7, 13, and 21).

In a first step, the fluorescence signal was monitored for the affinity binding of high analyte concentrations (1 and 10 nM); therefore, the reader was configured for the monitoring of strong fluorescence intensities F (intensity of the excitation beam irradiating the sensor chip surface at λ_{ex} was 30 µW cm^{-2}, irradiation time of 0.3 s, with image accumulation of 10). Figure 7A compares the fluorescence signal kinetics $F(t)$ for two spots on the surface with gold MPG (red-colored curves) and two reference spots with flat gold surface (green-colored curves) where baseline signal F_b was subtracted from the acquired signal. Each sample was flowed over the surface for 20 min followed by 10 min rinsing. These data reveal the affinity binding manifests itself as a gradual increase in the fluorescence signal ΔF until saturation is reached, then upon the rinsing step a

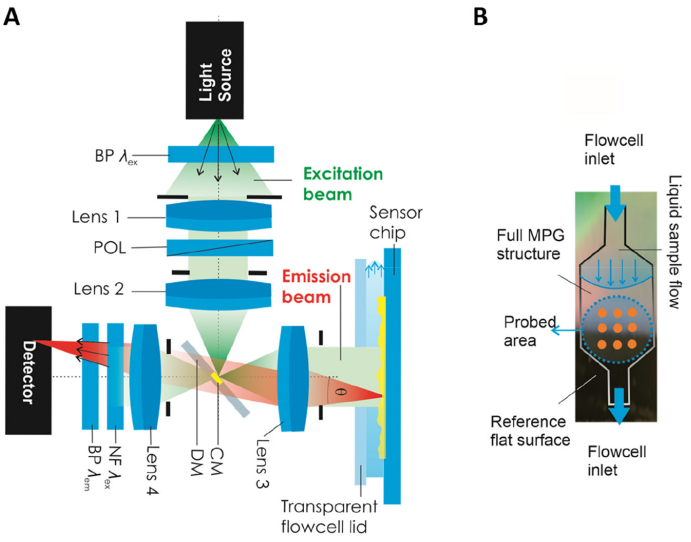

Figure 6: Optical biosensor reader. (A) Schematics of the optical configuration for the measurement of fluorescence signal kinetics from arrays of spots on the MPG sensor surface imaged to the detector. (B) Sensor chip with MPG structure that is interfaced with a flow cell and indication of the selected sensing spots. POL, polarizer; BP, bandpass filter; NF, notch filter; DM, dichroic mirror; CM, center mirror.

slow decrease in the fluorescence signal occurs due to dissociation of affinity bound molecules. The irradiation power at λ_{ex} was selected to prevent the fluorophore labels from bleaching within the reaction time. The sensor response ΔF to the analyzed sample was defined as a difference in the fluorescence signal between the original baseline and after the 5 min rinsing. The measured data show that the MPG structure enhanced the fluorescence sensor response by a factor of 292 with respect to the flat surface, which is consistent with previous observations performed without the kinetics readout (see Figure 5).

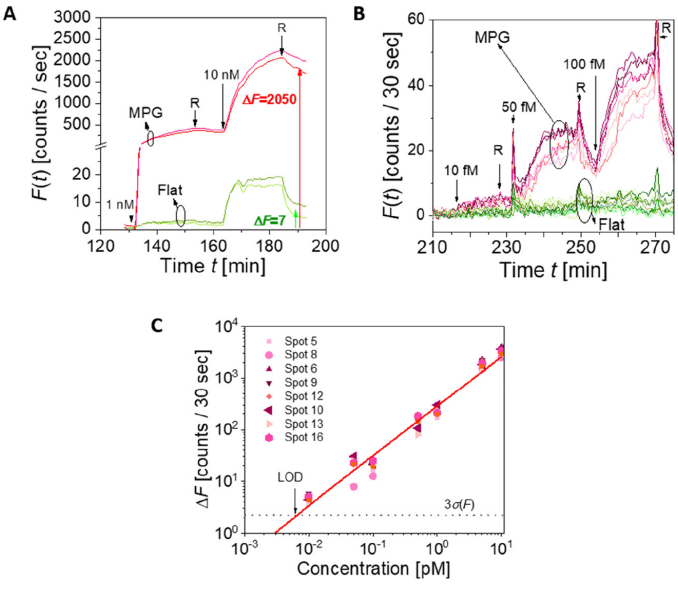

Figure 7: Biomolecular binding kinetics observed for a model IgG–anti-IgG on the MPG surface. The fluorescence reader was configured for detection of (A) high fluorescence intensities and (B) low fluorescence intensities for which the respective (C) calibration curve was established. The caption R states for the rinsing and red curves correspond to data measured on the MPG surface and green curves on the reference flat gold surface.

In a second step, the reader was configured for the monitoring of weak fluorescence signal in order to decrease the limit of detection (LOD) of the performed model assay (intensity of the excitation beam irradiating the sensor chip surface at λ_{ex} was raised to 265 μW cm^{-2}, irradiation time 30 s, without accumulation of images). In Figure 7B, the kinetic measurement of the fluorescence signal $F(t)$ for the target analyte concentrations of 10, 50, and 100 fM is shown. For the spots on the nonstructured reference area (green-colored curves), no measurable change in signal was observed, while on the area structured with gold MPG, a clear increase in $F(t)$ for all shown concentrations is detected. The kinetics of the reaction presented in Figure 7B is qualitatively different from that in Figure 7A. The fluorescence signal intensity $F(t)$ faster saturates at already low concentrations where only a small fraction of available binding sites is occupied by the target analyte conjugated with AF790 and it also faster decreases upon the rising step. These effects are caused by the more pronounced bleaching occurring due to the more intense irradiation power at λ_{ex}.

From the measured kinetic data, the calibration curve presented in Figure 7C was established and the respective LOD was determined. The fluorescence response ΔF on the MPG structure was plotted against the analyte concentrations of 10 fM, 50 fM, 100 fM, 0.5 pM, 1 pM, and 5 pM in log-log scale and fitted by a linear function with a slope S = 0.95 counts/30 s/fM. The LOD was determined from the intersection of the fitted calibration curve with three times the standard deviation of the fluorescence background $3\sigma(F)$, where $\sigma(F)$ = 0.75 counts/30 s. The achieved (average) LOD is 6 fM for the used measuring spot numbers 5, 8, 6, 9, 12, 10, 13, and 16. It should be noted that the imaged area of 4 × 4 mm can accommodate up to 270 of these spots, which can be used for parallel monitoring of biomolecular binding kinetics undisturbed by the background signal originating from the bulk, owing to the local enhancement of emitted fluorescence signal at the sensor chip surface.

4 Conclusions

A novel metallic nanostructure with a delocalized plasmonic hotspot and multiple SPR wavelengths is reported and its tailoring for PEF is discussed. It is based on a MPG that supports series of spectrally narrow (15 nm width) resonances associated with the diffraction coupling to PSP modes. These substrates were utilized for fluorescence immunoassay measurements, which show an enhancement factor of 300× on the MPG surface with respect to a nonstructured surface carrying the same biointerface architecture. This enhancement factor is about 2× as high as previously reported by our group for single period crossed grating tuned for the excitation enhancement only [48] and more than 5× higher than what has been reported for PEF with the ATR method and Kretschmann configuration [49]. In conjunction with a reader allowing spatially resolved monitoring of fluorescence intensity from multiple spots arranged in a footprint of 16 mm^2, there is demonstrated the possibility of highly parallelized measurement of affinity binding kinetics that is not masked by the background single originating from the bulk and with high sensitivity enabling reaching the LOD of 6 fM. The reported LOD is about 66× improved compared to similar assays reported by our previous work on single period crossed gratings and ATR-based PEF [49]. By changing the periods of the superimposed periodic structures, the proposed MPG concept can be utilized for arbitrary emitters in the red and infrared part of the spectrum (for a gold surface) or at shorter wavelengths (for silver or aluminum) covering a wide range of available fluorophore labels. In addition, the ability to translate the MPG preparation process to mass production compatible technologies such as UV-NIL in roll-to-roll format in conjunction with deploying of novel antifouling biointerface architectures [50] may open a pathway for future industrial applications (including analysis of trace amounts of diseases biomarkers in bodily fluids, which is a topic for the follow-up work).

Abbreviations

AF790	Alexa Fluor 790 fluorescent dye
CM	Central mirror
DM	Dichroic mirror
EBL	Electron beam lithography
LIL	Laser interference lithography
LSP	Localized surface plasmon
MPG	Multi-period plasmonic grating
NA	Numerical aperture
PEF	Plasmon-enhanced fluorescence
PSP	Propagating surface plasmon
SAM	Self-assembled monolayer
SP	Surface plasmon
SPR	Surface plasmon resonance
UV-NIL	UV-nanoimprint lithography
UV-LIL	UV-laser interference lithography

Author contribution: All the authors have accepted responsibility for the entire content of this submitted manuscript and approved submission.

Research funding: S.F., S.H., S.M. E.M., and J.D. received support from the European Union's Horizon 2020 research and the innovation program under Grant agreement no.

633937, project ULTRAPLACAD. In addition, S.H., S.F., and J.D. were partially supported by the Austrian Research Promotion Agency (FFG) with Grant agreement no. 861578 (ERANET project PLABAN), and J.D. acknowledges support from the ESIF and MEYS (Project 'FZU researchers, technical and administrative staff mobility' – CZ.02.2.69/ 0.0/ 0.0/18_053/0016627).

Conflict of interest statement: The authors declare no conflicts of interest regarding this article.

References

[1] B. Liedberg, C. Nylander, and I. Lunström, "Surface plasmon resonance for gas detection and biosensing," *Sens. Actuators*, vol. 4, pp. 299–304, Jan. 1983.

[2] J. Homola, *Surface Plasmon Resonance Based Sensors*, 2006.

[3] M. F. Cardinal, E. Vander Ende, R. Hackler, et al., "Expanding applications of SERS through versatile nanomaterials engineering," *Chem. Soc. Rev.*, vol. 46, no. 13, pp. 3886–3903, 2017.

[4] Y. Jeong, Y. M. Kook, K. Lee, and W. G. Koh, "Metal enhanced fluorescence (MEF) for biosensors: general approaches and a review of recent developments," *Biosens. Bioelectron.*, 2018. https://doi.org/10.1016/j.bios.2018.04.007.

[5] M. Li, S. K. Cushing, and N. Wu, "Plasmon-enhanced optical sensors: a review," *Analyst*, vol. 140, no. 2, pp. 386–406, 2015.

[6] G. W. Ford and W. H. Weber, "Electromagnetic interactions of molecules with metal surfaces," *Phys. Rep.*, vol. 113, no. 4, pp. 195–287, 1984.

[7] J. R. Lakowicz, K. Ray, M. Chowdhury, H. Szmacinski, Y. Fu, J. Zhang, and K. Nowaczyk, "Plasmon-controlled fluorescence: a new paradigm in fluorescence spectroscopy," *Analyst*, vol. 133, no. 10, pp. 1308–1346, 2008.

[8] E. Fort and S. Grésillon, "Surface enhanced fluorescence," *J. Phys. D Appl. Phys.*, vol. 41, no. 1, p. 013001, 2008.

[9] J. R. Lakowicz, K. Ray, M. Chowdhury et al., "Plasmon-controlled fluorescence: a new paradigm in fluorescence spectroscopy," *Analyst*, vol. 133, no. 10, pp. 1308–1346, 2008.

[10] F. D. Stefani, K. Vasilev, N. Bocchio, N. Stoyanova, and M. Kreiter, "Surface-plasmon-mediated single-molecule fluorescence through a thin metallic film," *Phys. Rev. Lett.*, vol. 94, no. 2, pp. 1–4, 2005.

[11] B. Auguié and W. L. Barnes, "Collective resonances in gold nanoparticle arrays," *Phys. Rev. Lett.*, vol. 101, no. 14, p. 143902, Sep. 2008.

[12] M. Bauch and J. Dostalek, "Collective localized surface plasmons for high performance fluorescence biosensing," *Opt. Express*, vol. 21, no. 17, p. 20470, Aug. 2013.

[13] E. Petryayeva and U. J. Krull, "Localized surface plasmon resonance: nanostructures, bioassays and biosensing-A review," *Anal. Chim. Acta*, vol. 706, no. 1, pp. 8–24, 2011.

[14] Y. Chen, K. Munechika, and D. S. Ginger, "Dependence of fluorescence intensity on the spectral overlap between fluorophores and plasmon resonant single silver nanoparticles," *Nano Lett.*, vol. 7, no. 3, pp. 690–696, Mar. 2007.

[15] G. Vecchi, V. Giannini, and J. Gómez Rivas, "Shaping the fluorescent emission by lattice resonances in plasmonic crystals of nanoantennas," *Phys. Rev. Lett.*, vol. 102, no. 14, Apr. 2009, https://doi.org/10.1103/physrevlett.102.146807.

[16] Y. Wang, L. Wu, T.I. Wong, et al., "Directional fluorescence emission co-enhanced by localized and propagating surface plasmons for biosensing," *Nanoscale*, vol. 8, no. 15, pp. 8008–8016, Apr. 2016.

[17] V. G. Kravets, A. V. Kabashin, W. L. Barnes, and A. N. Grigorenko, "Plasmonic surface lattice resonances: a review of properties and applications," *Chem. Rev.*, vol. 118, pp. 1–72, 2018.

[18] P. Biagioni, J.-S. Huang, and B. Hecht, "Nanoantennas for visible and infrared radiation," *Reports Prog. Phys.*, vol. 75, no. 2, p. 024402, Feb. 2012.

[19] A. Devilez, B. Stout, and N. Bonod, "Compact metallo-dielectric optical antenna for ultra directional and enhanced radiative emission," *ACS Nano*, vol. 4, no. 6, pp. 3390–3396, Jun. 2010.

[20] T. Coenen, E. J. R. Vesseur, A. Polman, and A. F. Koenderink, "Directional emission from plasmonic Yagi-Uda antennas probed by angle-resolved cathodoluminescence spectroscopy," *Nano Lett.*, vol. 11, no. 9, pp. 3779–3784, Sep. 2011.

[21] T. Kosako, Y. Kadoya, and H. F. Hofmann, "Directional control of light by a nano-optical Yagi-Uda antenna," *Nat. Photonics*, vol. 4, no. 5, pp. 312–315, May 2010.

[22] A. B. Taylor and P. Zijlstra, "Single-molecule plasmon sensing: current status and future prospects," *ACS Sensors*, vol. 2, no. 8. American Chemical Society, pp. 1103–1122, Aug. 2017.

[23] J. R. Lakowicz, J. Malicka, I. Gryczynski, and Z. Gryczynski, "Directional surface plasmon-coupled emission: a new method for high sensitivity detection," *Biochem. Biophys. Res. Commun.*, vol. 307, no. 3, pp. 435–439, 2003.

[24] I. I. Smolyaninov, Y. J. Hung, and C. C. Davis, "Fluorescence enhancement by surface gratings," *Opt. InfoBase Conf. Pap.*, vol. 14, no. 22, pp. 10825–10830, 2007.

[25] A. Nicol and W. Knoll, "Characteristics of fluorescence emission excited by grating-coupled surface plasmons," *Plasmonics*, vol. 13, no. 6, pp. 2337–2343, 2018.

[26] K. Tawa, H. Hori, K. Kintaka, K. Kiyosue, Y. Tatsu, and J. Nishii, "Optical microscopic observation of fluorescence enhanced by grating-coupled surface plasmon resonance," *Opt. Express*, vol. 16, no. 13, p. 9781, Jun. 2008.

[27] E. Prodan, "A hybridization model for the plasmon response of complex nanostructures," *Science (80-.)*, vol. 302, no. 5644, pp. 419–422, Oct. 2003.

[28] S. A. Safiabadi Tali and W. Zhou, "Multiresonant plasmonics with spatial mode overlap: overview and outlook," *Nanophotonics*, vol. 8, no. 7, pp. 1199–1225, Jul. 2019.

[29] J. Parsons, E. Hendry, C. P. Burrows, B. Auguié, J. R. Sambles, and W. L. Barnes, "Localized surface-plasmon resonances in periodic nondiffracting metallic nanoparticle and nanohole arrays," *Phys. Rev. B Condens. Matter Mater. Phys.*, vol. 79, no. 7, 2009, https://doi.org/10.1103/physrevb.79.073412.

[30] J. S. Pang, I. G. Theodorou, A. Centeno, et al., "Tunable three-dimensional plasmonic arrays for large near-infrared fluorescence enhancement," *ACS Appl. Mater. Interfaces*, vol. 11, no. 26, 23083–23092, Jul. 2019.

[31] K. M. McPeak, S. V. Jayanti, S. J. P. Kress, et al., "Plasmonic films can easily be better: rules and recipes," *ACS Photonics*, vol. 2, no. 3, pp. 326–333, 2015.

[32] R. Gupta, M. J. Dyer, and W. A. Weimer, "Preparation and characterization of surface plasmon resonance tunable gold and

silver films," *J. Appl. Phys.*, vol. 92, no. 9, pp. 5264–5271, Nov. 2002.
[33] B. Ai, Y. Yu, H. Möhwald, G. Zhang, and B. Yang, "Plasmonic films based on colloidal lithography," *Adv. Colloid Interface Sci.*, vol. 206. Elsevier B.V., pp. 5–16, 2014.
[34] T. H. P. Chang, M. Mankos, K. Y. Lee, and L. P. Muray, "Multiple electron-beam lithography," *Microelectron. Eng.*, vols. 57–58, pp. 117–135, Sep. 2001.
[35] C. Lu and R. H. Lipson, "Interference lithography: a powerful tool for fabricating periodic structures," *Laser Photonics Rev.*, vol. 4, no. 4, pp. 568–580, 2010.
[36] A. Rodriguez, A. Echeverría, M. Ellman, et al., "Laser interference lithography for nanoscale structuring of materials: from laboratory to industry," *Microelectron. Eng.*, vol. 86, nos. 4–6, pp. 937–940, Apr. 2009.
[37] H. Schift, "Nanoimprint lithography: an old story in modern times? A review," *J. Vac. Sci. Technol. B Microelectron. Nanom. Struct.*, vol. 26, no. 2, pp. 458–480, Mar. 2008.
[38] S. V. Sreenivasan, "Nanoimprint lithography steppers for volume fabrication of leading-edge semiconductor integrated circuits," *Microsyst. Nanoeng.*, vol. 3, no. 1, pp. 1–19, 2017.
[39] N. Kooy, K. Mohamed, L. T. Pin, and O. S. Guan, "A review of roll-to-roll nanoimprint lithography," *Nanoscale Res. Lett.*, vol. 9, no. 1, pp. 1–13, Jun. 2014.
[40] I. Khan, H. Keshmiri, F. Kolb, T. Dimopoulos, E. J. W. List-Kratochvil, and J. Dostalek, "Multidiffractive broadband plasmonic absorber," *Adv. Opt. Mater.*, vol. 4, no. 3, pp. 435–443, 2016.
[41] K. Jans, K. Bonroy, K. De Palmas, et al., "Stability of mixed PEO–thiol SAMs for biosensing applications," *Langmuir*, vol. 24, no. 8, pp. 3949–3954, 2008.
[42] P. Adam, J. Dostálek, and J. Homola, "Multiple surface plasmon spectroscopy for study of biomolecular systems," *Sens. Actuators B Chem.*, vol. 113, no. 2, pp. 774–781, Feb. 2006.
[43] Y. H. Tan, M. Liu, B. Nolting, J. G. Go, J. Gervay-Hague, and G. Liu, "A nanoengineering approach for investigation and regulation of protein immobilization," *ACS Nano*, vol. 2, no. 11, pp. 2374–2384, Nov. 2008.
[44] K. Sergelen, S. Fossati, A. Turupcu, et al., "Plasmon field-enhanced fluorescence energy transfer for hairpin aptamer assay readout," *ACS Sensors*, vol. 2, no. 7, pp. 916–923, 2017.
[45] F. Michelotti and E. Sepe, "Anisotropic fluorescence emission and photobleaching at the surface of one-dimensional photonic crystals sustaining Bloch surface waves. I. Theory," *J. Phys. Chem. C*, vol. 123, no. 34, pp. 21167–21175, Aug. 2019.
[46] E. Sepe, A. Sinibaldi, N. Danz, P. Munzert, and F. Michelotti, "Anisotropic fluorescence emission and photobleaching at the surface of one-dimensional photonic crystals sustaining Bloch surface waves. II. Experiments," *J. Phys. Chem. C*, vol. 123, no. 34, pp. 21176–21184, Aug. 2019.
[47] M. Bauch, K. Toma, M. Toma, Q. Zhang, and J. Dostalek, "Plasmon-enhanced fluorescence biosensors: a review," *Plasmonics*, vol. 9, no. 4, pp. 781–799, Aug. 2014.
[48] M. Bauch, S. Hageneder, and J. Dostalek, "Plasmonic amplification for bioassays with epi-fluorescence readout," *Opt. Express*, vol. 22, no. 26, p. 32026, 2014.
[49] S. Hageneder, M. Bauch, and J. Dostalek, "Plasmonically amplified bioassay - total internal reflection fluorescence vs. epifluorescence geometry," *Talanta*, vols. 156–157, pp. 225–231, Aug. 2016.
[50] D. Kotlarek, M. Vorobii, W. Ogieglo, W. Knoll, C. Rodriguez-Emmenegger, and J. Dostálek, "Compact grating-coupled biosensor for the analysis of thrombin," *ACS Sensors*, vol. 4, no. 8, pp. 2109–2116, 2019.

Supplementary material: The online version of this article offers supplementary material (https://doi.org/10.1556/nanoph-2020-0270).

Supporting Information

Stefan Fossati, Simone Hageneder, Samia Menad, Emmanuel Maillart, Jakub Dostalek*

Multi-resonant plasmonic nanostructure for ultrasensitive fluorescence biosensing

Fabrication process

The multi-period plasmonic grating – MPG – nanostructures were prepared using a series of nanolithography steps. UV-laser interference lithography – UV-LIL – was employed to generate a master structure in photoresist layer on the top of a glass substrate by using multiple exposures of an interference field followed by etching with a developer. Lloyd's mirror configuration was used as showed in Figure S1A to record an interference field formed by two overlapping plane waves. Precise control of the pattern period Λ is achieved by adjusting the angle θ while the modulation depth is adjusted by the exposure time and development parameters.

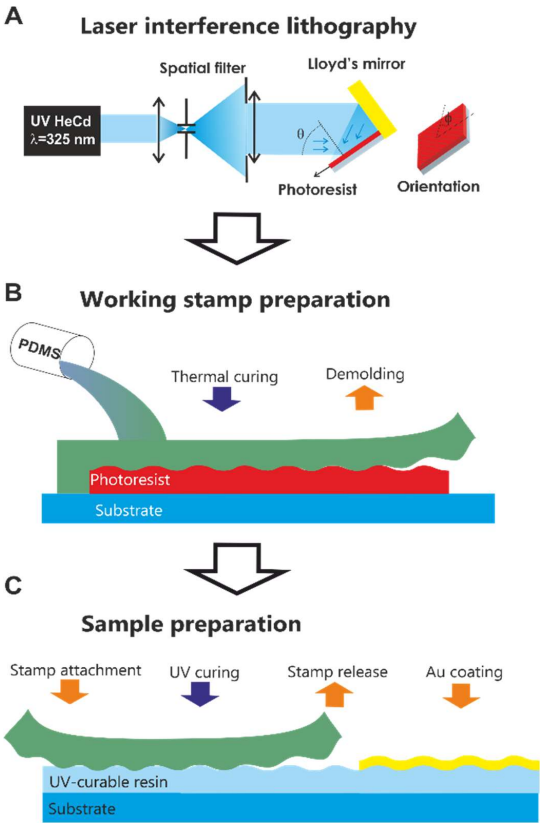

Figure. S1: A) UV–LIL setup in Lloyd's mirror configuration, where the photoresist layer (red) is exposed to the interference pattern formed by two overlaid parts of the expanded collimated UV laser beam. Between multiple exposures, the sample is rotated around its normal axis by an azimuthal angle ϕ. B) Working stamp preparation by casting the prepared MPG topography

to PDMS for C) UV-nanoimprint lithography replication, where the stamp is imprinted in thin layer of imprint resist, followed by curing with UV light before demolding of the PDMS working stamp.

Since preparation of higher numbers of MPG structures with identical parameters by using UV-LIL is impractical, UV-nanoimprint lithography – UV-NIL – was employed to replicate the master structure. First, a working stamp was prepared by casting the master structure to polydimethylsiloxane (PDMS) that was cured at controlled temperature (Figure S1B). After the curing, the stamp is demolded and used to replicate the pattern to nanoimprint resist (Amonil) on a glass substrate. Such copies with MPG topography were subsequently coated with a 100 nm gold film by vacuum thermal evaporation (Figure S1C).

Optical properties of grating coupled plasmon resonances

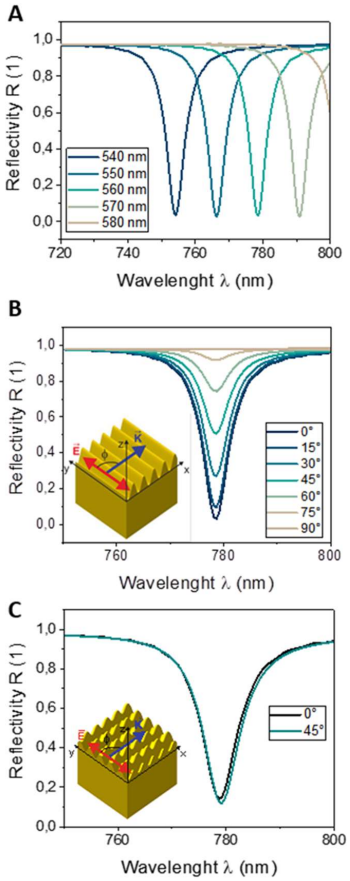

Figure S2: (A) Change of the spectral position of SPR with grating period for a single sinusoidal grating, 15 nm modulation depth, and gold – water interface. Coupling efficiency dependence on the polar angle φ between grating vector and electric field vector is shown for linear gratings in (B) and for crossed grating in (C).

Plasmon near-field intensity profile

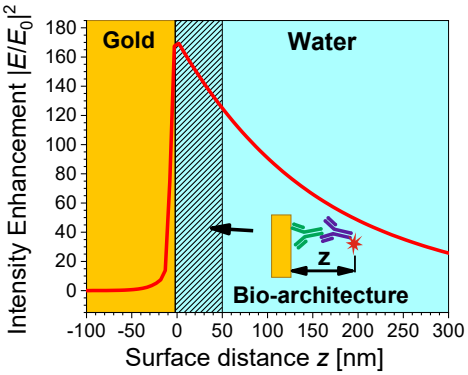

Figure. S3: Distance dependence of the local electrical field enhancement averaged over the MPG along the axis perpendicular to the surface.

Measurement of fluorescence angular distribution

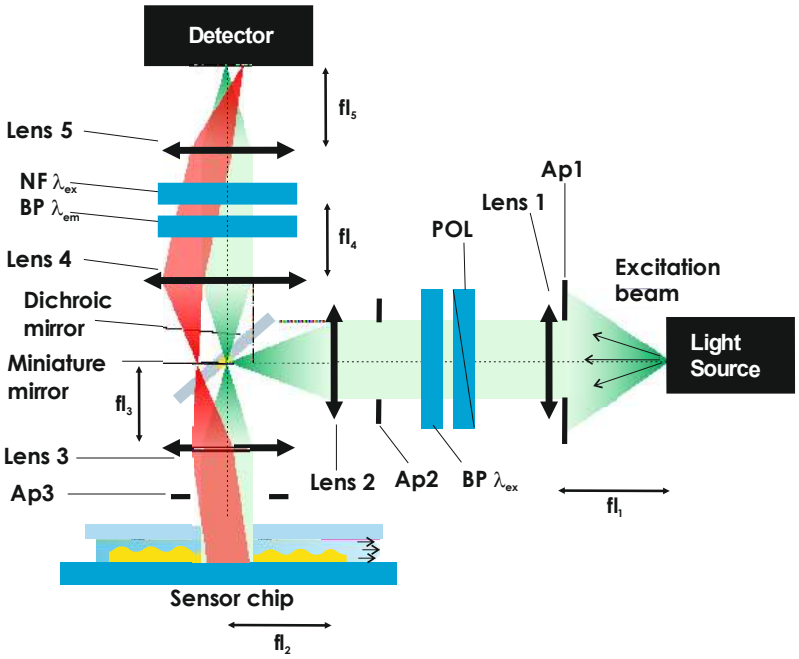

Figure. S4: The reader configured to image the back-focal plane of the objective lens, where the miniature mirror is located, by an additional lens (Lens 5).

Experimental observation of a fluorescence assay

A

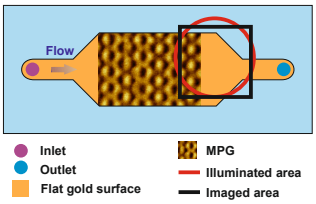

B

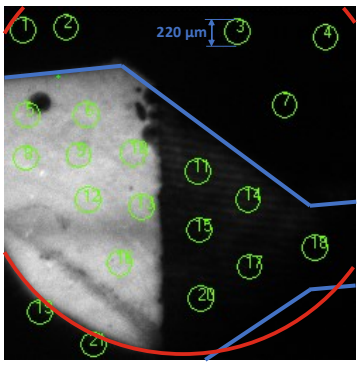

Class	Spots
Dark reference	19, 21
Illuminated but not functionalized	1, 2, 3, 4, 7
MPG functionalized	5, 6, 8, 9, 10, 12, 13, 16
Flat gold functionalized	11, 14, 15, 17, 18, 20

Figure. S5: A) A schematic of the sensor chip with part of its area structured with gold-coated MPG and part of its area carrying flat gold surface that is clamped against a microfluidic flow-cell. The illuminated area is indicated by a red circle, the imaged area by a black square. In B) a fluorescence image obtained during the measurement in Figure 7 b) after titration up to 50 pM target analyte concertation is shown. The microfluidic channel is indicated in blue, the illuminated area with a red circle and the spots averaged to calculate the fluorescence signal are indicated in green.

NIL reproducibility

Reproducibility of the UV-NIL process was tested on 5 samples prepared using a PDMS stamp. The spectra were acquired in air to prevent contamination, before the samples were chemically modified (therefore the spectral positions differ from those presented in Figure 3 measured in contact with water). The spectral position of the resonances deviate by less than 2 nm, significantly smaller value than the resonance width.

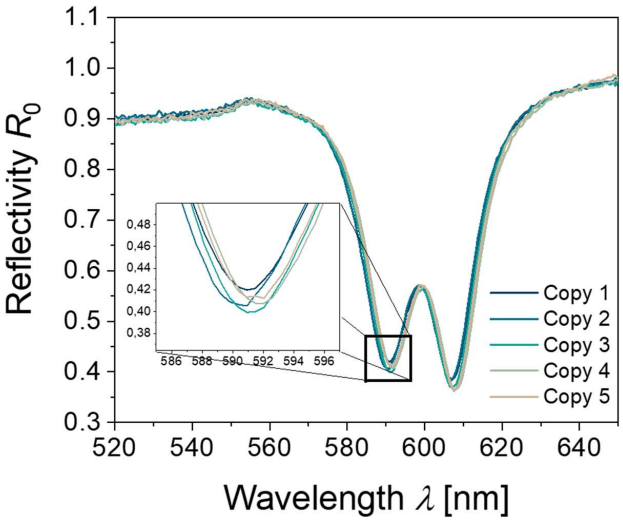

Figure S6: Reflectivity spectra acquired from 5 nanoimprinted samples from the same master structure

Collection efficiency enhancement

A key challenge in making sensitive fluorescence assays is the collection efficiency of emitted fluorescence light for practical optical systems. For a freely rotating fluorophore in homogeneous medium, the emission is assumed to be isotropic despite the orientation sensitive absorption characteristics of the electrical dipole model, due to the random change of orientation during fluorescence lifetime. For an optical system with a given numerical aperture $NA = n \sin\theta$ the collection only part of fluorescence light emitted to a cone with half angle θ can be collected. In the case of isotropic emission, the fraction can be determined analytically by calculating the ratio of the surface of the emission cone to the overall surface.

$$A_{collected} = \int_0^{\Theta} \int_0^{2\pi} sin\theta \, d\phi \, d\theta = 2\pi \, (1 - cos\Theta) \tag{1}$$

$$CE = \frac{A_{collected}}{A_{sphe}} = \frac{A_{collected}}{4\,\pi} = \frac{1}{2}(1 - cos\Theta) \tag{2}$$

For the MPG structure, collection efficiency was determined by calculating the farfield emission of a dipole in 15 nm distance from the surface. Four polar orientations of the dipole (0, 45°, 90°, 135°) with respect to the linear grating were considered. The emitted power to a cone of opening angle Θ perpendicular to the interface was computed by numerical integration. A similar calculation was performed for an emitter on a flat gold surface. In this work, an optical system with numerical aperture NA=0.2 was used to image a large sample area in a flow cell. Collection efficiencies for this system were calculated and are shown in Figure S7.

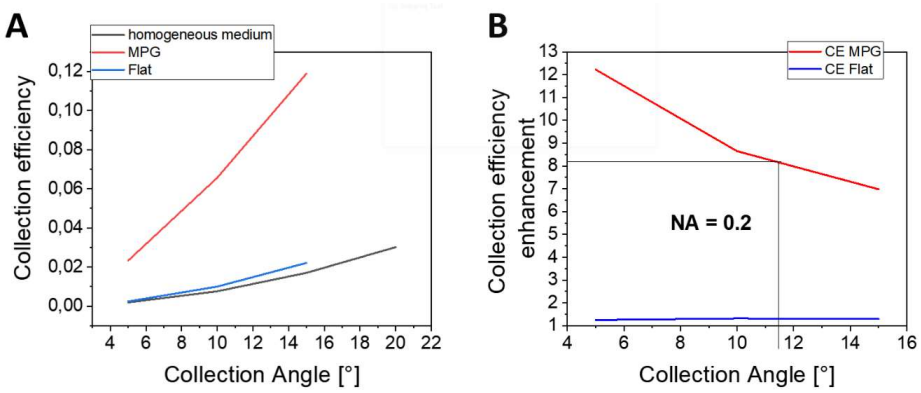

Figure S7: (A) Collection efficiency of an optical system with NA = 0.2 opt for an emitter located in a homogeneous medium (black), on a flat gold surface (blue) and on the MPG structure (red). (B) Enhancement of collection efficiency with respect to emitter in homogeneous medium for MPG and flat surfaces.

3.6 UV-Laser Interference Lithography for Local Functionalization of Plasmonic Nanostructures with Responsive Hydrogel

Quilis, N.G., **Hageneder, S.,** Fossati, S., Auer, S.K., Venugopalan, P., Bozdogan, A., Petri, C., Moreno-Cencerrado, A., Toca-Herrera, J.L., Jonas, U. and Dostalek, J. UV-Laser Interference Lithography for Local Functionalization of Plasmonic Nanostructures with Responsive Hydrogel, 2020, Journal of Physical Chemistry C, 124 (5) 3297-3305. https://doi.org/10.1021/acs.jpcc.9b11059

Co-authorship paper: I was responsible for bioassay design and experiments and was involved in data processing and manuscript drafting. NGQ was responsible for fabricating chips with laser interference lithography, discussion, graphs, and manuscript writing. SF and PV were responsible for simulations and involved in chip design. SKA and AB were conducting chip fabrication. AM-C and JLT-H were involved in AFM observation, CP and UJ were synthesizing and characterizing the responsive polymer, and UJ was involved in concept design. JD was supervising, responsible for the concept, involved in interpreting results and drafting the manuscript.

In this final publication, LSPR was combined with PEF sensing using the developed PEF sensor modality. Fluorescence emitters were placed at the areas of highest electromagnetic field confinement, close to the walls of prepared gold nanoparticle structures. This was done by selectively crosslinking a pNIPAAm bioarchitecture around the nanoparticle array structure and post-modifying the network with the BREs and the target analyte at exactly these areas and achieving a LOD of the immunoassay in the pM range. The analyte with the fluorescent label was compacted precisely in the areas with the highest electromagnetic (EM) field enhancement through the collapse after the assay by temperature increase above the lower critial solution temperature (LCST) of the responsive pNIPAAm polymer, leading to a fluorescent increase of 6 times.

THE JOURNAL OF PHYSICAL CHEMISTRY C

pubs.acs.org/JPCC Article

UV-Laser Interference Lithography for Local Functionalization of Plasmonic Nanostructures with Responsive Hydrogel

Nestor Gisbert Quilis, Simone Hageneder, Stefan Fossati, Simone K. Auer, Priyamvada Venugopalan, Anil Bozdogan, Christian Petri, Alberto Moreno-Cencerrado, Jose Luis Toca-Herrera, Ulrich Jonas, and Jakub Dostalek*

Cite This: https://dx.doi.org/10.1021/acs.jpcc.9b11059 Read Online

ACCESS | Metrics & More | Article Recommendations | Supporting Information

ABSTRACT: A novel approach to local functionalization of plasmonic hotspots at gold nanoparticles with biofunctional moieties is reported. It relies on photocrosslinking and attachment of a responsive hydrogel binding matrix by the use of a UV interference field. A thermoresponsive poly(*N*-isopropylacrylamide)-based (pNIPAAm) hydrogel with photocrosslinkable benzophenone groups and carboxylic groups for its postmodification was employed. UV-laser interference lithography with a phase mask configuration allowed for the generation of a high-contrast interference field that was used for the recording of periodic arrays of pNIPAAm-based hydrogel features with the size as small as 170 nm. These hydrogel arrays were overlaid and attached on the top of periodic arrays of gold nanoparticles, exhibiting a diameter of 130 nm and employed as a three-dimensional binding matrix in a plasmonic biosensor. Such a hybrid material was postmodified with ligand biomolecules and utilized for plasmon-enhanced fluorescence readout of an immunoassay. Additional enhancement of the fluorescence sensor signal by the collapse of the responsive hydrogel binding matrix that compacts the target analyte at the plasmonic hotspot is demonstrated.

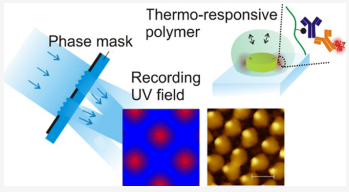

INTRODUCTION

A variety of naturally occurring or synthetic biopolymers has been tailored for specific biomedical[1] and analytical[2] applications, and among these, stimuli-responsive polymers represent particularly attractive "smart" materials capitalizing on their ability to undergo physical or chemical changes triggered by an external stimulus.[3−5] Such materials can be incorporated into architectures that are on-demand actuated by stimuli, including temperature, pH, or electric current.[6−8] A prominent example of a responsive polymer is the poly(*N*-isopropylacrylamide) (pNIPAAm), which is well-known for its thermoresponsive behavior. pNIPAAm exhibits a lower critical solution temperature (LCST) with pronounced and fully reversible hydrophobic-to-hydrophilic transition close to the body temperature.[9] pNIPAAm has been utilized in drug delivery micro/nanogels,[10] for modulating cellular interactions,[5,11] biosensors,[12] and in opto-responsive coatings.[13]

The nanoscale patterning of responsive polymer materials is important to let them serve in diverse areas ranging from sensing,[14] optical components,[15] and catalysis[16] to tissue engineering[17] and cell biology.[18] Self-assembly represents a widely used method for the preparation of nano- and microstructures based on, for instance, block-copolymer that combines hydrophobic and hydrophilic segments.[19,20] In addition, casting of microstructures by polymerization in template cavities has been utilized for the fabrication of miniature responsive polymer objects actuated in aqueous solution.[21] To prepare structures that are attached to a solid surface, photolithography has been extensively used for various types of responsive polymer structures.[22] Shadow mask photolithography-based methods typically enable facile means for the patterning of microstructures over macroscopic areas. To gain finer nanoscale control of the morphology of responsive polymer structures, electron beam lithography was employed for the structuring on a small footprint.[23,24] In addition, UV nanoimprint lithography has been introduced to harness both nanoscale precision and compatibility with scaled-up production.[25] This method is based on a transfer of a target motif carried by a stamp to a polymer layer by the subsequent polymerization[26] or photocrosslinking.[27]

Metallic nanostructures can be incorporated into responsive polymer architectures to provide means for their optical actuating[28,29] or to be employed for the optical readout in bioanalytical applications.[30] Metallic nanostructures support localized surface plasmons (LSPs) that tightly confine the electromagnetic field in their vicinity through its coupling with collective charge density oscillations. The resonant excitation of LSPs is accompanied by a strongly enhanced electromagnetic field intensity,[31] locally increased temperature[32] or, for instance, an emission of hot electrons.[33] In bioanalytical

Received: November 26, 2019
Revised: January 9, 2020
Published: January 10, 2020

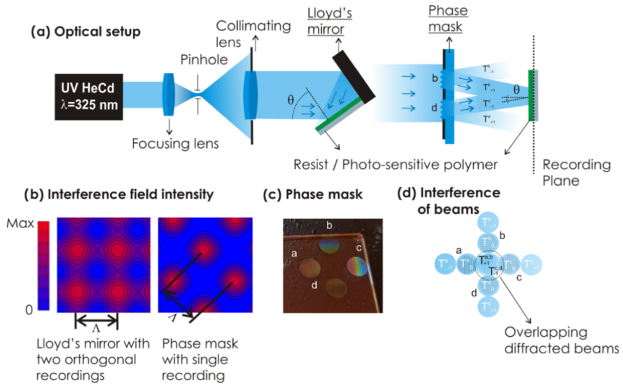

Figure 1. (a) Optical configuration of the UV-laser interference lithography with Lloyd's mirror configuration (left) and the phase mask configuration (right). (b) Simulations of the interference field generated by Lloyd's mirror configuration (left) and developed phase mask (right). (c) Schematics of the phase mask carrying four circular transmission gratings marked as a, b, c, and d. (d) Schematics of the overlapping of collimated waves at the recording plane with zero-order T_0 and first-order diffracted $T_{+/-1}$ beams.

sensing applications, the LSPs are utilized for the probing of target molecules that are brought in contact with the metallic nanoparticles. In affinity-based plasmonic biosensors, mostly thiol self-assembled monolayers are deployed at the two-dimensional (2D) surface of plasmonic nanoparticles for attaching of ligand molecules that specifically capture target molecules from the analyzed liquid sample.[34] In general, the sensitivity of LSP-based biosensors can be advanced by strategies that allow for selective capture of target analytes only at the regions where the electromagnetic field is confined (e.g., edges and walls of cylindrical gold nanoparticles), commonly referred as to "plasmonic hotspots". To deploy ligand molecules that specifically capture target species at the plasmonic hotspot, 2D surface architectures were combined with lithography-based strategies generating masks.[35,36] In addition, other strategies, including material-orthogonal chemistries,[37] surface plasmon-triggered polymerization,[38] and surface plasmon-enhanced two-photon cleavage of photosensitive organic moieties,[39] have been reported to attain local functionalization of metallic nanostructures.

The LSPs typically probe rather small subareas of the metallic nanoparticles, and their field reaches only a short distance of several tens of nanometers away from their surface.[40] Therefore, the performance of various LSP-based biosensor modalities is hindered by the reduced probability of analyte capture in these narrow spatial zones, where the electromagnetic field is confined. The use of biointerfaces composed of 3D polymer brushes or networks provides means to increase the surface area and respective binding capacity,[41,42] offering higher capture probability of the target analyte in the hotspot zones probed by LSPs. The present paper reports on the local attachment of a 3D hydrogel binding matrix in the vicinity of well-ordered gold nanoparticles, which can be postmodified for specific affinity capture of target analytes and actuated for their compacting at the plasmonic hotspot.

METHODS

Materials. OrmoPrime08, S1805 and SU-8 photoresist, SU-8 2000 thinner, and an AZ303 developer were purchased from Micro Resist Technology (Germany). Dimethyl sulfoxide (DMSO), acetic acid, propylene glycol monomethyl ether acetate, and 1-ethyl-3-(3-dimethylaminopropyl)carbodiimide (EDC) were obtained from Sigma Aldrich (Germany). pNIPAAm-based terpolymer composed of *N*-isopropylacrylamide, methacrylic acid, and 4-methacryloyloxybenzophenone (in a ratio of 94:5:1), benzophenone disulfide, and 4-sulfotetrafluorophenol (TFPS) were synthesized in our laboratory as previously reported.[43−45]

IgG from mouse serum (mIgG, I 5381), Tween 20 (P9416), and bovine serum albumin (A2153) were purchased from Sigma Aldrich (Austria). Phosphate-buffered saline (PBS) and sodium acetate were obtained from VWR Chemicals (Austria). Alexa Fluor 790 goat anti-mouse IgG (a-mIgG, A11375) was acquired from Life Technologies (Eugene, OR).

Optical Configuration of Laser Interference Lithography. A He-Cd laser (IK 3031 R-C) from Kimmon (Japan) emitting at λ = 325 nm with 4 mW was employed. The coherent beam was expanded with a spatial filter consisting of a pinhole (10 μm) and ×40 microscope lens. For Lloyd's mirror configuration, the expanded beam was collimated and impinged at a substrate carrying a photosensitive polymer and a UV-reflecting mirror with the area of several cm^2. The measured intensity of the beam in the recording plane was around 30 μW cm^{-2}. For recording with the phase mask configuration, the power of the recording field in the recording plane was increased to 400 μW cm^{-2}.

Preparation of a Phase Mask. OrmoPrime08 was employed as an adhesion promoter to prevent delamination of the resist. A Quartz substrate (20 × 20 × 1 mm) was dehydrated on a hot plate for 5 min at 200 °C, and the Ormoprime solution composed of organofunctional silanes was subsequently spun on the top at 4000 rpm for 60 s. Then, the substrate was placed on the hot plate for 5 min at 150 °C. Afterward, undiluted S1805 positive photoresist was deposited at a spin rate of 4500 rpm applied for 45 s followed by a hard-bake treatment at 100 °C for 2 min. The substrate with a photoresist was placed in Lloyd's mirror setup for recording by laser interference lithography as previously reported.[46] An interference pattern, originating from two interfering beams,

https://dx.doi.org/10.1021/acs.jpcc.9b11059
J. Phys. Chem. C XXXX, XXX, XXX−XXX

was recorded in the photoresist layer, and a stencil mask with two symmetric circular apertures was utilized to define the area to be exposed. Custom-made stainless stencil masks were fabricated from PIU-PRINTEX (Austria) and carefully placed on top of the photoresist-coated glass substrates. The irradiation dose of 18 mJ cm^{-2} was used for the recording of two circular gratings, and subsequently, the substrate was rotated 90° and exposed once more to the same interference field with the same dose. Finally, the phase mask carrying 4 transmission gratings with two perpendicular orientations was obtained by immersing the substrate in the AZ303 developer solution diluted with deionized water (1:15 ratio) for 40 s. The angle of the collimated interfering beams was set to $\theta = 13.6°$, yielding a period of the four gratings of $\Lambda_{PM} = 690$ nm. The circular patterned area of each of the four gratings exhibited a diameter of 4 mm (see Figure 1). The measured depth of the resist gratings was about 250 nm (see Figure S1). This depth was achieved by optimizing the developing time after the recording step, and it corresponds to that providing the maximum efficiency of the first-order diffraction in transmission mode (of about 30%, data not shown).

Preparation of Gold Nanoparticles. Gold nanoparticle arrays were prepared as previously reported by the use of two-beam laser interference lithography with Lloyd's configuration.[46] Briefly, 2 nm Cr and 50 nm Au were evaporated (HHV AUTO 306 from HHV Ltd) on top of BK7 glass slides with the size of 20 × 20 mm. Subsequently, a 100 nm thick layer of S1805 positive photoresist (diluted 1:2 with propylene glycol monomethyl ether acetate) was deposited at a spin rate of 4500 rpm applied for 45 s. Hard-baking of the resist was conducted at 100 °C for 2 min. The angle between the interfering beams was set to $\theta = 20.69°$ yielding a period of $\Lambda_G = 460$ nm, and the dose was set to 6.75 mJ cm^{-2}. The parameters were adjusted to obtain arrays of cylindrical resist features with a diameter of $D = 132 \pm 5$ nm after the development step using the AZ303 developer (1:15 ratio deionized water). The arrays of resist features were transferred to the underlying gold layer using a dry etching process consisting of the bombardment of the surface with argon ions (Roth & Rau IonSys 500). Resist-free gold nanoparticles were finally obtained by exposing the substrate to an oxygen plasma process.

Preparation of Hydrogel Nanostructures. Covalent attachment of the pNIPAAm-based polymer to a BK7 glass substrate was achieved using a thin SU-8 linker layer. SU-8 was dissolved with its thinner (2% solution) and spun onto the surface of the BK7 glass substrate at the spin rate of 5000 rpm for 60 s. Afterward, the coated substrate was thermally cured in an oven at 50 °C for 2 h. To attach the pNIPAAm-based polymer to gold nanoparticles, their gold surface was modified with UV-reactive benzophenone moieties by reacting overnight with 1 mM benzophenone disulfide dissolved in DMSO. Subsequently, a 2% pNIPAAm-based polymer dissolved in ethanol was spun (2000 rpm for 2 min) over the flat substrate (with SU-8 or with gold nanoparticle arrays carrying benzophenone disulfide), followed by its overnight drying in a vacuum oven ($T = 50$ °C). The pNIPAAm-coated substrate was placed in the laser interference lithography setup. The 4-beam phase mask with $\Lambda_{PM} = 690$ nm and the pNIPAAm-based polymer-coated substrate were made parallel to each other and separated by a distance of 5.6 mm by in-house made dedicated holders. The recording was carried out by four interfering beams transmitted through the phase mask (T_{-1} and T_{+1} transmission diffraction orders) with the middle part blocked to prevent the interference with a normally propagating beam (T_0). The irradiation dose was set between 84 and 240 mJ cm^{-2} for the SU-8 substrates by adjusting the irradiation time and by keeping the intensity of the UV beam fixed (400 μW cm^{-2}). Local crosslinking of the pNIPAAm-based polymer on top of gold nanoparticle arrays was attained by exposure to the UV interference field with a dose of 108 mJ cm^{-2} and the same UV beam intensity (400 μW cm^{-2}). The irradiation dose was obtained as a product of the power of the collimated UV beam and the irradiation time that was set between 210 and 600 s. The pNIPAAm-based polymer in the nonexposed regions was washed away with deionized water, and the obtained structure was dried on the hot plate at a temperature above the LCST of pNIPAAm. For the control experiment, a 30 nm thick pNIPAAm hydrogel layer was attached and crosslinked on a flat 100 nm Au film that was reacted with benzophenone disulfide using a UV lamp (365 nm) and an irradiation dose of 2 J cm^{-2}.

Morphological Characterization. Atomic force microscopy (AFM) measurements of the patterned structures in contact with air were performed in tapping mode with the PicoPlus instrument (Molecular Imaging, Agilent Technologies). The topography in contact with water was observed in situ with the Nanowizard III (JPK Instruments, Germany) using a temperature-controlled module consisting of a flow cell with a Peltier element. Silicon nitride cantilevers DNP-S10 (Bruker) with a nominal spring constant of 0.24 N m^{-1} were utilized. Height, diameter, and lateral spacing of the nanoscale features were determined by employing Gwyddion free software.

LSPR Transmission Measurements. The polychromatic light beam emitted from a halogen lamp (LSH102 LOT-Oriel, Germany) was coupled to a multimode optical fiber. This beam was out-coupled from the fiber, collimated with a lens, and made normally incident at a substrate carrying arrays of gold nanoparticles. The transmitted beam was collected by a lens to another multimode optical fiber and delivered to a Shamrock SR-303I-B spectrometer from Andor Technology (Ireland). The obtained transmission spectra were normalized with that obtained without the investigated substrate. A flow cell with a Peltier element[12] was clamped against the substrate with the gold nanoparticles to control the temperature of the liquid flowed over its surface. Deionized water was flowed through using a peristaltic pump from Ismatec (Switzerland).

Plasmon-Enhanced Fluorescence Instrument. Fluorescence experiments were conducted with an in-house-developed fluorescence reader utilizing epifluorescence geometry.[47] The biochip carrying arrays of gold nanoparticles wrapped by the pNIPAAm-based hydrogel was placed in a microfluidic module with a flow cell and illuminated with a collimated beam at a wavelength of 785 nm and an intensity of 1.2 mW cm^{-2}. The spatial distribution of intensity of fluorescence light emitted at a wavelength of 810 nm at the biochip surface was collected and then detected with a cooled CCD camera. The optical system can be seen in Figure S2. It consisted of a diode laser (IBeam Smart 785 nm, TOptica, DE) that emitted a collimated monochromatic beam, which passed through a narrow bandwidth laser clean-up filter (LL01-785, Semrock) and a spatial filter built from a 60× microscope objective, a 40 μm pinhole, and a collimating lens (AC-254-40-B, Thorlabs) to reduce the speckles. The excitation beam traveled through a lens (AC-254-35-B, Thorlabs) and was

https://dx.doi.org/10.1021/acs.jpcc.9b11059
J. Phys. Chem. C XXXX, XXX, XXX−XXX

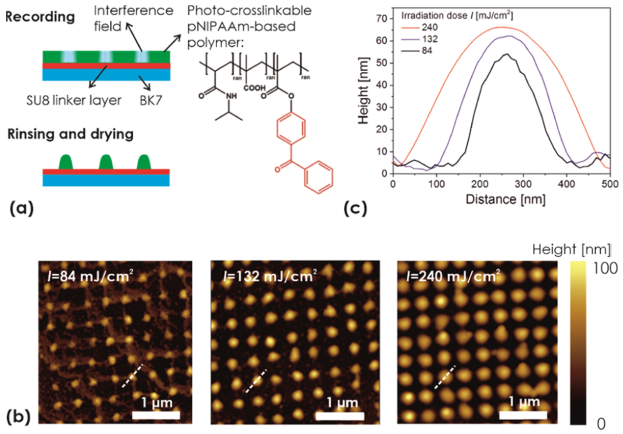

Figure 2. (a) Schematics of the local crosslinking of a responsive pNIPAAm-based polymer layer with arrays of interference maxima. The effect of the irradiation dose on (b) overall topography as observed with AFM and (c) the polymer feature cross-section.

reflected at a dichroic mirror (Di02-R785, Semrock) toward the biochip with arrays of gold nanoparticles. The incident excitation beam was then passed through another lens (AC-254-35-B, Thorlabs) to become recollimated before impinging on the biochip. The biochip was placed in the focal plane of the last lens in an in-house built microfluidic device. It was clamped against a flow cell that was temperature-controlled by the use of a Peltier device. Fluorescence light emitted at the biochip surface at a wavelength of 810 nm was collected by the same lens and passed through the dichroic mirror toward the detector. After passing an imaging lens (AC-254-80-B, Thorlabs), the remaining light at the excitation wavelength of 785 nm was blocked with a notch filter (NF03-785E-25, Semrock) and a fluorescence bandpass filter (FF01-810/10-25, Semrock) before hitting a scientific EM-CCD camera (Ixon 885K, Andor, UK). The camera was operated at a stable temperature of −70 °C, and 10 images for 1 s exposure time were accumulated for an increased dynamic range. The whole device was controlled, and the data were collected by the in-house developed dedicated LabView-based software. It was used for the acquisition of fluorescence intensity from arrays of circular spots (each spot exhibited a diameter of 220 μm). The acquired fluorescence intensity from each spot was averaged over its area from the raw image acquired by the optical system with an optical resolution limited to about 4 μm owing to the size of the CCD camera pixel of 8 μm and optical magnification of 2.

Immunoassay Experiment. COOH groups carried by the pNIPAAm-based polymer chains on the biochip surface were activated by reacting for 15 min with EDC and TFPS dissolved in water at a concentration of 75 and 21 mg/mL, respectively. A substrate with pNIPAAm-based polymer networks forming a hydrogel nanostructure overlaid with gold nanoparticle arrays or a thin hydrogel layer on the top of a flat gold film was then rinsed with deionized water, dried, and reacted with mIgG dissolved at a concentration of 50 μg/mL in acetate buffer (pH 4) for 90 min under shaking. Afterward, the surface was washed two times for 15 min with PBS working buffer, which contained 0.05% Tween 20 and 1 mg/mL BSA. Then, the substrate was rinsed, dried, and clamped into a flow cell to perform plasmon-enhanced fluorescence observation of affinity binding inside the pNIPAAm-based hydrogel matrix. The flow cell was connected to a peristaltic pump through a microfluidic tubing system with a total volume of ≈1 mL. After establishing a stable baseline in the fluorescence signal upon a flow of working buffer (PBS with Tween and BSA), changes in the fluorescence signal emitted from different spots on the biochip due to the affinity binding were measured using dedicated LabView-based software. A dilution series of a-mIgG (conjugated with Alexa Fluor 790) at concentrations of 1, 5, 10, 50, and 100 pM and a volume of 1 mL were flowed over the biochip surface for 15 min, followed by a 5 min rinsing with the working buffer in between.

■ RESULTS AND DISCUSSION

At first, the patterning of pNIPAAm-based nanostructures by UV-laser interference lithography (UV-LIL) with a phase mask configuration is described. This approach allows for generating a high-contrast UV interference field pattern that is used for nanoscale control of the attachment and crosslinking of a responsive pNIPAAm-based polymer. This strategy is then employed to overlay at the nanoscale pNIPAAm structure with periodic arrays of gold nanoparticles supporting LSPs. The LSPs supported by these nanoparticles are employed to observe swelling and collapsing of the pNIPAAm hydrogel, which caps the gold nanoparticle surface, by means of detuning the resonant wavelength at which the LSPs are optically excited. In addition, this wavelength is closely tuned to the absorption and emission wavelengths of a fluorophore that serves as a label in fluorescence immunoassays. Consequently, the pNIPAAm-based hydrogel is employed as a binding matrix that is postmodified with a protein ligand and utilized for surface plasmon-amplified fluorescence readout of the assay. Additional signal enhancement by the collapse of the gel is demonstrated using the developed hybrid plasmonic material.

UV-Laser Interference Lithography with a Phase Mask. As illustrated in Figure 1a, laser interference lithography relies on the recording of an interference pattern formed by overlapping coherent optical beams to a photosensitive polymer layer. In the UV-LIL configuration with Lloyd's

https://dx.doi.org/10.1021/acs.jpcc.9b11059
J. Phys. Chem. C XXXX, XXX, XXX−XXX

mirror shown in Figure 1b, a periodic sinusoidal pattern is recorded by two plane waves impinging on a layer of the photosensitive polymer at an angle θ. The recorded structure typically exhibits smoothly varying features[48] arranged in an array with a period equal to $\Lambda = \lambda/2\sin(\theta)$, where λ is the wavelength of the recording interference beam. To record a periodic pattern with higher contrast, we employed four interfering waves with a setup shown in Figure 1a, featuring a phase mask. This phase mask consists of four transmission gratings a, b, c, and d on a UV-transparent glass slide, as depicted in Figure 1c. The area between the gratings is made reflective; thus, only the coherent plane wave impinging on the grating regions of the mask is transmitted. Each grating diffracts the coherent incident beam to a series of transmission orders marked as T_{-1}, T_0, and T_{+1}, as shown in Figure 1d. These orders propagate to different directions, and the mask was designed so that four coherent diffractive beams T_{-1} and T_{+1} overlap in the central zone at a distance of 5.6 mm, forming an interference field as indicated in Figure 1c. This pattern exhibits arrays of more confined peaks in the harmonic spatial distribution of the interference field intensity when compared to that achieved by the conventional Lloyd's mirror configuration with two interfering beams, see Figure 1b. The intensity of the pattern generated by four interfering beams (phase mask configuration) drops to zero between the peaks, while that for the sequential orthogonal recording of two interfering beams (Lloyd's mirror configuration) does not. The period of the pattern generated by the four coherent interfering beams is $\Lambda = \Lambda_{PM}/\sqrt{2}$, where Λ_{PM} is the period of the transmission gratings on the phase mask. The full width of the half maximum (FWHM) of the peaks in this pattern is of $\Lambda/2$. To observe the interference pattern formed by the phase mask with a grating period of Λ_{PM} = 690 nm at a wavelength of λ = 325 nm, it was recorded to a layer of S1805 positive-tone photoresist with a thickness of 100 nm. After developing the recorded field distribution (an irradiation dose of 27 mJ cm^{-2}), atomic force microscopy (AFM) was employed for the observation of the structured resist topography. The obtained results presented in Figure S1 show a series of circular holes in the resist layer with a periodicity of $\Lambda = 490 \pm 4$ nm, which is in agreement with the simulated profile of the interference field distribution, as shown in Figure 1b.

Recording of pNIPAAm-Based Hydrogel Arrays. To prepare arrays of responsive pNIPAAm-based hydrogel features, the terpolymer shown in Figure 2a was used. This terpolymer carries pendant benzophenone groups for photocrosslinking and covalent attachment to a solid surface upon irradiation with UV light.[43] In addition, methacrylic acid was copolymerized, as the incorporated carboxyl groups promote swelling in water and provide a chemical postmodification site for the incorporation of biomolecules via amine coupling.[49]

The pNIPAAm-based polymer layer with a thickness of 70 nm was spun onto a glass substrate carrying a thin adhesion-promoting SU-8 film. After complete drying of the pNIPAAm polymer layer, the substrate was placed in the 4-beam UV-LIL optical system and exposed to the interference pattern generated by a phase mask to record a crosslinked structure with a period of Λ_H = 488 nm. Upon irradiation, the pNIPAAm-based polymer in the area of high UV intensities is crosslinked and attached to the substrate, while the unexposed areas remain unchanged. Therefore, after subsequent rinsing of the layer with ethanol and water, the crosslinked pNIPAAm network remains in the exposed zones and only noncrosslinked polymer is washed away in the area in between. After drying on a hot plate at temperature T = 100 °C, AFM images of the pNIPAAm surface topography were acquired. In Figure 2b, a periodic pattern of nonconnected domains of crosslinked pNIPAAm with a height similar to the initial thickness of the original polymer layer can be seen. When increasing the irradiation dose of the UV light from I = 84 to 132 and 240 mJ cm^{-2}, the pNIPAAm domains exhibit an increasing diameter (FWHM) of $D = 168 \pm 9$, 208 ± 8, and 293 ± 9 nm, respectively, which were determined from the cross-sections presented in Figure 2c. These values are around FWHM of the peaks in the interference field pattern of $\Lambda_H/2$ = 244 nm, and the changes in D reflect the nonlinear dependence of the crosslinking on the irradiation dose. In addition, the height of the structure between 50 and 65 nm determined from the cross-sections in Figure 2c are lower than the thickness of the original (noncrosslinked) pNIPAAm film, which can be ascribed to the effect of smearing of the recorded features after their swelling and drying before the AFM observation.

Interestingly, the topography of the pNIPAAm-based domains changes depending on the conditions in which they are dried prior to the AFM observation in air. As Figure 3 illustrates, the height of the features strongly decreases, and the diameter increases when the surface is rinsed with water and dried at room temperature. This observation relates to what is already reported for sinusoidal corrugation of similar pNIPAAm crosslinked layers[48] and nanoimprinted nanopillars.[27] It can be attributed to the strong deformation of the elastic polymer network by the surface tension of the aqueous medium upon evaporation. The elasticity of the wet pNIPAAm network is strongly temperature-dependent due to its thermoresponsive solvation properties: below the LCST of 32 °C, the network swells in water and forms a soft structure that is planarized in the drying process (the height decreases by a factor of about 10). However, above the LCST in water, the polymer network collapses and forms more compact, rigid domains that are resistant to mechanical deformation upon drying. This swelling behavior was also investigated by acquiring AFM images of the prepared thermoresponsive nanostructures in water at varying temperatures around the LCST. As shown in Figure 4, at T = 30 °C, the topography of the swollen soft pNIPAAm structure is barely captured by the AFM tip. However, when the temperature is increased above

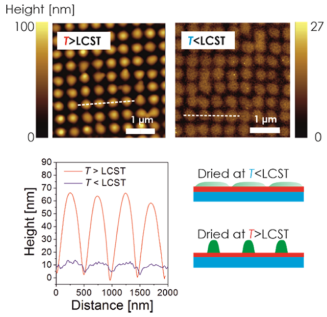

Figure 3. AFM observation of nanostructured pNIPAAm hydrogel topography dried at a temperature below and above the LCST. The structure was prepared with an irradiation dose of 240 mJ/cm^2.

https://dx.doi.org/10.1021/acs.jpcc.9b11059
J. Phys. Chem. C XXXX, XXX, XXX−XXX

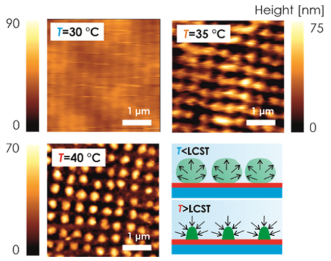

Figure 4. AFM observation of nanostructured pNIPAAm hydrogel topology in water for the temperature T = 30, 35, and 40 °C. The structure was prepared with an irradiation dose of 240 mJ/cm^2.

the LCST to T = 35 °C, the inscribed pattern becomes apparent for the collapsed and more rigid hydrogel network. Interestingly, upon further temperature increase to T = 40 °C, the observed geometry in water fully resembles the morphology that was recorded in air, as presented in Figure 2b.

Hybrid Au-pNIPAAm Nanostructures. The developed approach for the preparation of arrays with thermoresponsive pNIPAAm-based features was further applied to gold nanoparticle arrays to yield a hybrid plasmonic nanomaterial. First, gold nanoparticle arrays were prepared on a glass surface using UV-LIL with Lloyd's mirror configuration and a dry etching protocol, as previously reported.[46] The obtained cylindrical gold nanoparticle exhibited a diameter of D = 132 ± 5 nm, a height of about 50 nm, and an array periodicity of Λ_G = 463 ± 2 nm, as revealed by the AFM image in Figure 5a. Afterward, the gold surface of the nanoparticles was modified with a self-assembled monolayer (SAM) of benzophenone disulfide, on top of which a pNIPAAm polymer film was deposited (the benzophenone disulfide serves here as a linker for the covalent photoattachment of the polymer chains to gold[44]).

Then, the same phase mask-based procedure (for recording the four-beam UV interference field with the period of Λ_H = 488 ± 2 nm) was applied to generate arrays of pNIPAAm-based polymer structures, followed by rinsing with water and drying.

To circumvent the difficulty to precisely align both arrays of the hydrogel features and the gold nanoparticles, a slight mismatch of the array periodicities by 5% was intentionally applied to yield a Moiré effect between both features. As a result, it is expected that the topography will vary periodically across the surface, resulting in a repeating pattern of areas with aligned and with misaligned geometry. The characteristic size of these domains can be estimated as $\Lambda_H \cdot \Lambda_G/(\Lambda_H - \Lambda_G)$ in the range of about 8 μm. Figure 5b shows an AFM image for the topography of a 2 × 2 μm subarea of the structure that exhibits hydrogel features aligned with the gold nanoparticle arrays after drying below the LCST. Apparently, the gold nanoparticles are visible as areas with an increased height of about 85 nm surrounded by partially planarized pNIPAAm zones of lower height that spread to a diameter of about 400 nm (see also the representative cross-section in Figure S3). When the structure is exposed to water and dried again above the LCST, the morphology changes, as shown in Figure 5c. The metallic nanoparticle topography is not protruding through the pNIPAAm hydrogel, which appears more compacted and spreading to a smaller diameter of about 300 nm. The maximum height of the pNIPAAm features (with metallic nanoparticle inside) of 90 nm is slightly higher than for the structure dried below LCST. The morphology variations due to drying in the swollen and collapsed state of pNIPAAm networks attached to gold nanoparticles are less pronounced than on the flat SU-8 film. It can be attributed to different means of the attachment (swelling and collapsing on the curved surface of Au nanoparticle walls) and to the potential difference in the interaction of pNIPAAm chains with SU-8 and BK7 glass (surrounding the hydrogel structure). For comparison, an area where the gold nanoparticles and hydrogel features are misaligned is presented in Figure 5d. The patterned hydrogel features around the metallic structures exhibit more irregular morphology compared to those measured without the gold nanoparticles in Figures 2−4. This observation can be attributed to gradually changing alignment between the center of the hydrogel feature and the gold nanoparticle along the surface and the fact that the collapse tends to pull pNIPAAm-based polymer toward gold where the attachment is utilized via the benzophenone disulfide linker.

Actuating of LSP. The collapse of the pNIPAAm hydrogel is associated with an increase of the polymer volume fraction and the refractive index on the surface of gold nanoparticles. Therefore, the pNIPAAm collapse around these metallic objects detunes the localized surface plasmon resonance

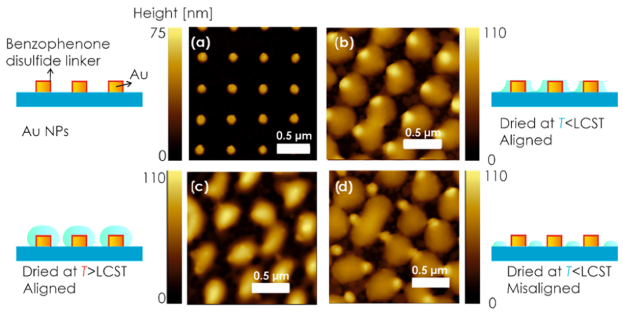

Figure 5. AFM topography of (a) gold nanoparticle arrays subsequently covered with covalently attached pNIPAAm-based nanostructures that are aligned with the gold nanoparticles and dried (b) below and (c) above the LCST. (d) Example of misaligned arrays of gold nanoparticles with pNIPAAm-based nanostructures dried below the LCST.

https://dx.doi.org/10.1021/acs.jpcc.9b11059
J. Phys. Chem. C XXXX, XXX, XXX−XXX

(LSPR) and manifests itself as a redshift of the resonant wavelength. Figure 6a shows the transmission spectra

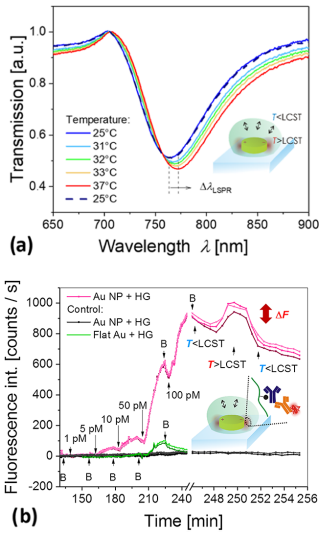

Figure 6. (a) Measured reversible shift in LSPR spectra upon temperature-induced swelling and collapse of the pNIPAAm-based hydrogel wrapped over metallic nanoparticles. (b) Employment of the hybrid material for plasmonic amplification of a fluorescence immunoassay with the pNIPAAm-based hydrogel serving as an affinity binding matrix that can be swollen and collapsed by an external temperature stimulus. The red-colored lines show the fluorescence signal acquired from spots with a diameter of 220 μm at different locations on the same biochip carrying the pNIPAAm-based hydrogel that was functionalized with ligands. The black curves correspond to control spots on the same biochip that were not functionalized with the ligand molecules, and the green curves show the control experiment on a planar-functionalized hydrogel binding matrix attached to the flat gold film. The analyte concentration is clearly indicated in the graph, and B corresponds to the rinsing step with working buffer.

measured over the area of about 1 mm^2, which averages the variations in the alignment between gold nanoparticles and hydrogel features with a domain size <10 μm. LSPR for the structure at the temperature T = 25 °C manifests itself as a dip in the transmission spectrum centered at a wavelength of λ_{LSPR} = 763.9 nm. The gradual collapse of the hydrogel induces a red-shift of the LSPR wavelength upon an increase in the temperature. At a temperature of T = 37 °C, far above the LCST, the LSPR wavelength shifts to 771.9 nm. These changes are fully reversible, as after cooling to T = 25 °C, the LSPR spectrum shifts back to the original shape. It is worth noting that the observed shift of about 6 nm is half of that measured for a structure covered with a compact pNIPAAm hydrogel film (data not shown), which can be ascribed to the fact that about half of the nanoparticles is not in contact with the polymer due to the periodic regions of misalignment in the Moiré pattern.

LSP-Enhanced Fluorescence Assay. Finally, the developed structure was tested to serve as a biochip interface for the fluorescence readout of an immunoassay. First, the responsive pNIPAAm-based hydrogel features wrapping (about half) of the gold nanoparticles that were postmodified with mouse IgG antibodies (mIgG). The polymer carboxylic groups were employed for establishing covalent bonds between the lysine groups of the protein and the polymer chain based on the established amine coupling scheme.[49] Then, the substrate was clamped against a flow cell, and a series of liquid samples with an increasing concentration of goat antibodies specific to mIgG (a-mIgG) were pumped over its surface. To detect the affinity binding, the goat antibody a-mIgG was labeled with an organic dye (Alexa Fluor 790). This label exhibits its absorption and emission wavelengths (λ_{ex} = 785 nm, λ_{em} = 810 nm) in the vicinity of the LSPR wavelength (λ_{LSPR} = 764 nm). Therefore, the kinetics of the affinity binding of a-mIgG from the liquid sample was measured using plasmon-enhanced fluorescence.[50] The surface of the sample was irradiated by a laser beam at a wavelength of 785 nm that resonantly couples to LSPs and locally excites the bound fluorophores with its enhanced field intensity. The emitted light at a wavelength of 810 nm was collected with a home built instrument[47] separated from the excitation beam using a dichroic mirror, bandpass filter, and notch filter and detected with a cooled CCD camera. The fluorescence signal was acquired with dedicated software from a series of spots carrying the gold nanoparticle arrays in reference to an area without nanoparticles, and the data were tracked in time upon sequential flow of analyte samples. The fluorescence intensity was averaged over the surface of each circular spot with a diameter of 220 μm that was much larger than the size of domains with aligned and misaligned arrays of gold nanoparticles and hydrogel features. The liquid samples were prepared from phosphate-buffered saline that was spiked with a-mIgG at concentrations of 1, 5, 10, 50, and 100 pM. Each sample was flushed over the surface for 15 min, followed by 5 min rinsing. As Figure 6b shows, the binding of a-mIgG manifests itself as a gradual increase in the fluorescence signal, and upon rinsing, a fluorescence intensity decrease occurs due to bleaching of the emitters. The fluorescence signal on gold nanoparticle arrays capped with the pNIPAAm hydrogel matrix (red curves in Figure 6a) is about 6 times higher compared to a control experiment (green curves in 6a). The control experiment was carried out on the hydrogel biointerface prepared in the form of a layer attached to a flat nonstructured gold film. It is worth noting that the plasmonic enhancement on the structured surface is probably higher than the factor of 6 due to the fact that the control flat architecture exhibits a larger area for the capture of the target analyte and that at least half of the metallic nanoparticles are not capped with the hydrogel binding matrix due to the miss-alignment. The measured data for a structured hydrogel biointerface overlaid with gold nanoparticles indicate that the limit of detection of the prepared biochip is 0.7 pM (determined for the standard deviation fluorescence signal baseline of 2 counts/s and the slope of the fluorescence signal of 9 counts/s/pM). After this titration experiment, the temperature of the biochip surface was increased from 25 to 40 °C, above the LCST of the hydrogel. As seen in Figure 6b, the induced collapse of the responsive hydrogel with the affinity-captured and fluorophore-labeled a-mIgG leads to an increase of the fluorescence signal by about 20%. This is due to the collapse and compacting of the hydrogel, which increases the polymer volume fraction and affinity-bound analyte molecules closer to the gold surface, where the plasmonic hotspot is located. This observation corroborates that affinity binding occurs in the

https://dx.doi.org/10.1021/acs.jpcc.9b11059
J. Phys. Chem. C XXXX, XXX, XXX−XXX

vicinity of the metallic nanoparticles within the matrix of the responsive pNIPAAm-based polymer network and indicates that the triggered collapse can provide an additional enhancement mechanism for high sensitivity fluorescence assays.

CONCLUSIONS

A technique based on four-beam laser interference lithography utilizing a phase mask-based configuration allows for the preparation of well-defined responsive hydrogel nanostructures with the tailored spacing and diameter. Periodic arrays of pNIPAAm-based hydrogel nanostructures exhibiting a disk shape with a tunable diameter, as low as 170 nm, were prepared with a submicron period. The temperature-induced swelling and collapse of the inscribed polymer features were investigated, and their local attachment on top of the periodic gold nanoparticle arrays was achieved based on the Moiré effect. The fully reversible actuation by temperature changes was demonstrated by measuring the variations in LSPR of the gold nanoparticle arrays. In addition, the pNIPAAm-based hydrogel was postmodified with biorecognition elements to serve as a 3D high binding capacity matrix, and a model bioassay based on fluorescence readout was conducted. The limit of detection was proven to be in the sub-picomolar range owing to the plasmonic amplification of the fluorescence signal by the plasmonic nanoparticles. Finally, the capability of the pNIPAAm network to compact the affinity-captured analyte at the plasmonic hotspots by a temperature-induced polymer collapse was tested. The presented hybrid architecture provides a novel approach for the local attachment of chemical and biological species in the vicinity of metallic nanostructures to fully exploit the probing with the LSP field at the so-called plasmonic hotspots, where the optical field intensity is the strongest.

ASSOCIATED CONTENT

Supporting Information

The Supporting Information is available free of charge at https://pubs.acs.org/doi/10.1021/acs.jpcc.9b11059.

Schematic and atomic force spectroscopy images of the phase mask and recorded interference pattern employing a positive photoresist; schematic of the optical setup used for the plasmon-enhanced spectroscopy assay; cross-sections of AFM topography of hydrogel nanostructures (PDF)

AUTHOR INFORMATION

Authors

Nestor Gisbert Quilis − *BioSensor Technologies, AIT-Austrian Institute of Technology GmbH, 3430 Tulln, Austria*

Simone Hageneder − *BioSensor Technologies, AIT-Austrian Institute of Technology GmbH, 3430 Tulln, Austria*

Stefan Fossati − *BioSensor Technologies, AIT-Austrian Institute of Technology GmbH, 3430 Tulln, Austria*

Simone K. Auer − *BioSensor Technologies, AIT-Austrian Institute of Technology GmbH, 3430 Tulln, Austria*

Priyamvada Venugopalan − *BioSensor Technologies, AIT-Austrian Institute of Technology GmbH, 3430 Tulln, Austria; CEST Kompetenzzentrum für elektrochemische Oberflächentechnologie GmbH, TFZ, Wiener Neustadt, 2700 Wiener Neustadt, Austria*

Anil Bozdogan − *CEST Kompetenzzentrum für elektrochemische Oberflächentechnologie GmbH, TFZ, Wiener Neustadt, 2700 Wiener Neustadt, Austria*

Christian Petri − *Macromolecular Chemistry, Department Chemistry-Biology, University of Siegen, Siegen 57076, Germany*

Alberto Moreno-Cencerrado − *Institute for Biophysics, Department of Nanobiotechnology, University of Natural Resources and Life Sciences Vienna (BOKU), Vienna 1190, Austria*

Jose Luis Toca-Herrera − *Institute for Biophysics, Department of Nanobiotechnology, University of Natural Resources and Life Sciences Vienna (BOKU), Vienna 1190, Austria*

Ulrich Jonas − *Macromolecular Chemistry, Department Chemistry-Biology, University of Siegen, Siegen 57076, Germany;* orcid.org/0000-0002-2161-4541

Jakub Dostalek − *BioSensor Technologies, AIT-Austrian Institute of Technology GmbH, 3430 Tulln, Austria;* orcid.org/0000-0002-0431-2170

Complete contact information is available at: https://pubs.acs.org/10.1021/acs.jpcc.9b11059

Notes

The authors declare no competing financial interest.

ACKNOWLEDGMENTS

N.G.Q. acknowledges funding from the European Union's Horizon 2020 research and innovation program under Grant agreement no. 642787, Marie Sklodowska-Curie Innovative Training Network BIOGEL. P.V. was supported by the project jointly funded by Agence Nationale de la Recherche (ANR) and the Austrian Science Fund (FWF) under the grant agreements ANR-15-CE29-0026 and I 2647, respectively. S.H., S.F., C.P., and J.D. received support from the European Union's Horizon 2020 research and the innovation program under Grant Agreement no. 633937, project ULTRAPLACAD. S.A. is grateful for the support from FEMTEC and S.H., S.F., and J.D. were supported by the Austrian Research Promotion Agency (FFG) with Grant agreement no. 861578 (ERANET project PLABAN).

REFERENCES

(1) Green, J. J.; Elisseeff, J. H. Mimicking Biological Functionality with Polymers for Biomedical Applications. *Nature* **2016**, *540*, 386.

(2) Mateescu, A.; Wang, Y.; Dostalek, J.; Jonas, U. Thin Hydrogel Films for Optical Biosensor Applications. *Membranes* **2012**, *2*, 40−69.

(3) Liu, F.; Urban, M. W. Recent Advances and Challenges in Designing Stimuli-Responsive Polymers. *Prog. Polym. Sci.* **2010**, *35*, 3−23.

(4) Wei, M.; Gao, Y.; Li, X.; Serpe, M. J. Stimuli-Responsive Polymers and Their Applications. *Polym. Chem.* **2017**, *8*, 127−143.

(5) De las Heras Alarcón, C.; Pennadam, S.; Alexander, C. Stimuli Responsive Polymers for Biomedical Applications. *Chem. Soc. Rev.* **2005**, *34*, 276−285.

(6) Jiang, N.; Zhuo, X.; Wang, J. Active Plasmonics: Principles, Structures, and Applications. *Chem. Rev.* **2017**, *118*, 3054−3099.

(7) Huck, W. T. Responsive Polymers for Nanoscale Actuation. *Mater. Today* **2008**, *11*, 24−32.

(8) Sidorenko, A.; Krupenkin, T.; Taylor, A.; Fratzl, P.; Aizenberg, J. Reversible Switching of Hydrogel-Actuated Nanostructures into Complex Micropatterns. *Science* **2007**, *315*, 487−490.

(9) Haq, M. A.; Su, Y.; Wang, D. Mechanical Properties of Pnipam Based Hydrogels: A Review. *Mater. Sci. Eng., C* **2017**, *70*, 842−855.

https://dx.doi.org/10.1021/acs.jpcc.9b11059
J. Phys. Chem. C XXXX, XXX, XXX−XXX

(10) Guan, Y.; Zhang, Y. Pnipam Microgels for Biomedical Applications: From Dispersed Particles to 3d Assemblies. *Soft Matter* **2011**, *7*, 6375−6384.
(11) Nash, M. E.; Healy, D.; Carroll, W. M.; Elvira, C.; Rochev, Y. A. Cell and Cell Sheet Recovery from Pnipam Coatings; Motivation and History to Present Day Approaches. *J. Mater. Chem.* **2012**, *22*, 19376−19389.
(12) Toma, M.; Jonas, U.; Mateescu, A.; Knoll, W.; Dostalek, J. Active Control of Spr by Thermoresponsive Hydrogels for Biosensor Applications. *J. Phys. Chem. C* **2013**, *117*, 11705−11712.
(13) Kawano, T.; Niidome, Y.; Mori, T.; Katayama, Y.; Niidome, T. Pnipam Gel-Coated Gold Nanorods for Targeted Delivery Responding to a near-Infrared Laser. *Bioconjugate Chem.* **2009**, *20*, 209−212.
(14) Erickson, D.; Mandal, S.; Yang, A. H.; Cordovez, B. Nanobiosensors: Optofluidic, Electrical and Mechanical Approaches to Biomolecular Detection at the Nanoscale. *Microfluid. Nanofluid.* **2008**, *4*, 33−52.
(15) Paquet, C.; Kumacheva, E. Nanostructured Polymers for Photonics. *Mater. Today* **2008**, *11*, 48−56.
(16) Ghosh, S.; Kouamé, N. A.; Ramos, L.; Remita, S.; Dazzi, A.; Deniset-Besseau, A.; Beaunier, P.; Goubard, F.; Aubert, P.-H.; Remita, H. Conducting Polymer Nanostructures for Photocatalysis under Visible Light. *Nat. Mater.* **2015**, *14*, 505.
(17) Slepicka, P.; Kasalkova, N. S.; Siegel, J.; Kolska, Z.; Bacakova, L.; Svorcik, V. Nano-Structured and Functionalized Surfaces for Cytocompatibility Improvement and Bactericidal Action. *Biotechnol. Adv.* **2015**, *33*, 1120−1129.
(18) Nie, Z.; Kumacheva, E. Patterning Surfaces with Functional Polymers. *Nat. Mater.* **2008**, *7*, 277.
(19) Cheng, J. Y.; Mayes, A. M.; Ross, C. A. Nanostructure Engineering by Templated Self-Assembly of Block Copolymers. *Nat. Mater.* **2004**, *3*, 823.
(20) Hu, H.; Gopinadhan, M.; Osuji, C. O. Directed Self-Assembly of Block Copolymers: A Tutorial Review of Strategies for Enabling Nanotechnology with Soft Matter. *Soft Matter* **2014**, *10*, 3867−3889.
(21) Zhang, H.; Mourran, A.; Möller, M. Dynamic Switching of Helical Microgel Ribbons. *Nano Lett.* **2017**, *17*, 2010−2014.
(22) Chen, J.-K.; Chang, C.-J. Fabrications and Applications of Stimulus-Responsive Polymer Films and Patterns on Surfaces: A Review. *Materials* **2014**, *7*, 805−875.
(23) Yu, Q.; Ista, L. K.; Gu, R.; Zauscher, S.; López, G. P. Nanopatterned Polymer Brushes: Conformation, Fabrication and Applications. *Nanoscale* **2016**, *8*, 680−700.
(24) Idota, N.; Tsukahara, T.; Sato, K.; Okano, T.; Kitamori, T. The Use of Electron Beam Lithographic Graft-Polymerization on Thermoresponsive Polymers for Regulating the Directionality of Cell Attachment and Detachment. *Biomaterials* **2009**, *30*, 2095−2101.
(25) Traub, M. C.; Longsine, W.; Truskett, V. N. Advances in Nanoimprint Lithography. *Annu. Rev. Chem. Biomol. Eng.* **2016**, *7*, 583−604.
(26) Guo, L. J. Nanoimprint Lithography: Methods and Material Requirements. *Adv. Mater.* **2007**, *19*, 495−513.
(27) Pirani, F.; Sharma, N.; Moreno-Cencerrado, A.; Fossati, S.; Petri, C.; Descrovi, E.; Toca-Herrera, J. L.; Jonas, U.; Dostalek, J. Optical Waveguide-Enhanced Diffraction for Observation of Responsive Hydrogel Nanostructures. *Macromol. Chem. Phys.* **2017**, *218*, No. 1600400.
(28) Mourran, A.; Zhang, H.; Vinokur, R.; Möller, M. Soft Microrobots Employing Nonequilibrium Actuation Via Plasmonic Heating. *Adv. Mater.* **2017**, *29*, No. 1604825.
(29) Volk, K.; Fitzgerald, J. P. S.; Retsch, M.; Karg, M. Time-Controlled Colloidal Superstructures: Long-Range Plasmon Resonance Coupling in Particle Monolayers. *Adv. Mater.* **2015**, *27*, 7332.
(30) Valsecchi, C.; Brolo, A. G. Periodic Metallic Nanostructures as Plasmonic Chemical Sensors. *Langmuir* **2013**, *29*, 5638−5649.
(31) Halas, N. J.; Lal, S.; Chang, W.-S.; Link, S.; Nordlander, P. Plasmons in Strongly Coupled Metallic Nanostructures. *Chem. Rev.* **2011**, *111*, 3913−3961.
(32) Baffou, G.; Quidant, R. Thermo-Plasmonics: Using Metallic Nanostructures as Nano-Sources of Heat. *Laser Photonics Rev.* **2013**, *7*, 171−187.
(33) Brongersma, M. L.; Halas, N. J.; Nordlander, P. Plasmon-Induced Hot Carrier Science and Technology. *Nat. Nanotechnol.* **2015**, *10*, 25.
(34) Mayer, K. M.; Hafner, J. H. Localized Surface Plasmon Resonance Sensors. *Chem. Rev.* **2011**, *111*, 3828−3857.
(35) Goerlitzer, E. S. A.; Speichermann, L. E.; Mirzaa, T. A.; Mohammadia, R.; Vogel, N. Addressing the Plasmonic Hotspot Region by Site-Specific Functionalization of Nanostructures. *Nanoscale Adv.* **2020**, *2*, 136.
(36) Piliarik, M.; Kvasnicka, P.; Galler, N.; Krenn, J. R.; Homola, J. Local Refractive Index Sensitivity of Plasmonic Nanoparticles. *Opt. Express* **2011**, *19*, 9213−9220.
(37) Jonsson, M. P.; Dahlin, A. B.; Feuz, L.; Petronis, S.; Hook, F. Locally Functionalized Short-Range Ordered Nanoplasmonic Pores for Bioanalytical Sensing. *Anal. Chem.* **2010**, *82*, 2087−2094.
(38) Herzog, N.; Kind, J.; Hess, C.; Andrieu-Brunsen, A. Surface Plasmon & Visible Light for Polymer Functionalization of Mesopores and Manipulation of Ionic Permselectivity. *Chem. Commun.* **2015**, *51*, 11697−11700.
(39) Dostert, K.-H.; Álvarez, M.; Koynov, K.; del Campo, An.; Butt, H.-J. r.; Kreiter, M. Near Field Guided Chemical Nanopatterning. *Langmuir* **2012**, *28*, 3699−3703.
(40) Mazzotta, F.; Johnson, T. W.; Dahlin, A. B.; Shaver, J.; Oh, S. H.; Hook, F. Influence of the Evanescent Field Decay Length on the Sensitivity of Plasmonic Nanodisks and Nanoholes. *ACS Photonics* **2015**, *2*, 256−262.
(41) Wang, Y.; Brunsen, A.; Jonas, U.; Dostalek, J.; Knoll, W. Prostate Specific Antigen Biosensor Based on Long Range Surface Plasmon-Enhanced Fluorescence Spectroscopy and Dextran Hydrogel Binding Matrix. *Anal. Chem.* **2009**, *81*, 9625−9632.
(42) Huang, C. J.; Dostalek, J.; Knoll, W. Long Range Surface Plasmon and Hydrogel Optical Waveguide Field-Enhanced Fluorescence Biosensor with 3d Hydrogel Binding Matrix: On the Role of Diffusion Mass Transfer. *Biosens. Bioelectron.* **2010**, *26*, 1425−1431.
(43) Beines, P. W.; Klosterkamp, I.; Menges, B.; Jonas, U.; Knoll, W. Responsive Thin Hydrogel Layers from Photo-Cross-Linkable Poly (N-Isopropylacrylamide) Terpolymers. *Langmuir* **2007**, *23*, 2231−2238.
(44) Sergelen, K.; Petri, C.; Jonas, U.; Dostalek, J. Free-Standing Hydrogel-Particle Composite Membrane with Dynamically Controlled Permeability. *Biointerphases* **2017**, *12*, No. 051002.
(45) Gee, K. R.; Archer, E. A.; Kang, H. C. 4-Sulfotetrafluorophenyl (Stp) Esters: New Water-Soluble Amine-Reactive Reagents for Labeling Biomolecules. *Tetrahedron Lett.* **1999**, *40*, 1471−1474.
(46) Quilis, N. G.; Lequeux, M.; Venugopalan, P.; Khan, I.; Knoll, W.; Boujday, S.; de la Chapelle, M. L.; Dostalek, J. Tunable Laser Interference Lithography Preparation of Plasmonic Nanoparticle Arrays Tailored for Sers. *Nanoscale* **2018**, *10*, 10268.
(47) Dostalek, J.; Knoll, W.; Fossati, S.; Hageneder, S.; Jungbluth, V. Plasmon-Enhanced Fluorescence Spectroscopy Imaging by Multi-Resonant Nanostructures. European Patent Application No. 19164960.72019.
(48) Sharma, N.; Petri, C.; Jonas, U.; Dostalek, J. Reversibly Tunable Plasmonic Bandgap by Responsive Hydrogel Grating. *Opt. Express* **2016**, *24*, 2457−2465.
(49) Aulasevich, A.; Roskamp, R. F.; Jonas, U.; Menges, B.; Dostálek, J.; Knoll, W. Optical Waveguide Spectroscopy for the Investigation of Protein-Functionalized Hydrogel Films. *Macromol. Rapid Commun.* **2009**, *30*, 872−877.
(50) Bauch, M.; Toma, K.; Toma, M.; Zhang, Q.; Dostalek, J. Plasmon-Enhanced Fluorescence Biosensors: A Review. *Plasmonics* **2014**, *9*, 781−799.

https://dx.doi.org/10.1021/acs.jpcc.9b11059
J. Phys. Chem. C XXXX, XXX, XXX−XXX

Supporting Information

UV-Laser Interference Lithography for Local Functionalization of Plasmonic Nanostructures with Responsive Hydrogel

*Nestor Gisbert Quilis[a], Simone Hageneder[a], Stefan Fossati[a], Simone K. Auer[a], Priyamvada Venugopalan[a,b†], Anil Bozdogan[b], Christian Petri[c], Alberto Moreno-Cencerrado[d], Jose Luis Toca-Herrera[d], Ulrich Jonas[c] and Jakub Dostalek[a]**

[a]BioSensor Technologies, AIT-Austrian Institute of Technology GmbH, Konrad-Lorenz-Strasse 24, 3430 Tulln, Austria

[b]CEST Kompetenzzentrum für elektrochemische Oberflächentechnologie GmbH, TFZ, Wiener Neustadt, Viktor-Kaplan-Strasse 2, 2700 Wiener Neustadt, Austria

[c]Macromolecular Chemistry, Department Chemistry-Biology, University of Siegen, Adolf Reichwein-Strasse 2, Siegen 57076, Germany

[d]Institute for Biophysics, Department of Nanobiotechnology, University of Natural Resources and Life Sciences Vienna (BOKU), Muthgasse 11, Vienna 1190, Austria

Observation of the interference field profile formed by the phase mask. A thin layer of the S1805 positive photoresist (diluted 1:2 with propylene glycol monomethyl ether acetate) with a thickness of 120 nm was deposited by spin-coating (4500 rpm, 45 s) on top of a BK7 substrate. Afterward, the sample was mounted in a home-built set-up together with the phase mask to verify the recording pattern. The distance of the photoresist-coated substrate in respect with the phase mask (recording plane) was kept to 5.6 mm. At this distance the first order diffraction gratings overlap at the center of the mask for a Λ=690 nm. Thus, the samples were irradiated once to 27 mJ cm^{-2} and developed for 35 sec.

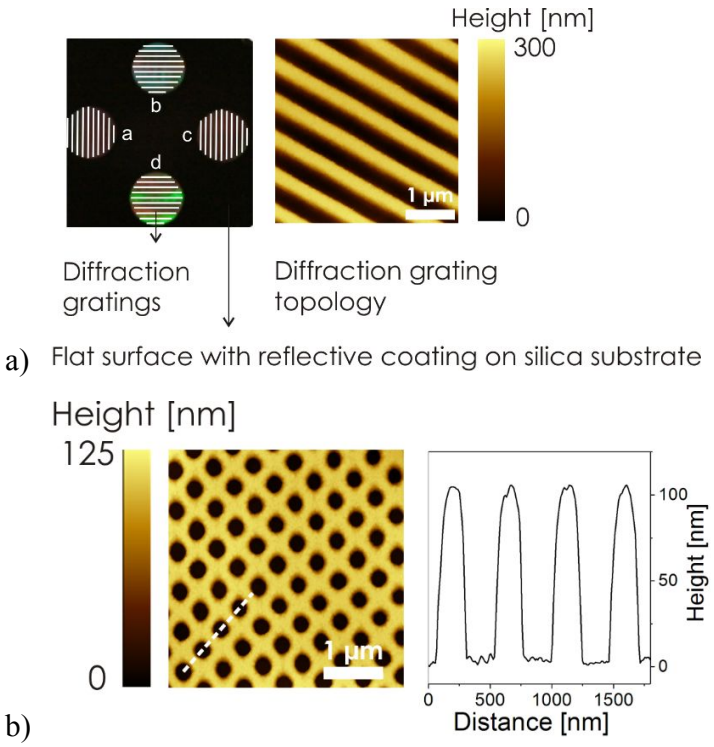

Figure S1. (a) Schematics of the prepared phase mask with orientation of the transmission gratings (left) and their topography obtained by AFM (right). (b) Recorded interference pattern into the S1805 positive photoresist using the prepared phase mask.

Plasmon-enhanced fluorescence readout of model assay

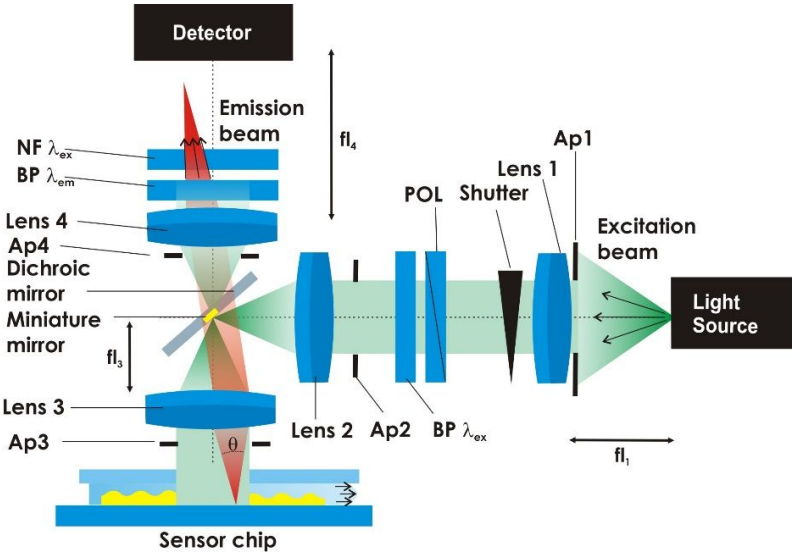

Figure S2. Schematics of the optical setup configuration of the reader that enables in situ readout of fluorescence signal kinetics from the sensing spots on a sensor chip: NF – notch filter, BP – bandpass filter, Ap – aperture, POL – polarizer, fl – focal length.

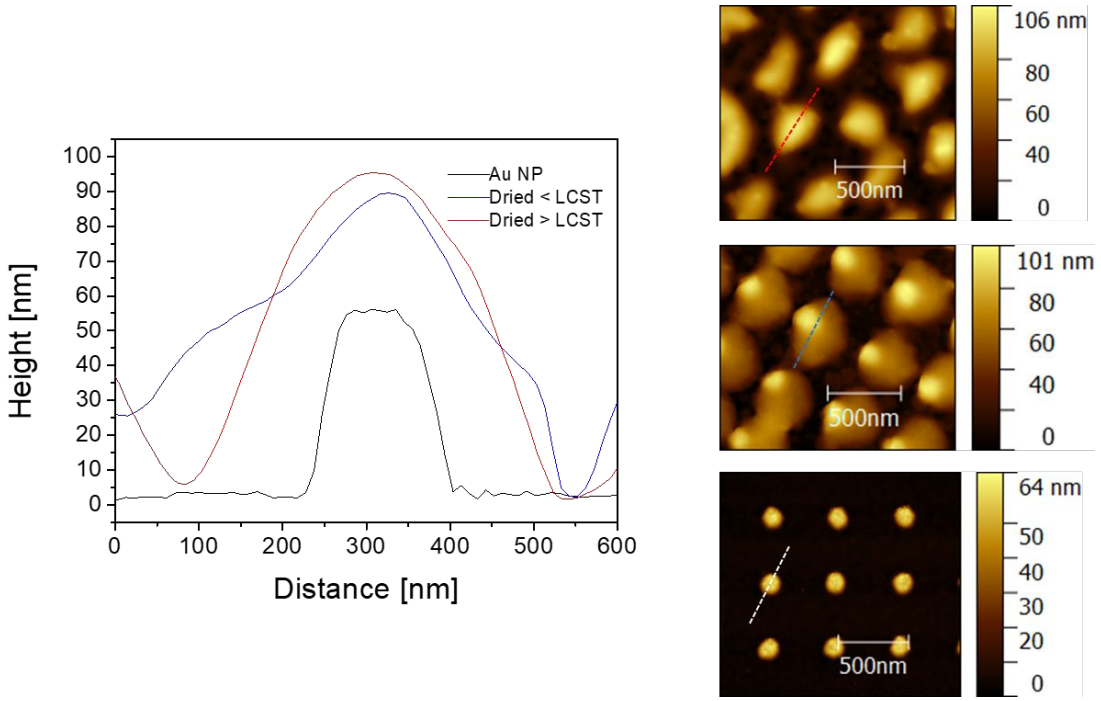

Figure S3. Cross-sections of representative areas of AFM topography showed in Figure 5 for bare gold nanoparticles (black curve), gold nanoparticles capped with pNIPAAm-based hydrogel dried below its LCST (blue curve) and above its LCST (red curve) and associated AFM images.

CHAPTER 4

Summary and Outlook

In recent times the pace of development of point-of-care devices has increased, particularly in light of the current Covid-19 pandemic, which is bringing biosensors closer to small laboratories, doctors' offices, and into people's everyday lives. Moreover, the trend towards miniaturized, simplified, and cost-effective biosensors could improve medical diagnosis and monitoring of diseases in economically disadvantaged or rural areas with limited access to medical infrastructure.

Within the scope of this thesis, several projects were completed, which are addressing key aspects for practical biosensor technology development.

Chapter 3.1 of this thesis demonstrates the application of *grafted-from* polymer brushes to enhance the antifouling properties of a sensor interface for detecting disease markers present in complex biological fluids. The subsequent chapter (3.2) deals with the real-time observation of the growth and (ion-) responsiveness of polyelectrolyte ssDNA brushes tethered to a surface, which can serve as an efficient amplification step in high sensitivity assays. Chapter 3.3 explores the use of a thermoresponsive polymer networks as an element for fluorescence affinity biosensors and peptide microarrays, able to host a high density of specific ligands and to provide enhanced antifouling properties. Whereas chapters 3.1-3.3 utilize already established prism coupled SPR/SPFS/OWS methods, chapters 3.4-3.6 deal with different optical sensing schemes based on specially designed metallic nanostructured surfaces which are tested for their sensing capabilities for a more sensitive and selective analysis. Chapter 3.4 describes an easy-to-use refractometric sensing approach based on a nanostructured plasmonic chip that is back-side illuminated for readout of TNF-α protein

affinity binding studies as an alternative to regular grating-coupled SPR. The study in chapter 3.5 also deals with developing a plasmonic grating-based biosensor for protein detection but on the principle of plasmon-enhanced fluorescence and a spatially resolved readout for observation of multiple spots on one chip. Finally, in the last chapter in 3.6, the same sensing mechanisms are also exploited to investigate the local and selective attachment of responsive hydrogel networks to plasmonic nanoparticle arrays.

The critical challenges of biosensor development covered in this thesis contribute towards the development of an "ideal" biosensor described throughout this work: a sensor that is capable of rapid, high-throughput, multiplexed and sensitive biomarker detection in complex matrices outside of centralized laboratories with the ability to solve some of the open challenges in the fields of medicine and healthcare.

Further research will explore the concept of isothermal amplification like the herein investigated rolling circle amplification (RCA) as an alternative to polymerase chain reaction (PCR) techniques for nucleic acid biomarkers. This approach can also lower the complexity of such assays and allow the implementation into sensing devices which do not rely on specialized laboratory infrastructure. Additionally, isothermal amplification concepts can enhance the sensitivity of biosensors by shifting from the interrogation of ensembles of molecules to resolving single molecule binding events.[186]

At the optical transducer level, cost-effective preparation methods of optically functional substrates are important. UV- nanoimprint lithography (UV-NIL) with roll-to-roll processes and other techniques used in this work can be scaled up for the production of large quantities of structures. Straightforward and cost-effective sensing chips may support the application of surface plasmon-based optical sensor techniques and open door for their implementations into standard laboratory environment and beyond, which has historically been prohibitively expensive. Furthermore, the combination of tailored, responsive polymers with plasmonic nanostructures has already contributed to the fabrication of smart materials, which offer the possibility to serve as autonomous functional objects and devices, like micro-and nanorobots.[187, 188, 189]

Most notably, antifouling brushes and networks can be tailored to be deployed for detecting analytes in bodily fluids, which are minimally or even completely noninvasively collected ("liquid biopsy") and even can pave the way towards implantable sensors and continuous monitoring inside the body.

Bibliography

[1] Turner, A. P. Biosensors: Fundamentals and applications. *Biosensors and Bioelectronics* **65**, A1 (2015).

[2] Thévenot, D. R., Toth, K., Durst, R. A. & Wilson, G. S. Electrochemical biosensors: Recommended definitions and classification. *Biosensors and Bioelectronics* **16**, 121–131 (2001).

[3] Sethi, R. S. Transducer aspects of biosensors. *Biosensors and Bioelectronics* **9**, 243–264 (1994).

[4] Du, Y. & Dong, S. Nucleic acid biosensors: Recent advances and perspectives. *Analytical Chemistry* **89**, 189–215 (2017).

[5] Liu, Q., Wang, J. & Boyd, B. J. Peptide-based biosensors. *Talanta* **136**, 114–127 (2015).

[6] Socorro-Leránoz, A. B., Santano, D., Del Villar, I. & Matias, I. R. Trends in the design of wavelength-based optical fibre biosensors (2008–2018). *Biosensors and Bioelectronics: X* **1**, 100015 (2019).

[7] Clark, L. C. & Lyons, C. ELECTRODE SYSTEMS FOR CONTINUOUS MONITORING IN CARDIOVASCULAR SURGERY. *Annals of the New York Academy of Sciences* **102**, 29–45 (1962).

[8] Biosensors Market worth $36.7 billion by 2026. URL `https://www.marketsandmarkets.com/PressReleases/biosensors.asp`.

[9] Das, J. *et al.* An electrochemical clamp assay for direct, rapid analysis of circulating nucleic acids in serum. *Nature Chemistry* **7**, 569–575 (2015).

[10] Cheng, T. & Zhan, X. Pattern recognition for predictive, preventive, and personalized medicine in cancer. *EPMA Journal* **8**, 51–60 (2017).

[11] Babamiri, B., Salimi, A. & Hallaj, R. A molecularly imprinted electrochemiluminescence sensor for ultrasensitive HIV-1 gene detection using EuS nanocrystals as luminophore. *Biosensors and Bioelectronics* **117**, 332–339 (2018).

[12] Azimzadeh, M., Nasirizadeh, N., Rahaie, M. & Naderi-Manesh, H. Early detection of Alzheimer's disease using a biosensor based on electrochemically-reduced graphene oxide and gold nanowires for the quantification of serum microRNA-137. *RSC Advances* **7**, 55709–55719 (2017).

[13] Liu, Q. *et al.* Highly Sensitive and Quick Detection of Acute Myocardial Infarction Biomarkers Using In2O3 Nanoribbon Biosensors Fabricated Using Shadow Masks. *ACS Nano* **10**, 10117–10125 (2016).

[14] Kelley, S. O. What Are Clinically Relevant Levels of Cellular and Biomolecular Analytes? *ACS Sensors* **2**, 193–197 (2017).

[15] Gooding, J. J. What Does Ultrasensitive Really Mean? (2019).

[16] Lee, H., Thirunavukkarasu, G. K., Kim, S. & Lee, J. Y. Remote induction of in situ hydrogelation in a deep tissue, using an alternating magnetic field and superparamagnetic nanoparticles. *Nano Research* (2018).

[17] Turner, A. P. Biosensors - Sense and sensitivity. *Science* **290**, 1315–1317 (2000).

[18] Pollard, T. D. A Guide to Simple and Informative Binding Assays. *Molecular Biology of the Cell* **21**, 4061–4067 (2017).

[19] Wu, Y., Tilley, R. D. & Gooding, J. J. Challenges and Solutions in Developing Ultrasensitive Biosensors. *Journal of the American Chemical Society* **141**, 1162–1170 (2019).

[20] Glaser, R. W. Antigen-antibody binding and mass transport by convection and diffusion to a surface: A two-dimensional computer model of binding and dissociation kinetics. *Analytical Biochemistry* **213**, 152–161 (1993).

[21] Lynn, N. S. Microfluidic Mixing for Biosensors. In Oh SH., B. A., Escobedo C. (ed.) *Miniature Fluidic Devices for Rapid Biological Detection. Integrated Analytical Systems*, 69–103 (Springer, Cham, 2018).

[22] Romeo, A., Leung, T. S. & Sánchez, S. Smart biosensors for multiplexed and fully integrated point-of-care diagnostics. *Lab on a Chip* **16**, 1957–1961 (2016).

[23] Mo, M. H., Chen, L., Fu, Y., Wang, W. & Fu, S. W. Cell-free Circulating miRNA Biomarkers in Cancer. *Journal of Cancer* **3**, 432–448 (2012).

[24] Zamay, T. N. *et al.* Current and prospective protein biomarkers of lung cancer. *Cancers* **9**, 155 (2017).

[25] Chen, H., Werner, S., Tao, S., Zörnig, I. & Brenner, H. Blood autoantibodies against tumor-associated antigens as biomarkers in early detection of colorectal cancer. *Cancer Letters* **346**, 178–187 (2014).

[26] Wang, C. *et al.* Point-of-care diagnostics for infectious diseases: From methods to devices. *Nano Today* **37**, 101092 (2021).

[27] Mytton, O. T., McCarthy, N., Watson, J. & Whiting, P. Interpreting a lateral flow SARS-CoV-2 antigen test. *BMJ* **373**, n1411 (2021).

[28] Urusov, A. E., Zherdev, A. V. & Dzantiev, B. B. Towards lateral flow quantitative assays: Detection approaches. *Biosensors* **9**, 89 (2019).

[29] Asif, M. *et al.* The role of biosensors in coronavirus disease-2019 outbreak. *Current Opinion in Electrochemistry* **23**, 174–184 (2020).

[30] Kim, J., Campbell, A. S., de Ávila, B. E. F. & Wang, J. Wearable biosensors for healthcare monitoring. *Nature Biotechnology* **37**, 389–406 (2019).

[31] Tu, J. *et al.* The Era of Digital Health: A Review of Portable and Wearable Affinity Biosensors. *Advanced Functional Materials* **30**, 1906713 (2020).

[32] Kumar, S. *et al.* Mobile health technology evaluation: The mHealth evidence workshop. *American Journal of Preventive Medicine* **45**, 228–236 (2013).

[33] Jin, X., Liu, C., Xu, T., Su, L. & Zhang, X. Artificial intelligence biosensors: Challenges and prospects. *Biosensors and Bioelectronics* **165**, 112412 (2020).

[34] Barnes, W. L., Dereux, A. & Ebbesen, T. W. Surface plasmon subwavelength optics. *Nature* **424**, 824–830 (2003).

[35] Reiner, A. T. *et al.* Plasmonic exosome biosensors for medical diagnostics. In Olivo, M. & Dinish, U. (eds.) *Frontiers in Biophotonics for Translational Medicine: In the Celebration of Year of Light (2015)*, 249–272 (Springer, Singapore, 2015).

[36] Wood, R. W. On a remarkable case of uneven distribution of light in a diffraction grating spectrum. *Proceedings of the Physical Society of London* **18**, 269–275 (1901).

[37] Fano, U. The Theory of Anomalous Diffraction Gratings and of Quasi-Stationary Waves on Metallic Surfaces (Sommerfeld's Waves). *Journal of the Optical Society of America* **31**, 213 (1941).

[38] Ritchie, R. H. Plasma Losses by Fast Electrons in Thin Films. *Physical Review* **106**, 874–881 (1957).

[39] Kanazawa, H. On the Plasma Oscillations in Metal Foils. *Progress of Theoretical Physics* **26**, 851–860 (1961).

[40] Stern, E. A. & Ferrell, R. A. Surface plasma oscillations of a degenerate electron gas. *Physical Review* **120**, 130–136 (1960).

[41] Otto, A. Excitation of nonradiative surface plasma waves in silver by the method of frustrated total reflection. *Zeitschrift für Physik* **216**, 398–410 (1968).

[42] Kretschmann, E. & Raether, H. Radiative Decay of Non Radiative Surface Plasmons Excited by Light. *Zeitschrift fur Naturforschung - Section A Journal of Physical Sciences* **23**, 2135–2136 (1968).

[43] Kretschmann, E. Die Bestimmung optischer Konstanten von Metallen durch Anregung von Oberflächenplasmaschwingungen. *Zeitschrift für Physik* **241**, 313–324 (1971).

[44] Liedberg, B., Nylander, C. & Lunström, I. Surface plasmon resonance for gas detection and biosensing. *Sensors and Actuators* **4**, 299–304 (1983).

[45] Liedberg, B., Nylander, C. & Lundström, I. Biosensing with surface plasmon resonance - how it all started. *Biosensors and Bioelectronics* **10**, i–ix (1995).

[46] Dostalek, J., Wang, Y., Huang, C. & Knoll, W. Evanescent Wave Biosensors with a Hydrogel Binding Matrix. In Knoll, W. (ed.) *Handbook of Biofunctional Surfaces*, 361–406 (Pan Stanford Publishing, 2013).

[47] Homola, J. Electromagnetic Theory of Surface Plasmons. In Homola, J. (ed.) *Surface Plasmon Resonance Based Sensors*, 3–44 (Springer, Berlin, Heidelberg, 2006).

[48] Couture, M., Zhao, S. S. & Masson, J.-F. Modern surface plasmon resonance for bioanalytics and biophysics. *Physical Chemistry Chemical Physics* **15**, 11190–11216 (2013).

[49] Knoll, W. Interfaces and thin films as seen by bound electromagnetic waves. *Annual Review of Physical Chemistry* **49**, 569–638 (1998).

[50] Maier, S. A. Excitation of Surface Plasmon Polaritons at Planar Interfaces. In Maier, S. A. (ed.) *Plasmonics: Fundamentals and Applications*, 39–52 (Springer, New York, NY, 2007).

[51] Wijaya, E. *et al.* Surface plasmon resonance-based biosensors: From the development of different SPR structures to novel surface functionalization strategies. *Current Opinion in Solid State and Materials Science* **15**, 208–224 (2011).

[52] Ruffato, G., Zacco, G. & Romanato, F. Innovative Exploitation of Grating-Coupled Surface Plasmon Resonance for Sensing. In Ki Young Kim (ed.) *Plasmonics - Principles and Applications* (IntechOpen, 2012).

[53] Schasfoort, R. B. M. Chapter 2: History and Physics of Surface Plasmon Resonance. In Schasfoort, R. B. (ed.) *Handbook of Surface Plasmon Resonance*, 27–59 (Royal Society of Chemistry, 2017).

[54] Marquart, A., Kuncová-Kallio, J., Albers, M., Bombera, R. & Ståhlberg, R. *Handbook of Multi-Parametric Surface Plasmon Resonance for Molecular Interaction Analysis - Theory and Practice* (Bionavis, Tampere, Finland, 2019), vol 1 edn.

[55] Schasfoort, R. B. M. Chapter 1. Introduction to Surface Plasmon Resonance. In Schasfoort, R. B. (ed.) *Handbook of Surface Plasmon Resonance*, 1–26 (Royal Society of Chemistry, 2017).

[56] Piliarik, M. & Homola, J. SPR Sensor Instrumentation. In Homola, J. (ed.) *Surface Plasmon Resonance Based Sensors*, vol. 4 of *Springer Series on Chemical Sensors and Biosensors*, 95–116 (Springer Berlin Heidelberg, Berlin, Heidelberg, 2006).

[57] Homola, J. *et al.* Spectral surface plasmon resonance biosensor for detection of staphylococcal enterotoxin B in milk. *International Journal of Food Microbiology* **75**, 61–69 (2002).

[58] Homola, J., Yee, S. S. & Gauglitz, G. Surface plasmon resonance sensors: review. *Sensors and Actuators B: Chemical* **54**, 3–15 (1999).

[59] Schasfoort, R. B. & McWhirter, A. Chapter 3: SPR Instrumentation. In Schasfoort, R. B. (ed.) *Handbook of Surface Plasmon Resonance*, 35–80 (Royal Society of Chemistry, 2008).

[60] Jory, M. J., Bradberry, G. W., Cann, P. S. & Sambles, J. R. Surface-plasmon opto-electrochemistry. *Sensors and Actuators, B: Chemical* **35**, 197–201 (1996).

[61] Lawrence, C. R., Geddes, N. J., Furlong, D. N. & Sambles, J. R. Surface plasmon resonance studies of immunoreactions utilizing disposable diffraction gratings. *Biosensors and Bioelectronics* **11**, 389–400 (1996).

[62] Cullen, D. C., Brown, R. G. & Lowe, C. R. Detection of immuno-complex formation via surface plasmon resonance on gold-coated diffraction gratings. *Biosensors* **3**, 211–225 (1987).

[63] Liley, M. Optical transducers. In Gizeli, E. & Lowe, C. R. (eds.) *Biomolecular Sensors*, 53 (Taylor & Francis, London; New York, 2002).

[64] Harris, R. D. & Wilkinson, J. S. Waveguide surface plasmon resonance sensors. *Sensors and Actuators: B. Chemical* **29**, 261–267 (1995).

[65] Homola, J., Ctyroky, J., Slavik, R. & Skalsky, M. Surface plasmon resonance sensors using optical waveguides. In *Third Conference on Photonic Systems for Ecological Monitoring*, vol. 3200, 100 (SPIE, 1997).

[66] Dostálek, J. *et al.* Surface plasmon resonance biosensor based on integrated optical waveguide. *Sensors and Actuators, B: Chemical* **76**, 8–12 (2001).

[67] Yildizhan, Y. *et al.* FO-SPR biosensor calibrated with recombinant extracellular vesicles enables specific and sensitive detection directly in complex matrices. *Journal of Extracellular Vesicles* **10** (2021).

[68] Homepage - Breaking Limits in Bioanalysis | FOx BIOSYSTEMS. URL `https://foxbiosystems.com/`.

[69] Arghir, I., Delport, F., Spasic, D. & Lammertyn, J. Smart design of fiber optic surfaces for improved plasmonic biosensing. *New Biotechnology* **32**, 473–484 (2015).

[70] Wilkinson, J. S. Optical Waveguide Spectroscopy. *Handbook of Spectroscopy: Second, Enlarged Edition* **4-4**, 1611–1642 (2014).

[71] Dostálek, J. & Knoll, W. Plasmonics. *Polymer Science: A Comprehensive Reference, 10 Volume Set* **2**, 647–659 (2012).

[72] Wang, Y. *et al.* Biosensor based on hydrogel optical waveguide spectroscopy. *Biosensors and Bioelectronics* **25**, 1663–1668 (2010).

[73] Dostálek, J. & Knoll, W. Plasmonics. In Matyjaszewski, K. & Möller, M. (eds.) *Polymer Science: A Comprehensive Reference*, vol. 2, 647–659 (Elsevier B.V., Amsterdam, 2012).

[74] Willets, K. A. & Van Duyne, R. P. Localized surface plasmon resonance spectroscopy and sensing. *Annual Review of Physical Chemistry* **58**, 267–297 (2007).

[75] Zhou, J., Wang, Y., Zhang, L. & Li, X. Plasmonic biosensing based on non-noble-metal materials. *Chinese Chemical Letters* **29**, 54–60 (2018).

[76] Chen, H., Kou, X., Yang, Z., Ni, W. & Wang, J. Shape- and size-dependent refractive index sensitivity of gold nanoparticles. *Langmuir* **24**, 5233–5237 (2008).

[77] Jain, P. K. & El-Sayed, M. A. Plasmonic coupling in noble metal nanostructures. *Chemical Physics Letters* **487**, 153–164 (2010).

[78] Haes, A. J., Stuart, D. A., Nie, S. & Van Duyne, R. P. Using solution-phase nanoparticles, surface-confined nanoparticle arrays and single nanoparticles as biological sensing platforms. *Journal of Fluorescence* **14**, 355–367 (2004).

[79] Mazzotta, F. *et al.* Influence of the evanescent field decay length on the sensitivity of plasmonic nanodisks and nanoholes. *ACS Photonics* **2**, 256–262 (2015).

[80] Theisen, A. *Refractive increment data-book for polymer and biomolecular scientists* (Nottingham University Press, 2000).

[81] Tumolo, T., Angnes, L. & Baptista, M. S. Determination of the refractive index increment (dn/dc) of molecule and macromolecule solutions by surface plasmon resonance. *Analytical Biochemistry* **333**, 273–279 (2004).

[82] Bozdogan, A., Hageneder, S. & Dostalek, J. Plasmonic biosensors relying on biomolecular conformational changes: Case of odorant binding proteins. In *Methods in Enzymology* (Elsevier, 2020).

[83] Skoog, D. A., Holler, F. J. & Crouch, S. R. *Principles of Instrumental Analysis.* International student edition (Thomson Brooks/Cole, 2007).

[84] Biosensing Instrument. Technical Note #102 SPR Sensitivity and Detection Limit (2010).

[85] Li, J. *et al.* Revisiting the surface sensitivity of nanoplasmonic biosensors. *ACS Photonics* **2**, 425–431 (2015).

[86] Zalyubovskiy, S. J. *et al.* Theoretical limit of localized surface plasmon resonance sensitivity to local refractive index change and its comparison to conventional surface plasmon resonance sensor. *Journal of the Optical Society of America A* **29**, 994 (2012).

[87] Svedendahl, M., Chen, S., Dmitriev, A. & Käll, M. Refractometric sensing using propagating versus localized surface plasmons: A direct comparison. *Nano Letters* **9**, 4428–4433 (2009).

[88] Rahman, M. M. *et al.* Sensitivity enhancement of SPR biosensors employing heterostructure of PtSe2 and 2D materials. *Optical Materials* **107**, 110123 (2020).

[89] Karlsson, R. & Ståhlberg, R. Surface Plasmon Resonance Detection and Multispot Sensing for Direct Monitoring of Interactions Involving Low-Molecular-Weight Analytes and for Determination of Low Affinities. *Analytical Biochemistry* **228**, 274–280 (1995).

[90] Lappas, N. T. & Lappas, C. M. Methods of Detection, Identification, and Quantitation. *Forensic Toxicology* 161–181 (2016).

[91] Homola, J. & Piliarik, M. *Surface Plasmon Resonance (SPR) Sensors*, 45–67 (Springer Berlin Heidelberg, Berlin, Heidelberg, 2006).

[92] Dostálek, J., Přibyl, J., Homola, J. & Skládal, P. Multichannel SPR biosensor for detection of endocrine-disrupting compounds. *Analytical and Bioanalytical Chemistry* **389**, 1841–1847 (2007).

[93] Reiner, A. T. *et al.* Magnetic nanoparticle-enhanced surface plasmon resonance biosensor for extracellular vesicle analysis. *Analyst* **142**, 3913–3921 (2017).

[94] Hall, W. P. *et al.* A conformation- and ion-sensitive plasmonic biosensor. *Nano Letters* **11**, 1098–1105 (2011).

[95] Wei, M., Li, X. & Serpe, M. J. Stimuli-Responsive Microgel-Based Surface Plasmon Resonance Transducer for Glucose Detection Using a Competitive Assay with Concanavalin A. *ACS Applied Polymer Materials* **1**, 519–525 (2019).

[96] Jeanmaire, D. L. & Van Duyne, R. P. Surface raman spectroelectrochemistry: Part I. Heterocyclic, aromatic, and aliphatic amines adsorbed on the anodized silver electrode. *Journal of Electroanalytical Chemistry and Interfacial Electrochemistry* **84**, 1–20 (1977).

[97] Heberle, J. & Ataka, K. Surface Enhanced Infrared Absorption Spectroscopy. In *Encyclopedia of Biophysics*, 2528–2531 (Springer, Berlin, Heidelberg, 2013).

[98] Liebermann, T. & Knoll, W. Surface-plasmon field-enhanced fluorescence spectroscopy. *Colloids and Surfaces A: Physicochemical and Engineering Aspects* **171**, 115–130 (2000).

[99] Lakowicz, J. R. Introduction to Fluorescence. In Lakowicz, J. R. (ed.) *Principles of Fluorescence Spectroscopy*, 1–26 (Springer US, Boston, MA, 2006).

[100] Jabłoński, A. Über den Mechanismus der Photolumineszenz von Farbstoffphosphoren. *Zeitschrift für Physik* **94**, 38–46 (1935).

[101] Bauch, M., Toma, K., Toma, M., Zhang, Q. & Dostalek, J. Plasmon-Enhanced Fluorescence Biosensors: a Review. *Plasmonics* **9**, 781–799 (2014).

[102] Neumann, T., Johansson, M.-L., Kambhampati, D. & Knoll, W. Surface Plasmon Fluorescence Spectroscopy. *Advanced Functional Materials* **12**, 575–586 (2002).

[103] Huang, C.-J., Jonas, U., Dostálek, J. & Knoll, W. Biosensor platform based on surface plasmon-enhanced fluorescence spectroscopy and responsive hydrogel binding matrix. In *Optical Sensors 2009*, vol. 7356, 735625–735625 (International Society for Optics and Photonics, 2009).

[104] Chen, X. & Wu, Y.-W. Selective chemical labeling of proteins. *Organic & biomolecular chemistry* **14**, 5417–5439 (2016).

[105] Kitson, S. C., Barnes, W. L., Sambles, J. R. & Cotter, N. P. K. Excitation of molecular fluorescence via surface plasmon polaritons. *Journal of modern optics* **43**, 573–582 (1996).

[106] Ford, G. W. & Weber, W. H. Electromagnetic interactions of molecules with metal surfaces. *Physics Reports* **113**, 195–287 (1984).

[107] Aslan, K. *et al.* Metal-enhanced fluorescence: An emerging tool in biotechnology. *Current Opinion in Biotechnology* **16**, 55–62 (2005).

[108] Lakowicz, J. R. Radiative decay engineering 5: Metal-enhanced fluorescence and plasmon emission. *Analytical Biochemistry* **337**, 171–194 (2005).

[109] Szunerits, S., Castel, X. & Boukherroub, R. Surface Plasmon Resonance Investigation of Silver and Gold Films Coated with Thin Indium Tin Oxide Layers: Influence on Stability and Sensitivity. *Journal of Physical Chemistry C* **112**, 15813–15817 (2008).

[110] Gedig, E. T. Chapter 6. Surface Chemistry in SPR Technology. In *Handbook of Surface Plasmon Resonance*, 173–220 (Royal Society of Chemistry, 2008).

[111] Huang, H. W., Tibbitt, M. W., Huang, T. Y. & Nelson, B. J. Matryoshka-Inspired Micro-Origami Capsules to Enhance Loading, Encapsulation, and Transport of Drugs. *Soft Robotics* **6**, 150–159 (2019).

[112] Johnsson, B., Löfås, S. & Lindquist, G. Immobilization of proteins to a carboxymethyldextran-modified gold surface for biospecific interaction analysis in surface plasmon resonance sensors. *Analytical Biochemistry* **198**, 268–277 (1991).

[113] Thermo Scientific. Crosslinking Technology. *Crosslinking Technical Handbook* 1–54 (2009).

[114] Blangmack20. EDC Mechanism - Wikimedia Commons (2019). URL `https://commons.wikimedia.org/wiki/File:EDC_Mechanism_.tif#/media/File:EDC_Mechanism_.tif`.

[115] Fischer, M. J. E. Amine Coupling Through EDC/NHS: A Practical Approach. *Methods in molecular biology (Clifton, N.J.)* **627**, 55–73 (2010).

[116] Löfås, S. & Mcwhirter, A. The Art of Immobilization for SPR Sensors. In Homola, J. (ed.) *Surface Plasmon Resonance Based Sensors*, 117–151 (Springer, Berlin, Heidelberg, 2006).

[117] Moses, J. E. & Moorhouse, A. D. The growing applications of click chemistry. *Chemical Society Reviews* **36**, 1249–1262 (2007).

[118] Jewett, J. C. & Bertozzi, C. R. Cu-free click cycloaddition reactions in chemical biology. *Chemical Society Reviews* **39**, 1272–1279 (2010).

[119] Meldal, M. & Tomøe, C. W. Cu-catalyzed azide - Alkyne cycloaddition. *Chemical Reviews* **108**, 2952–3015 (2008).

[120] Healthcare, G. E. Biacore concentration analysis handbook. *Uppsala: GE Healthcare* (2007).

[121] Bergström, G. & Mandenius, C. F. Orientation and capturing of antibody affinity ligands: Applications to surface plasmon resonance biochips. *Sensors and Actuators, B: Chemical* **158**, 265–270 (2011).

[122] Turková, J. Oriented immobilization of biologically active proteins as a tool for revealing protein interactions and function. *Journal of Chromatography B: Biomedical Sciences and Applications* **722**, 11–31 (1999).

[123] Wilchek, M. & Bayer, E. A. Introduction to avidin-biotin technology. *Methods in Enzymology* **184**, 5–13 (1990).

[124] GREEN, N. M. AVIDIN. 3. THE NATURE OF THE BIOTIN-BINDING SITE. *The Biochemical journal* **89**, 599–609 (1963).

[125] Sunasee, R. & Narain, R. Covalent and Noncovalent Bioconjugation Strategies. In Narain, R. (ed.) *Chemistry of Bioconjugates: Synthesis, Characterization, and Biomedical Applications*, vol. 9781118359, 1–75 (Wiley Blackwell, 2014).

[126] Yalow, R. S. & Berson, S. A. Assay of plasma insulin in human subjects by immunological methods. *Nature* **184**, 1648–1649 (1959).

[127] Davies, C. Principles of competitive and immunometric assays (including ELISA). In Wild, D. (ed.) *The Immunoassay Handbook* (Elsevier Oxford, UK:, 2013).

[128] Janeway, C. A. J., Travers, P., Walport, M. & Shlomchik, M. J. The structure of a typical antibody molecule. In *Immunobiology: The Immune System in Health and Disease. 5th edition.* (Garland Science, 2001).

[129] Reading, C. L. Theory and methods for immunization in culture and monoclonal antibody production. *Journal of Immunological Methods* **53**, 261–291 (1982).

[130] Engvall, E. & Perlmann, P. Enzyme-linked immunosorbent assay (ELISA) quantitative assay of immunoglobulin G. *Immunochemistry* **8**, 871–874 (1971).

[131] Van Weemen, B. K. & Schuurs, A. H. Immunoassay using antigen-enzyme conjugates. *FEBS Letters* **15**, 232–236 (1971).

[132] Ghassabeh, G. H., Muyldermans, S. & Saerens, D. Nanobodies, Single-Domain Antigen-Binding Fragments of Camelid Heavy-Chain Antibodies. In Shire, S. J., Gombotz, W., Bechtold-Peters, K. & Andya, J. (eds.) *Current Trends in Monoclonal Antibody Development and Manufacturing*, 29–48 (Springer New York, 2010).

[133] Chambers, J. P., Arulanandam, B. P., Matta, L. L., Weis, A. & Valdes, J. J. Biosensor recognition elements. *Current Issues in Molecular Biology* **10**, 1–12 (2008).

[134] Ariga, K., Nakanishi, T. & Michinobu, T. Immobilization of biomaterials to nano-assembled films (self-assembled monolayers, langmuir-blodgett films, and layer-by-layer assemblies) and their related functions. *Journal of Nanoscience and Nanotechnology* **6**, 2278–2301 (2006).

[135] Nuzzo, R. G. & Allara, D. L. Adsorption of bifunctional organic disulfides on gold surfaces. *Journal of the American Chemical Society* **105**, 4481–4483 (1983).

[136] Knoll, W., Liley, M., Piscevic, D., Spinke, J. & Tarlov, M. J. Supramolecular Architectures for the functionalization of solid surfaces. *Advances in Biophysics* **34**, 231–251 (1997).

[137] Vericat, C., Vela, M. E., Benitez, G., Carro, P. & Salvarezza, R. C. Self-assembled monolayers of thiols and dithiols on gold: new challenges for a well-known system. *Chemical Society Reviews* **39**, 1805–1834 (2010).

[138] Bergstrom, J., Lofas, S. & Johnsson, B. Sensing surfaces capable of selective biomolecular interactions, to be used in biosensor systems (1993).

[139] Tanaka, M., Hayashi, T. & Morita, S. The roles of water molecules at the biointerface of medical polymers. *Polymer Journal* **45**, 701–710 (2013).

[140] Rühe, J. *Polymer Brushes: On the Way to Tailor-Made Surfaces*, 1–31 (John Wiley & Sons, Ltd, 2004).

[141] Ayres, N. Polymer brushes: Applications in biomaterials and nanotechnology. *Polymer Chemistry* **1**, 769–777 (2010).

[142] Wang, S., Wang, Z., Li, J., Li, L. & Hu, W. Surface-grafting polymers: From chemistry to organic electronics. *Materials Chemistry Frontiers* **4**, 692–714 (2020).

[143] Kim, M., Schmitt, S. K., Choi, J. W., Krutty, J. D. & Gopalan, P. From Self-Assembled Monolayers to Coatings: Advances in the Synthesis and Nanobio Applications of Polymer Brushes. *Polymers 2015, Vol. 7, Pages 1346-1378* **7**, 1346–1378 (2015).

[144] Karim, A. *et al.* Self-organization of polymer brush layers in a poor solvent. *Journal de physique. II* **5**, 1441–1456 (1995).

[145] Taylor, W. & Jones, R. A. Producing high-density high-molecular-weight polymer brushes by a "grafting to" method from a concentrated homopolymer solution. *Langmuir* **26**, 13954–13958 (2010).

[146] Zdyrko, B. & Luzinov, I. Polymer Brushes by the "Grafting to" Method. *Macromolecular Rapid Communications* **32**, 859–869 (2011).

[147] Zhao, B. & Brittain, W. J. Polymer brushes: surface-immobilized macromolecules. *Progress in Polymer Science* **25**, 677–710 (2000).

[148] Otsu, T., Yoshida, M. & Tazaki, T. A model for living radical polymerization. *Die Makromolekulare Chemie, Rapid Communications* **3**, 133–140 (1982).

[149] Blaszykowski, C., Sheikh, S. & Thompson, M. Surface chemistry to minimize fouling from blood-based fluids. *Chemical Society Reviews* **41**, 5599–5612 (2012).

[150] Matyjaszewski, K. Atom Transfer Radical Polymerization (ATRP): Current status and future perspectives. *Macromolecules* **45**, 4015–4039 (2012).

[151] Krishnamoorthy, M., Hakobyan, S., Ramstedt, M. & Gautrot, J. E. Surface-Initiated Polymer Brushes in the Biomedical Field: Applications in Membrane Science, Biosensing, Cell Culture, Regenerative Medicine and Antibacterial Coatings. *Chemical Reviews* **114**, 10976–11026 (2014).

[152] Teraoka, I. *Polymer Solutions: An Introduction to Physical Properties* (John Wiley & Sons, Inc., 2002).

[153] Jonas, U., van den Brom, C. R., Brunsen, A. & Roskamp, R. F. Surface attached polymeric hydrogel films. In Knoll, W. (ed.) *Handbook of Biofunctional Surfaces. Pan Stanford Publishing*, 277 (Pan Stanford Publishing, 2013).

[154] Moh, L. C., Losego, M. D. & Braun, P. V. Solvent quality effects on scaling behavior of poly(methyl methacrylate) brushes in the moderate- and high-density regimes. *Langmuir* **27**, 3698–3702 (2011).

[155] Milner, S. T., Witten, T. A. & Cates, M. E. Theory of the Grafted Polymer Brush. *Macromolecules* **21**, 2610–2619 (1988).

[156] Mateescu, A., Wang, Y., Dostalek, J. & Jonas, U. Thin hydrogel films for optical biosensor applications. *Membranes* **2**, 49–69 (2012).

[157] Hennink, W. E. & van Nostrum, C. F. Novel crosslinking methods to design hydrogels. *Advanced Drug Delivery Reviews* **64**, 223–236 (2012).

[158] Kuckling, D., Harmon, M. E. & Frank, C. W. Photo-cross-linkable PNIPAAm copolymers. 1. Synthesis and characterization of constrained temperature-responsive hydrogel layers. *Macromolecules* **35**, 6377–6383 (2002).

[159] Mutschler, T., Kieser, B., Frank, R. & Gauglitz, G. Characterization of thin polymer and biopolymer layers by ellipsometry and evanescent field technology. *Analytical and Bioanalytical Chemistry* **374**, 658–664 (2002).

[160] Kirillova, A., Maxson, R., Stoychev, G., Gomillion, C. T. & Ionov, L. 4D Biofabrication Using Shape-Morphing Hydrogels. *Advanced Materials* **29**, 1–8 (2017).

[161] Zhao, L. *et al.* Engineering Nonmechanical Protein-Based Hydrogels with Highly Mechanical Properties: Comparison with Natural Muscles. *Biomacromolecules* **21**, 4212–4219 (2020).

[162] Pandiyarajan, C. K., Prucker, O. & Rühe, J. Humidity Driven Swelling of the Surface-Attached Poly(N -alkylacrylamide) Hydrogels. *Macromolecules* **49**, 8254–8264 (2016).

[163] Liu, B. *et al.* Design and mechanisms of antifouling materials for surface plasmon resonance sensors. *Acta biomaterialia* **40**, 100–118 (2016).

[164] Peppas, N. A., Hilt, J. Z., Khademhosseini, A. & Langer, R. Hydrogels in biology and medicine: From molecular principles to bionanotechnology. *Advanced Materials* **18**, 1345–1360 (2006).

[165] Chen, T., Ferris, R., Zhang, J., Ducker, R. & Zauscher, S. Stimulus-responsive polymer brushes on surfaces: Transduction mechanisms and applications. *Progress in Polymer Science (Oxford)* **35**, 94–112 (2010).

[166] Saunders, B. R. *et al.* Microgels: From responsive polymer colloids to biomaterials. *Advances in Colloid and Interface Science* **147-148**, 251–262 (2009).

[167] Junk, M. J., Ilke, A., Menges, B. & Jonas, U. Analysis of optical gradient profiles during temperature- and salt-dependent swelling of thin responsive hydrogel films. *Langmuir* **26**, 12253–12259 (2010).

[168] Beines, P. W., Klosterkamp, I., Menges, B., Jonas, U. & Knoll, W. Responsive thin hydrogel layers from photo-cross-linkable poly(N-isopropylacrylamide) terpolymers. *Langmuir* **23**, 2231–2238 (2007).

[169] Harmon, M. E., Kuckling, D. & Frank, C. W. Photo-cross-linkable PNIPAAm copolymers. 2. Effects of constraint on temperature and pH-responsive hydrogel layers. *Macromolecules* **36**, 162–172 (2003).

[170] Schenderlein, H., Voss, A., Stark, R. W. & Biesalski, M. Preparation and characterization of light-switchable polymer networks attached to solid substrates. *Langmuir* **29**, 4525–4534 (2013).

[171] Amaral, A. J. & Pasparakis, G. Stimuli responsive self-healing polymers: Gels, elastomers and membranes. *Polymer Chemistry* **8**, 6464–6484 (2017).

[172] Jiang, S. & Cao, Z. Ultralow-fouling, functionalizable, and hydrolyzable zwitterionic materials and their derivatives for biological applications. *Advanced Materials* **22**, 920–932 (2010).

[173] Ostuni, E. *et al.* Self-Assembled Monolayers That Resist the Adsorption of Proteins and the Adhesion of Bacterial and Mammalian Cells. *Langmuir* **17**, 6336–6343 (2001).

[174] Ostuni, E., Chapman, R. G., Holmlin, R. E., Takayama, S. & Whitesides, G. M. A Survey of Structure - Property Relationships of Surfaces that Resist the Adsorption of Protein. *Langmuir* **17**, 5605–5620 (2001).

[175] Pasut, G. & Veronese, F. M. State of the art in PEGylation: The great versatility achieved after forty years of research. *Journal of Controlled Release* **161**, 461–472 (2012).

[176] Li, B. & Ye, Q. Antifouling surfaces of self-assembled thin layer. In Zhou, F. (ed.) *Antifouling Surfaces and Materials*, chap. 2, 31–54 (Springer-Verlag, Berlin, 2015).

[177] Chen, S., Li, L., Boozer, C. L. & Jiang, S. Controlled chemical and structural properties of mixed self-assembled monolayers of alkanethiols on Au(111). *Langmuir* **16**, 9287–9293 (2000).

[178] Nelson, K. E. *et al.* Surface characterization of mixed self-assembled monolayers designed for streptavidin immobilization. *Langmuir* **17**, 2807–2816 (2001).

[179] Chen, S., Li, L., Zhao, C. & Zheng, J. Surface hydration: Principles and applications toward low-fouling/nonfouling biomaterials. *Polymer* **51**, 5283–5293 (2010).

[180] Choudhury, R. R., Gohil, J. M., Mohanty, S. & Nayak, S. K. Antifouling, fouling release and antimicrobial materials for surface modification of reverse osmosis and nanofiltration membranes. *Journal of Materials Chemistry A* **6**, 313–333 (2018).

[181] Wang, Y. S., Yau, S., Chau, L. K., Mohamed, A. & Huang, C. J. Functional Biointerfaces Based on Mixed Zwitterionic Self-Assembled Monolayers for Biosensing Applications. *Langmuir* **35**, 1652–1661 (2019).

[182] Riedel, T. *et al.* Hepatitis B plasmonic biosensor for the analysis of clinical serum samples. *Biosensors and Bioelectronics* **85**, 272–279 (2016).

[183] Rodriguez-Emmenegger, C., Houska, M., Alles, A. B. & Brynda, E. Surfaces Resistant to Fouling from Biological Fluids: Towards Bioactive Surfaces for Real Applications. *Macromolecular Bioscience* **12**, 1413–1422 (2012).

[184] Han, Y. *et al.* Bottom-up fabrication of zwitterionic polymer brushes on intraocular lens for improved biocompatibility. *International Journal of Nanomedicine* **12**, 127–135 (2017).

[185] Sin, M. C., Chen, S. H. & Chang, Y. Hemocompatibility of zwitterionic interfaces and membranes. *Polymer Journal* **46**, 436–443 (2014).

[186] Jarvius, J. *et al.* Digital quantification using amplified single-molecule detection. *Nature methods* **3**, 725–727 (2006).

[187] Ionov, L. Hydrogel-based actuators: Possibilities and limitations. *Materials Today* **17**, 494–503 (2014).

[188] Pastoriza-Santos, I., Kinnear, C., Pérez-Juste, J., Mulvaney, P. & Liz-Marzán, L. M. Plasmonic polymer nanocomposites. *Nature Reviews Materials* **3**, 375–391 (2018).

[189] Umar, M., Min, K. & Kim, S. Advances in hydrogel photonics and their applications. *APL Photonics* **4** (2019).